Miniaturization and Integration of Photoacoustic Detection

by

Samara Louise Firebaugh

B. S. E. Princeton University (1995)
S. M. Massachusetts Institute of Technology (1997)

Submitted to the Department of Electrical Engineering and Computer Science
in partial fulfillment of the requirements for the degree of

Doctor of Philosophy

at the

MASSACHUSETTS INSTITUTE OF TECHNOLOGY

May 2001
[June 2001]

Signature of Author _____
Department of Electrical Engineering and Computer Science
May 25, 2001

Certified by _____ 5/21/01
Martin A. Schmidt
Professor of Electrical Engineering
Thesis Supervisor

Certified by _____
Klavs F. Jensen
Lammot du Pont Professor of Chemical Engineering
Thesis Supervisor

Accepted by _____
Arthur C. Smith
Chair, Department Committee for Graduate Students

Miniaturization and Integration of Photoacoustic Detection

by
Samara Louise Firebaugh

Submitted to the Department of Electrical Engineering and Computer Science
on May 25, 2001, in partial fulfillment of the
requirements for the degree of
Doctor of Philosophy

Abstract

Photoacoustic spectroscopy (PAS) is an absorption spectroscopy technique that is currently used for low-level gas detection, biological studies, and catalyst characterization. In PAS, the incident radiation is modulated at an acoustic frequency. In the presence of an absorbing species, the periodic radiation is translated into periodic heat generation, which launches an acoustic signal. PAS is a promising technique for chemical analysis in mesoscale analysis systems because the detection limit scales favorably with miniaturization. This work focuses on the miniaturization of gas-phase photoacoustic detection of propane in a nitrogen or carbon dioxide ambient. This work could be expanded to other chemical species or to spectroscopy with a change of light source.

The detection system was modeled with a transmission line analogy, which was verified with a set of experiments. The model includes the effects of acoustic leaks and absorption saturation. These two phenomena degrade the performance of the PA detector and must be controlled to realize the scaling advantages of PA systems. The miniature brass cells used to verify the model used hearing aid microphones and optical excitation from a mechanically-chopped, 3.39-μm He-Ne laser, transmitted into the cells with an optical fiber. I was able to detect 10 ppm of propane in nitrogen with these cells (a signal level of ~ 1 Pa/W).

This thesis describes the development of two more miniaturized PA systems-- one formed by microfabrication and another in which PA detection is integrated with another miniaturized system. The microfabricated PA detector used the He-Ne laser and a less-sensitive optical microphone. I was able to detect 5% propane in nitrogen with this detector, which had a signal level of about 100 Pa/W. In the integrated system, a PA cell was machined into the mounting chuck of a microfabricated chemical reactor. The detector used a hearing aid microphone and a 3.4 μm infrared diode that was modulated at the first acoustic resonance of the cell. The integrated system was not as well characterized as the others, but demonstrates the potential for portability and integration of PA detection systems.

These systems have shown that PA detection may be inappropriate for systems with large variations in gas concentration because of absorption saturation and changing gas acoustic properties. However, it is a promising technique for the analysis of dilute mixtures in miniature chemical systems and may also be useful in miniaturized multi-phase systems.

Thesis Supervisor: Martin A. Schmidt
Title: Professor of Electrical Engineering

Thesis Supervisor: Klavs F. Jensen
Title: Lammot du Pont Professor of Chemical Engineering

Acknowledgements

This work was sponsored by the National Science Foundation and by the DARPA Microflumes program. In addition to my sponsors, there is a long list of people who contributed to this thesis. First and foremost, I would like to thank my advisors, Marty Schmidt and Klavs Jensen. Without their faith, encouragement, and guidance this thesis would never have been possible. I am also grateful to the other members of my committee, to Rajeev Ram for all his help with the optics and for encouraging me to think "out of the box" and to Steve Senturia for raising the bar.

George Turner and his staff at Lincoln Labs provided the He-Ne laser that became the backbone of my experiments. I am also extremely grateful to Harry Lee and the other members of Professor Ram's research group who taught me how to work with and package optical fibers. I did most of my conventional machining in the Edgerton Center student shop with the help of machine shop guru Fred Cote. For the rest of the machining, I am grateful for the services of Peter Morley and his crew in the Central Machine Shop. The fabrication of my μPA cells was made possible by the hard work of the Microsystems Technology Laboratories staff, particularly Vicky Diadiuk, Kurt Broderick, and Tom Takacs. Mark Sheplak and Stephen Horowitz at the University of Florida were of invaluable assistance in the packaging and calibration of my microphones.

I also would like to thank all of the past and present members of the Schmidt and Jensen groups, who have been my teachers and cheerleaders, particularly Joel Voldman, Rebecca Jackman, Ravi Srinivasan, Lalitha Parameswaran, Professor Sheplak, Errol Arkilic, Kathy Vaeth, Tamara Floyd, Aleks Franz, Matt Losey, and Sameer Ajmera. Thanks also to my workout buddy, Iliana Fujimori, who helped me stay sane, and forgave my occasional indolence.

I'm grateful to the housemasters, residents, staff and fellow tutors of Baker House – particularly Carrie and Jason Hendricks – for giving me a home outside of the lab. Special thanks to the residents of the sixth floor who cheerfully put up with a scarcity of study breaks in my last semester.

I never would have gotten to MIT or through this thesis without the support of my family – Mom, Dad and my brother Josh – and the love (and editorial comments) of my husband, Will. Finally, for the ability to achieve even this small thing, I am grateful for the grace of the Lord.

Table of Contents

Table of Figures

List of Tables

1. Introduction

Miniature chemical sensing systems have a broad range of applications including portable environmental monitoring and process control. In particular, the integration of chemical analysis with microfabricated chemical reactor systems would facilitate the quantitative, parallel testing of large catalyst arrays, which is currently a bottleneck for chemical process development [1, 2]. As a simple, general, optical method for gas-phase detection, photoacoustic spectroscopy offers several advantages [3]. It applies to many chemical compounds, and, unlike conventional absorption spectroscopy, the sensitivity of photoacoustic spectroscopy scales inversely with dimensions [3]. The detection element for a photoacoustic cell is a microphone, a device that has been microfabricated and integrated into other microelectromechanical systems [4].

In photoacoustic (also called optoacoustic) spectroscopy, incident light is modulated at an acoustic frequency. If the optical wavelength couples to an energy transition in the gas, the gas absorbs the light resulting in a periodic gas expansion that can be detected by a microphone. Photoacoustic phenomena were largely ignored until Kreuzer [5] built a photoacoustic detector based on a laser source. Photoacoustic detection is now commonly used for low-level gas sensing [6] and catalyst studies [7], and is also used for liquids and solids [8]. Little work has been done with the miniaturization of photoacoustic devices. This thesis presents an analysis of the potential for miniaturization and integration of photoacoustic detection, and describes the first demonstration of a micromachined photoacoustic detection system [9].

1.1. *Strategy*

The ultimate objective is to fully integrate photoacoustic spectroscopy and chemical reaction in a self-contained system. However, this is far too large a project for a single thesis. Instead, this thesis aims to lay the groundwork for such a system by focusing on the miniaturization of photoacoustic detection, using a single, well-characterized, light source and a well-known absorption peak (the "C-H" stretch of propane at 3.4 μm). Once detection is established, the system can be extended to spectroscopy by using a tunable light source, or a broadband light source coupled with an interferometer or monochromator. A wide range of

broadband light sources already exist for conventional spectroscopy systems, so the expansion of a detection system into a spectroscopy system should be possible.

The miniaturization of such a light source, along with modulation capability, for an integrated photoacoustic spectroscopy system would be non-trivial. A more readily implemented integration scheme, envisioned in this thesis, is shown in Figure 1-1. A conventional light source could be shared among multiple detectors. Such a scheme could facilitate the parallel monitoring of multiple chemical reactors.

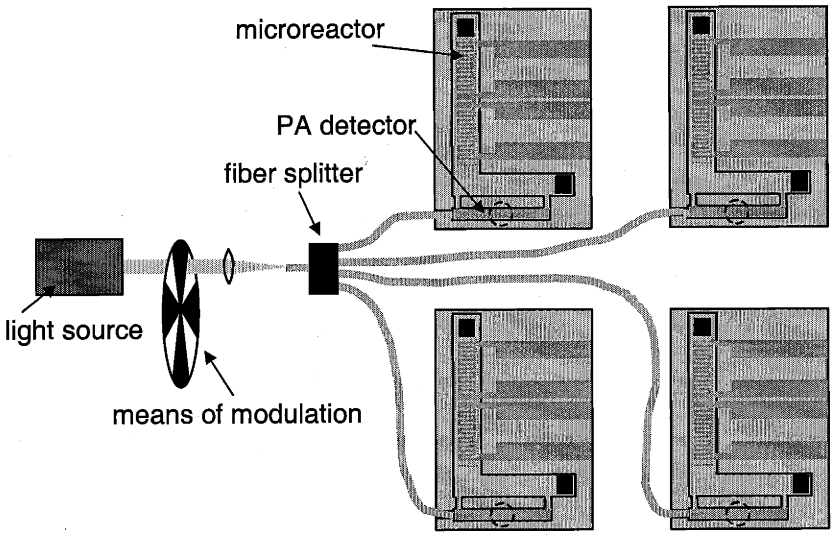

Figure 1-1: Illustration of integration concept

1.2. *Goals of the thesis*

The aim of this thesis was to fully consider how photoacoustic analysis might be applicable to meso-scale systems. Specifically, this thesis set out to meet the following goals:

- Quantitative analysis of photoacoustic effect on miniature scale and correlation with experiment
- Demonstration of photoacoustic detection on the miniature scale
- Demonstration of a microfabricated photoacoustic detector
- Demonstration of miniaturized photoacoustic detection in a system

1.3. *Overview*

Chapter 2 focuses on the other work in integrated analysis and photoacoustic spectroscopy. A transmission line model for photoacoustic detection is described in Chapter 3. Chapter 4 describes a series of miniature photoacoustic detectors, manufactured out of brass, that

were used to validate the predictions of the model. I chose this detector design for theory validation because of its ease of manufacture, and its ready integration with a commercial microphone. It was therefore more easily calibrated and varied than a microfabricated system. Chapter 4 also describes the integration of a brass photoacoustic detection cell with a microreactor.

Chapter 5 describes the microfabrication of a photoacoustic detector. For simplicity, I used an optical microphone that relied on a commercial displacement sensor. As was the case with the light source, the integration of a more sophisticated and self-contained microphone would greatly enhance the performance of the device, but could be another thesis.

There are two special issues with photoacoustic detection that repeatedly appear in this thesis: the first is the issue of signal saturation, and the second is the problem of confining the acoustic signal while allowing for mass flow. These considerations place special constraints on the range and integration of photoacoustic detection that may not exist for other detection methods. Chapter 6 summarizes the work in the thesis and discusses the systems for which photoacoustic detection is appropriate.

1.4. *Terminology*

1.4.1. *Optoacoustic or photoacoustic?*

Different terminology has been used to describe the effect of sound being generated from the absorption of a periodically-modulated beam. The original term used by Bell [10] was the "optoacoustic" effect. The term "optoacoustic" was also used in the seventies by the pioneers that rejuvenated the idea of photoacoustic detection with the use of lasers as light sources [3, 5, 11]. In his work with the solid-phase effect, Rosencwaig changed to the term "photoacoustic" in order to avoid confusion with the acousto-optic effect, in which light interacts with the acoustic or elastic waves in a crystal [12]. A few researchers still make the distinction of "photoacoustic" applying to nongaseous matter and "optoacoustic" applying to gases. However, the term "photoacoustic" is now widely used for all photocalorimetric studies, regardless of material phase. In order to remain allied with the current literature, I have chosen to use the term "photoacoustic" with my work, even though it is in the gas phase.

1.4.2. *Radius, resistance, or gas constant?*

Part of the allure of photoacoustic spectroscopy is that it combines so many disciplines--chemistry, optics, and acoustics as well as linear circuit theory. The price of such breadth, however, is a morass of confusing and often contradictory symbols. (I've found R to be particularly problematic.) The reconciliation of the different lexicons inevitably results in a few awkward labels such as W for light power and $\mathcal{R}$ for resistance in acoustic circuit analogies. I have tried to make the variables clear in context, however the reader may occasionally wish to refer to Appendix A, which contains a listing of the symbols used throughout the thesis.

1.4.3. *Cavities, cells, detectors and systems*

There are several layers to the photoacoustic device structures described in this thesis. The basic device structure is termed a photoacoustic "cell." The "cell" consists of a photoacoustic "cavity" where the gas is illuminated and the sound generated, gas flow "channels" through which the analyte enters and leaves the cavity, an optical "port" through which light enters the cell, a "window" through which light exits the cell, and a microphone "tap," where the sound pressure is sampled. Figure 1-2 shows a sketch of a generic photoacoustic cell. The form of these elements varies in different cells. For example, in the microfabricated photoacoustic cell the "microphone tap" is a membrane that also serves as a wall to the photoacoustic cavity, and the "window" is made up of the entire cavity wall surface.

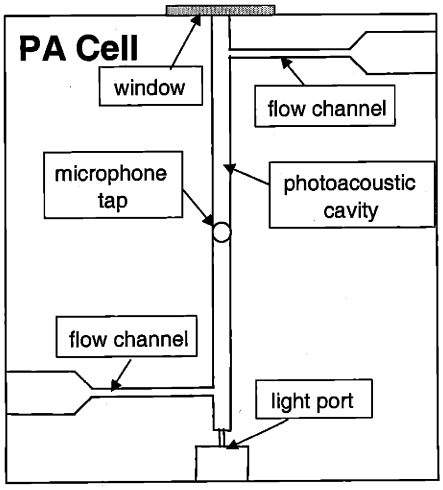

Figure 1-2: A generic photoacoustic "cell"

The photoacoustic "cell," combined with the modulated light source, pressure transducer, flow manifold, lock-in amplifier, data acquisition and control electronics, make up a

"photoacoustic detector." Finally, a "photoacoustic detector" combined with a microreactor is a "microchemical system."

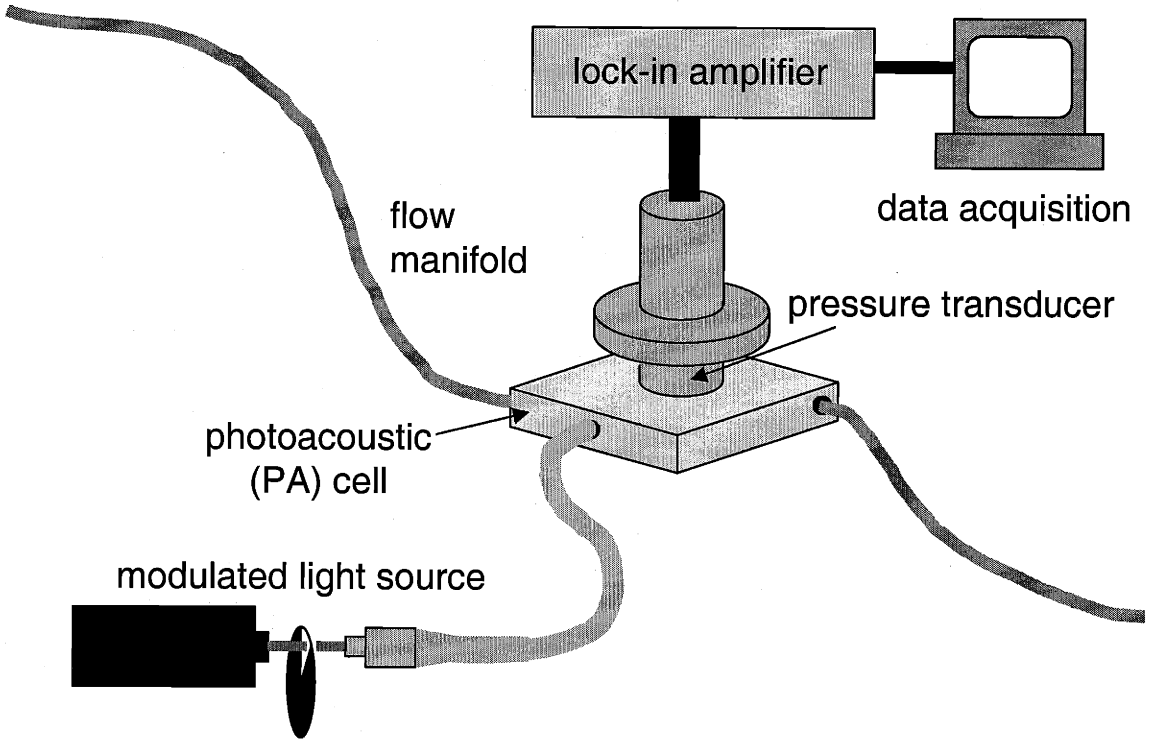

Figure 1-3: The components of a photoacoustic detector

2. Background

2.1. *Microreactor systems*

While the miniaturization of photoacoustic spectroscopy (PAS) is broadly applicable to the integrated chemical analysis field, this work focuses on the use of PAS with microfabricated chemical reactor systems. A microfabricated reactor system consists not of one large reactor chamber, but of several reactors operating in parallel. This has two essential differences from conventional reactor systems: modularity and high surface to volume ratio.

In conventional manufacturing, chemicals are synthesized in meter-scale reactors. Even if only small amounts are required, the chemical is made in bulk and then stored or shipped to where it is needed. The typical R&D to market cycle has three distinct stages: bench scale, pilot scale and full scale. Because performance parameters do not simply scale with reactor volume, every stage requires investigation and optimization. The modular nature of a microreactor system would allow flexibility in meeting a fluctuating demand and also reduce the lab to market time. Microreactors would also allow point-of-use manufacture; intermediates could be made on location in the quantities needed, rather than being stored or shipped. Eliminating the need for storage and transport increases the safety of these systems. The increased surface-to-volume ratio allows greater control and safety. Heat can be quickly removed from the reactor chamber, avoiding runaway reactions.

Many groups outside of MIT are also working on microreactor systems [13-16]. Some of this work focuses on uninstrumented arrays of microchannels that would take the place of the catalyst bed in a fixed bed reactor [17-20]. Other groups have developed systems that incorporate integrated sensors [21-25], such as the systems under development at MIT [1, 26-29].

Companies such as Symyx Technologies and Affymetrix have applied the advantages of microfabrication to the task of screening catalysts. Such systems allow multiple reactions to be tested simultaneously [30]. The screening work to date appears to be limited not by the ability to fabricate the arrays of catalyst, but by the detection of the many different product streams.

Sequential sampling methods are often used. At Symyx, for example, Weinberg *et al.* [2] sequentially sample the reaction from each cell with a capillary that directs the gases into a mass spectrometer. Parallel monitoring has been accomplished using fluorescent indicators [31] and thermographic screening [32]. Senkan [33] has developed a technique to photoionize reaction products and detect them locally with an array of microelectrodes. These techniques are either limited to a particular chemistry or are bulky and expensive to implement. A general chemical analysis unit integrated with each catalyst cell could allow parallel screening of a broad range of combinatorial chemistry systems. Such integrated units would be particularly useful for the second-level of catalyst screening—quantifying reaction kinetics and subtle differences between catalysts once the general catalyst system has been identified by higher throughput approach.

Other microreactor groups have integrated liquid-phase chemical analysis techniques, such as fluorescence and visible absorption spectroscopy [34, 35]. Kitamori *et al.* [36] demonstrated photothermal spectroscopy with a liquid phase integrated chemistry system. Photothermal spectroscopy, like PAS, relies on molecules heating with light absorption. In the case of photothermal spectroscopy, the temperature change is detected as a change in the refractive index of the media. Frye-Mason *et al.* at Sandia [23] combined a gas chromatograph with their "integrated chemical laboratory" system that used surface acoustic wave (SAW) detection.

At MIT, Srinivasan [37] built a reactor for gas-phase, catalytic, partial-oxidation reactions. The MIT microreactor consists of a channel etched through a silicon wafer, capped on the top by silicon nitride and on the bottom by an aluminum plate. Platinum lines on the membrane are used for ohmic heating and temperature sensing. Catalysts are deposited on the underside of the membrane using several different techniques, including electron beam evaporation and solution preparation. Reactants enter through inlet holes in the aluminum plate, react along the catalyst, and exit at an outlet hole at the other end of the channel. Other reactors, made by capping silicon channels with Pyrex, have also been built for liquid-phase and multi-phase reactions [38]. One advantage of the MIT microreactor design is the capability for integration of elements such as valves, mixers and sensors. The focus of this work is the development of a chemical analysis tool that could be integrated with a gas-phase microreactor.

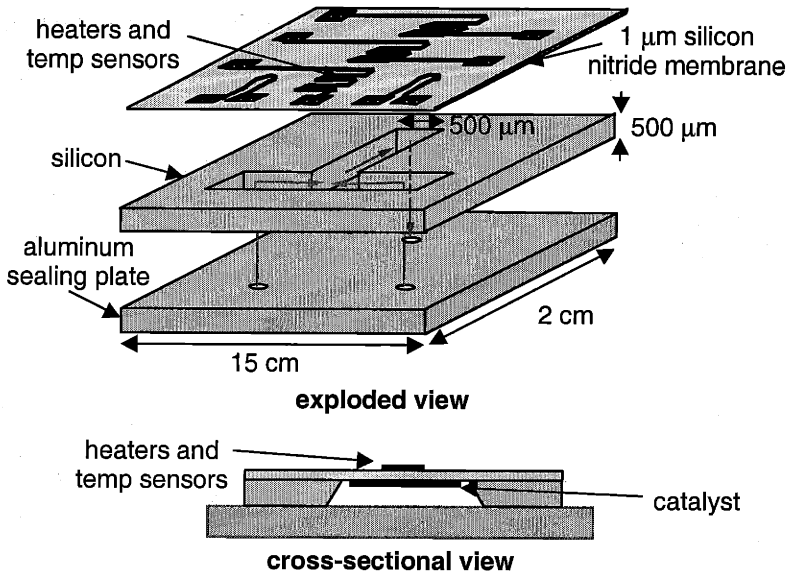

Figure 2-1: A sketch of the microreactor developed by Srinivasan *et. al* [1]

2.2. *Miniaturized chemical analysis*

Integrated chemical analysis is a broad field that includes both general analysis tools and species-specific detectors. Such devices, along with miniaturized biological and biochemical analysis and synthesis systems, are the focus of the Micro Total Analysis Systems (μTAS) community. A full review of these methods is out of the scope of this thesis, but a summary is given here.

Ion mass spectroscopy is perhaps the most commonly used tool for conventional chemical analysis of gaseous species. Miniaturization is beneficial to the operation of mass spectrometers because of the reduction in the required mean free path, extending the pressure range in which these devices can operate. In addition, the reduction of the pumping volume allows for simple, less expensive vacuum systems to be used with these devices. A mass spectrometer typically has three elements: an ionizer, an ion filter, and a vacuum system. Several types of miniaturized filters have been developed including time-of-flight filters [39] and quadrupole lens filters [40-44]. Little work has been done on complete integrated systems or on integrating the miniaturized mass spectroscopes with other systems. Also, most of the miniaturized devices are large compared to the size of the microreactor. Mass spectroscopy may eventually be a promising tool for use with microreactor systems. However, optical analysis methods, such as the work proposed in this thesis, are more easily integrated with other systems.

Several groups have demonstrated sensors that detect differences in thermal conductivity. These sensors can be used to identify concentrations of a single gas within a known diluent [45-49]. Thermal conductivity sensors have also been used in conjunction with gas chromatography to identify components of multi-species mixtures [50, 51]. The advantage of thermal conductivity sensors is their small size and the ease by which they can be integrated. In order to be useful in conjunction with the microreactor, however, the integrated chemical system must be able to analyze mixtures of several components, some of which may be unknown. This would require a chromatograph unit in conjunction with the detector. Field ionization tips have also been used as another means to detect gases [52, 53]. Like thermal conductivity detectors, these devices need to be implemented in conjunction with a gas chromatograph unit to yield information about mixtures of gases.

Many such integrated analysis methods require the addition of a gas chromatography unit to identify components in a mixture of gases. Other methods such as mass spectroscopy and infrared spectroscopy also benefit from separation, particularly in the case of complex mixtures, or when the spectra of the components in the mixture overlap. Terry *et al.* [50] and Reston *et al.* [54] have demonstrated miniaturized gas chromatographs. While these efforts offer a remarkable reduction in the size of a chromatography system—often the largest component in conventional chemical analysis systems—the size of these systems is still relatively large. It would be impractical to combine a gas chromatograph analysis unit with each microreactor cell; a system with a gas chromatograph analysis unit and detector serving a bank of cells is possible, however.

A variety of integrated gas detectors rely on changes in the characteristics of a thin film. The property change is transformed into an electrical signal with a transducer. Common transducers include Surface Acoustic Wave (SAW) devices [55], Metal Oxide Semiconductor (MOS)-based detectors [56, 57], Mach-Zehnder detectors [58-60] and Distributed-Bragg-Reflector (DBR) laser detectors [61]. Sensors such as these have performed well in their specific applications. The goal of this work, however, is to develop a broadly applicable tool.

Attenuated total reflectance (ATR) spectroscopy is also used for integrated chemical analysis. Such systems consist of a light source, a waveguide that passes through the media of interest, and a detector. As the light reflects off the wall of the waveguide, it samples the media in the near vicinity of the fiber. Absorption by the ambient materials alters the spectra of light

observed at the detector. This technique is also referred to as evanescent field spectroscopy in literature [62-64], particularly in the case of optical fibers acting as the waveguide. The technique is used more often for liquids and solids [65] than for gases where it is fairly insensitive. To achieve the sensitivity of a 1 cm-long open-path cell, for example, would require 5-10 m of uncoated fiber [64], although the sensitivity could be increased with the use of a coating layer. In addition, the integration of an ATR technique would also require the integration of an infrared sensor if multiple reactors were to be monitored simultaneously.

Several approaches have been pursued in integrated absorption spectroscopy systems. Most of the work is focused on the miniaturization or integration of the source and spectral modulation. Collins *et al.* [66] have demonstrated a miniature (1 x 5 x 10 cm) Fourier transform spectrometer that operates in the near infrared. Another group has demonstrated a Michelson interferometer where the mirror is moved by comb-drive actuation over 50 μm [67]. One issue with these miniaturized spectroscopy systems is that the resolution of such spectrometers is dependent upon the ratio between the total travel distance, which is reduced in the miniaturized system, and the optical wavelength.

Other methods may be more suitable for spectroscopy on the millimeter scale. One such approach is to shift the wavelength selection from the source to the detector. Correia *et al.* [68] have built integrated detector arrays on a single chip. Each detector is coupled to a Fabry-Perot optical filter tuned to a different portion of the visible spectrum. The chip is much less bulky than a Michelson interferometer, although the resolution is limited by the software's ability to simultaneously monitor multiple signals.

Recently, Corman *et al.* [69] have used correlation spectroscopy for a microfabricated carbon dioxide detector, in which the light source, carbon dioxide chamber, sample gas chamber and detector were all monolithically integrated. Sinclair *et al.* have developed a correlation spectroscopy system that uses synthetic spectra produced with microfabricated diffraction gratings [70-72]. This miniature synthetic spectra producer, dubbed "the polychromator," would be an ideal source for photoacoustic spectroscopy.

These integrated absorption spectroscopy methods mainly focus on the miniaturization of individual device components. Most are not meant for incorporation into microscale systems, and so they generally assume conventional optical path lengths. However, in small volumes such as those required by microreactors, there may not be adequate path length for sensitive gas-

phase spectroscopy. This consideration has led us to consider photoacoustic spectroscopy, in which the signal strength should increase with miniaturization.

2.3. *Photoacoustic spectroscopy*

The photoacoustic effect was discovered by Alexander Graham Bell in 1880 [10, 73], when he observed how focusing a "rapidly-interrupted" beam of sunlight onto a thin diaphragm of material resulted in a "clear, musical tone [73]." Positing that "sonorousness" under these conditions was a fundamental property of matter, Bell devised a method for studying the effect in solids, liquids and gases. He tested a variety of substances including potash, selenium, tobacco smoke, cork, platinum, ink, wool, and even a cigar. Bell, who had just made his famous telephone call to Watson in the spring of 1876, hoped to use the photoacoustic effect to create a "photophone," a device like the telephone, but with the signal transmitted as light rather than electricity. Perhaps Bell anticipated the advantages of optical networks.

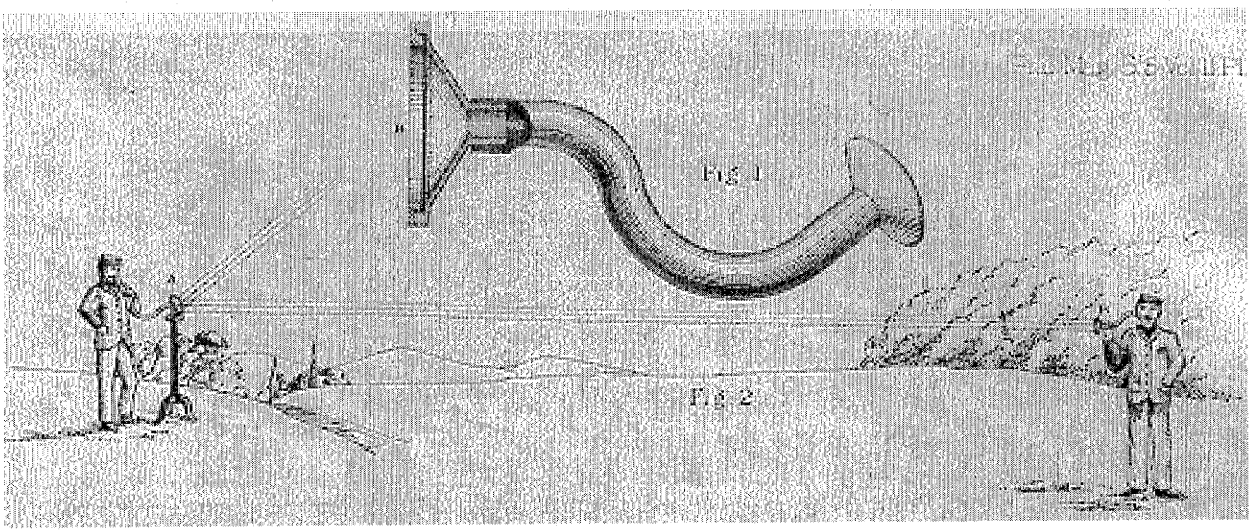

Figure 2-2: Bell's plan for the photophone [73]

Inspired by Bell, Tyndall [74] investigated the effect further in gases. Röntgen [75] conducted similar work independently. Early work in photoacoustics relied on broadband light sources, such as the sun or lime lamps, although Tyndall did observe the wavelength dependence of the effect, noting that the use of glass lenses "withdrew from the beam its most effectual rays," and replaced the glass lenses with silvered mirrors [74].

As he was conducting his photoacoustic experiments in Paris, Bell wrote to his friend, Sumner Tainter, "I have tried a large number of substances in this way with great success, although it is extremely difficult to get a glimpse of the sun here, and when it does shine the

intensity of the light is not to be compared with that to be obtained in Washington." The lack of suitable light sources impeded the development of photoacoustic devices, although some work was done with light sources coupled to monochromators, as is documented by Delany's [76] mid-century review of the field.

Consequently, the photoacoustic (PA) effect remained largely a scientific curiosity until Kreuzer combined photoacoustic detection with lasers to demonstrate extremely sensitive gas detection in 1971 [5]. Kreuzer then went on to demonstrate PA detection for pollution monitoring [77, 78], and for gas chromatograph detection [79]. Dewey *et al.* [80] improved the sensitivity of photoacoustic detection systems further by modulating the optical excitation at a frequency corresponding to an acoustic mode in the cavity. In the late seventies, the field of photoacoustics exploded, finding commercial applicability today in trace gas analysis, solid-phase spectroscopy, biological studies and research devices for kinetic parameter determination. Two books have been written that provide a thorough, although dated, discussion of PA theory and design [3, 12]. There are also a few review articles [8, 81, 82].

2.3.1. *Non-resonant, resonant, and pulsed mode detection*

Photoacoustic devices can be divided into three categories depending on design of the acoustic cavity and the acoustic excitation frequency: non-resonant, resonant and pulsed mode. In non-resonant detection, the cell is operated at a frequency that is much lower than the first acoustic resonance frequency of the system [5]. In this case, the pressure of the entire system is spatially uniform while it changes in time.

In resonant operation [80, 81, 83], the cell is excited at an acoustic resonance of the cavity. This has a number of advantages: the sensitivity is increased by coupling to the mode, and the spatial non-uniformity of the signal allows the designer to place windows and flow inlets at the signal nodes, which reduces their influence on the system [81, 84, 85]. One disadvantage of resonant detection is that the resonance frequency is very sensitive to gas composition, temperature and pressure. Consequently, in systems where these parameters cannot be tightly controlled, resonant detectors rely either on a feedback loop to actively tune the modulation or are built with low Q's to reduce the environmental sensitivity.

In pulsed photoacoustics, the system is illuminated with a light pulse rather than with periodic modulation [82, 86-92]. Unlike non-resonant and resonant detection, which are performed in the frequency domain with periodic modulation and lock-in detection, pulsed

photoacoustic detection is performed in the time domain. After each pulse, the sample is monitored with an integrator or recorder to determine the total fraction of energy that was converted into acoustic energy through absorption [89]. Pulsed cells are usually designed to have a single, high-Q resonant peak, so that the acoustic signal is a decaying sine wave. An advantage of this technique is that it is insensitive to shifts in the resonance frequency. The sensitivity that is lost by the removal of lock-in detection can be partially compensated for with the use of an extremely high Q resonator [89]. Another advantage of pulsed photoacoustics is that it allows for high-energy, pulsed-mode lasers to be used as light sources [89].

2.3.2. *Photoacoustic gas cell design*

The canonical photoacoustic gas cell is a cylinder capped by windows and excited along its length. Figure 2-3 shows a drawing of Kreuzer's original gas cell, which operated in the non-resonant mode. Kreuzer filled the cell with the analyte gas off-line and then sealed the cell before analysis.

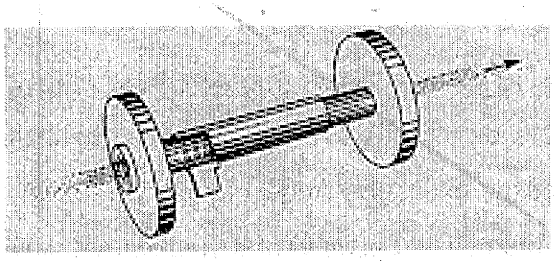

Figure 2-3: Kreuzer's [5] original cell was a simple cylinder. The light passed along the axis of the cylinder, which was capped at either end by glass windows. Tiny holes along the cavity body allowed the pressure variation to be communicated to the aluminized Teflon layer, which was the membrane for a capacitive microphone. The cell was 5 cm long and 1/8 inches in diameter.

One method for greatly increasing the cell sensitivity--at some cost in complexity--is to place the photoacoustic cell inside the laser cavity. This configuration, called intracavity photoacoustic detection, allows for much higher optical power in the cell and has been used to detect gases with parts per trillion sensitivity [93-95]. Multipass cells, in which the photoacoustic cavity is designed to facilitate multiple light passes, have also been demonstrated [96].

The early resonant photoacoustic cells were also simple cylinders. Dewey *et al.* [80] used a cylindrical cavity that was 102 mm in diameter and 92 mm long, excited at the first radial mode (3933 Hz) with a Q of 164. The radial mode is convenient because illumination along the

axis of the cavity couples well to the spatial profile of the mode. However, azimuthal [97] and longitudinal [81, 85, 98-100] resonance modes have also been used.

In the early low-level gas detection experiments, it was widely observed that absorption by the glass windows of the cell could limit the sensitivity of the device [101]. Techniques such as the addition of tunable air columns by the windows [99, 102], acoustic baffles [84, 85], windows angled at the Brewster angle [8, 103], or differential cells [81, 84] have been used to reduce the background in photoacoustic systems. Also, the use of frequency modulation rather than amplitude modulation can eliminate the background, as the background absorption is often not wavelength-specific [11, 101]. Another technique for reducing the background absorption in resonant cells is to orient the cell such that the windows are at the pressure node of the excited resonant mode [103, 104].

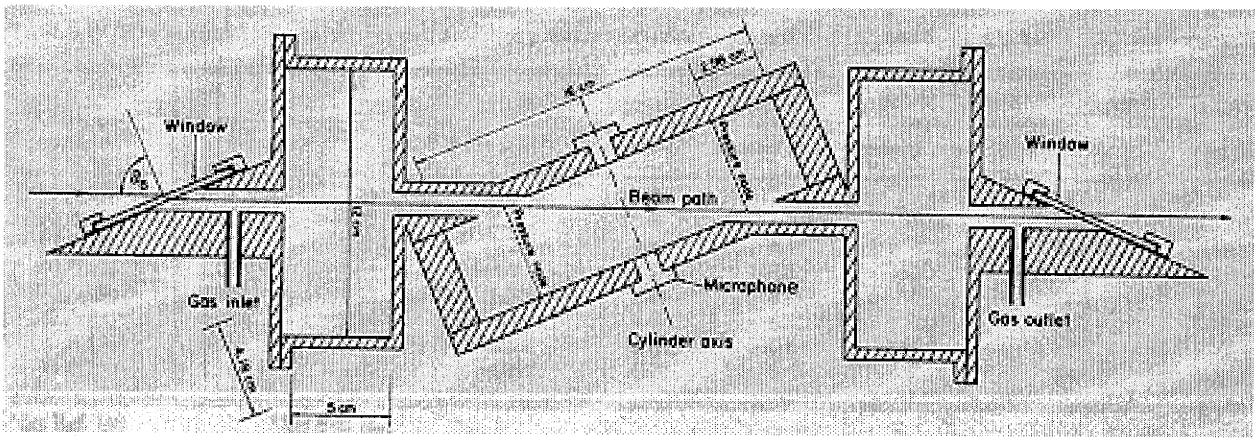

Figure 2-4: A cross-section of a radially-resonant photoacoustic cell [103]. Note the different orientation of the light relative to the cavity axis, which is a short, wide cylinder. This design illustrates many background reducing features: Brewster-angled windows, baffles, and the flow inlets and windows placed at the pressure nodes of the resonant mode. The cavity diameter is 16 cm. This cell operated at 2650 Hz with a Q of 340.

Longitudinal modes are often preferable to radial or azimuthal modes because they allow for a relatively low resonance frequency while maintaining a small volume and low window background. Bernegger and Sigrist [81] demonstrated one approach to longitudinal mode coupling, illustrated in Figure 2-5.

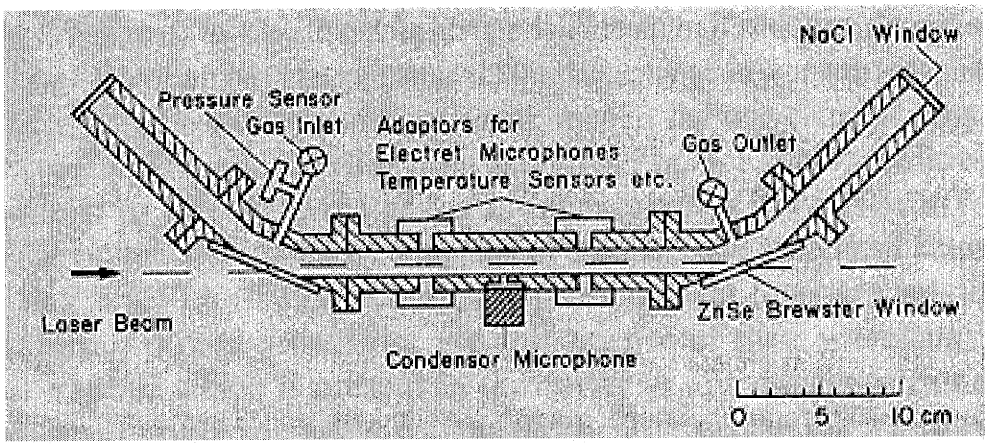

Figure 2-5: A sketch of Bernegger's longitudinal resonance cell design [81].

A more common design for longitudinal resonant cells is the H-shape cell [6, 98-100, 105], as is illustrated in Figure 2-6. The larger diameter and presence of the flow inlets creates the boundary condition of pressure nodes at either end of the cell.

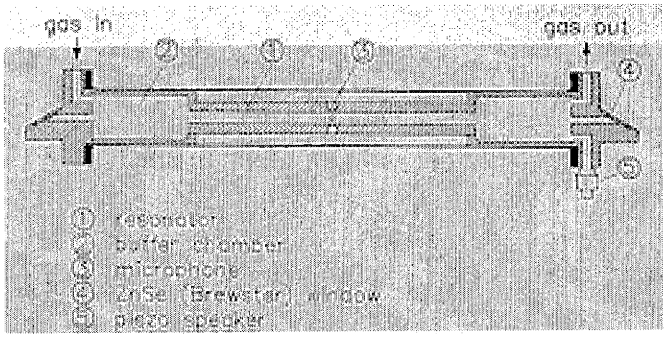

Figure 2-6: A sketch of an H-type resonant cell [98]. This image represents a cross-section along the z-axis of the cylinder. The length of the resonator was 30 cm. This cell operated at 556 Hz with a Q of 20.

The microphone is a key component of the photoacoustic cell. Most gas-phase photoacoustic systems use commercial condenser microphones [8, 81, 82]. However, some systems have utilized optical microphones [106-108]. Many condensed matter systems use piezosensors rather than microphones [8].

2.3.3. *Extending photoacoustic detection to spectroscopy*

Spectroscopy is achieved by scanning the light source through several frequencies. Three techniques have been used for achieving spectroscopy – tunable lasers [81, 102, 109-111], broadband light sources coupled with tunable monochromators [76], and broadband sources coupled with Michelson inteferometers [112-117]. In addition, an array of 8 near-IR laser diodes has been used in a portable, biomedical device [118].

2.3.3.1. *Tunable lasers*

Many systems use high-power gas lasers, such as CO_2 and CO lasers, that can be step-tuned over significant ranges of the mid-infrared [81, 110, 111, 119]. The optical system for such excitation is straightforward, and the power level high, allowing for extreme sensitivities. For example, a CO laser can be tuned to a number of lines in the region of 5-6.5 μm, covering more than 350 cm^{-1} of the range with a power as high as 1 W [81]. For many applications, however, continuous coverage of the spectrum is desirable.

Lead-salt diode lasers can typically be continuously tuned over ~20 cm^{-1} in multimode operation. However they have several disadvantages: they are relatively low power (< 1mW) and require accurate current and temperature stabilization [81]. Tunable spin-flip Raman lasers and dye lasers have also been used [81]. Kühnemann *et al.* [120] have demonstrated an excitation system consisting of a Nd:YAG laser coupled to an optical parametric oscillator that was continuously tunable over the wavelength range of 2.3 – 4 μm. Difference frequency generation has also been used to achieve broad spectral tuning in the mid-infrared [121, 122]. A recent development in tunable lasers, mid-infrared quantum-cascade distributed-feedback (QC-DFB) lasers, appears to be quite promising. Paldus *et al.* [102] have demonstrated spectroscopy over a 35 nm wavelength range at a rate of 5 nm/min using temperature tuning. Lasers with wavelengths ranging from 3.5 to 13 μm have been fabricated with the same material system but varying geometries [123, 124]. The disadvantage of the tunable laser methods for mid-infrared spectroscopy is that in general they suffer from a slow time response and require the controlled variation of several parameters.

Many of the published photoacoustic work using tunable lasers have been in the near infrared, where more low-cost and stable lasers are available. A number of studies have looked at the overtone spectra of gases [94, 105, 109]. Overtone absorption lines are much weaker than fundamental lines, so these devices are typically less sensitive than those that rely on fundamental modes. However, this loss of sensitivity can be compensated for by the higher power of lasers available. Weaker absorption lines also result in a larger signal range, as will be discussed later in this thesis.

2.3.3.2. *Fourier transform photoacoustic spectroscopy (FT-PAS)*

The use of a monochromator or an interferometer greatly simplifies the light source selection. Early PAS work was conducted with white light sources coupled to monochromators

[76]. However, Fourier transform spectrometers are generally preferred to dispersive methods (such as the monochromator) because of the higher signal-to-noise ratio [125]. Fourier transform photoacoustic spectroscopy (FT-PAS) couples photoacoustic detection with Fourier transform spectroscopy. Busse and Bullemer [112] and Farrow *et al.* [113] pioneered this technique. Lloyd *et al.* [114] and Débarre *et al.* [115] have demonstrated FT-PAS in the visible and near infrared spectrum. The Nicolet Corporation [126] developed a commercial infrared FT-PAS system for the study of solid and liquid phase samples, the analysis of which would otherwise require significant sample preparation.

Two methods are used in FT-PAS to modulate the light. In step and integrate devices, the path length in the interferometer is stepped through the total range. A mechanical chopper or the periodic modulation of one of the interferometer mirrors provides the modulation [115, 117]. The advantage of the step and integrate method is that it allows the user to set the acoustic frequency, facilitating lock-in detection and allowing the use of high-Q resonant cells. The disadvantage of step-and-integrate methods is that its implementation requires more of a modification to a conventional FTIR system.

In constant scan rate systems, the illumination of a sample results in the simultaneous production of several tones, each of which corresponds to an absorption line. No chopper is required. The frequency of the tone resulting from an absorption line is proportional to the mirror velocity multiplied by the wavenumber of that tone [112, 117, 126]. Because of the frequency spread of the signal, most continuous-scan FT-PAS cells are designed to be non-resonant. However, Kinney and Staley have demonstrated a cell that uses a broad Helmholtz resonance to enhance sensitivity over the frequency range of 125 to 550 Hz [116].

2.3.4. *Common PA Applications*

2.3.4.1. *Pollution monitoring*

Many groups have applied photoacoustic detection to pollution monitoring [81] [103]. Photoacoustic spectroscopy is well suited to this application because of its large sensitivity to small concentrations. Both non-resonant [78, 127] and resonant cells [80, 81, 94, 96-98, 100, 103, 128] have been developed for this purpose.

Some of these systems have been tested in real world situations. Gondal [128], for example, has demonstrated the detection of car exhaust from a distance of 60 meters from an

idling car. Meyer and Sigrist [103] have built a mobile pollution detection apparatus that is contained in a trailer, and have been able to measure ethylene, carbon dioxide and water vapor levels by the side of a well-traveled road in Zurich during a typical weekday.

2.3.4.2. *Liquid and solid-phase analysis*

Condensed matter photoacoustic systems can be divided into two categories: multiphase cells in which the signal must be transmitted from the sample to the microphone through an inert carrier gas [116, 126], and systems that sense the acoustic wave directly from the sample. The direct sensor method is generally more sensitive [8]. Piezoelectric transducers are commonly used for this purpose [87, 129], although capacitive and optical interferometric methods have also been demonstrated [8]. Most liquid photoacoustic spectroscopy systems use the direct sensor method [8, 87, 108, 118, 130].

Multiphase cells, however, have the advantage of requiring little sample preparation [8, 126], which has been the key to the commercial success of PAS. The lack of sample preparation facilitates the study of catalysts, where material form is critical to the performance. It also allows for the study of heterogeneous reactions *in situ* [116, 117]. Furthermore, as the penetration depth of the light depends in part on the modulation rate, PAS can be used for non-destructive depth profiling [126, 131]. Many FTIR systems today have the option of a photoacoustic cell accessory that uses the multiphase method [131].

2.3.4.3. *Biological studies*

As a non-invasive technique that can operate in real time, PAS is ideally suited to many biological applications. For example, Harren *et al.* [6] have used photoacoustic detection to measure ethane in the exhalation from human skin as an indicator of ultraviolet radiation damage. The measurement requires a sensitivity of parts per trillion. Hoping to replace the invasive sugar monitoring techniques required for diabetics, Spanner and Niessner have demonstrated the *in vivo* measurement of human blood glucose levels using an array of laser diodes operating in the near infrared [118]. Photoacoustic detection has also been used to monitor the breathing pattern of cockroaches [132] and the postharvest metabolic processes of produce [133].

2.3.4.4. *Direct measurement of reaction kinetics*

Photoacoustic resonance can also be used to determine the chemical relaxation times of molecules or system equilibria, which can affect the resonance quality factor [8, 134, 135]. Monitoring the phase shift between the excitation and response can also be used to determine molecular relaxation times [136]. Hey and Gollnick have applied non-resonant PA detection to measure radiationless transition rates [137] by plotting the acoustic signal times frequency ($P*f$) versus excitation frequency. In an ideal two-level system, the dependence is constant. With the addition of competing radiationless transitions, however, the dependence of $P*f$ may exhibit steps at frequencies which correspond to the transition rates of other processes.

2.3.4.5. *Other applications*

PA monitoring has been used to study photochemistry and photoelectricity [8, 138]. Also, the photoacoustic effect, which is sensitive to the propagating medium, has been used to measure material properties other than absorptivity such as elastic constants [139] and thin film adhesion [7]. The photoacoustic devices in these applications are quite similar in concept to other acoustic wave sensors, but where optical absorption launches the acoustic wave.

Photoacoustic detection has also been used with Raman spectroscopy [140, 141]. Raman spectroscopy relies on the inelastic collision between a photon and a molecule; it is often used to complement infrared spectroscopy because it can detect the rotational transitions on many symmetric molecules that are invisible in infrared spectroscopy [125]. Oki *et al.* [141] have demonstrated sensitive (ppm) hydrogen detection in a photoacoustic Raman spectroscopy system.

2.3.5. ***Previous work with miniaturized PAS***

Little work has been done with the miniaturization of photoacoustic devices, but some work has been done with the microfabrication of Golay cells [142-144], which are infrared detectors that rely on a sealed gas chamber expanding due to light absorption [145]. As was described in section 2.1, Kitamori's group at the University of Tokyo have integrated a photothermal detector with a liquid-phase microreactor system [36, 146]. Their "thermal lens microscope" relies on the refractive index change that occurs with optical absorption and subsequent heating. Also, Honeywell [147] was issued a patent on micromachined photoacoustic sensors. These groups have pursued this work because photothermal techniques, which include Golay cells and photoacoustics, generally benefit from miniaturization. The

photoacoustic effect languished for nearly a century after its discovery until it found practical application with the invention of appropriate light sources. Will microfabrication techniques bring a similar revival?

3. Theory

3.1. *Conventional gas-phase photoacoustic theory*

Photoacoustic theory can be broken down into three processes: the absorption of light, the excitation of sound, and signal detection.

3.1.1. *Light absorption*

The first step in the generation of a photoacoustic signal is the absorption of light. In most cases, the heating that results from the absorption of light can be written [148]:

$$H = \alpha I \qquad (3\text{-}1)$$

where H is the heating (W/m^3), α is the absorbance (m^{-1}) and I is the light intensity (W/m^2). The absorbance is proportional to the density of absorbing molecules. (3-1) assumes that the intensity is sufficiently small that the upper state of the transition is not saturated, and that the time variation of I is much slower than the rate of transfer of absorbed energy into heat.

These two conditions can be illustrated by considering a simple two level system. Let n_1 be the density of absorbing molecules in the higher state and N the total density of absorbing molecules. The upper state population is described by [148]:

$$\frac{dn_1}{dt} = -n_1\left[\frac{I}{h\nu}\left(\frac{S_l}{\pi\Delta\nu}\right) + \tau_C^{-1} + \tau_R^{-1}\right] + \left(N - n_1\right)\left(\frac{I}{h\nu}\right)\left(\frac{S_l}{\pi\Delta\nu}\right) \qquad (3\text{-}2)$$

where $h\nu$ is the energy of the transition, $\Delta\nu$ the linewidth, S_l the line strength, τ_R the radiative lifetime, τ_C the collisional lifetime and $I = I_0 f(t)$.

If the variation in $f(t)$ is sufficiently slow, the system can be considered quasi-static, and the solution for the upper state population is given by:

$$\frac{n_1}{N} = \frac{\left(IS_l/h\nu\pi\Delta\nu\right)}{\left(2IS_l/h\nu\pi\Delta\nu\right) + \tau^{-1}} \qquad (3\text{-}3)$$

where $\tau^{-1} = \tau_R^{-1} + \tau_C^{-1}$. From (3-3), one can see that if I is sufficiently weak and slowly varying, the upper state population is proportional to the light intensity. Furthermore, as the

heating is related to n_1 by $H = (n_1/\tau_C)h\nu$, one can see that the $H = \alpha I$ holds, with α being given by [148]:

$$\alpha = N\frac{S_1\tau}{\pi\Delta\nu\tau_C} \qquad (3\text{-}4)$$

As a practical matter, the value of $\alpha(\omega)$ can be measured from the optical transmission through the gas, which for a cavity of length L is equal to $e^{-\alpha L}$. The absorbances of most common gases have been tabulated for a variety of wavelength, pressure and temperature conditions. In my calculations, I will also refer to the absorptivity a, which is more precisely called the decadic molar extinction coefficient. The decadic molar extinction coefficient has units m^2/mol, and is related to α by $\alpha = aN_{0,molar}Xln10$, where $N_{0,molar}$ is the overall molar concentration and X is the mole fraction of the absorbing gas.

Most work in PAS assumes that the excitation is sufficiently weak and slowly varying such that (3-1) applies. What is the design space in which this is true? The sufficiently weak criterion for light intensity can be written as $I_0 << h\nu N/(2\alpha\tau_C)$. Using a hard-sphere collision model, τ_C for a gas is typically ~0.1 ns at STP (room temperature and 1 atm. of pressure) [149]. For propane or methane at 3.392 μm, which have a relatively large α, the "sufficiently weak" criterion is met as long as the intensity is less than 1 x 10^{13} W/m^2. For a 1 mW source, that translates into a minimum chamber radius of 6 nm.

If the excitation is sinusoidal with radial frequency ω, the slowly varying criterion can be written as $\omega << 2I_0\alpha\tau_C/(h\nu N\tau) + \tau^{-1}$. The collisional lifetime τ_C is typically much less than the radiative lifetime, τ_R, so that $\tau \sim \tau_C$ [150]. τ_C is also typically much less than $h\nu N/2I_0\alpha$. This criterion can therefore be met with $\omega << 10^{10}$ rad/s or 1.6 GHz.

3.1.2. *The excitation of sound*

The heat from the light absorption acts as a source for the generation of sound. Ignoring the acoustic losses due to heat conduction and viscosity, the equation for the pressure in a sealed cavity is given by:

$$\nabla^2 p - \frac{1}{c^2}\frac{\partial^2 p}{\partial t^2} = -\left[\frac{\gamma - 1}{c^2}\right]\frac{\partial H}{\partial t} \qquad (3\text{-}5)$$

where p is the acoustic pressure ($p = P - P_0$), c is the speed of sound, γ is the ratio of specific heat at constant pressure to that at constant volume, and H is the rate of heat generation from the absorption of light, which is proportional to the light intensity as described in (3-1).

For acoustics it is more convenient to work in frequency space in which the light intensity, $I(\vec{r},t)$ has the form $I(\vec{r},\omega)e^{j\omega t}$. More complicated modulation functions can be analyzed with the use of superposition. Taking the Fourier transform of (3-5) yields:

$$\left(\nabla^2 + \frac{\omega^2}{c^2}\right)p(\vec{r},\omega) = -\left[\frac{\gamma - 1}{c^2}\right]j\omega H(z,\omega) \qquad (3\text{-}6)$$

The solution for $p(\mathbf{r},\omega)$ is of the form:

$$p(\vec{r},\omega) = \sum_j A_j(\omega)p_j(\vec{r}) \qquad (3\text{-}7)$$

where $p_j(\mathbf{r})$ are the normal mode solutions to the system, and $A_j(\omega)$ are the mode amplitudes. The normal modes of the chamber are determined by the boundary condition that the acoustic velocity must be zero at the chamber walls. The acoustic velocity is related to the pressure by:

$$u(\vec{r},\omega) = \frac{-1}{j\omega\rho_0}\nabla \cdot p(\vec{r},\omega) \qquad (3\text{-}8)$$

For a cylindrical geometry, the solutions for $p_j(r,\phi,z)$ are given by [11]:

$$p_j(r,\phi,z) = \begin{matrix}\cos \\ \sin\end{matrix}(m_\phi\phi)\cos(k_z z)J_m(k_r r) \qquad (3\text{-}9)$$

$$\omega_j = c\sqrt{k_z^2 + k_r^2} \qquad (3\text{-}10)$$

where m_ϕ is an integer and J_m represents Bessel functions of the first kind. The wavevector quantities k_z, and k_r are given by:

$$k_z = \frac{\pi}{L}n_z \qquad n_z = 1,2,3,... \qquad (3\text{-}11)$$

$$k_r = \frac{\pi}{R}\alpha_{mn} \qquad m,n = 1,2,3,... \qquad (3\text{-}12)$$

In (3-12), α_{mn} is the nth root of the mth order Bessel function, L is the cavity length and R the cavity radius. The solutions for $A_j(\omega)$ are given by:

$$A_j(\omega) = -\frac{j\omega}{\omega_j^2}\frac{[(\gamma - 1)/V_C]\int p_j * HdV}{[1 - \omega^2/\omega_j^2 - j\omega/\omega_j Q_j]} \qquad (3\text{-}13)$$

where Q_j was added to account for the energy losses due to thermal conduction, viscous damping, and scattering. V_C is the total cavity volume. The term $\int p_j * HdV$ represents the coupling between the heat source and the mode.

Photoacoustic systems operate in one of three modes: non-resonant, resonant, or pulsed mode. Non-resonant and resonant mode devices operate in the frequency domain, while pulsed mode devices operate in the time domain. In this thesis I have used non-resonant and resonant excitation.

3.1.2.1. *Non-resonant excitation*

In non-resonant systems, only the zeroth order mode of the cavity is excited, so that the pressure in the cavity is spatially uniform. The expression for cavity pressure, (3-7), reduces to $A_0(\omega)p_0$, which is given by:

$$p(\vec{r},\omega) = A_0(\omega)p_0(\vec{r}) = \frac{i\alpha(\gamma-1)W_0L}{\omega V_C} \qquad \textbf{(3-14)}$$

For the dilute mixtures to which Kreuzer applied this theory, γ was constant and α a linear function of concentration. With these approximations, (3-14) predicts a signal which is linear in concentration and inversely proportional to acoustic frequency. Kreuzer includes an additional term to take into account energy lost to heat conduction. Thermal conduction is characterized by the thermal damping time, τ_T, given by:

$$\tau_T = \frac{\rho_0 C_P R^2}{2\kappa} \qquad \textbf{(3-15)}$$

where κ is the thermal conductivity and C_P is the heat capacity at constant pressure. This results in a modified form of (3-14):

$$p(\vec{r},\omega) = A_0(\omega)p_0(\vec{r}) = \frac{j\alpha(\gamma-1)W_0L}{\omega(1+j/\omega\tau_T)V_C} \qquad \textbf{(3-16)}$$

The theory therefore predicts that the non-resonant signal should scale inversely with cross-sectional area. This is in contrast to conventional absorption spectroscopy, in which the light is monitored after it has passed through the sample. In such a system, the signal is proportional to cavity length and is reduced with miniaturization. The intuitive explanation for this difference in scaling is that conventional absorption spectroscopy is an integrating technique looking at total energy absorbed, while photoacoustic spectroscopy is a differential technique

where one senses the absorption as force *per unit surface area.* Increasing the length of the cavity may increase the total power absorbed, but it also increases the area over which the signal is distributed. Furthermore, decreasing the cross-sectional area increases the signal because it reduces the total surface area of the signal without reducing the amount of power absorbed.

Of course, there's a limit to this rosy vision of scaling, indicated by the inclusion of the thermal conduction term. At radii that are so small that the thermal damping time is short, (3-16) reduces to:

$$p(\vec{r},\omega) = A_0(\omega)p_0(\vec{r}) = \frac{\alpha(\gamma-1)W_0 L}{V_C}\tau_T = \frac{\alpha(\gamma-1)W_0\rho_0 C_P}{2\pi\kappa} \qquad (3\text{-}17)$$

In this state the response is limited by the diffusion of heat out the cavity, and so the effect loses its dimensional dependence. Figure 3-1 shows the scaling behavior predicted by (3-16).

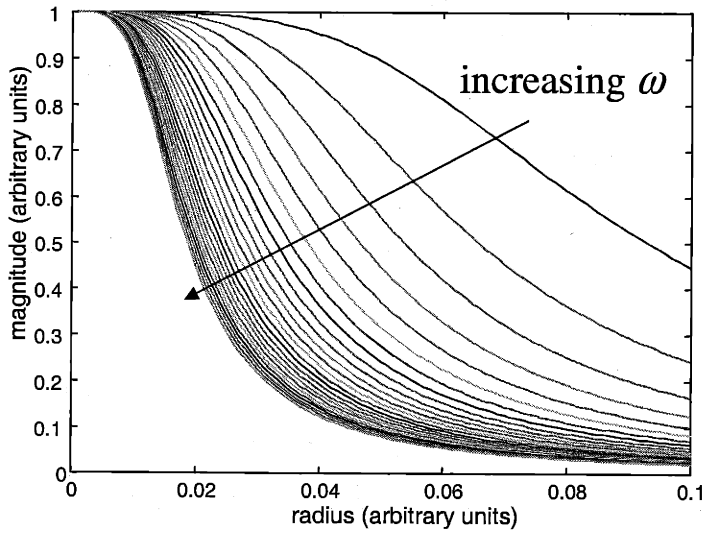

Figure 3-1: Scaling of the non-resonant photoacoustic signal for a constant analyte concentration, as predicted by (3-16).

3.1.2.2. *Resonant excitation*

If one can spatially couple all of the light into the first-order acoustic mode, the signal amplitude is given by [148]:

$$A_1(\omega) = -\frac{j\omega}{\omega_1^2}\frac{\alpha(\gamma-1)W_0 L}{V_C\left[1-\left(\omega^2/\omega_1^2\right)-j(\omega/\omega_1 Q_1)\right]} \qquad (3\text{-}18)$$

If one excites this cavity at ω_1, the amplitude simplifies to $Q_1\alpha(\gamma\text{-}1)WL/\omega_1 V_C$. According to Dewey, Q is mainly limited by viscous and thermal losses at the wall [11]. The energy

dissipated per cycle in a cylindrical container E_L, divided by the total acoustic energy in the standing wave E_T takes the form [83]:

$$\frac{E_L}{E_T} = \left(\frac{2\pi}{L}\right)[d_V + (\gamma - 1)d_H(1 + L/R)] \quad (3\text{-}19)$$

$$d_V = \sqrt{2\eta/\rho_0\omega} \quad (3\text{-}20)$$

$$d_H = \sqrt{2\kappa/\rho_0 C_P\omega} \quad (3\text{-}21)$$

where L is the cylinder length, R is the chamber radius, d_V is the viscous boundary layer thickness, and d_H is the thermal boundary layer thickness. The viscosity is given by η. The Q determined by viscous and thermal losses is then given by

$$Q = \frac{2\pi}{(E_L/E_T)} \quad (3\text{-}22)$$

This Q is an upper limit for the system. Other sources for loss including imperfect wave reflection, dissipation at the microphone diaphragm, and losses from wave scattering at surface obstructions, result in the actual Q being lower. Although for standard resonant photoacoustic systems, it's usually within a factor of 2 from the Q set by viscous and thermal losses [11].

3.1.3. *Signal detection*

In gas-phase photoacoustics, the signal is detected with a microphone, usually of the condenser type. The presence of the microphone alters the behavior of the system. For example, in the case of non-resonant operation, the microphone can be treated as an additional volume in the system. This results in a modified form of (3-14):

$$A_0(\omega) = \frac{j\alpha(\gamma - 1)W_0 L}{\omega(1 + j/\omega\tau_T)(V_C + V_M)} \quad (3\text{-}23)$$

In the sealed cavity and low-level gas conditions for which this theory was developed, this results in a signal that is linear with gas concentration, and inversely proportional to frequency.

3.2. *Variations from the ideal model*

Kreuzer's theory was developed for idealized cylindrical systems without gas flow channels or geometrical variations. It also assumes low levels of analyte gases, so that the light

power is spatially uniform, and the acoustic properties of the cavity unvarying. However, my devices have gas flow channels and microphone inlets. Furthermore, I must examine the effects of large gas concentrations, so that I can know the limits of device operation. The use of high gas levels and the presence of the flow channels profoundly affect the behavior of the system.

3.2.1. *Absorption saturation*

The power at any point along the cavity is given by:

$$W(z) = W(0)e^{-\alpha z} \qquad (3\text{-}24)$$

where α is the absorbance. Figure 3-2 shows a plot of the light profile along the axis of the cavity in the case of $\alpha \sim 921\ m^{-1}$, which is the case for pure propane at 3.392 μm (a very strong absorption peak) and STP. Under these conditions, the assumption that the light is uniform along the cavity is invalid for all cases but for extremely dilute mixtures.

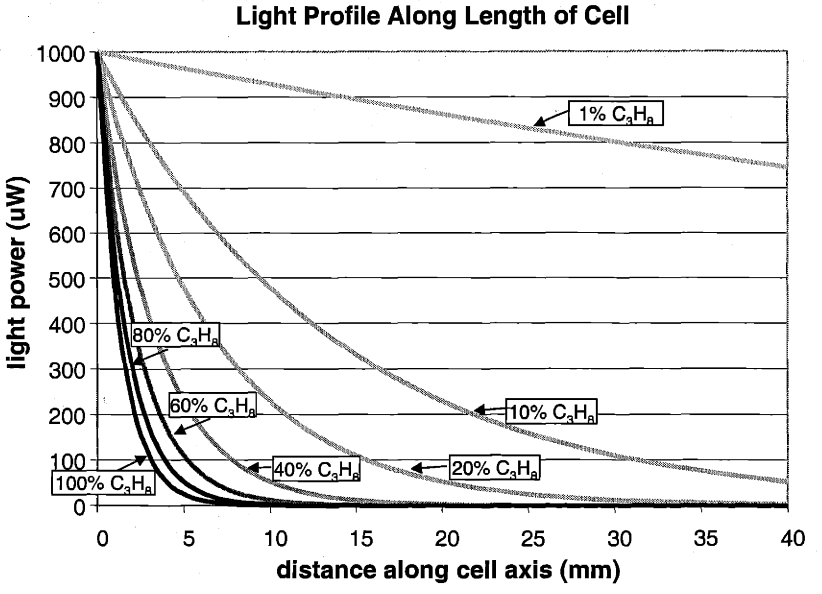

Figure 3-2: The power variation along the length of the cavity is significant for propane at 3.392 μm and STP

One way to incorporate the changing power level into (3-24) is to make the following substitution for the total light power absorbed:

$$\alpha WL \Rightarrow \alpha \int_0^L W(z)dz = \alpha \frac{W(0)}{\alpha}\left(1 - e^{-\alpha L}\right) = W_0\left(1 - e^{-\alpha L}\right) \qquad (3\text{-}25)$$

As a check, we can confirm that this expression has the expected behavior at the limits. When αL is very small we expect the light intensity to be uniform along the cavity axis, and in that case (3-25) simplifies to $\alpha W_0 L$. When αL is very large all of the light power will be

absorbed, and in that case (3-25) simplifies to W_0. Incorporating (3-25) into our model, the expression for the non-resonant response should be given by:

$$A_0 \approx \frac{j[\gamma - 1]}{\omega(1 + j/\omega\tau_{th})(V_C + V_M)} W_0 \left(1 - e^{-\alpha L}\right) \qquad (3\text{-}26)$$

3.2.2. *Sidewall Absorption*

The conventional photoacoustic model also assumed that the sidewalls of the photoacoustic cavity are perfectly reflective. However for real systems this is not the case. I have observed a significant attenuation in the light transmitted through the brass photoacoustic cavities, even in the absence of the absorbing gas and the exit window. This absorption does not contribute to the noise level (the resulting background absorption noise level is insignificant compared to ambient noise) because of the much greater thermal conductivity of the cavity wall as compared to the gas. However, it does contribute to the light gradient through the cavity. This additional light loss is characterized by δ with the units of inverse length. Including this factor, the power distribution through the cavity is given by:

$$W(z) = W_0 e^{-(\alpha+\delta)z} \qquad (3\text{-}27)$$

where δ can be calculated from the empty cavity transmission, $\mathbf{T}_{empty}$:

$$\delta = \frac{-\ln(\mathbf{T}_{empty})}{L} \qquad (3\text{-}28)$$

With this modification, the power absorption that contributes to the photoacoustic signal is given by:

$$\alpha WL \Rightarrow \alpha \int_0^L W(z)dz = \alpha \frac{W(0)}{\alpha + \delta}\left(1 - e^{-(\alpha+\delta)L}\right) = \frac{\alpha}{\alpha + \delta} W_0 \left(1 - e^{-(\alpha+\delta)L}\right) \qquad (3\text{-}29)$$

For pure propane, α is about 921 m^{-1}, while the δ measured for the brass cell cavities (described in Chapter 4) ranged from about 15 to 25 m^{-1}. Consequently, the sidewall absorption had little effect at high gas concentrations. However, δ could have a significant effect with low gas concentrations.

3.2.3. *Changing gas properties*

Another consequence of working with high gas concentrations is that the gas material properties such as viscosity, thermal conductivity and the speed of sound also vary with gas composition. Even in the absence of variations in light power absorbed, these changing

properties can dramatically alter the photoacoustic effect. Furthermore, many of these properties do not vary in a simple linear fashion, but follow a more complex dependence, as is discussed in more detail in section 3.3. Variation in gas properties introduces an additional source of uncertainty into the prediction of the response that does not exist for dilute mixtures, where the acoustic properties, determined by the diluent, remain constant.

3.2.4. *Acoustic leak effects*

The model for sound excitation, discussed above in 3.1.2, assumes that the cavity is sealed, so that the acoustic velocity is constrained to zero at the ends of the cavity. However, the presence of flow channels at either end of the cavity changes this boundary condition. In the limit of an open cell (where the cavity is completely open at either end) the non-resonant response would be strongly attenuated. The amplitude of the higher resonant modes, however, would be unaffected (while the node and anti-node locations would be transposed). The flow channels result in a cavity that is neither completely sealed nor open. Furthermore, the boundary condition set by the flow channels depends on the acoustic frequency and on gas properties.

A simple model for the "acoustic leak" effect is shown below in Figure 3-3. This model makes use of an acoustic circuit analogy [151]. In this circuit, the pressure is likened to electrical voltage, and the volumetric flow velocity to electrical current. A resistor represents the fluid channel, while a capacitor represents the cavity compliance.

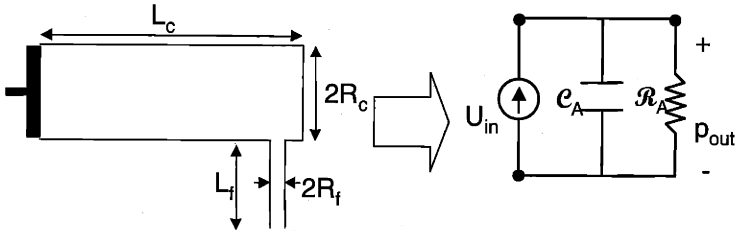

Figure 3-3: Simple circuit analogy for acoustic leak effect

In this "lumped element" model, which assumes that cell dimensions are much smaller than the acoustic wavelength, the values of $\mathcal{C}_A$ and $\mathcal{R}_A$ are given by [151]:

$$\mathcal{R}_A = \frac{8\eta L_f}{\pi R_f^4} \qquad (3\text{-}30)$$

$$\mathcal{C}_A = \frac{\pi L_c R_c^2}{\rho_0 c^2} \qquad (3\text{-}31)$$

where η is the viscosity, l_f the channel length, R_f the channel radius, l_c the photoacoustic chamber length, R_c the photoacoustic chamber radius, ρ_0 the steady-state gas density, and c is the speed of sound.

This model can be used to gain some insight into the leak effect. It indicates that the leak acts as a high-pass filter—at low frequencies the leak suppresses the signal, while at high frequencies it can be ignored. Furthermore, the leak can be reduced by decreasing the fluid channel radius, increasing the channel length, or by increasing the cavity volume.

In practice, however, this model has some fatal flaws. By using the lumped approximation, this model ignores the wave nature of the acoustic signal. Also, this model does not account for the losses that occur from thermal conduction and viscous dissipation in the photoacoustic cavity itself. A transmission line model, such as that discussed in 3.4, more accurately describes this effect.

3.2.5. *Viscous and thermal losses*

Viscous losses occur because of the no-slip boundary condition at the cavity wall. The gas molecules near the wall will exert a drag force on the molecules nearer to the center of the cavity. Thermal losses occur because of the thermal conductivity of the gas, causing some of the heat generated by the optical absorption to flow into the cavity walls. These loss mechanisms have already been discussed above in 3.1.2.2, in the context of the limits to resonance quality. They can be characterized by d_V and d_H, which are the viscous boundary layer and thermal boundary layer, respectively. As can be seen from Figure 3-4, d_V and d_H are comparable in size.

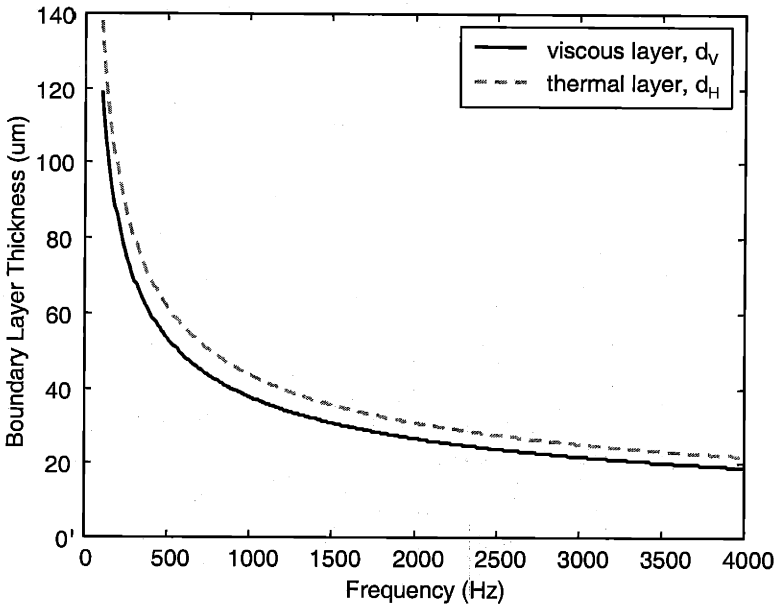

Figure 3-4: d_V and d_H as a function of frequency for pure propane

Both thermal and viscous losses should increase with the surface-to-volume ratio of the cavity. Therefore, we should use a model for miniaturized PAS that includes these effects from the beginning, rather than treating them as perturbations. We also need our model to accommodate the effects of flow channels, absorption saturation and changing gas properties. The easiest way to accomplish this is with the use of transmission line models.

3.3. *Gas properties*

The model can only be as accurate as its assumed gas properties. The determination of pertinent gas properties is discussed below. In particular, I have focused on propane, carbon dioxide and nitrogen, which are used in this thesis.

3.3.1. *Absorptivity*

Libraries of FTIR absorption spectra are widely available. These figures plot the transmission of the gas against the wavelength and wavenumber. The transmission is given by $10^{-aLN_{molar}}$, where a is the decadic molar extinction coefficient, L is the cavity length, and N_{molar} is the molar concentration. The decadic molar extinction coefficient form of absorptivity is related to the α form by $\alpha=aN_{molar}\ln 10$. The propane absorption spectrum is shown in Figure 3-5. At 3.39 μm, the background transmission is about 85%, while the transmission with propane is 26%. The transmission, is therefore 0.26/0.85 or 30.6%. The cavity is 88 mm long, and the gas

is at 55 °C and 20 mbar. The molar concentration can be calculated from the ideal gas law to be 0.734 mol/m^3. The result for a is 8.0 m^2/mol.

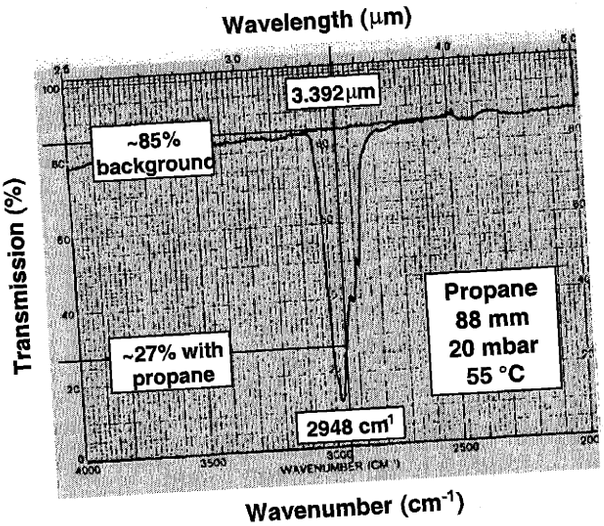

Figure 3-5: FTIR spectra for propane [152]

This calculation assumes that the absorptivity is independent of gas conditions. However, the absorptivity for some species depends on pressure, temperature, and mixture composition, due to collision and Doppler broadening. The variation can be significant. For example, the absorptivity of 100% methane at 3.39 μm decreases by a factor of 10 between a total pressure of 20 and 200 mbar, while the absorptivity of 1% methane in argon decreases by a factor 5 [153].

A few groups have examined the extinction coefficient for propane at the 3.39 μm He-Ne laser line under STP conditions. Antipov *et al.* [154] measured a value of 9.6 m^2/mol at STP, with little variation over the pressure range of 150 – 1000 mbar. Tsuboi *et al.* [153] observed a value of a varying between 8 and 11 m^2/mol for a variety of temperature, pressure, and dilution conditions. For the model, I used a value for a of 10 m^2/mol which at STP corresponds to α = 921 m^{-1}. The survey of literature suggests that the actual value may be anywhere within the range of 737 to 1013 m^{-1}*.

3.3.2. *Other properties of pure gases*

Properties used for propane, nitrogen and carbon dioxide are listed below in Table 3-1.

Property	C_3H_8	source	N_2	source	CO_2	source
viscosity, η (Pa-s)	8.0×10^{-6}	[155]	1.78×10^{-5}	[156]	1.49×10^{-5}	[156]
thermal conductivity, κ (W/(m K))	0.018	[157]	0.026	[156]	0.0168	[157]
gamma, γ	1.124	[158]	1.400	[158]	1.288	[158]
density, ρ_0 (kg/m^3)	1.796	$= \frac{M_{C_3H_8}}{M_{CO_2}} \rho_{0,CO_2}$	1.123	[156]	1.773	[156]
molecular weight, M (g/mol)	44.094	[158]	28.013	[158]	44.010	[158]
heat capacity at constant pressure, C_p (J/(kg K))	1.68×10^3	[158]	1.04×10^3	[158]	0.85×10^3	[158]
speed of sound, c (m/s)	250	$= \sqrt{\gamma P_0 / \rho_0}$	353	$= \sqrt{\gamma P_0 / \rho_0}$	270	$= \sqrt{\gamma P_0 / \rho_0}$

Table 3-1: Pure gas properties for propane, nitrogen and carbon dioxide

3.3.3. *Mixture properties*

The viscosity of a mixture is found using Wilke's approximation [159], which says that the viscosity of a low-pressure, non-polar gas mixture is given by:

$$\eta_m = \frac{y_1 \eta_1}{y_1 + y_2 \Phi_{12}} + \frac{y_2 \eta_2}{y_2 + y_1 \Phi_{21}} \qquad (3\text{-}32)$$

where η_m is the viscosity of the mixture, η_1 and η_2 are the viscosities of the component gases, y_1 and y_2 are the fractions of the component gases and Φ_{12} and Φ_{21} are given by:

$$\Phi_{12} = \frac{\left[1 + (\eta_1/\eta_2)^{1/2} (M_2/M_1)^{1/4}\right]^2}{\left\{8\left[1 + (M_1/M_2)\right]\right\}^{1/2}} \quad \Phi_{21} = \Phi_{12} \frac{\eta_2}{\eta_1} \frac{M_1}{M_2} \qquad (3\text{-}33)$$

M_1 and M_2 are the molecular weights of the respective gases. This model appears to be fairly accurate when compared against literature values for gas mixtures, as is illustrated in Figure 3-6 below.

---

* This also assumes that the average pressure remains at 1 atm and the average temperature at 298K. Can we make this assumption in the presence of light absorption, which may cause a temperature rise? Appendix D shows how even for the worst case of constant illumination, the temperature rise is insignificant compared to room temperature.

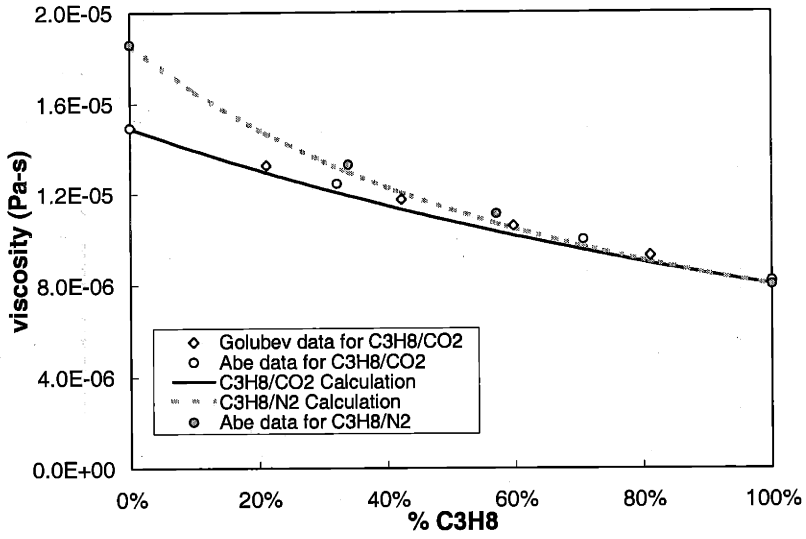

Figure 3-6: Comparison of viscosity model against values measured by Golubev *et al.* [160] and Abe *et al.* [161] for C_3H_8/CO_2 and C_3H_8/N_2 mixtures

The thermal conductivity of a mixture has a similar dependence [159]:

$$\kappa_m = \frac{y_1\kappa_1}{y_1+y_2\Phi_{12}} + \frac{y_2\kappa_2}{y_2+y_1\Phi_{21}} \qquad (3\text{-}34)$$

where Φ_{12} and Φ_{21} are as is given in (3-33).

The heat capacities and γ of an ideal gas are related to the thermal conductivity and the viscosity, and can be estimated by [159]:

$$C_P = \frac{\kappa}{\eta} - \frac{5R_d}{4M} \qquad (3\text{-}35)$$

$$C_V = C_P - \frac{R_d}{M} \qquad (3\text{-}36)$$

$$\gamma = \frac{C_P}{C_V} \qquad (3\text{-}37)$$

where R_d is the gas constant (8.3144 J $mol^{-1}K^{-1}$). By using the mixture values for κ and η, and assuming that the molecular weight of a mixture is a linear combination of the components, one can use these equations to predict the value of γ for a mixture. The speed of sound can be derived from the gas density, pressure and γ, from:

$$c = \sqrt{\frac{\gamma P_0}{\rho_0}} \qquad (3\text{-}38)$$

3.4. *Transmission line model of the photoacoustic effect*

The photoacoustic effect in a cylinder has been modeled with a circuit analogy to a transmission line [81, 99]. As in the lumped element model above, the acoustic pressure, p, is the acoustic analog of the electric voltage, while the volumetric flow velocity, U, is the analog of the current. Like the more established theory described in section 3.1, this treatment of wave propagation is conducted in frequency space, with the implicit modulation function $e^{j\omega t}$.

3.4.1. *Overview of transmission line analogy*

Transmission lines can be considered as a cascade of lumped circuit models each describing a unit length of tubing, Δz.

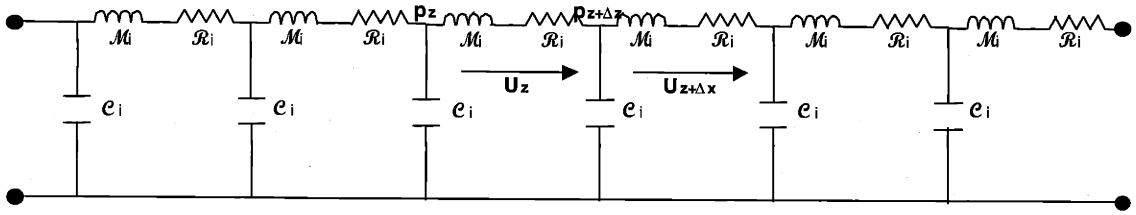

Figure 3-7: Circuit model for a transmission line

Transmission lines are simply an accounting system for energy. In modeling an electromagnetic waveguide, the incremental inductance $\mathcal{M}_i$ represents the energy stored in the magnetic field, the incremental capacitance $\mathcal{C}_i$ represents the energy stored in the electric field, and the incremental resistance $\mathcal{R}_i$ represents the energy dissipated at each point along the waveguide.

3.4.1.1. *Acoustic analogy*

In the acoustic analogy, the inductance represents the kinetic energy, the capacitance represents the potential energy, and the resistance accounts for incremental viscous and thermal dissipation. Since the energy, E, stored by an inductor of value $\mathcal{M}$ is given by $E = \frac{1}{2}\mathcal{M}U^2$, the value of the acoustic incremental inductance is derived to be [162]:

$$\mathcal{M}_i = \frac{2}{U^2}(K.E./length) = \frac{2}{S^2u^2}\left(\frac{1}{2}S\rho_0u^2\right) = \frac{\rho_0}{S} \qquad (3\text{-}39)$$

(3-39) takes advantage of the relations $U = Su$, and $mass = SL\rho_0$, where u is the velocity, S the cross-sectional area, L the length and ρ_0 the density.

Similarly, one can derive the unit length capacitance by saying that the potential energy per unit length is given by $\frac{1}{2}\mathcal{C}_ip^2$ [162]:

$$\mathcal{C}_i = \frac{2}{p^2}(P.E./length) = \frac{2}{p^2}\left(\frac{Sp^2}{2\rho_0 c^2}\right) = \frac{S}{\rho_0 c^2} \qquad (3\text{-}40)$$

Energy is lost in the acoustic system through viscous damping and thermal conduction. These two loss mechanisms can be represented with separate resistors, as is shown in Figure 3-8. Viscous damping is represented by a resistance, $\mathcal{R}_i$, to the volumetric flow through the cavity. Thermal conduction losses can be represented by a shunting conductance, $\mathcal{G}_i$.

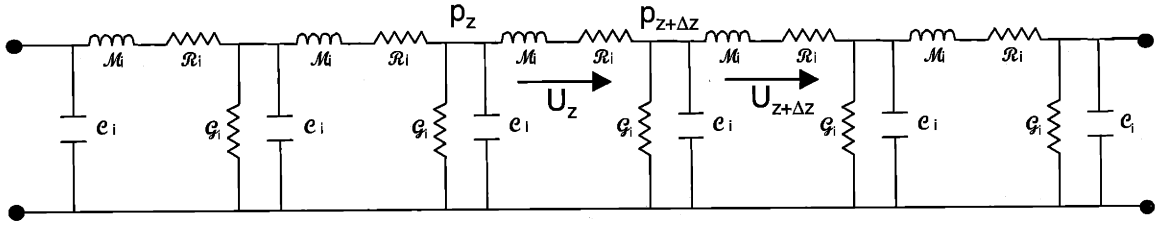

Figure 3-8: Acoustic transmission line analogy

The viscous power loss per unit length is $\mathcal{R}_i|U|^2$. The power lost to viscous damping per unit of surface is given by [162]:

$$\text{power loss/unit surface} = \frac{\rho_0 \omega d_v |U|^2}{2S^2} \qquad (3\text{-}41)$$

Here, d_V is the viscous boundary layer, already discussed. Its value is given by:

$$d_V = \sqrt{2\eta/\rho_0\omega} \qquad (3\text{-}42)$$

Using D as the perimeter of the tube cross-section, the analogous resistance is given by:

$$\mathcal{R}_i = \frac{\rho_0 \omega D d_v}{2S^2} \qquad (3\text{-}43)$$

Similarly, the conduction loss per unit length is $\mathcal{G}_i|p|^2$, so the analogous conductance is given by [162]:

$$\mathcal{G}_i = \frac{(\gamma - 1)\omega D d_H}{2\rho_0 c^2} \qquad (3\text{-}44)$$

where d_H is the thermal boundary layer, given by:

$$d_H = \sqrt{2\kappa/\rho_0 C_P \omega} \qquad (3\text{-}45)$$

3.4.1.2. *Transmission line equations*

Referring to Figure 3-8, the pressure at the point $z+\Delta z$ is related to the pressure at point z by:

$$p(z+\Delta z) = p(z) - Z_i U(z) \quad \text{(3-46)}$$

$$\text{where: } \mathcal{Z}_i = j\omega \mathcal{M}_i + \mathcal{R}_i \quad \text{(3-47)}$$

$\mathcal{Z}_i$ is the impedance/unit length and has units of ohms/m. In the limit of Δz going to 0, the following equation results:

$$\frac{dp(z)}{dz} = -\mathcal{Z}_i U(z) \quad \text{(3-48)}$$

Similarly, the volumetric velocity at point $z+\Delta z$ is related to the that at point z by:

$$U(z+\Delta z) = U(z) - \mathcal{Y}_i p(z) \quad \text{(3-49)}$$

$$\text{where: } \mathcal{Y}_i = j\omega \mathcal{C}_i + \mathcal{G}_i \quad \text{(3-50)}$$

$\mathcal{Y}_i$ is the admittance/unit length, and it has the units Siemens/m. By taking the limit of Δz going to 0, one derives:

$$\frac{dU(z)}{dz} = -\mathcal{Y}_i p(z) \quad \text{(3-51)}$$

The solution to this set of differential equations is given by:

$$U(z) = Ae^{\beta z} + Be^{-\beta z} \quad \text{(3-52)}$$

$$p(z) = -\mathcal{Z}_c \left(Ae^{\beta z} - Be^{-\beta z}\right) \quad \text{(3-53)}$$

where $\beta = (\mathcal{Z}_i \mathcal{Y}_i)^{1/2}$ and $\mathcal{Z}_c = (\mathcal{Z}_i / \mathcal{Y}_i)^{1/2}$. A and B are found by matching boundary conditions.

So to summarize, the parameters of the transmission-line analogy for a tube of cross-sectional area S and perimeter D are given by:

d_V	$\sqrt{2\eta/\rho_0\omega}$
d_H	$\sqrt{2\kappa/\rho_0 C_P \omega}$
$\mathcal{M}_i$	ρ_0/S
$\mathcal{C}_i$	$S/\rho_0 c^2$
$\mathcal{R}_i$	$\frac{\rho_0 \omega D d_V}{2S^2}$
$\mathcal{G}_i$	$\frac{\omega D(\gamma-1)d_H}{2\rho_0 c^2}$
$\mathcal{Z}_i$	$j\omega\mathcal{M}_i + \mathcal{R}_i$
$\mathcal{Y}_i$	$j\omega\mathcal{C}_i + \mathcal{G}_i$
β	$(\mathcal{Z}_i\mathcal{Y}_i)^{1/2}$
$\mathcal{Z}_c$	$(\mathcal{Z}_i/\mathcal{Y}_i)^{1/2}$

Table 3-2: Transmission line parameters for acoustic analogy

3.4.2. *Localized excitation model*

In Figure 3-2 on page 43 it is apparent that for high concentrations of the absorbing gas, all of the light is absorbed near the front of the cavity. The heat generation in this case can be approximated by a current source at the front of the cavity. The circuit model for this case is shown in Figure 3-9. The value of U_s is given by:

$$U_S = \frac{(\gamma - 1)W_0}{\rho_0 c^2} \qquad (3\text{-}54)$$

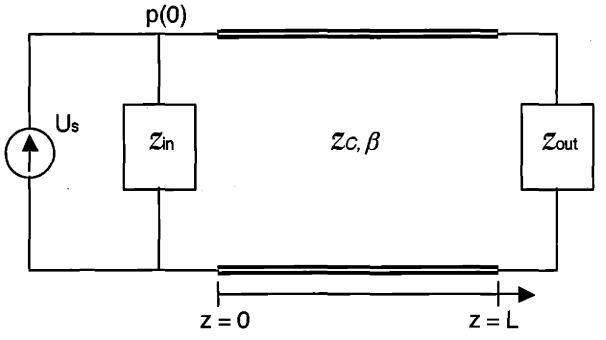

Figure 3-9: Circuit model for localized absorption

The boundary conditions are set by the channel impedances, Z_{in} and Z_{out}, as well as by the heat source. The impedance seen looking into the transmission line at $z = 0$ is given by:

$$Z_{z=0} = Z_c \frac{1-\Gamma}{1+\Gamma} \qquad (3\text{-}55)$$

$$\text{where } \Gamma = \frac{A}{B} = e^{-2\beta L} \frac{Z_C - Z_{out}}{Z_C + Z_{out}} \qquad (3\text{-}56)$$

The acoustic pressure at $z = 0$ is given by:

$$p(0) = p_0 = U_S \frac{1}{\frac{1}{Z_{in}} + \frac{1}{Z_{z=0}}} \qquad (3\text{-}57)$$

Finally, the expression for the acoustic pressure at any point z along the transmission line is given by:

$$p(z) = p_0 \frac{e^{-\beta z} - \Gamma e^{\beta z}}{1-\Gamma} \qquad (3\text{-}58)$$

---

* Note that with the implied $e^{j\omega t}$ dependence, $e^{-\beta z}$ represents the forward moving wave, while $e^{\beta z}$ the reverse going wave. Acoustic models often assume a $e^{-j\omega t}$ dependence, resulting in an inverted definition of Γ.

In order to solve for the signal, we need the channel impedances $\mathcal{Z}_{in}$ and $\mathcal{Z}_{out}$. These, too, can be found with transmission line models.

3.4.3. *Determination of $\mathcal{Z}_{in}$ and $\mathcal{Z}_{out}$*

The flow channels are also acoustic tubes, and can be modeled just as was described in 3.4.1. In some cases, $\mathcal{Z}_{in}$ and $\mathcal{Z}_{out}$ can also be affected by exterior tubing connections. Figure 3-10 shows a sketch of a photoacoustic cell connected to tubing, as is the case for the brass cell tests.

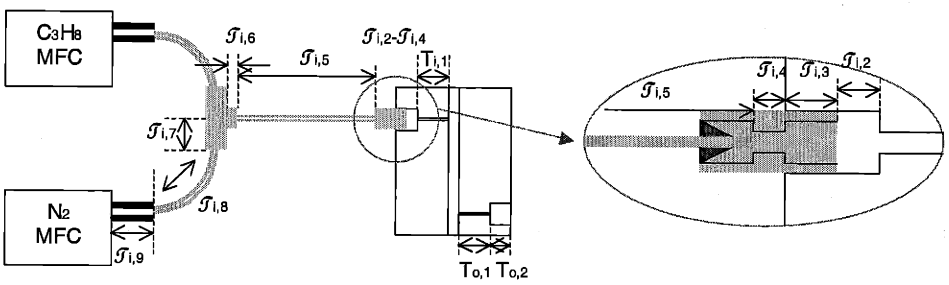

Figure 3-10: Sketch for determining effect of exterior flow connections

The impedance can be calculated by approximating the channel and tubing as a series of perfect tubes, which can be modeled as cascaded transmission lines. The properties β_n and $\mathcal{Z}_{c,n}$ can be calculated for each section from its dimensions. The effective impedance seen looking into the flow channel at the nth location is given by:

$$\mathcal{Z}_{eff,n} = \mathcal{Z}_{c,n}\frac{1-\Gamma_n}{1+\Gamma_n} \qquad \textbf{(3-59)}$$

$$\Gamma_n = e^{-2\beta_n L_n}\frac{\mathcal{Z}_{c,n}-\mathcal{Z}_{eff,n+1}}{\mathcal{Z}_{c,n}+\mathcal{Z}_{eff,n+1}} \qquad \textbf{(3-60)}$$

Splits, such as the one that occurs between sections $\ell_{i,6}$ and $\ell_{i,7}$ in Figure 3-10, can be handled by treating the two branches as impedances in parallel. While the algebra for cascading the transmission lines would be onerous if done by hand, these equations can be solved readily with a program such as Matlab. Appendix C contains the Matlab program used to solve for $\mathcal{Z}_{in}$ and $\mathcal{Z}_{out}$, as well as the code for the other transmission line models discussed in this chapter.

Figure 3-11 shows $\mathcal{Z}_{in}$ and $\mathcal{Z}_{out}$ as a function of frequency for a particular brass cell. On the same plot, I've also shown the cavity impedance, $\mathcal{Z}_c$, and the channel impedance calculated without tubing effects. $\mathcal{Z}_{out}$ is plotted for the case where the outlet is left unconnected, so the only additional segment included in the full model is the Swagelock-threaded hole. As can be seen from the figure, the tubing dramatically affects the value of $\mathcal{Z}_{in}$ at low frequencies.

Furthermore, at high frequencies, $\mathcal{Z}_{in}$ and $\mathcal{Z}_{out}$ are much higher than the cavity impedance $\mathcal{Z}_c$, so that the acoustic leak is small.

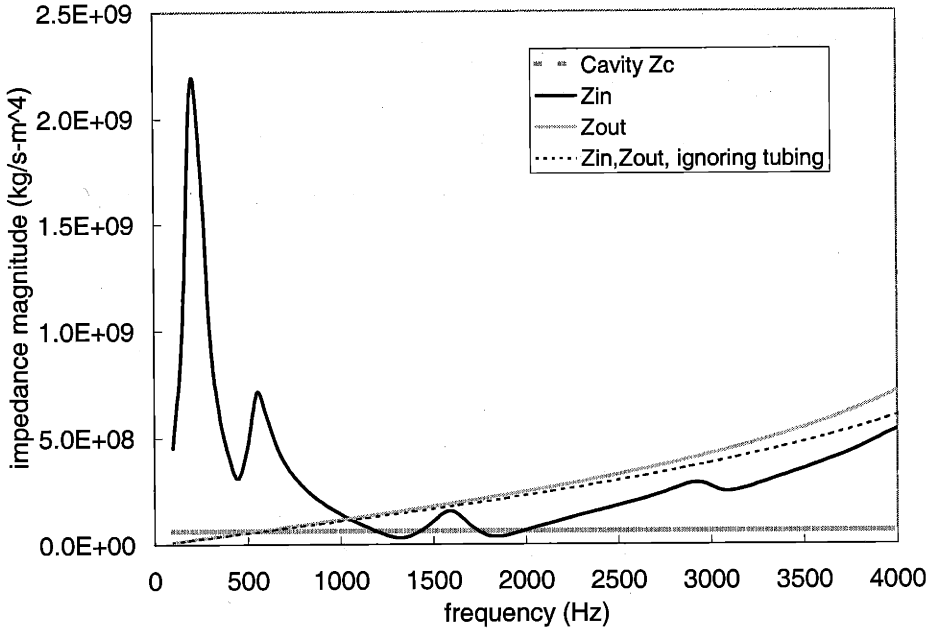

Figure 3-11: $\mathcal{Z}_{in}$ and $\mathcal{Z}_{out}$ as a function of frequency, for a cell with a large leak. The cavity impedance and impedance of the channels alone are also plotted for comparison.

Once $\mathcal{Z}_{in}$ and $\mathcal{Z}_{out}$ are determined, the localized generation model described above in 3.4.2 can be used to model the frequency response in the case of pure propane. Figure 3-12 shows the result for a typical brass cell. I have plotted the signal for a square wave with the peak-to-peak excitation of 1 W, monitored at its fundamental frequency (taking into account that the fundamental mode amplitude is $2/\pi$ times the square wave amplitude). This normalization will allow experimental data with different power levels to be more easily compared. At low frequencies, tubing effects dominate, resulting in low-order resonant peaks. The first longitudinal resonance, which occurs near 3500 Hz, is negligible in this figure because the sample point at the center of the cavity is at a pressure node for this mode. A remnant of the peak appears because the loss in the cell has dampened the mode.

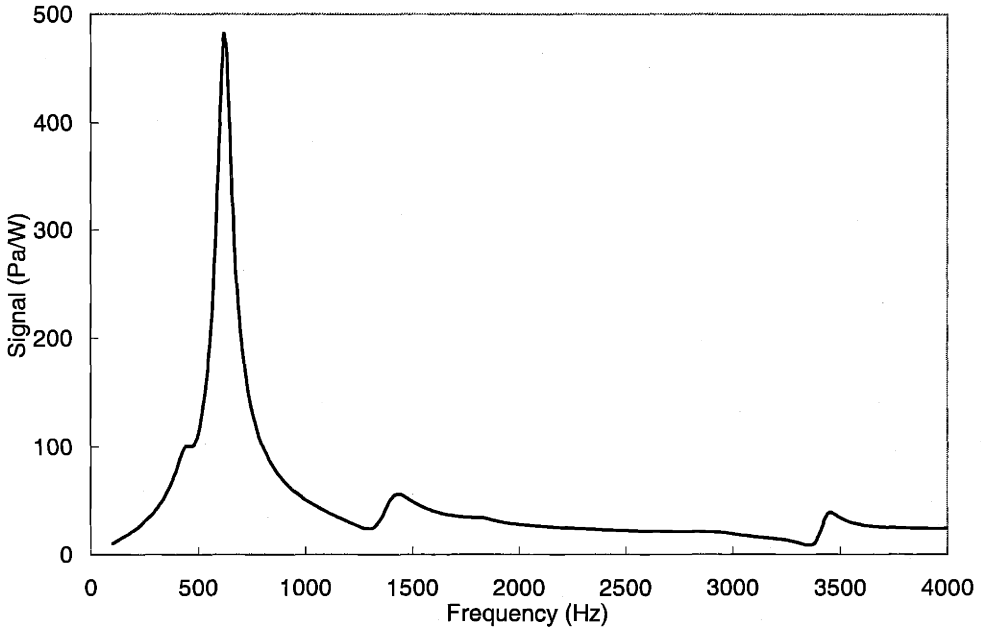

Figure 3-12: Localized excitation model for the frequency response in a brass cell

3.4.4. *Distributed heat generation model*

The localized heat generation model ignores the spatial distribution of light absorption in the cavity. I have accounted for the distribution along the cavity length with the addition of a distributed current source, as is illustrated in Figure 3-13. While others have considered the transmission line model of a photoacoustic cavity with a distributed source [81, 99], I have extended the model to include the axial dependence of the excitation, which (as was discussed above in 3.2.1) is significant for high gas concentrations.

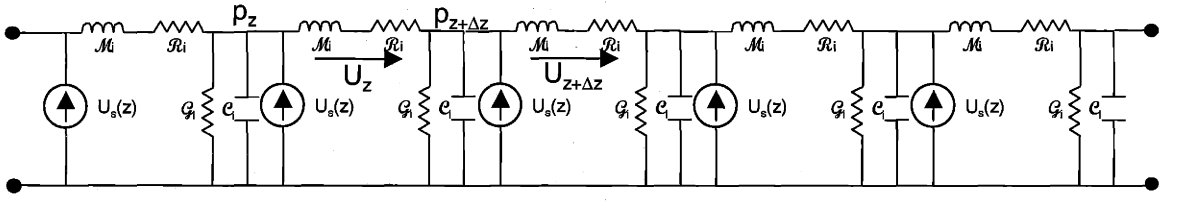

Figure 3-13: Circuit model for distributed source

The distributed source, $U_s(z)$, is given by:

$$U_S(z) = \frac{(\gamma - 1)\alpha W e^{-(\alpha+\delta)z}}{\rho_0 c^2} = U_0 e^{-\alpha' z} \qquad (3\text{-}61)$$

where for simplicity I've made the substitutions: $U_0 = (\gamma\text{-}1)\alpha W/(\rho_0 c^2)$ and $\alpha' = \alpha + \delta$. The differential equations governing $p(z)$ and $U(z)$ are now given by:

$$\frac{dp(z)}{dz} = -\mathcal{Z}_i U(z) \tag{3-62}$$

$$\frac{dU(z)}{dz} = U_0 e^{-\alpha' z} - \mathcal{Y}_i p(z) \tag{3-63}$$

where $\mathcal{Z}_i$ and $\mathcal{Y}_i$ are as in Table 3-2. The solution to (3-62) and (3-63) is given by:

$$U(z) = Ae^{\beta z} + Be^{-\beta z} - \frac{\alpha'}{\alpha'^2 - \beta^2} U_0 e^{-\alpha' z} \tag{3-64}$$

$$p(z) = -\mathcal{Z}_c \left(Ae^{\beta z} - Be^{-\beta z} + \frac{\beta}{\alpha'^2 - \beta^2} U_0 e^{-\alpha' z} \right) \tag{3-65}$$

where β and $\mathcal{Z}_c$ are also as in Table 3-2. The circuit model for our system with the distributed source is given by Figure 3-14, below.

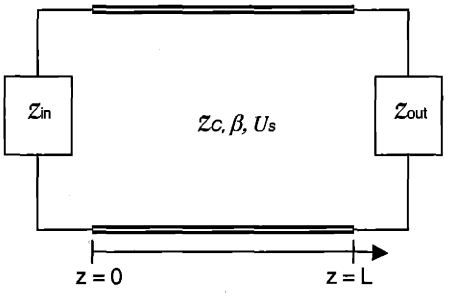

Figure 3-14: Circuit model for distributed source system

Matching the boundary condition at $z = L$ establishes the following relation:

$$B = \frac{A}{\Gamma_{out}} + \frac{U_0 e^{(\beta-\alpha')L}}{\alpha'^2 - \beta^2} \left[\frac{\beta Z_C - \alpha' Z_{out}}{Z_C - Z_{out}} \right] \tag{3-66}$$

$$\text{where: } \Gamma_{out} = e^{-2\beta L} \frac{Z_C - Z_{out}}{Z_C + Z_{out}}, \text{ as before} \tag{3-67}$$

Similarly, matching the boundary condition at $z = 0$ establishes the relation:

$$B = \frac{A}{\Gamma_{in}} + \frac{U_0}{\alpha'^2 - \beta^2} \left[\frac{\beta Z_C + \alpha' Z_{in}}{Z_C + Z_{in}} \right] \tag{3-68}$$

$$\text{where: } \Gamma_{in} = \frac{Z_c + Z_{in}}{Z_c - Z_{in}} \tag{3-69}$$

The solution for A is therefore given by:

$$A = \frac{\dfrac{U_0}{\alpha'^2 - \beta^2}\left(\dfrac{\beta Z_c - \alpha' Z_{out}}{Z_c - Z_{out}} e^{(\beta-\alpha')L} - \dfrac{\beta Z_c + \alpha' Z_{in}}{Z_c + Z_{in}}\right)}{\dfrac{1}{\Gamma_{in}} - \dfrac{1}{\Gamma_{out}}} \qquad (3\text{-}70)$$

B can then be found from either (3-68) or (3-70). Given A and B, the model can be solved for the pressure at $L/2$ where the microphone is located. Figure 3-15 compares both the localized and distributed excitation model for the frequency dependence of the pure propane signal; they are almost indistinguishable, as was expected.

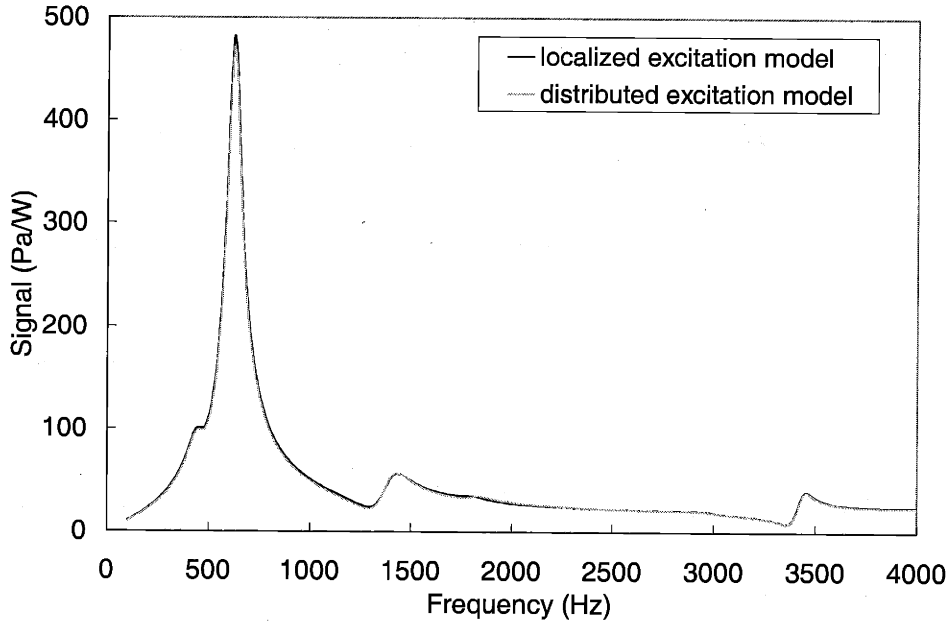

Figure 3-15: Comparison between frequency behavior predicted by localized excitation and distributed excitation model for pure propane

3.4.5. *Addition of the microphone to the model*

Up to this point we have assumed that adding the microphone does not disturb the system. However the microphone volume is on the same order as the geometry of our system, and so must be considered. Furthermore, the details of the interface between the microphone and the cavity can also be significant. A close up of the microphone connection for the brass cells is shown in Figure 3-16. The microphone inlet is separated from the photoacoustic cavity by a small connecting hole. The inlet has a small dead volume, which adds to the dead volume of the entrance tube on the microphone itself. Figure 3-17 shows a circuit model of the system that includes the microphone.

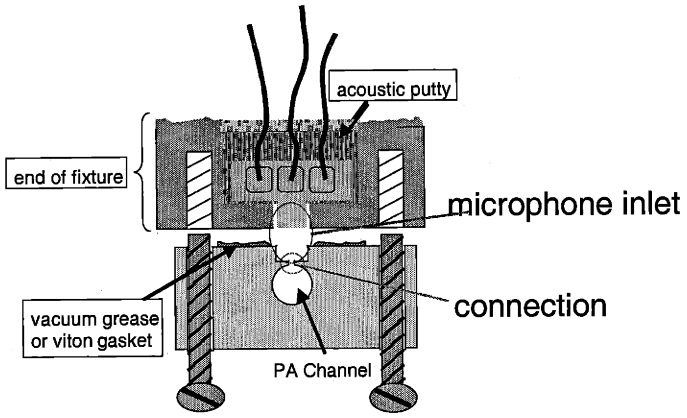

Figure 3-16: Close up of connection to microphone

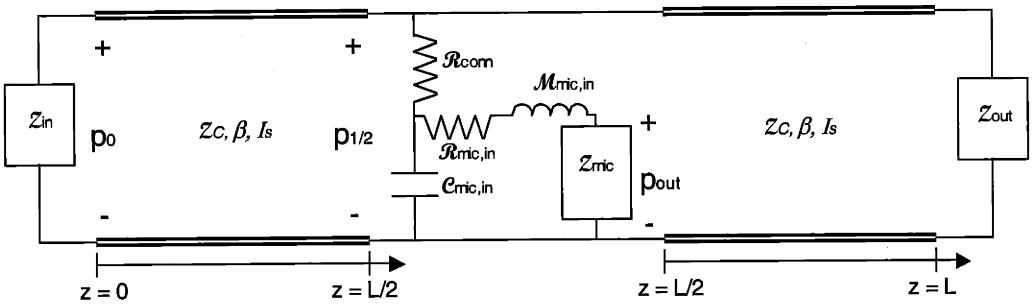

Figure 3-17: Including microphone connection in the transmission line model

The values of $\mathcal{R}_{conn}$, $\mathcal{R}_{mic,in}$, $\mathcal{C}_{mic,in}$ and $\mathcal{M}_{mic,in}$ can be calculated from the connection geometry and material properties [151], as are listed in Table 3-3.

Element	Value
$\mathcal{R}_{conn}$	$\frac{\rho_0}{\pi R_{conn}^3}(L_{conn})\sqrt{2\omega\frac{\eta}{\rho_0}}$ [kg s^{-1} m^{-4}]
$\mathcal{R}_{mic,in}$	$\frac{\rho_0}{\pi R_{mic}^3}(L_{mic,in}+L_{mic})\sqrt{2\omega\frac{\eta}{\rho_0}}$ [kg s^{-1} m^{-4}]
$\mathcal{M}_{mic,in}$	$\frac{\rho_0}{\pi R_{mic}^2}(L_{mic,in}+L_{mic})$ [kg/m^4]
$\mathcal{C}_{mic,in}$	$\frac{V_{mic}+V_{mic,in}}{\rho_0 c^2}$ [m^{4}s^2/kg]

Table 3-3: Formula for computing analogs for microphone connection acoustic elements

This model takes into account viscous losses, but ignores thermal conduction losses. The microphone impedance can be estimated from the literature provided by Knowles. The full circuit model for the EA-1954 is shown below.

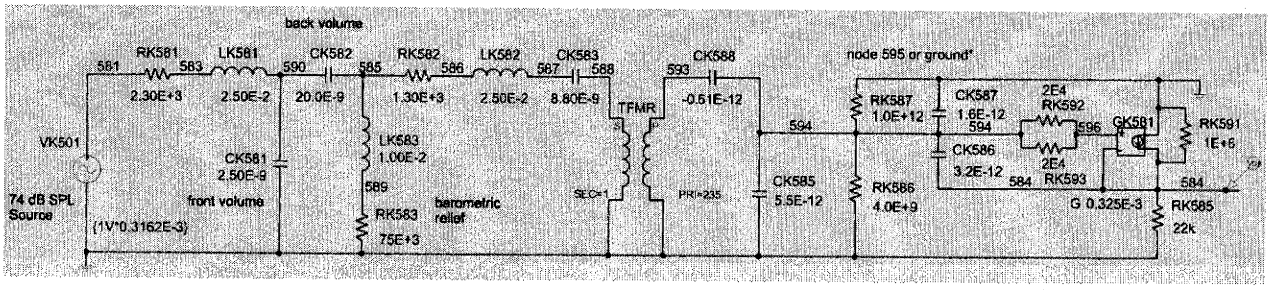

Figure 3-18: Knowles diagram for the EA-1954 microphone (units are in CGS)

At low frequencies (200 Hz $< f <$ 7 kHz) this circuit simplifies considerably. In this simplification I also have accounted for changing gas properties.

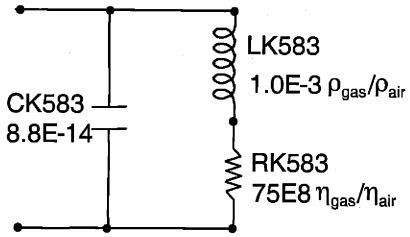

Figure 3-19: Simplified circuit model for the Knowles EA-1954 (The element labels are taken from the Knowles circuit diagram above)

The pressure that the microphone actually samples is given by p_{out}, while the pressure at the point of the microphone tap is $p_{1/2}$. Furthermore, the effect of the microphone and the inlet can be lumped together as an impedance, $\mathcal{Z}_{mic,tot}$, in the center of the cavity. Once the transfer function $p_{out}/p_{1/2}$ and $\mathcal{Z}_{mic,tot}$ are determined they can be easily incorporated into the model, by dividing the cavity transmission line into two halves, as is illustrated in Figure 3-20.

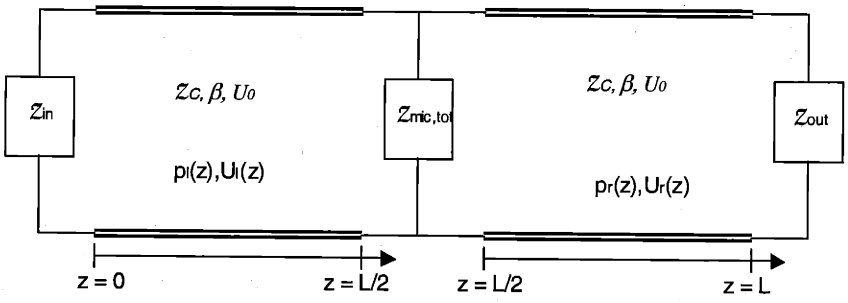

Figure 3-20: Transmission line model incorporating microphone

The left half has the pressure and volumetric velocity of $p_l(z)$ and $U_l(z)$, while the right half is characterized by $p_r(z)$ and $U_r(z)$. The boundary conditions for the solution are then given by:

$$p_r(L) = U_r(L)\mathcal{Z}_{out} \qquad (3\text{-}71)$$

$$p_r(0) = -U_r(0)Z_{in} \quad (3\text{-}72)$$

$$p_l\left(\frac{L}{2}\right) = p_r\left(\frac{L}{2}\right) \quad (3\text{-}73)$$

$$U_l\left(\frac{L}{2}\right) = U_r\left(\frac{L}{2}\right) + p_r\left(\frac{L}{2}\right)Z_{mic,tot} \quad (3\text{-}74)$$

The addition of the microphone has little effect on the signal in the acoustic frequency range of 100-4000 Hz, as can be seen from Figure 3-21.

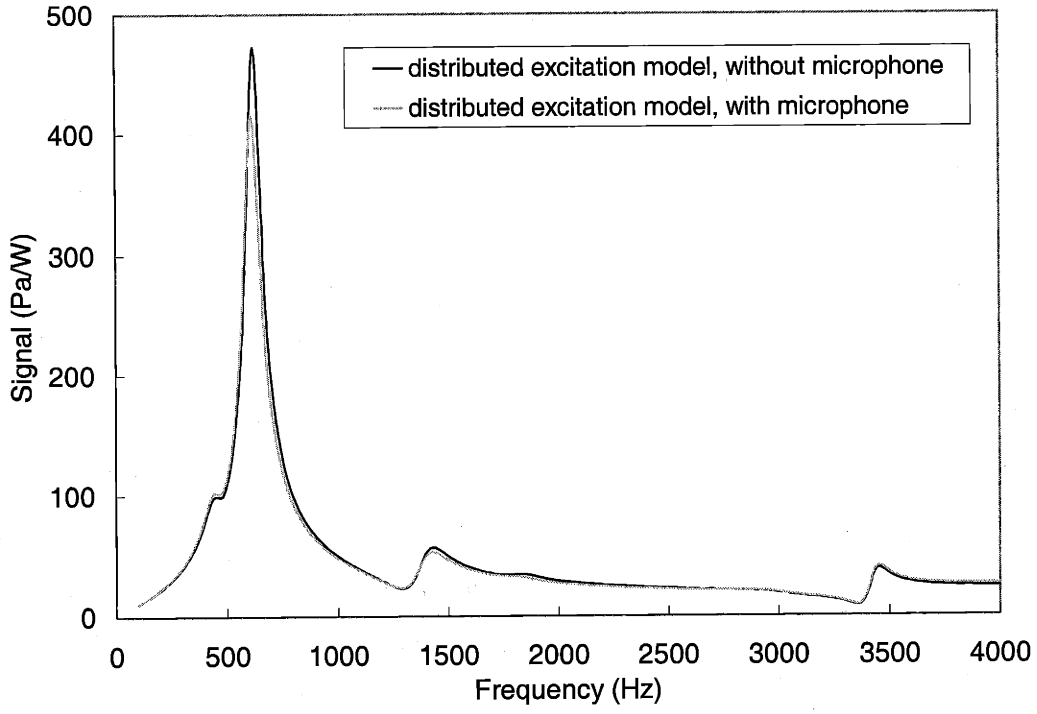

Figure 3-21: The effect of the microphone on the distributed excitation model

3.4.6. *Modeling the concentration dependence*

With the distributed model, one can also consider the effect of concentration on the signal, as in Figure 3-22. The concentration dependence for strongly absorbing gases have a distinctive saturation shape. At very low concentrations, the signal increases sharply with concentration, as is expected from the established photoacoustic theory for dilute mixtures. However, once the concentration is high enough that all of the light is absorbed, the total heat generation becomes independent of concentration. In this region the concentration dependence of the signal is determined not by absorption but by gas properties such as γ, and η. For propane

at 3.39 μm, this transition occurs at very low concentrations, because this absorption line is particularly strong.

The model also shows that while light loss from sidewall absorption has little effect at high concentrations, it has a strong effect at low gas concentrations where it is comparable in strength to the optical absorption of the gas mixture. The microphone has little effect on the concentration dependence.

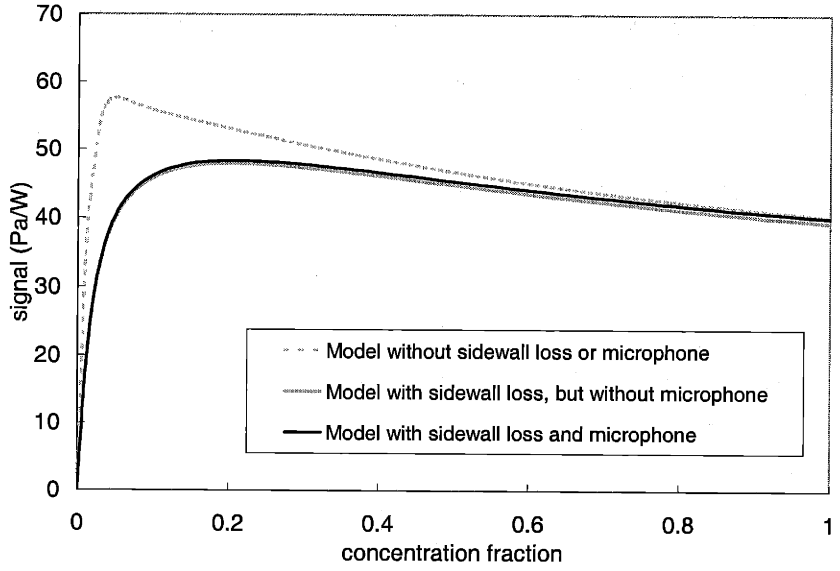

Figure 3-22: Concentration dependence of distributed excitation model with different variations (f = 326 Hz)

From Figure 3-22 one can see that PAS will be unable to quantitatively determine concentration fractions for highly-concentrated mixtures of strongly absorbing species. However, as will be discussed further in Chapter 6, saturation is not a problem for dilute mixtures, weak absorption lines, or short path-length cavities—the exact conditions for which other spectroscopy methods are inadequate.

3.4.7. *A summary of the transmission line model*

The transmission line model of the cavity includes thermal and viscous losses, absorption saturation, wall absorption, changing gas properties, and acoustic leaks due to the fluid channel and gas manifold. Some additional sources of losses have been neglected, such as the compliance of the cavity and tubing walls and the additional losses that occur from the direction change between the cavity and channels. Also, the model assumes simplified geometries for the elements of the flow manifold. Also, the model assumes that the pressure is sampled at a point at

the exact center of the cavity. These simplifications are discussed further in Chapter 4, when the predictions of the model are compared to experimental data.

3.5. *Noise sources*

A discussion of theory would not be complete without touching upon the subject of noise, which sets the sensitivity limit. There are several sources of noise for photoacoustic studies. The fundamental limit for PAS sensitivity is set by thermal fluctuation noise, which no amount of careful engineering can avoid. Much of the photoacoustic literature has also been devoted to the reduction of "background" noise, which is the signal generated by the non-selective absorption of light by the cavity walls and windows. In my own experiments, my sensitivity was limited by "ambient" noise—the underlying sound level in the room.

3.5.1. *Thermal fluctuation noise—the absolute limit*

The fundamental limit of acoustic signal detection sensitivity is set by the noise created by the excitation of the acoustic nodes from thermal fluctuations. The power spectrum of this noise has the acoustic coefficients given by [148]:

$$\left|A_{jn}(\omega)\right|^2 = \frac{4\rho_0 c^2 kT}{V_C \omega_j Q_j \left[\left(1-\omega^2/\omega_j^2\right)^2 + \left(\omega/\omega_j Q_j\right)^2\right]} \qquad (3\text{-}75)$$

where ρ_0 is the gas density, c the speed of sound, k is the Boltzmann constant, T is the temperature, V_c is the chamber volume, and ω_j is the resonance frequency of mode j with a quality factor Q_j. While the total noise energy is kT, the values of Q_j change the frequency distribution of the noise. From (3-75), one can see that there is no contribution from the zeroth-order mode in the thermal fluctuation noise power spectrum. In non-resonant systems, in which the signal frequency is well below the lowest resonant frequency ($\omega << \omega_j$), (3-75) reduces to [148]:

$$\left|A_{jn}(\omega)\right|^2 = \frac{4\rho_0 c^2 kT}{V_C \omega_j Q_j} \qquad (3\text{-}76)$$

The effect of a noise source on an absorption spectroscopy system can be measured by examining the noise equivalent power (NEP), which is the amount of power that would have to be absorbed by the gas to produce a signal amplitude equal to the noise source. In the case of non-resonant PAS, where the signal amplitude is given by (3-14), and assuming the worst case,

which is that the noise is coupled entirely to the first-order mode, the noise equivalent power in watts per root hertz is given by [148]:

$$(NEP)^2 = \frac{8\pi\rho_0 c^2 kTV_C\omega^2}{\omega_1 Q_1(\gamma-1)^2} \qquad (3\text{-}77)$$

This is derived by setting $|A_0(\omega)|$ from (3-14) equal to $|A_{1n}(\omega)|$, and substituting the NEP for αWL. A factor 2π is added to convert from watts to watts/Hz$^{1/2}$. (3-77) indicates that the NEP is reduced by decreasing the volume and excitation frequency and by increasing the resonant mode spacing and Q.

3.5.2. *Background absorption*

Another source of noise in photoacoustic systems is the non-selective absorption of the incident radiation by the walls and windows of the cavity. Assuming that absorption in the walls and windows will result in a given source of heat flux, that heat will either flow into the solid with flux q_S or into the gas with flux q_V. The ratio q_V/q_S is given by [11]:

$$\frac{q_V}{q_S} = \sqrt{\frac{\rho_V C_{p_V} k_V}{\rho_S C_{p_S} k_S}} \qquad (3\text{-}78)$$

From (3-78), one can see that background absorption can be reduced by working at lower pressures or with highly-conductive wall materials. This is one advantage of silicon. However if there is a significant contribution from wall absorption, the higher surface to volume ratios of miniaturized systems could result in higher background levels.

3.5.3. *Other sources of noise*

There may also be significant noise sources in the electrical circuit of the microphone or amplifier. Johnson noise is thermal fluctuation noise in the resistors of the amplifier. At very low frequencies, "1/f" or "pink" noise could also be significant. In my experiments, the sensitivity was limited by ambient noise—sound that was generated by sources other than optical absorption in my testing area (see Figure 4-10 and Figure 5-9). The primary contributors to ambient noise were the ventilation fan for the chemical hood in which I conducted my experiments, and the mechanical vibration of the chopper. In theory, careful apparatus design could dramatically reduce the contribution of such noise sources.

4. Brass cell tests

4.1. *Detector design*

In order to test the theory described in the previous chapter, I used photoacoustic cells manufactured with conventional machining techniques out of brass. These brass cells offered several advantages over microfabricated cells for the purposes of theory validation. Each brass cell took less than a day to make, allowing dimensions to be easily and quickly varied. Also, conventional machining techniques allowed for the manufacture of photoacoustic cells with cavities that more closely matched the idealized cylindrical cavity. Figure 4-1 shows an overview of the brass photoacoustic detector. In addition to the photoacoustic cell, other elements of the experimental apparatus included the flow manifold, the optical excitation and detection, the microphone and the electronics. This section describes each of these elements in detail.

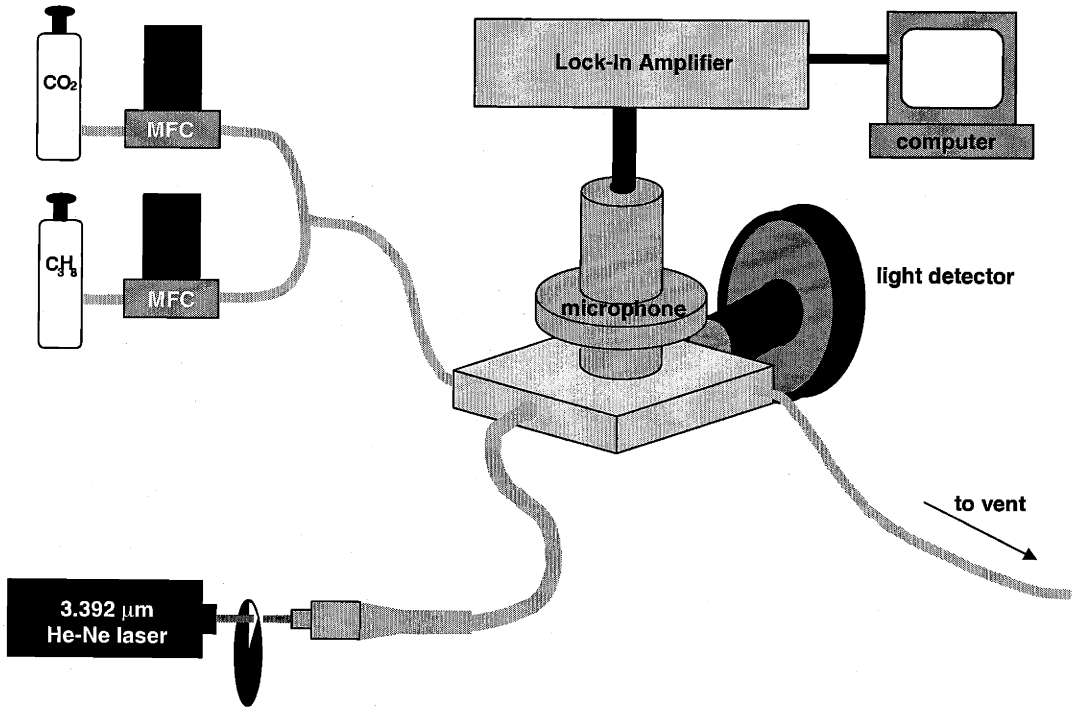

Figure 4-1: Overview of the brass photoacoustic detector

4.1.1. *The brass cell*

Figure 4-2 shows a schematic for a typical brass cell. It has a cylindrical photoacoustic cavity, with a fiber port at one end and a window at the other. The center of the cavity is tapped for the microphone fixture, which is held in place with bolts threaded through the cell. Gas flow channels intersect with the photoacoustic cavity at either end. The channel and cavity diameters, labeled in italics, were varied in different cells. AutoCAD drawings of the brass cells are included in the Appendix F.

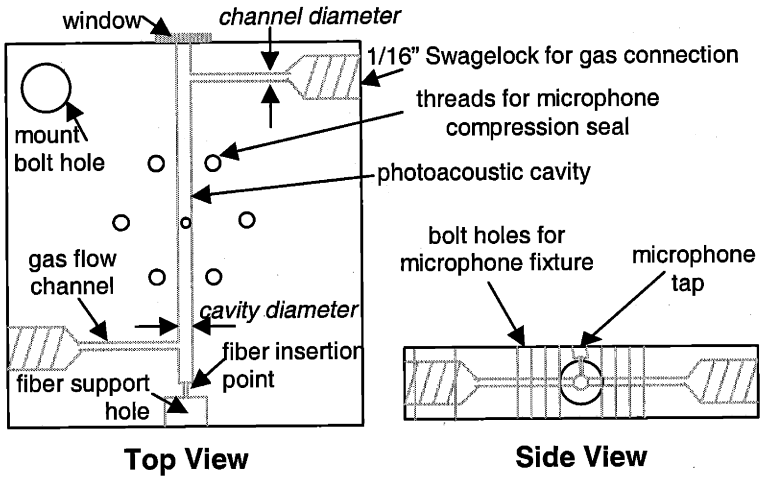

Figure 4-2: Brass cell schematic

Many cells were created with varying cavity and channel radii. All of the cells had a cavity length of 40 mm, and flow channels with a length of 9 mm from the cavity to the Swagelock threading. I focused on three cells in particular, the dimensions of which are listed in Table 4-1.

Cell type	R_{cavity}	$R_{channel}$
wide-big leak (WBL)	1.5 mm	0.55 mm
wide-small leak (WSL)	1.6 mm	0.17 mm
narrow-small leak (NSL)	0.75 mm	0.20 mm

Table 4-1: Brass cell dimensions

The optical fiber port had two parts: an outer 3-mm diameter hole sized to accommodate the fiber support tubing, and an inner 0.3 mm diameter bare fiber insertion hole. The bolt hole through the corner of the cell allowed for the cell to be mounted on an optical mount with XYZ-position control for alignment to the light detector. The gas channels widened into larger holes that were threaded for 1/16" Swagelock union fittings, allowing for standard tubing connections. Figure 4-3 shows a picture of the brass cell attached to an optical mount with the window and optical fiber already glued in place.

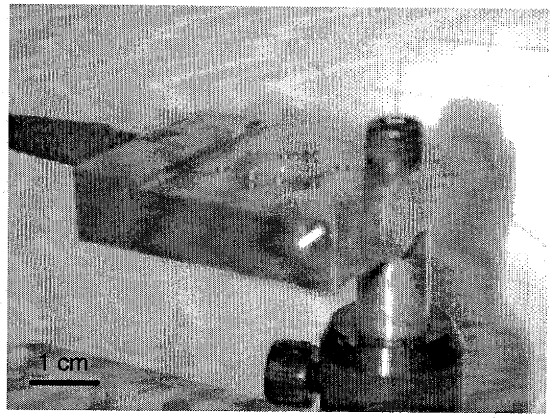

Figure 4-3: Brass cell with optical fiber and window attached

After machining, I cleaned the brass cells in an ultrasonic bath with acetone, methanol, isopropanol and deionized water. After drying the cells with an air gun and an hour bake in a 70°C oven, they were ready for assembly with the optical fiber and window.

4.1.2. *Optical excitation*

Optical excitation was provided by a 3.39 μm He-Ne laser (Jodon [163], model HN7G). The laser required a one-hour warm up period before producing a stable output. Once stabilized, the output power variation was less than 5%, and was reproducibly measured to be 2.0 mW. The light was modulated with an optical chopper from Stanford Research Systems [164], over either the 100-400 Hz or 400-4000 Hz frequency range, depending on the chopper blade. The modulation shape, as observed by a fast time-response infrared detector, was square.

The light was coupled through a lens to a ~0.3 m long fluoride fiber. In addition to having an anti-reflective coating for the mid-infrared range, the lens also had an SMA fiber mount aligned to its focal point. The optical fiber (Thor Labs [165], GF-F-160) had a core diameter of 160 μm, a cladding diameter of 200 μm, a buffer diameter of 500 μm, and could transmit light in the wavelength range of 500 nm to 4 μm with a specified loss of 40 dB/km at 3.4 μm. The optical fiber was packaged in the lab with furcation tubing (3.8 mm in diameter), an SMA connector at the lens end, and a stripped and cleaved fiber tip at the cell end.

In order to facilitate alignment, the mount for the fiber-coupling lens had XYZ-translational control as well as 3-axis angular control. The alignment of the laser to the fiber was monitored with the use of a custom-built, liquid nitrogen-cooled, indium antimony (InSb) detector from Galileo [166], which had a fast time-response. However, the InSb detector was not calibrated for absolute power level readings. For such measurements, I used a factory-

calibrated thermopile detector from Molectron [167] with the high sensitivity of 0.1 mW, but a very slow (~10 s) time response.

Before assembling each cell, I measured the transmission of the optical fiber as well as the window. The transmission of the 3-mm-thick CaF_2 window was consistently measured to be 85%, which matched that specified by the manufacturer [168]. The sidewall absorption in the cavity was measured by comparing the naked fiber output to light power exiting the cell cavity with the fiber inserted (but not epoxied) in place. The light was attenuated by ~50% after passing through each of the different cell cavities. Table 4-2 summarizes the results of the measurement of the power levels exiting the optical fiber before packaging. Each measurement was repeated 5-10 times. The standard deviation of the δ factor was calculated from the standard deviation of the power measurements by the "propagation of errors" technique described in Appendix J.

cell	power (W)	σ_w	δ	σ_δ
NSL	1.69 mW	0.05 mW	15 m^{-1}	3 m^{-1}
WSL	1.45 mW	0.05 mW	25 m^{-1}	5 m^{-1}
WBL	1.08 mW	0.13 mW	20 m^{-1}	3 m^{-1}

Table 4-2: Results of pre-packaged fiber power measurements

After these measurements, the stripped, cleaved end of the fiber was threaded into the optical port of the brass cell, and fixed in place with a dot of epoxy in the outer port hole. A spare connection mating sleeve, also affixed with epoxy, added further support. The 3 mm-thick CaF_2 window was also attached with epoxy. After assembly I measured the light transmission through the cell to confirm that it was consistent with the earlier measurements. The assembly process occasionally incurred undesired additional transmission loss with possible epoxy creep or damage to the optical fiber. Cells with such losses were disassembled, cleaned, and repackaged or, in an egregious case caused by an epoxy plug in the cavity, discarded.

4.1.3. *Acoustic transduction*

Pressure measurements were made with a Knowles EA-1954 microphone [169], a sketch of which is shown in Figure 4-4. The microphone was powered with a 'C'-type battery, and had a nominal sensitivity of 8 to 15 mV/Pa, over a broad frequency range (~100 – 6000 Hz). Sensitivity and range varied between microphones, and was determined by calibration as explained below.

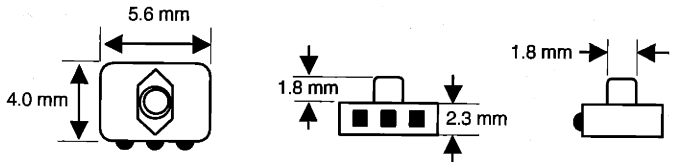

Figure 4-4: Different views of the Knowles EA-1954 microphone

The microphone was also extremely sensitive to mechanical stress, and therefore required a fixture that fully supported the microphone while facilitating a hermetic seal to the cell. The fixture also had to be compatible with the calibration apparatus at the University of Florida. The three-part aluminum fixture for the microphone is shown fully assembled in Figure 4-5. The microphone was embedded in acoustic putty inside the fixture with its inlet tube flush to the bottom. The fixture was bolted in place over the cell, sealed with either vacuum grease or a thin elastomer gasket. The fixture used an S-video connector for electrical connection to the microphone. Video cable allowed the microphone to communicate with a power/signal box, which contained the battery and a BNC output for the microphone signal. The details of the fixture and its assembly are included in Appendix G.

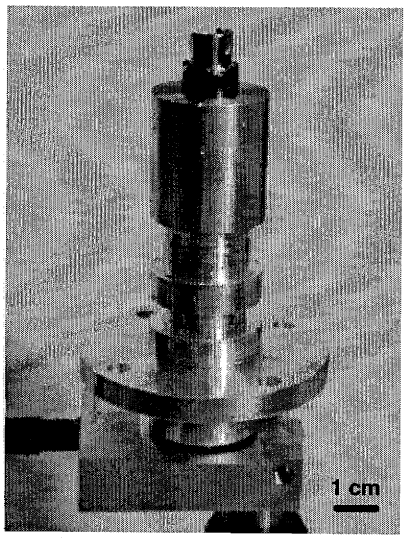

Figure 4-5: Packaged microphone connected to brass cell

Three different microphones were packaged in this manner and sent to the University of Florida for calibration in a plane-wave tube. The magnitude and phase of the frequency response for one of these microphones are shown below in Figure 4-6 and Figure 4-7. The response was observed to be linear with pressure, as can be shown in Figure 4-8. The calibration apparatus was limited to frequencies above 300 Hz. A small fraction of the data, however, was taken at frequencies below 300 Hz. For the interpretation of these few data points, I approximated the

sensitivity for lower frequencies with an extrapolation from a polynomial fit to the data in the range of 300-1000 Hz. The details of this extrapolation and the calculation of error for the microphone calibration are described in Appendix G.

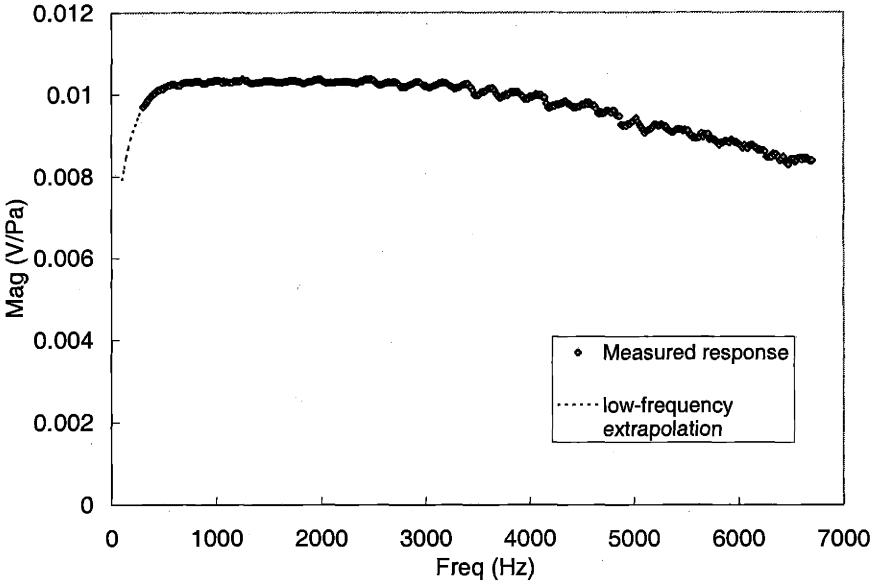

Figure 4-6: Frequency dependence of the sensitivity for one of the packaged microphones. A low frequency extrapolation was used to interpret the few measurements taken at frequencies less than 300 Hz.

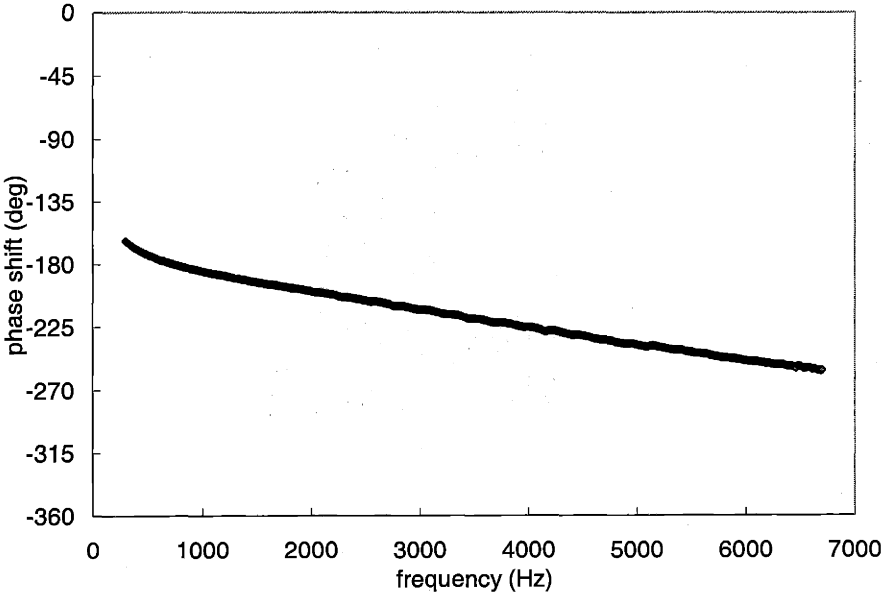

Figure 4-7: Phase of a the frequency response for one of the packaged microphones

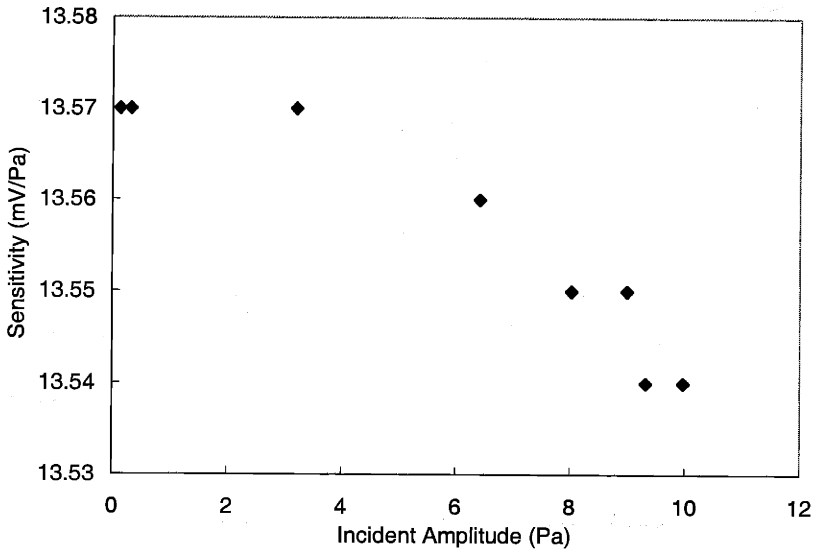

Figure 4-8: Linearity of one of the packaged microphones at 1 kHz

4.1.4. *Gas manifold*

Experiments were conducted with mixtures of propane and nitrogen. Flow rates were regulated with mass flow controllers (MFCs), which were calibrated using soap bubble tests. In this method, the gas line is fed into the bottom of a gradated cylinder just above a rubber sac filled with soapy water. By squeezing the sac one generates soap bubbles that then move up the column, pushed by the flow. As the bubbles move with very little friction, the rate of bubble movement can be correlated to the flow rate. Every combination of controller and gas required a separate calibration, the results of which are included in Appendix E. For the brass cell experiments I used flow rates ranging from 1 to 50 sccm. The MFCs occasionally had difficulties controlling the flow of propane at low rates (<2 sccm), allowing large fluctuations on the time scale of seconds. With the soap bubble tests it was determined that in these conditions the time-averaged flow velocity still matched the controller setting. However, I still avoided taking data under these conditions, which limited the dilutions that I could achieve with the flow manifold.

In order to reduce dead volumes and response time, I used 1/16" tubing with a small inner diameter (~500 μm) between the MFCs and the cell. Because of the leak effects discussed in section 3.4.3, the tubing dimensions had a significant effect on the signal.

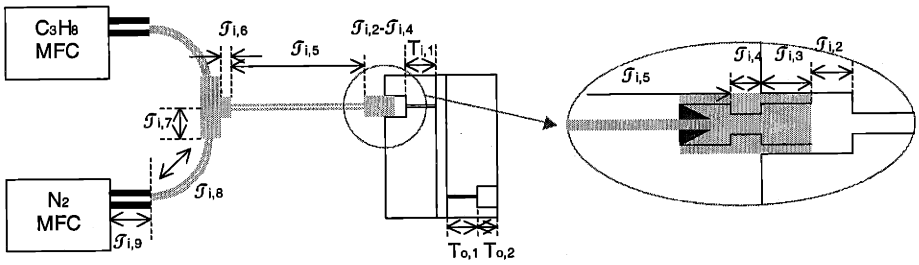

Figure 4-9: Sketch of tubing connections

Figure 4-9, which is a repetition of Figure 3-10, shows the elements of the gas flow manifold. Table 4-3 contains values for the dimensions of the different tubes that approximate the geometry of the manifold.

Element	Length	Radius
$\mathcal{T}_{i,1}$	9 mm	depends on cell
$\mathcal{T}_{i,2}$	2.5 mm	2.16 mm
$\mathcal{T}_{i,3}$	7 mm	0.794 mm
$\mathcal{T}_{i,4}$	8 mm	0.635 mm
$\mathcal{T}_{i,5}$	80 mm	0.254 mm
$\mathcal{T}_{i,6}$	14 mm	0.635 mm
$\mathcal{T}_{i,7}$	14 mm	0.635 mm
$\mathcal{T}_{i,8}$	50 mm	0.254 mm
$\mathcal{T}_{i,9}$	50 mm	3.2 mm
$\mathcal{T}_{o,1}$	9 mm	depends on cell
$\mathcal{T}_{o,2}$	9 mm	2.16 mm

Table 4-3: Dimensions for transmission line model of Z_{in} and Z_{out}

While the cell was designed to allow for the connection of venting tubing at the outlet, in most experiments the outlet was left unconnected. The cell and gas manifold were entirely contained in a vented, plexiglass hood, so the vent line was unnecessary.

4.1.5. *Lock-in electronics and data acquisition*

The microphone signal was sent to the input of a lock-in amplifier [164], which used the chopper modulation signal as its reference. The lock-in amplifier communicated with a computer using GPIB protocol. LabVIEW [170] was used to record the frequency and gas conditions and to tabulate the response, while the modulation frequency and gas flow were set manually. The microphone calibration data was used to translate the voltage level into an acoustic pressure.

4.2. *Brass cell results*

For model validation I studied mixtures of propane diluted in nitrogen. Three different cells were tested: the "wide-big leak" (WBL) cell, the "wide-small leak" (WSL) cell, and the "narrow-small leak" (NSL) cell. The WBL cell is similar in dimension to the WSL cell, but with much narrower channel dimensions. Comparing the performance of these two cells allows one to see the effect of acoustic leaks on the system. Similarly, the WSL cell and the NSL cell have similar channel dimensions but different cavity diameters. Comparing the performance of these two cells allows one to see the effect of cell volume on the system.

Two different types of tests were conducted. In frequency scans, the gas composition was kept at 100% propane, and the chopper frequency varied. In concentration scans the modulation frequency was kept constant, and the gas composition varied. In order to facilitate comparison between different cells, which had large variations in light power due to differences in fiber cleave quality, I plotted the data as the acoustic signal divided by the power entering the cell from the optical fiber. It was assumed that the laser power and fiber alignment remained fairly constant, so that the power levels measured for the prepackaged fiber (see Table 4-2), could be applied. I periodically confirmed this assumption by checking that the power exiting the window of the cell was consistent with earlier measurements.

4.2.1. *Establishing the baseline: noise, flow dependence, and reproducibility*

The brass photoacoustic detectors had a relatively high noise level, set by ambient noise in the room. However, their performance was highly reproducible, and exhibited no dependence on flow rate in the 5-50 sccm range.

4.2.1.1. *Noise*

Figure 4-10 shows the pressure signal measured in the cell for a variety of conditions where there was no absorbing gas in the cell. There are two remarkable aspects to this data. The first is that the noise levels are the same for all three conditions: the blocked laser/no flow case, the blocked laser/full flow case, and the unblocked laser/nitrogen case. This proves that the noise was not generated from gas flow or from background absorption in the cell, but by a noise source common to all three cases. The other remarkable aspect of the noise is its frequency dependence. The trend in the data matched my qualitative observation of the vibration noise of the chopper, which was audible, and increased in pitch and volume with the frequency.

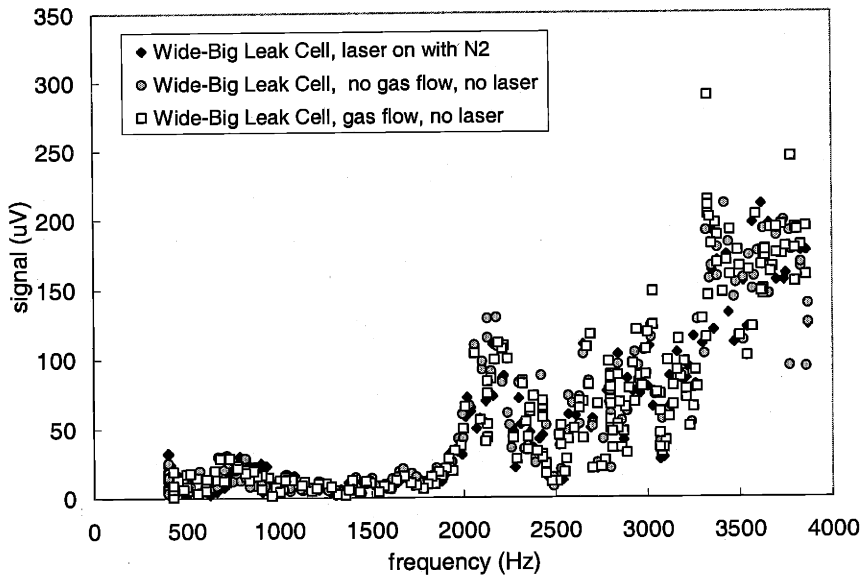

Figure 4-10: Signal in absence of propane under different conditions

For comparison, the noise level of 200 μV corresponded to about 0.02 Pa. In the dilute gas mixture tests described below in Section 4.5, I reduced the background to less than 0.001 Pa for the NSL cell at 2000 Hz by placing a piece of acoustic foam between the chopper and brass cell. This was further evidence that the chopper vibration was the dominant noise source for the photoacoustic detector. Noise levels varied between cells, as can be seen from Figure 4-11.

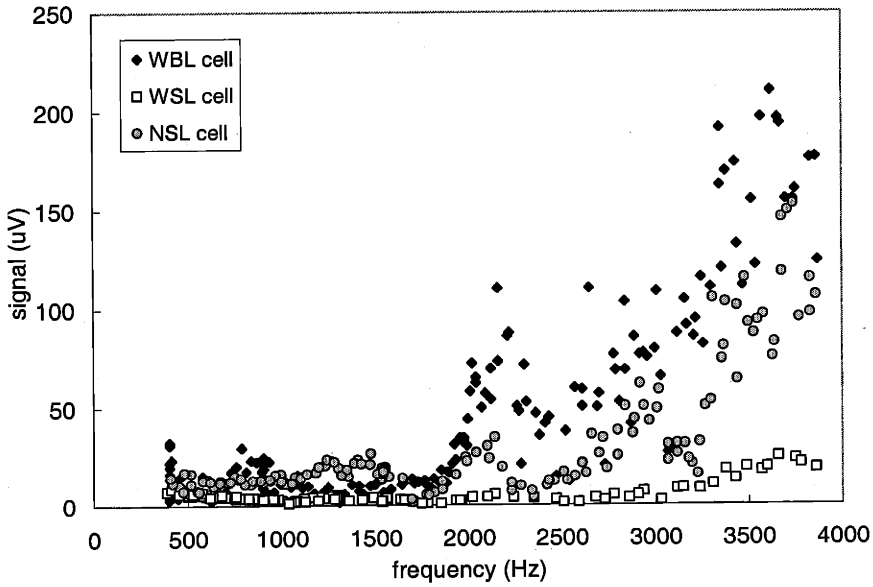

Figure 4-11: Noise levels for different cells

The variation between cells could be due not only to the differing dimensions, but also small differences in the orientation of the cell to the chopper. However, it is not surprising that

the cell with the largest leak, and therefore the greatest level of communication with the outside world, had the highest noise levels. The phase of the noise was random, suggesting that the noise could be assumed to simply add to the amplitude of photoacoustic signal, as was observed in the dilute tests (Figure 4-31).

Since the noise is dominated by ambient noise rather than background absorption, the noise is independent of power level. For example, in a brass photoacoustic detector in which the power level is 1 mW, a noise level of 0.02 Pa corresponds to a signal level of 20 Pa/W. The signal to noise ratio could be increased in the brass photoacoustic detector by increasing the power level.

4.2.1.2. *Reproducibility*

The brass cell performance was observed to be highly reproducible. Figure 4-12 shows the frequency behavior of the NSL cell with pure propane, measured on different days. Each data point represents a single voltage measurement, divided by the microphone sensitivity and the power level measured for the cell. All of the data in this thesis is presented with error bars of $\pm 2\sigma$. The interested reader should refer to Appendix J for more information on how the standard deviation of the data was determined.

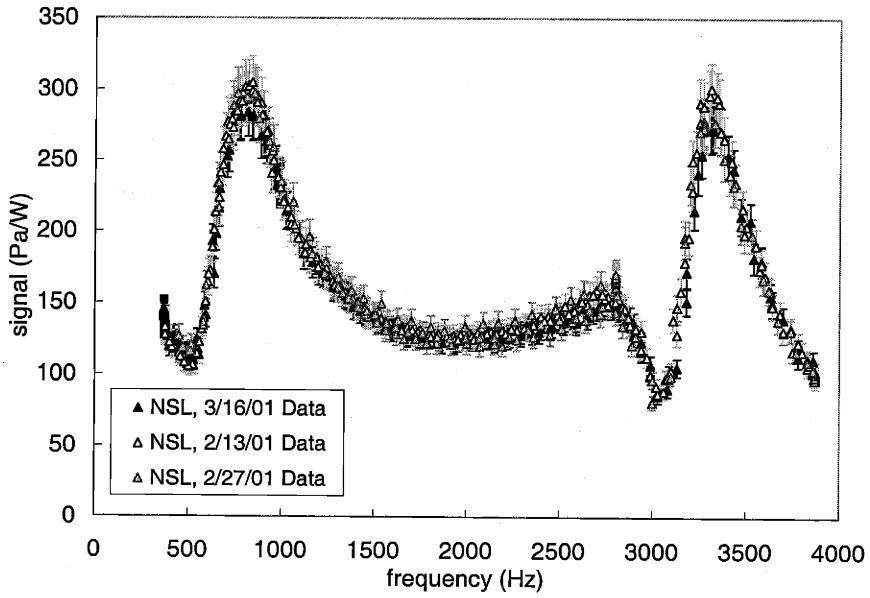

Figure 4-12: Reproducibility of frequency data

Similar levels of reproducibility were observed for the concentration dependence of the signal, as can be shown in Figure 4-13. Each data point in this figure represents the average of

20-50 voltage measurements, taken at the same composition, which is then divided by the microphone sensitivity and power level.

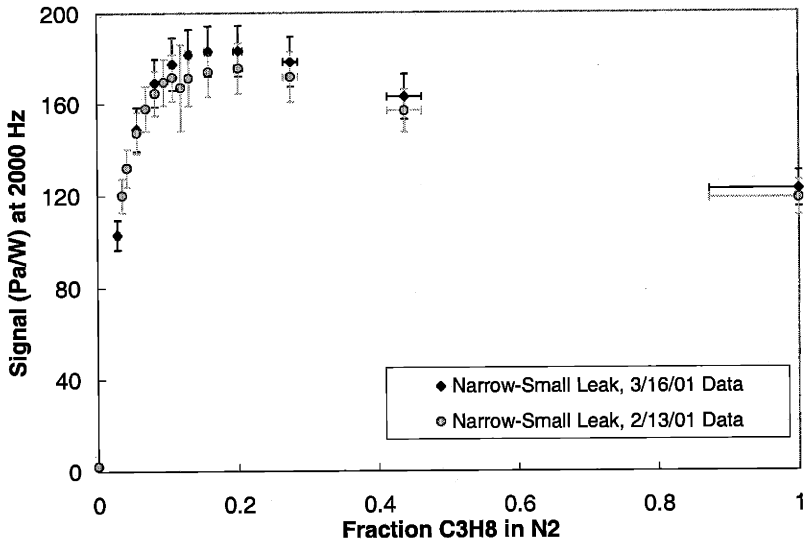

Figure 4-13: Reproducibility of concentration data

4.2.1.3. *Flow dependence*

Figure 4-14 shows a plot of signal versus flow rate for pure propane in a brass cell. Each data point represents the average of 20-40 points. This data was taken with an uncalibrated microphone, before I had the capability to measure power levels, so the signal is plotted as voltage level instead of Pa/W. However, it shows that there is little flow dependence to the signal, which is to be expected. The residence time in the smallest cavity at the maximum flow rate of 50 mL/min was 85 ms, which was much greater than the largest excitation period (10 ms for 100 Hz). Furthermore, low modulation frequencies were only used in frequency scans of the cavity with flow rates of 5 mL/min. The higher flow rates were only used with concentration scans (where the higher diluent flow rates were necessary to achieve small propane fractions), which were conducted at frequencies greater than 300 Hz.

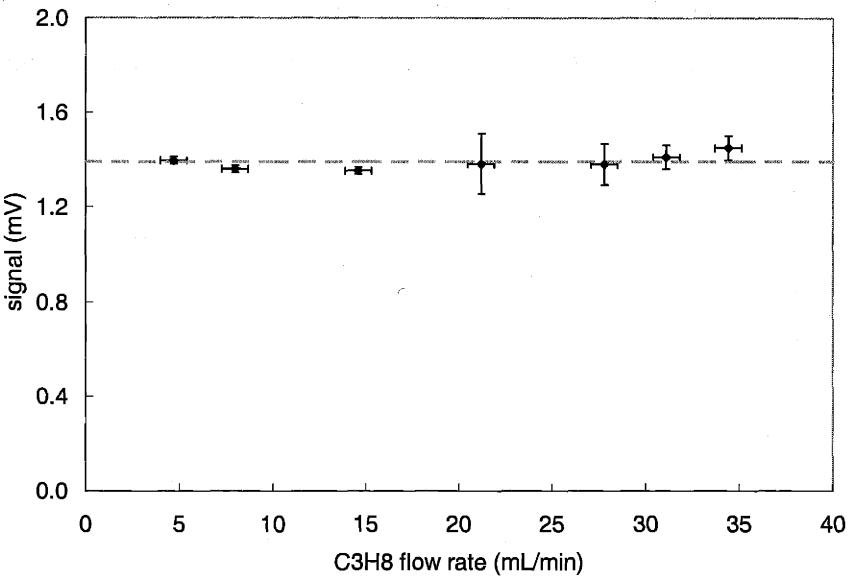

Figure 4-14: Flow rate dependence of the pure propane signal at 311 Hz in the NSL brass cell.

4.2.2. *Frequency response*

Having established the ambient noise levels and reproducibility of the brass photoacoustic detectors, we can then compare their behavior to that predicted by the transmission line model described in Chapter 3.

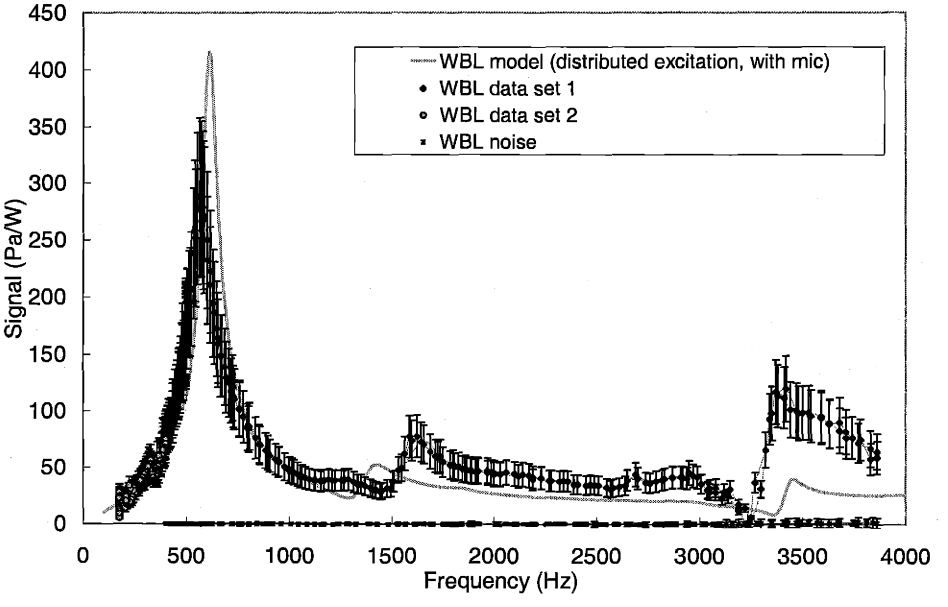

Figure 4-15: WBL data compared to model

Figure 4-15, Figure 4-16 and Figure 4-17 show the frequency response for the WBL, WSL and WNL cells. Each plot contains two sets of data, one taken with the low-frequency

(100 – 400 Hz) chopper blade, and one taken with the high frequency (400 – 4000 Hz) blade. The plots also include the transmission line model predictions, and measured ambient noise levels.

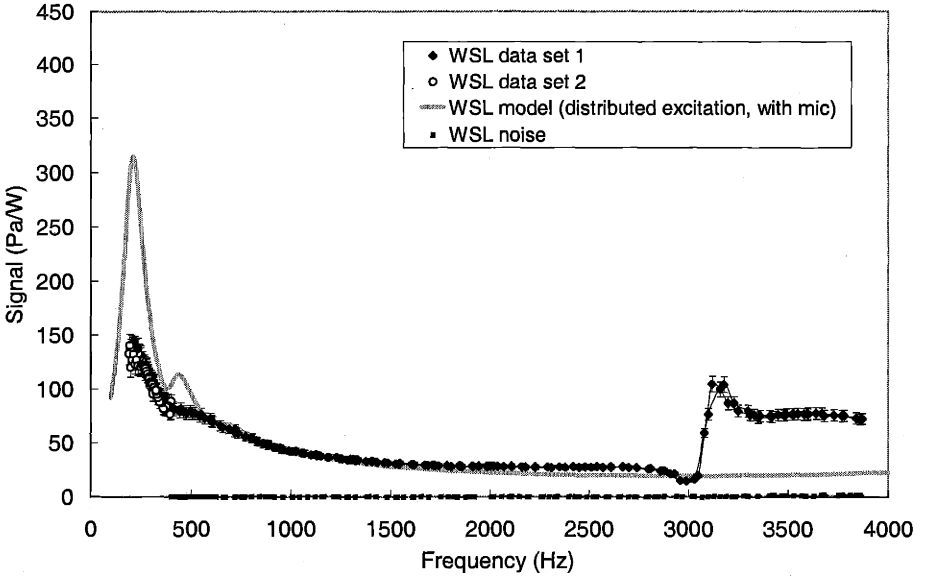

Figure 4-16: WSL data compared to model

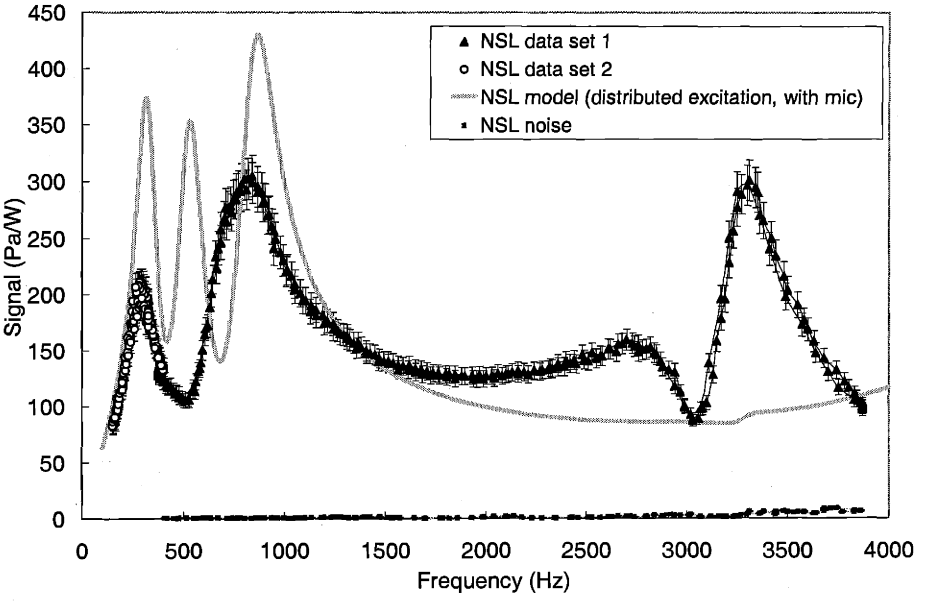

Figure 4-17: NSL data compared to model

Like the data described in the Section 4.2.1.2, each data point represents a single voltage reading which is divided by the microphone sensitivity and the power level. The measured

ambient noise level has not been subtracted from these sets of data; it is a small fraction of the signal, as can be seen from the figures.

4.2.3. *Concentration dependence*

Figure 4-18 shows the concentration dependence measured for the brass photoacoustic detector at 326 Hz. Each data point represents the average of 20-50 voltage measurements, divided by the microphone sensitivity the power level.

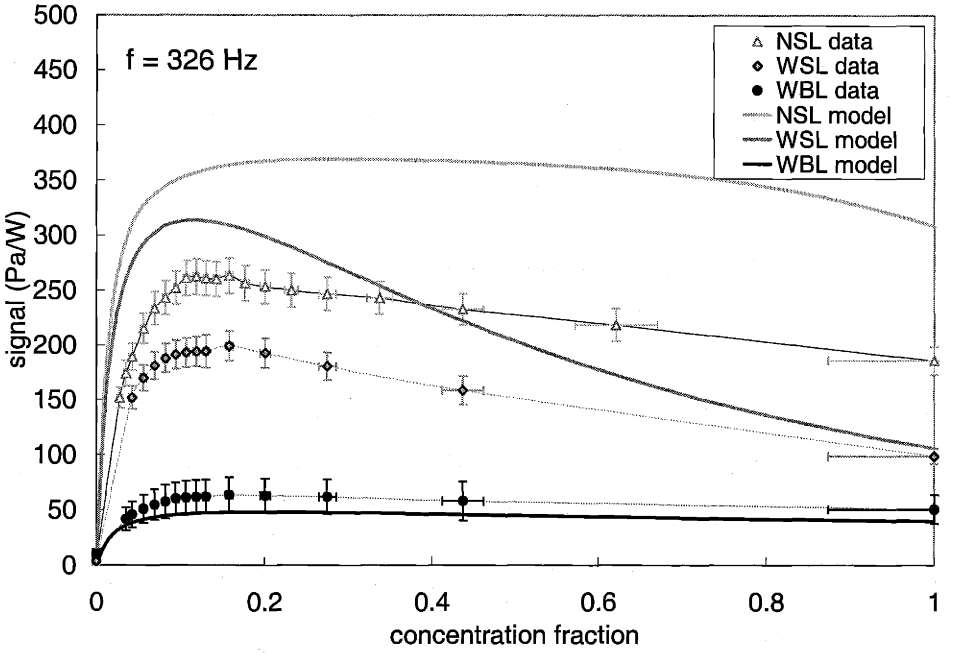

Figure 4-18: Concentration dependence at 326 Hz

Figure 4-19 shows the concentration dependence measured at 2000 Hz. Comparing Figure 4-19 to Figure 4-15 and Figure 4-17, one can see that the disparity in this concentration plot is consistent with the disparity observed in the frequency dependence. One can also see from the frequency plots above that the contribution of ambient noise is negligible at these excitation frequencies.

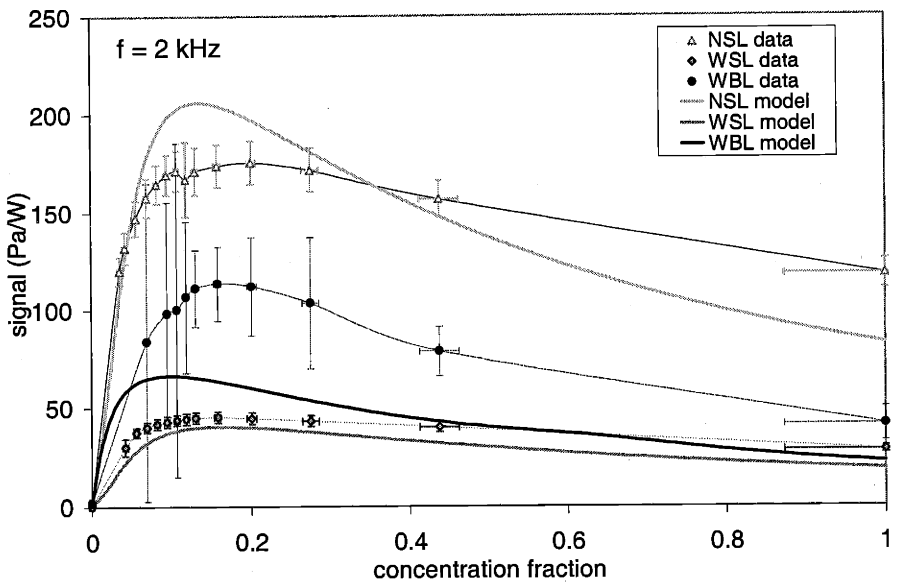

Figure 4-19: Concentration dependence at 2 kHz

4.3. *Resolving the disparity between model and data*

The goal of the brass cell experiments was to build confidence in the model developed in Chapter 3, in order to better understand the design parameters for the miniaturization of photoacoustic detection. While the model is not a perfect fit to the data, it does capture the general shape and magnitude of the response without relying on scalable parameters. This section examines the sources of disparity between the model and observed response.

The model is based on several approximations which may be responsible for the disparity between it and the data. In the frequency response, the model consistently overestimates the sharpness of the low-order, leak resonance peaks, while underestimating the effect of the first cavity resonance. Both phenomena are symptomatic of the underestimation of losses in the system. Furthermore, the model assumes that the pressure is sampled from an infinitely thin plane at the midpoint of the cavity, adding to the error observed at high frequencies. The addition of these factors to the model would improve the fit not only to the frequency data but also to the concentration data. A further source of error for the concentration data is the error in the estimation of α and δ, which are discussed in Sections 3.3.1 and 4.1.2.

4.3.1. *Improving the model fit at low frequencies*

Figure 4-20 shows how the addition of loss mechanisms to the channels and gas manifold dampened the low-frequency peaks, but left the high-frequency response unaffected. In this

test, the response of the regular NSL photoacoustic detector was compared to that of the same detector with pieces of sponge added between Swagelock unions and the flow channel.

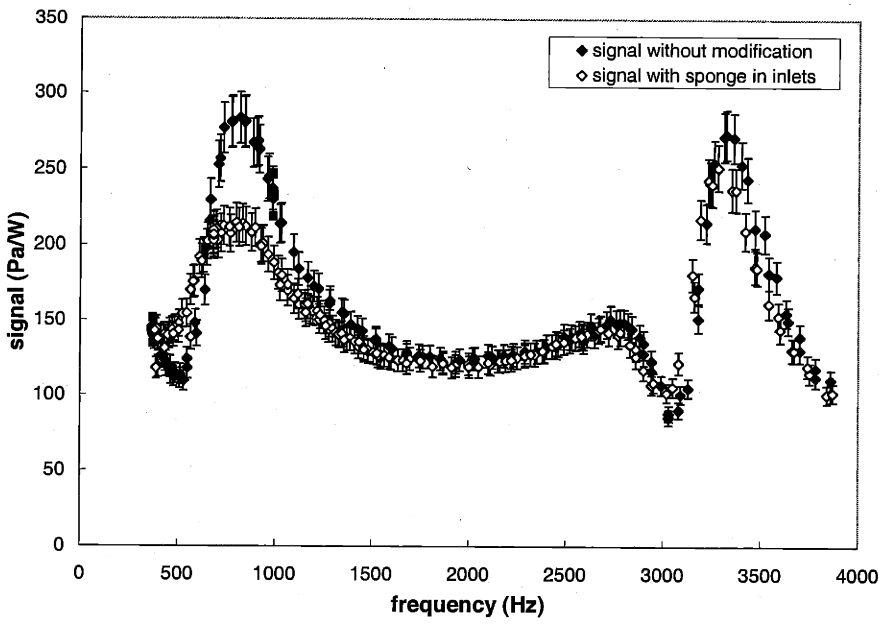

Figure 4-20: The effect of sponge in the Swagelock channel inlets of the NSL cell

Clearly, any approximation about the loss sources in the channels and flow manifold will affect the fit of the model at low frequencies. The model assumes that all of the channel and tubing walls are rigid and also ignores the additional coupling losses that are incurred in going from a large-diameter tube into a small-diameter tube, as well as ignoring the losses that occur as a result of the right angle between the channels and the cavity.

To approximate the effect of these additional losses on the model I adjusted the model by increasing (by a factor of 1.5) the incremental resistance and capacitance by in the transmission line models for the leak and added an additional impedance, $\mathcal{Z}_{add} = \mathcal{R}_{add} + \mathcal{L}_{add}$, in series with $\mathcal{Z}_{in}$ and $\mathcal{Z}_{out}$. $\mathcal{R}_{add}$ and $\mathcal{L}_{add}$ account for the additional impedance of a small opening in a large duct and are given by [99]:

$$\mathcal{R}_{add} = \frac{\sqrt{2\rho_0 \omega \eta}}{8S_{ch}} \qquad (4\text{-}1)$$

$$\mathcal{L}_{add} = \frac{\rho_0}{4R_{ch}} \qquad (4\text{-}2)$$

where ρ_0 is the density, ω the radial frequency, η the viscosity, S_{ch} the cross-sectional area of the flow channel and R_{ch} the channel radius.

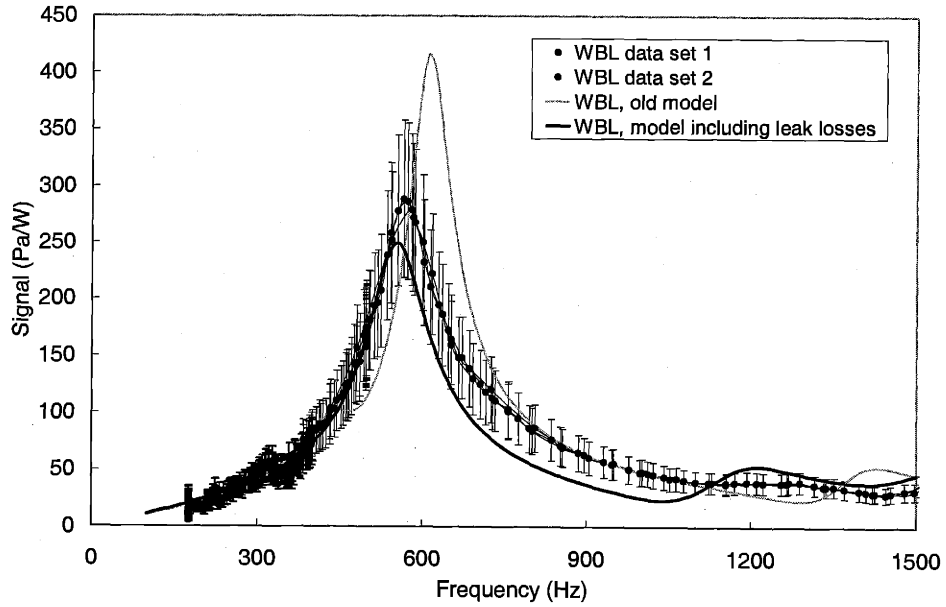

Figure 4-21: The effect of additional losses to the fit of the WBL model at low frequencies

Figure 4-21, Figure 4-22, and Figure 4-23 show how this modification of the model improves the fit at low frequencies.

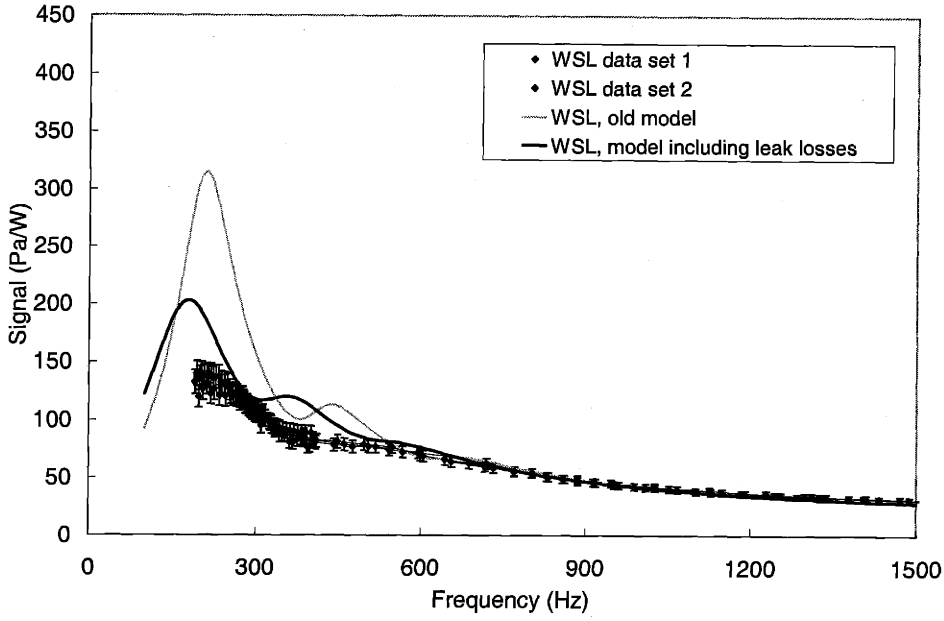

Figure 4-22: The effect of additional losses to the fit of the WSL model at low frequencies

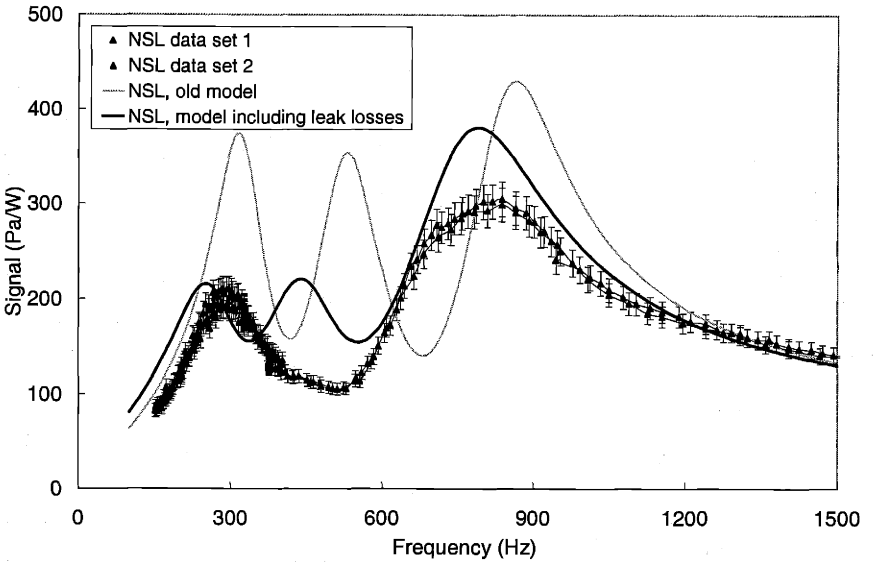

Figure 4-23: The effect of additional losses to the fit of the NSL model at low frequencies

4.3.2. *Improving the model fit at high frequencies*

The leak has little effect at high frequencies, and therefore the modifications described above to the leak model do not improve the high-frequency fit. On the other hand, adjusting the position of the microphone to accommodate machining tolerances changes the high-frequency behavior of the model while leaving the low-frequency behavior unchanged.

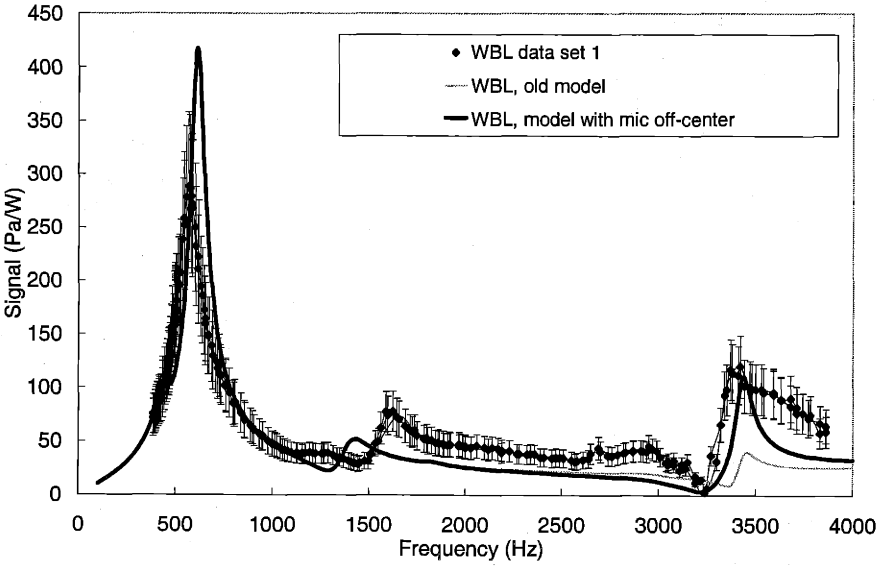

Figure 4-24: The effect of shifting the microphone position on the fit of the WBL model

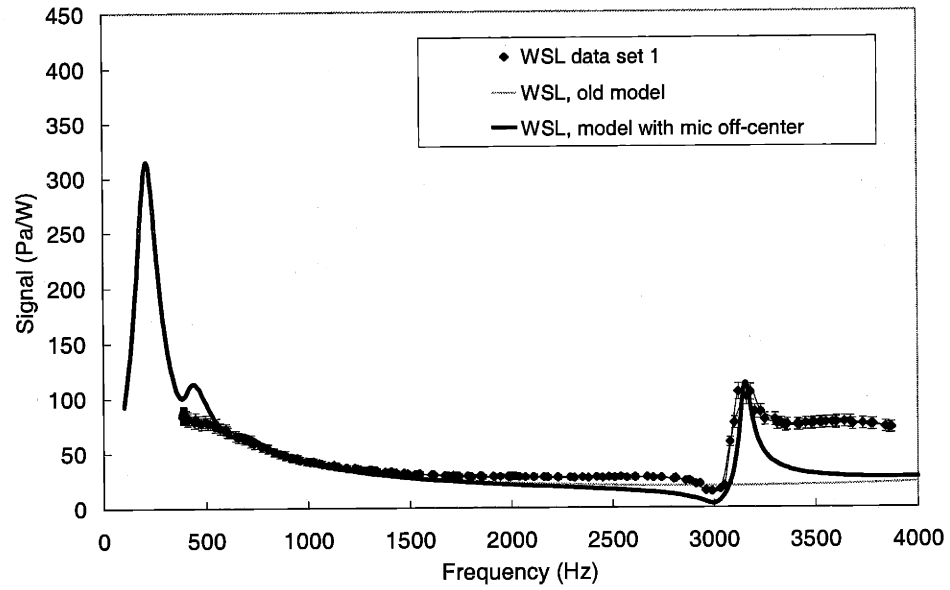

Figure 4-25: The effect of shifting the microphone position on the fit of the WSL model

Figure 4-24, Figure 4-25, and Figure 4-26 show the result of microphone being forward of the cavity midpoint by 1 mm, and also take into account the width of the microphone port.

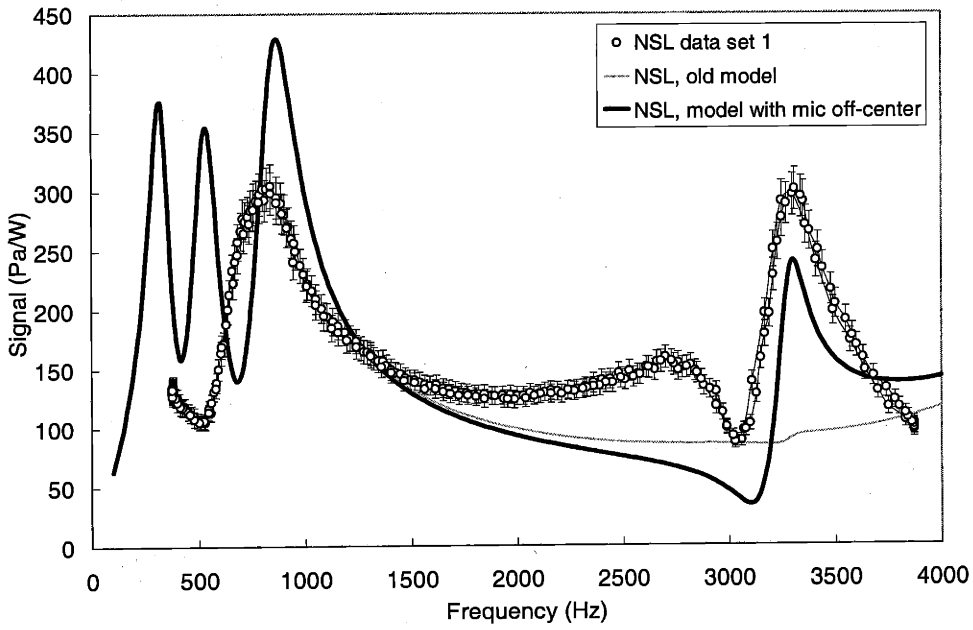

Figure 4-26: The effect of shifting the microphone position on the fit of the NSL model

Another factor that affects the high-frequency fit of the model is the approximation of a perfectly cylindrical cavity. The details of the optical port and window termination become more significant as the acoustic wavelength shortens.

4.3.3. *Improving the model fit to the concentration dependence*

In addition to the adjustments discussed above, the concentration model is also affected by the value used for the absorbance and for the sidewall absorption coefficient δ. As was discussed in Section 3.3.1, the reported values for α at the 3.392 He-Ne laser line range from 737 to 1013 m^{-1}. Table 4-2 summarizes the standard deviation in the measurement of δ. Figure 4-27 and Figure 4-28 show that for data over the full concentration range, where saturation occurs at low concentrations, α and δ have little effect on the shape of the concentration response.

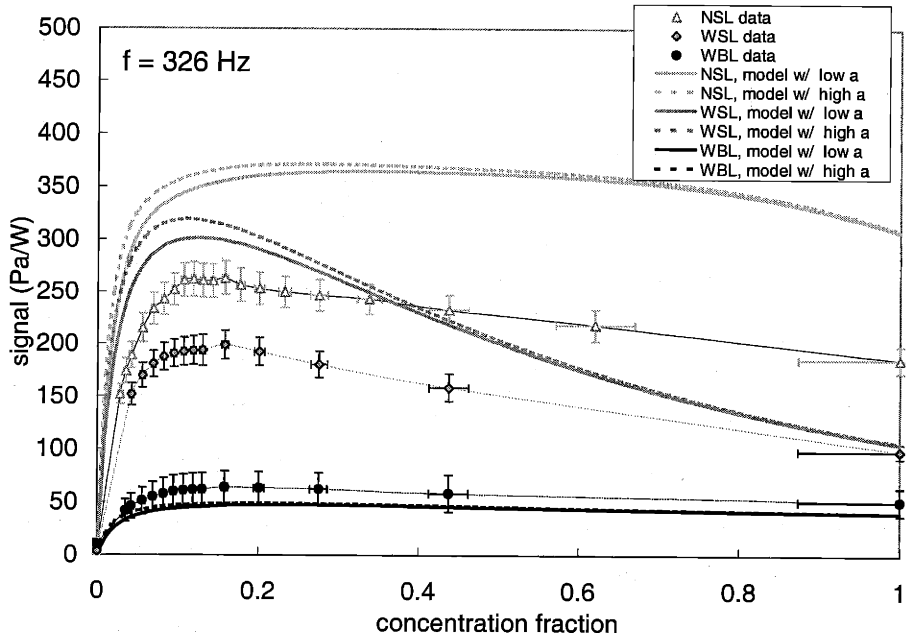

Figure 4-27: The absorbance value has a small effect on the full range concentration dependence

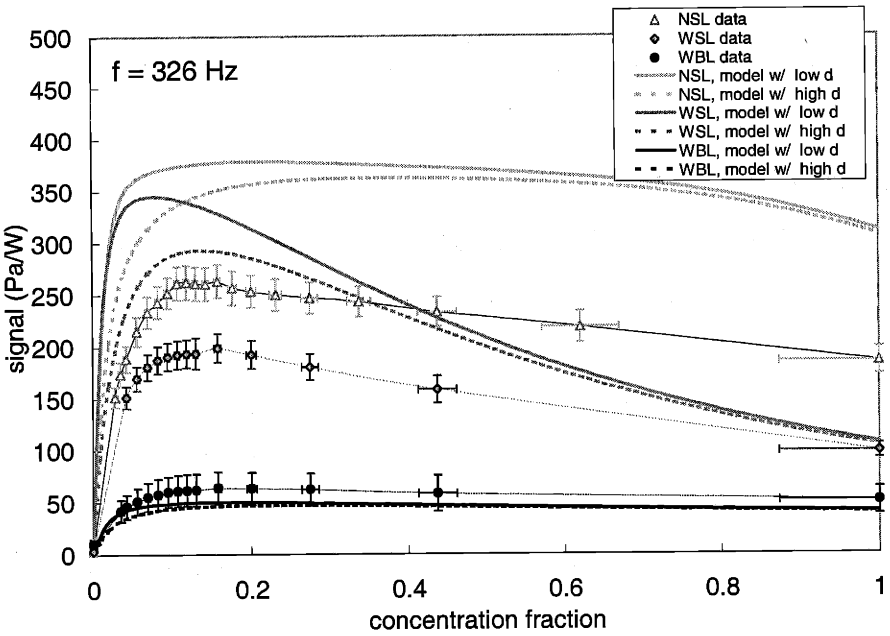

Figure 4-28: The effect of changing δ (here varied by ±2σ) is also small

4.3.4. *Summary of model parameter effects*

To summarize, the low frequency fit of the model is improved by including additional losses in the channels and flow manifold, while the high frequency fit of the model is improved by allowing for machining tolerances in the position of the microphone tap. The high frequency fit could be further improved by considering losses at the window and fiber ends of the cavity. The model has some variability in the choice of material properties, particularly the absorptivity and sidewall absorption coefficient. However, changing these values only alters the signal value at low concentrations.

4.4. *Implications for scaling*

The model, combined with the brass cell data, provides insight into the true scaling behavior of photoacoustic systems. This section discusses how these particular brass cells illustrate the leak effect and the dependence on dimension.

Figure 4-29 compares the frequency response of the WSL cell to the WBL cell. These cells are similar in cavity radius (the WSL cavity radius is 1.6 mm, while the WBL cavity radius is 1.5 mm), but have dramatically different channel radii (the WSL channel radius is 0.17 mm while the WBL channel radius is 0.55 mm). On the same plot I've included the response predicted by the model in the absence of the leak. In the WSL cell, the leak causes the data to

deviate from the expected response only at frequencies less than 300 Hz. In the WBL cell, however, the leak has a significant effect on cell performance until about 2000 Hz. At high frequencies, the WBL signal is slightly greater than the WSL signal, reflecting the slightly smaller cavity of the WBL cell.

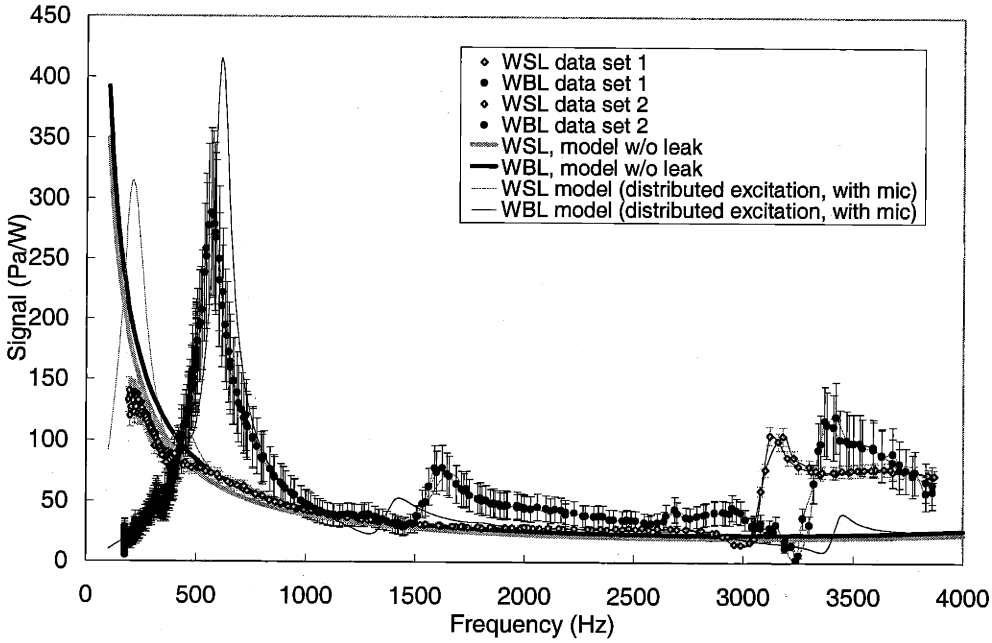

Figure 4-29: Comparing the frequency dependence of the WSL and WBL cells

Figure 4-30 compares the WSL cell to the NSL cell. These cells are similar in channel radius (the WSL channel radius is 0.17 mm, while the NSL channel radius is 0.20 mm), but have dramatically different cavity radii (the WSL cavity radius is 1.6 mm while the NSL cavity radius is 0.75 mm). As before, I've included the response predicted by the model in the absence of the leak on the same graph. Even though the two cells have similar channel dimensions, the effect of the leak on the NSL cell is much greater because the cavity volume is more than four times smaller than that of the WSL cell. Also, the response of the NSL cell is much greater than that of the WSL cell, particularly at high frequencies, which reflects the scaling advantage of the reduced volume. Figure 4-19, which showed the concentration dependence of all three cells at 2000 Hz, illustrates how the scaling advantages of miniaturization are recovered *if* the leak is negligible. This sets an additional constraint on the design of the photoacoustic cell—it either should be designed to operate at high frequencies, or the channels must be scaled with the photoacoustic cavity.

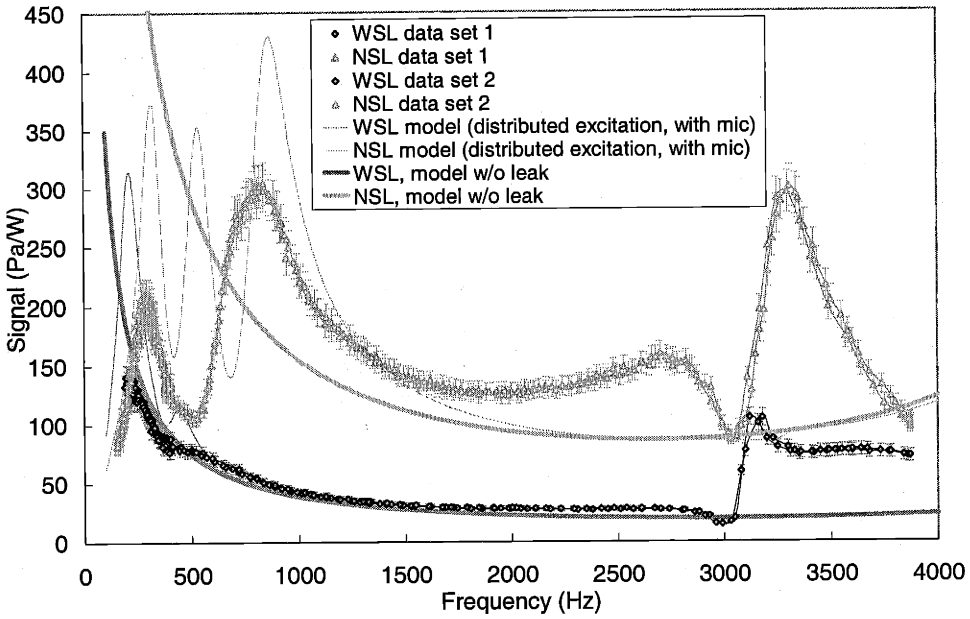

Figure 4-30: Comparing the frequency dependence of the WSL and NSL cells

We can obtain some intuition into the design rules for the cell dimensions by reconsidering the lumped element model for the leak described in Section 3.2.4. In this model, the time constant for an acoustic leak can be estimated from:

$$\tau_{leak} = \mathcal{R}_{inlet}\mathcal{C}_{cav} = \left(\frac{8\eta L_{ch}}{\pi R_{ch}^4}\right)\left(\frac{\pi L_{cav} R_{cav}^2}{\rho_0 c^2}\right) \qquad (4\text{-}3)$$

where η is the viscosity, L_{ch} the channel length, R_{ch} the channel radius, L_{cav} the cavity length, R_{cav} the cavity radius, ρ_0 the density, and c the speed of sound. The leak should have little effect as long as the modulation frequency is greater than critical frequency, given by $1/(2\pi\tau_{leak})$. Applying (4-3) to the brass cells with pure propane, one calculates a τ_{leak} of 72 μs (corresponding to a critical frequency 2.2 kHz) for the NSL cell, 630 μs (250 Hz) for the WSL cell, and 5 ms (31.5 kHz) for the WBL cell. These predictions are consistent with the observations of the brass cell experiments, particularly for the NSL and WSL cells. (The channel radius in the WBL cell is so large that it doesn't truly qualify for the small hole model, as is described by Beranek [151])

The lumped-element model assumes that the channel length is much less than the acoustic wavelength, and that no further tubing is connected to the channel. In cases where the leak is large, as in the brass photoacoustic detectors, however, the flow channel allows the pressure wave to penetrate into the flow manifold. This can be avoided by making the flow

channel very long in addition to very narrow. The "penetration depth" of the acoustic signal away from the cavity is characterized by $|1/\beta_{in}|$, where β_{in} is the propagation constant in the transmission line model of the channel. In order to avoid penetration into the fluid manifold, the length of the channel should be greater than the penetration depth. One can obtain the design rule for this requirement by substituting for the transmission line parameters described in Table 3-2:

$$L_{ch} > \frac{c}{\omega}\left(\frac{1}{1+\frac{1}{R_{ch}^2}\left(d_V+(\gamma-1)d_H\right)^2}\right)^{1/4} \underset{R_{inlet}\to 0}{\Rightarrow} \frac{\lambda_A}{2\pi}\left(\frac{R_{ch}}{d_V+(\gamma-1)d_H}\right)^{1/2} \qquad (4\text{-}4)$$

where d_V is the viscous boundary layer, d_H is the thermal boundary layer, and λ_A is the acoustic wavelength. For a 9 mm cavity length, this condition implies that the frequency must be above 2000 Hz for all three cells. An alternative method for reducing the effect of the leak would be to operate the cell in a resonant mode with the flow channels located at nodes of the cavity. The H-cell design described in Section 2.3.2, for example, could be readily implemented with microfabrication techniques.

In the absence of leak effects, one recovers the inverse area scaling behavior described in 3.1.2. In the case of non-resonant excitation, where the pressure can be assumed to be spatially uniform in the photoacoustic cavity, and without leak effects, the transmission line equations reduce to the simple solution:

$$p = \frac{U_0}{j\omega\mathcal{C}_i + \mathcal{G}_i} = \frac{(\gamma-1)W_0\left(1-e^{-\alpha' L}\right)}{j\omega V\left(1+\frac{D(\gamma-1)}{2jS}\sqrt{\frac{2\kappa}{\rho_0 C_P \omega}}\right)} \qquad (4\text{-}5)$$

Only heat conduction plays a role in the non-resonant response, because there is little flow to contribute to viscous losses.

Another undesirable characteristic of the brass cell chemical analysis system is the saturation of the photoacoustic signal at relatively low concentration levels. This effect is exaggerated by the long cavity, and by the choice of wavelength and analyte. (The 3.4 μm propane absorption peak is particularly strong) However, PA detection could be a powerful technique for analysis at low concentrations or at weak absorption peaks. For example, the absorption levels for overtone spectra in the near infrared are typically a factor of a thousand less than mid-infrared absorption levels. PA detection has also been shown to be sensitive to

extremely low gas concentrations. The following section describes a test of the sensitivity limits of the NSL photoacoustic detector.

4.5. *Dilute mixtures*

Low propane concentrations were achieved with a pre-mixed cylinder of 100 ppm propane in nitrogen, further diluted by flow-controlled mixing with nitrogen. The data was taken at a relatively high (2 kHz) frequency to reduce leak effects. Also a piece of acoustic foam was placed between the chopper and the cell to reduce ambient noise from the chopper vibration.

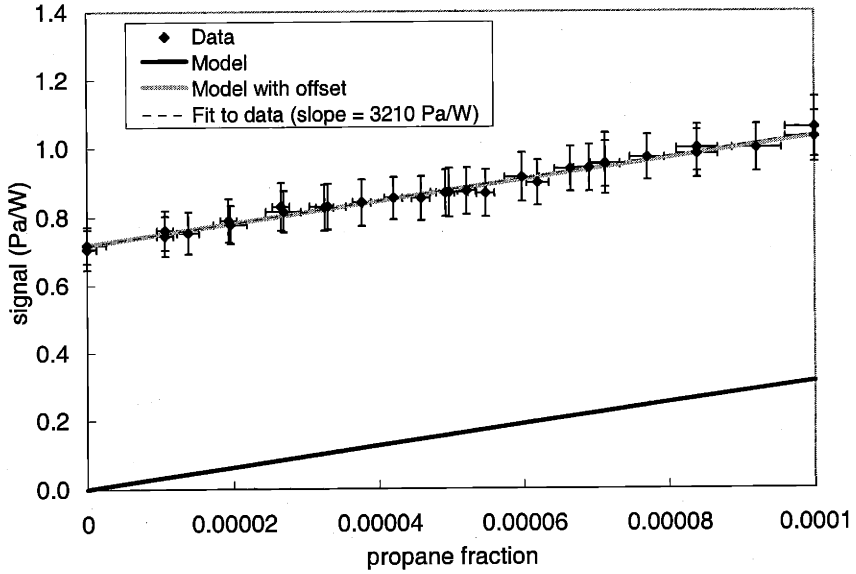

Figure 4-31: Data from the NSL at 2000 Hz for dilutions of propane in nitrogen

Figure 4-31 shows the concentration dependence of the response. The model prediction is plotted against the data. The data is offset by the ambient noise, which adds to the signal. The data fits a line with a slope of 3210 Pa/W. The transmission line model predicts a slope of 3150 Pa/W. The slope of the data is within 2% of the model, which is well-within the uncertainty of δ and α.

In the absence of leak effects, one could apply the formula described in Section 3.1 that describes the non-resonant photoacoustic signal for low-level gas detection:

$$slope = \left| \frac{j\alpha_0(\gamma - 1)L}{\omega(1 + j/\omega\tau_T)V_C} \right| \qquad (4\text{-}6)$$

Assuming $\alpha_0 = 921\ m^{-1}$, $R = 0.75$ mm, $\gamma = 1.124$, and $\omega = 2\pi(2000Hz)$, (3-16) yields a slope of 5143 Pa/W.

From Figure 4-31, one can see that the minimum detectable power level for the NSL photoacoustic detector at 2000 Hz was about 10 ppm. This is much higher than the 10 ppb sensitivity for methane at 3.39 μm reported by Kreuzer [5]. (The absorptivity of methane at 3.39 μm is near that of propane) However, since our sensitivity was limited not by background absorption but by ambient noise, the sensitivity would be 1 ppm for a 15 mW source such as was used by Kreuzer. A reduction in ambient noise could increase the detector's sensitivity further. The sensitivity of Kreuzer's detector was limited not by ambient noise but by background absorption [5]. Conventional theory for low-level gas detection in the absence of the leak effect predicts that miniaturization should increase the signal to noise ratio of a non-resonant detector at the fundamental thermal fluctuation noise limit (see Section 3.5.1). However, background absorption noise should increase with miniaturization.

4.6. *Integration of photoacoustic detection*

4.6.1. *Microchemical system design*

In order to illustrate how photoacoustic detection could be integrated with other miniaturized systems, I combined photoacoustic detection with a microreactor in a hybrid fashion. Figure 4-32 shows a microchemical system coupled to a PA detector cell, with the optical excitation—an infrared diode—inserted in the optical port. The cell was machined out of brass but with a different optical port than the brass cells described in section 4.1. I'll refer to this cell as the "diode cell," and the detector portion of the system as the "diode detector."

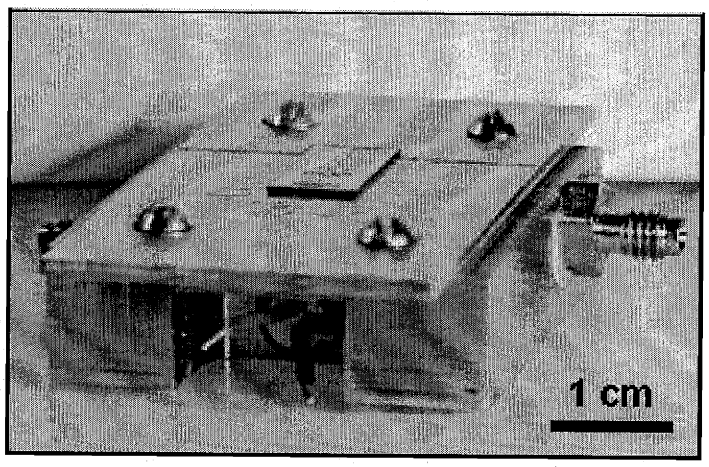

Figure 4-32: Photograph of the diode microchemical system (the gas manifold, microphone, and control electronics are not attached)

Figure 4-33 shows a schematic of the microchemical system. Gas enters through the Swagelock inlet and flows first through the microreactor, and then through the photoacoustic cavity before exiting the cell. In some respects, the diode detector was quite similar to the brass and μPA detectors. The acoustic transducer was a Knowles hearing aid microphone, like what was used with the brass cells, which was inserted into the underside of the cell, opposite the microreactor. However, the microphone in the diode detector was not packaged and calibrated. The lock-in electronics and data acquisition software were similar, as was the gas manifold (although carbon dioxide was used as the inert gas instead of nitrogen). A piece of double-side polished wafer was used for the window, instead of a CaF_2 disc, which had a transmission of about 50%. The elements of this design that varied significantly from the other detector are described below.

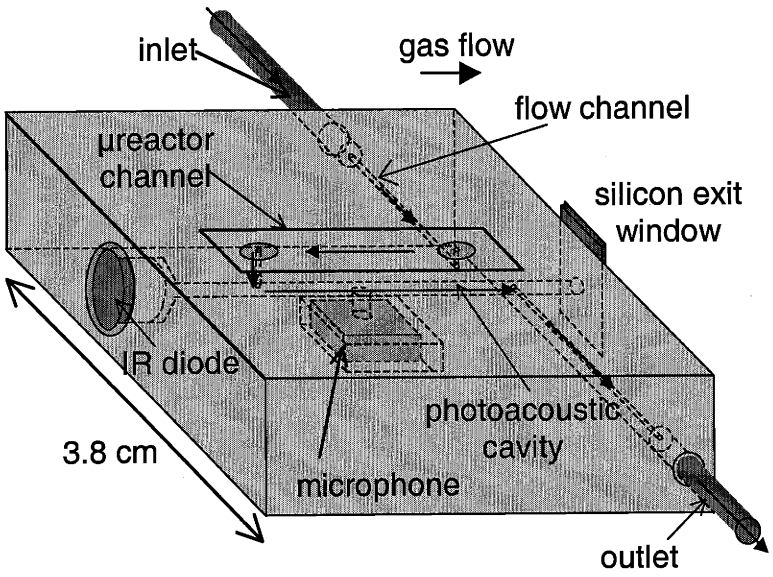

Figure 4-33: Schematic of diode microchemical system

4.6.1.1. *The microreactor*

The microreactor consisted of a channel etched through a silicon wafer, capped on the top by silicon nitride and on the bottom by an aluminum plate. Platinum lines on the membrane could act as heaters and temperature sensors. The microreactor was based on a design by Ravi Srinivasan which is documented elsewhere [1, 37]. The microreactor channel length was 14 mm, and had a cross-sectional area of 0.43 mm^2. The microreactor was normally mounted on a metal chuck, which connected its flow channels to standard gas tubing. The diode photoacoustic

cell was designed to be the same size as this microreactor chuck, so that the combined microchemical system took up no more room than the original reactor.

4.6.1.2. *Diode cell design*

Figure 4-34 shows a schematic of the diode cell, omitting the additional flow inlet for the microreactor. The cavity radius was 0.75 mm, and the length was 14 mm. The flow channel between the microreactor and the cavity was 6 mm long with a radius of 0.4 mm, and the flow channel from the cavity to the outlet was 9 mm long with a radius of 0.4 mm.

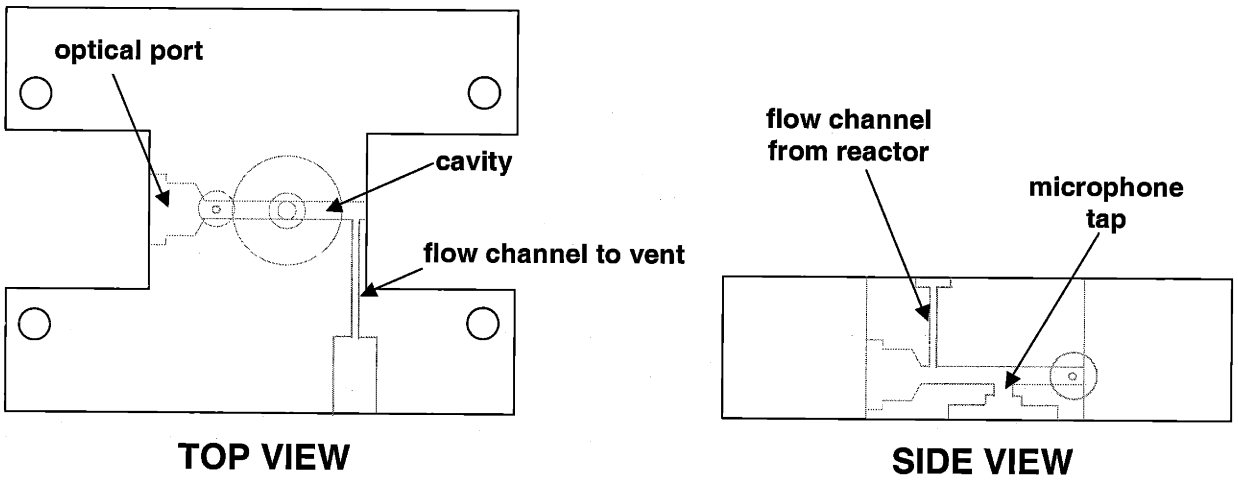

Figure 4-34: Sketch of diode cell (additional microreactor connections omitted for clarity)

4.6.1.3. *Optical excitation*

Instead of a laser, this system used an infrared diode for excitation [171]. According to the manufacturer's specifications, the diode had a center wavelength of 3.4 μm, a bandwidth of 400 nm and a maximum power of 20 μW, although only for pulses of short duration. For a sinusoidal drive, the maximum power was 7 μW. This power level was too small to be measured with my detector. The diode power spectrum was also highly dependent on temperature, which was not tightly controlled in my device.

Instead of mechanical chopping, electrical modulation was used to modulate the light source. The diode required a current drive with an amplitude of 1 A for the 7 μW power output. A simple driver circuit (Figure 4-35) converted a sinusoidal voltage source, created with a commercial frequency generator, into a current source. The current stage of the amplifier required the use of a high-power op-amp [172], and high power resistors. The amplifier stage provided the desired 1 A output with the frequency generator and high power resistors that were

already available in the lab. Later I switched to a more sophisticated frequency generator that could be controlled through GPIB, facilitating data acquisition. The circuit was pretty noisy, with a noise level of about 200 mA superimposed on the signal, but sufficient for demonstration purposes.

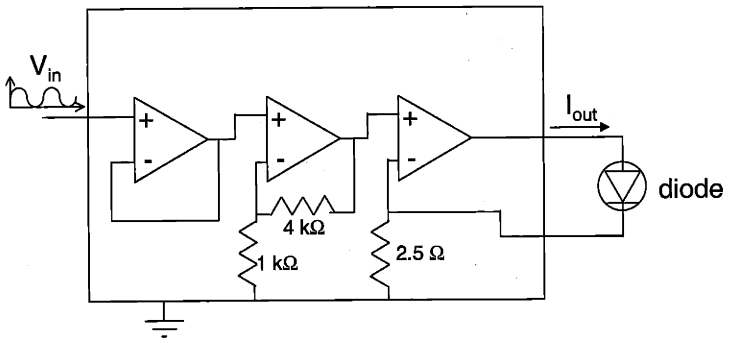

Figure 4-35: Driver circuit for the infrared diode

4.6.2. *Results*

The detector was critically affected by the pressure on the microphone and the placement of the diode into the cell, so that performance varied from run to run. Operation was consistent, however, once the cell was assembled. There was a lot of noise at low frequencies for the detector, completely masking any non-resonant signal. However, I did observe a resonant peak that was near that of the first longitudinal resonance frequency for the ideal sealed cavity, as is shown in Figure 4-36.

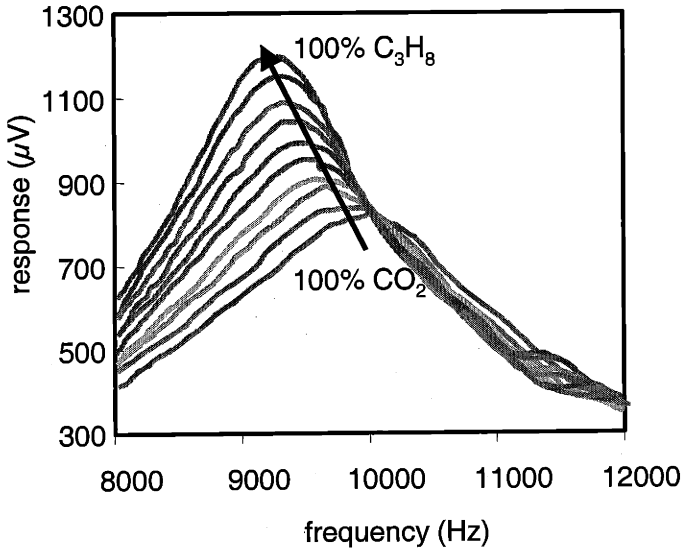

Figure 4-36: Dependence of resonance peak on gas composition

As the gas composition changed, the peak increased and shifted slightly. The shift was due to the slight change in the speed of sound between carbon dioxide (270 m/s) and propane (250 m/s). The first longitudinal resonance for a 14 mm-long sealed cavity should be 8.9 kHz for propane and 9.6 kHz for carbon dioxide. Figure 4-37 shows data over a larger frequency range.

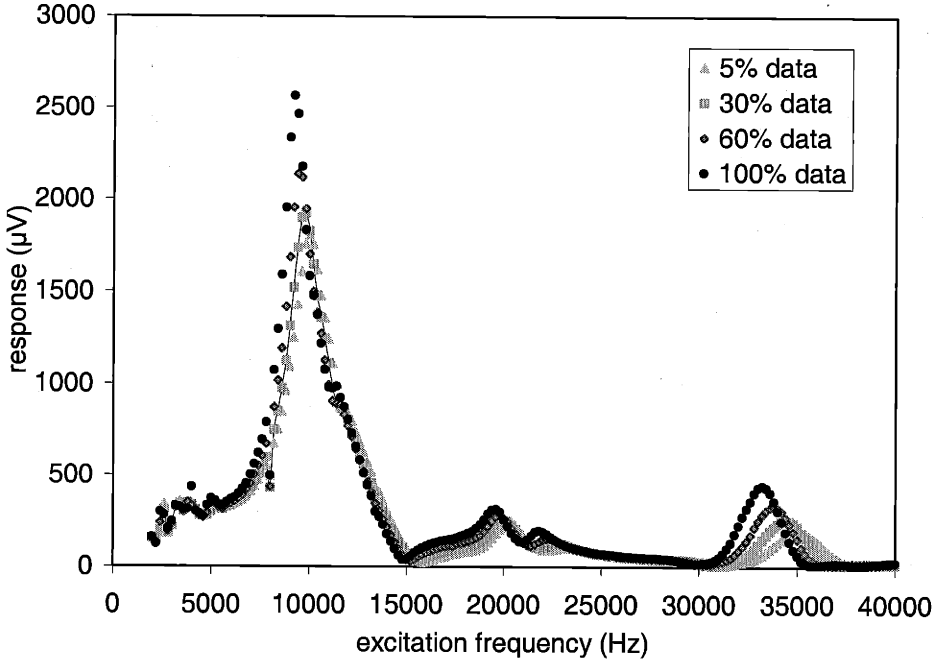

Figure 4-37: Data over a larger frequency range for the microchemical system

From Figure 4-36 and Figure 4-37, one can see both the large run-to-run variability of this detector as well as the large background absorption signal. The background was probably from the overlap of the diode spectra with the 4.2 μm carbon dioxide absorption peak. I did not combine detection with a microreactor in operation.

This microchemical system was used as an early demonstration of the potential of photoacoustic detection for integrated analysis. It was not a well-characterized system, and, because of leak effects, the detector performance depended on the acoustic properties of the microreactor structure as well as the flow manifold. The implications of this dependence are discussed further in 6.2.2. However, this system does illustrate how photoacoustic detection could be combined with the microreactor.

This system also demonstrates how infrared diodes might be used in place of lasers for photoacoustic detection. The advantage of diodes is that they could be used in a truly portable system. High-power laser diodes are available in the near-infrared for chemical analysis with

overtone spectra. Multiple photoacoustic cavities with diodes of different wavelengths could be used to examine multicomponent mixtures.

Whether diodes or lasers are used for the light source, as the size of the photoacoustic detector decreases the limits and dimensional tolerances of conventional fabrication methods grow in significance. The WSL brass cell, for example, used the smallest available drill bit diameter for the flow channels, and still was subject to significant leak effects at low frequencies. Microfabrication facilitate meso-scale photoacoustic detection, while creating the capability for monolithic integration where appropriate. The next chapter describes how a photoacoustic detector can be microfabricated.

5. A microfabricated photoacoustic detector

5.1. *Detector design*

Figure 5-1 shows a photograph of the microfabricated photoacoustic (μPA) detector. The microfabricated cell was mounted on a base plate, which was in turn mounted on a chuck that facilitated fluidic connections. The optical excitation, gas manifold, lock-in electronics and data acquisition for the μPA detector were the same as was used for the brass photoacoustic detector. The cell design and acoustic transduction method, however, were different.

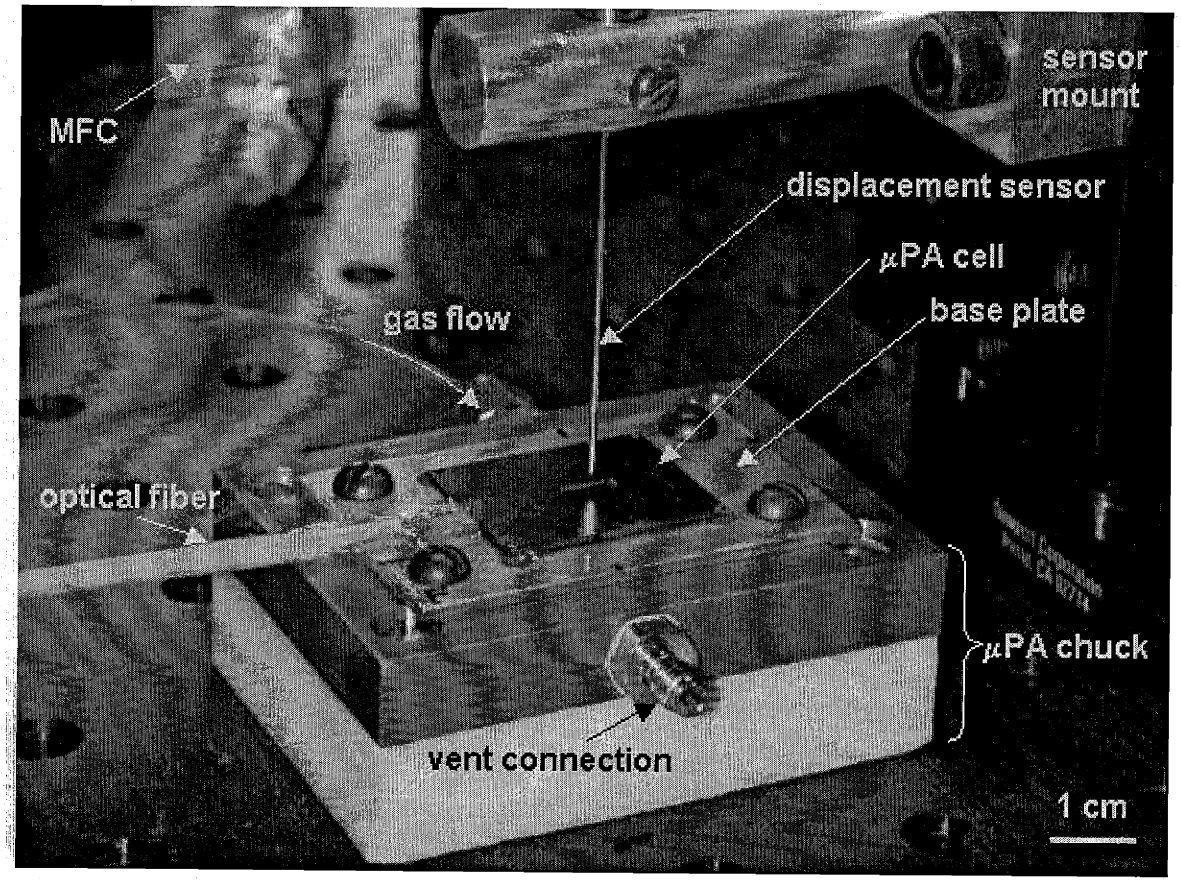

Figure 5-1: Close-up of the μPA detector

5.1.1. *Microfabricated cell structure*

Like the brass cell, the μPA cell had a photoacoustic cavity, flow channels, and an optical port. Part of the upper wall of the photoacoustic cavity was a flexible membrane that deflected with the changing pressure levels in the cavity. The walls of the μPA cavity were also semi-transparent to infrared light, so that light was lost all along the cavity rather than just through an exit window at the end. Figure 5-2 shows a schematic of the μPA cell, which was made by bonding two silicon wafers.

The cavity wafer was polished on both sides, and was about 460 μm in thickness. The photoacoustic cavity of the μPA cell was trapezoidal in cross-section, with the characteristic 54.7° sidewalls formed by potassium hydroxide (KOH) etching through the wafer. It was designed to be 15 mm long with a top width of 700 μm, which would narrow to a 50 μm slit in the bottom of the wafer. This design had the disadvantage of requiring the aluminum base plate to form the bottom wall of the photoacoustic cavity. However, the through-wafer cavity simplified fabrication and allowed for a wider sensing membrane without the addition of a third wafer. It also could facilitate the post-bonding lining of the cavity walls with metal, an option not pursued.

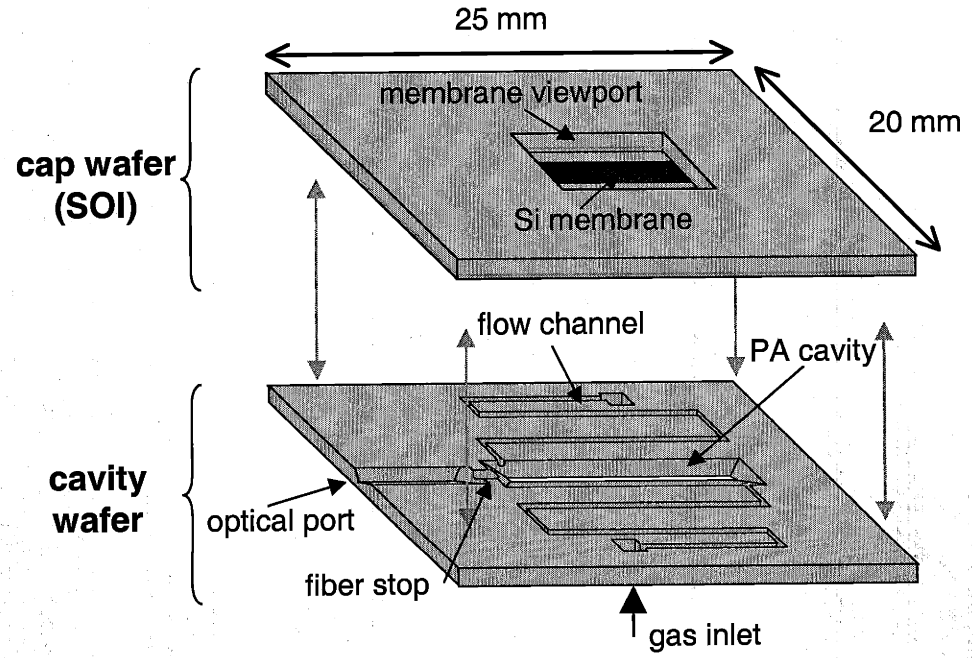

Figure 5-2: Drawing of the μPA cell, with the bonded wafer stack separated for illustration

A second KOH-etched trench, which was exposed with the die saw, formed the optical port. This port was designed to be 5 mm long with a maximum width of 500 μm, which was just large enough to accommodate the stripped optical fiber. A short (250 μm), isotropically etched trench, designed to be slightly narrower than the stripped optical fiber, separated the optical port from the cavity. The purpose of the connecting trench was to permit light to enter the cavity while providing a mechanical stop for the fiber.

The meandering flow channels were much longer than in the brass cell. They were designed to be 32.5 mm in length and semicircular in cross-section with a radius of ~150 μm. Flow inlets for the gas channels were etched into the back of the cavity wafer.

A silicon-on-insulator (SOI) wafer was used for the capping layer. The handle of the capping layer was etched away in a rectangular "viewport" over the photoacoustic cavity to create the sensing membrane. The membrane thickness was that of the device layer of the SOI wafer, specified by the manufacturer to have a thickness of 2.2 μm. The oxide layer of the SOI wafer was specified to be 1.1 μm.

5.1.2. *Cell fabrication*

Figure 5-3 shows an overview of the μPA cell fabrication process. The photoacoustic cavity, optical port, and gas inlets were created first by potassium hydroxide (KOH) etching. Then the gas channels and fiber stop were formed with an isotropic sulfur hexaflouride (SF_6) etch. An SOI wafer was bonded to the cavity wafer, and then etched back in the region of the cavity to create the pressure-sensing membrane. Finally, the wafer was cut into die, with the cut opening the fiber port. Appendix I contains a detailed account of the process flow. Most of the processing techniques used are well established for the field of microelectromechanical systems (MEMS), and are described elsewhere [173-175]. A few details about this process merit further discussion, however.

Instead of the conventional semiconductor industry masks produced from by an outside vendor I used high-resolution transparencies [176], which were converted to glass masks in the lab. The price of these masks was trivial, and they had only a 1-day turnaround from idea to mask. The disadvantage of these masks was their relatively poor (~25 μm) resolution. With the large features of the μPA design, this was not much of a problem. The poor resolution did,

however, result in rougher cavity sidewalls than are normally seen with KOH etches, and with a small increase in the final photoacoustic cavity top width (750 μm instead of 700 μm).

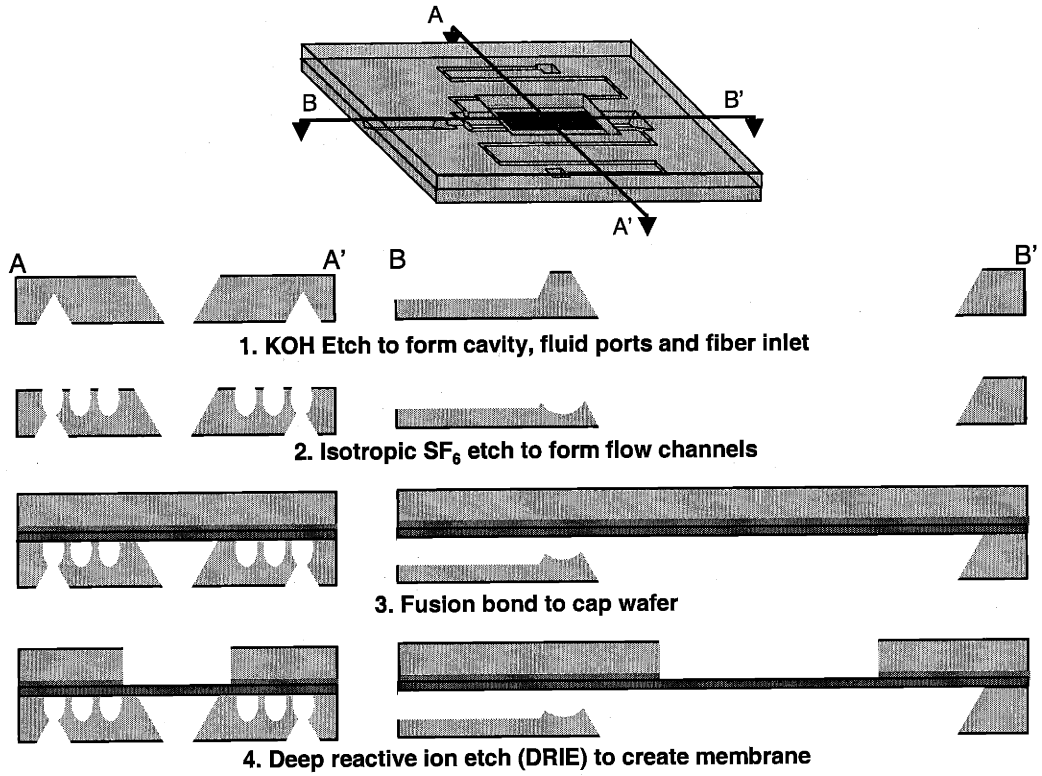

Figure 5-3: Overview of μPA cell process

Another interesting aspect of the process was its use of a nested mask. Photolithography is a highly planar process, and consequently it can be difficult to pattern new layers on a wafer with lots of surface "geography." Instead, MEMS researchers often make use of a nested mask procedure, where the mask for a future step is patterned onto the wafer and then buried until required. Such a technique was used here. Before patterning for the first etch step (the KOH etch of the cavity, inlets, and fiber port), a 1.5 μm layer of silicon dioxide ("oxide") was grown on the wafer and patterned for the later isotropic etch (which defined the flow channels). When creating this mask layer, it was extremely important to protect the oxide on the back of the cavity wafer, even though it was not necessary for the future etch mask. Neglect of this step resulted in extremely fragile wafers, particularly after the KOH etch, because of the stress placed on the wafer by the unbalanced oxide distribution. The oxide mask was then covered with a nitride layer that was used for the KOH mask. After the KOH etch, the nitride was stripped in hot phosphoric acid, leaving the oxide mask intact.

The role of oxide layers was not always positive in the device fabrication process. One goal of the process was to achieve a stress-free sensing membrane. The use of an SOI wafer facilitated this, by providing a single-crystal material for the layer. However, much care was required to avoid leaving oxide layers on the membrane. Figure 5-4 shows the wafer immediately after the DRIE step that releases the membrane. In addition to the buried oxide layer of the SOI wafer, some oxide formed on the underside of the membrane, even when the bond was carried out in nitrogen. While the SOI insulator oxide could be readily removed, the oxide layer on the cavity interior was more tenacious.

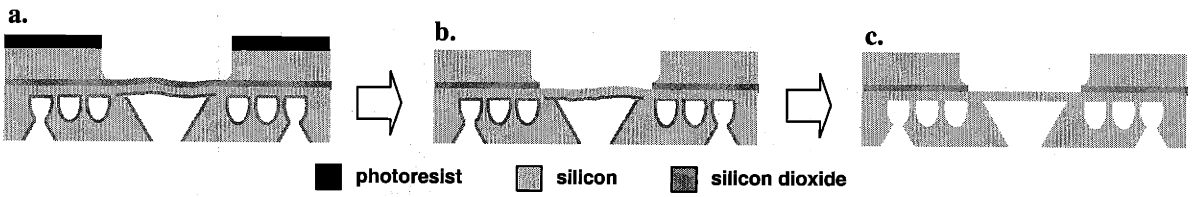

Figure 5-4: Care had to be taken during the release of the membrane to avoid oxide layers. a. The wafer immediately after the DRIE step. b. After a piranha clean and BOE dip, oxide was still present inside the channels and cavity. c. An HF vapor etch removed all of the oxide.

The usual wet etchant, buffered oxide etch (a mixture of hydrofluoric acid, ammonium fluoride and water), was ineffective because surface tension forces prevented it from entering the cavity. Instead, hydrofluoric acid (HF) vapor was used to remove the oxide on the underside of the wafer. The wafer was placed in a standard wafer boat, standing on its end in a beaker with a shallow layer of HF. Since the vapor pressure of HF is relatively high, this was sufficient to eventually remove the oxide from the cavity walls. The transport of the HF to the interior membrane surface was assisted by the slit on the bottom of the cavity.

The vapor etch was inconsistent, however. While the oxide at the center of the cavity disappeared rapidly (in seconds) the oxide at the edges of the cavity sometimes required much longer exposure times for removal. This was partially due to unintentional masking by photoresist contamination that entered the cavity during a piranha (a mixture of sulfuric acid and hydrogen peroxide) clean following the final DRIE etch. (The DRIE step not only used photoresist for the masking layer, but also to temporarily mount the device wafer on a larger silicon handle wafer.) Here the slit at the bottom of the cavity was a disadvantage, because it facilitated the transport of contaminants into the cavity interior.

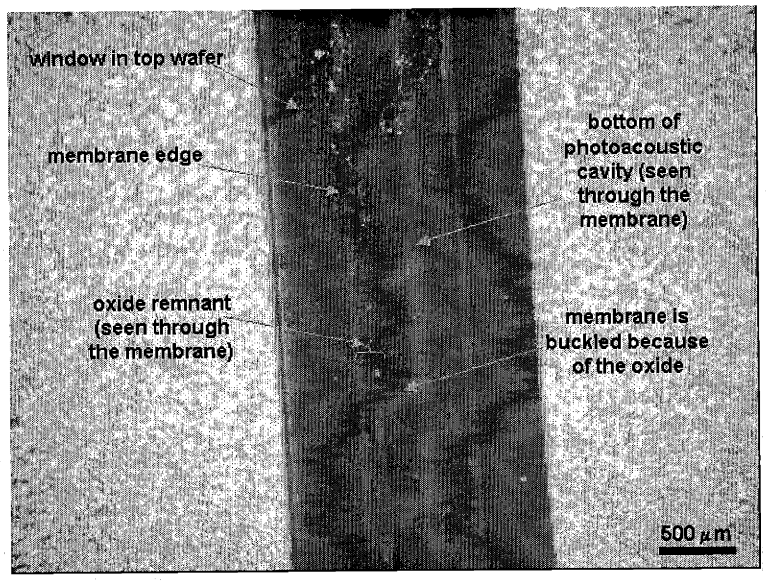

Figure 5-5: Image of a membrane for which the oxide was not completely removed

Figure 5-5 shows a microscope image of a membrane for which the oxide was only been partially removed. The oxide is visible at the cavity edges through the semi-transparent membrane. The slit at the bottom of the cavity is also visible. For the device in the figure, the stress from the remaining oxide layer was sufficient to buckle the membrane. This problem could be solved in future processing by using a handling method for the DRIE system that doesn't require photoresist or a wet release, and by using oxide, patterned before the bonding step, for the etch mask.

The HF vapor etch was continued, sometimes alternating with cleaning steps such as ashes or piranha cleans, until the oxide was no longer visible and the membranes appeared flat. Once the membranes were released, the wafers required delicate handling. This was particularly true on the die saw, where the tops of the wafers were covered with tape to protect the membranes from the water spray. After the dice were fully released, they were cleaned with acetone, methanol and isopropanol, and then baked at 70 °C for an hour. A few samples were coated with 50 nm of aluminum to increase reflectivity to the Philtec sensor. However, the Philtec sensor was found to be effective without the metal coating, which could affect the mechanical properties of the membrane.

The final dimensions of the cell were slightly different than as designed. As was discussed above, the top-width of the cavity (which also defined the membrane width) was 750 μm instead of 700 μm, and the flow channels were semicircular with a radius of about 220 μm instead of 150 μm.

5.1.3. *Mounting the cell*

The aluminum base plate was necessary not only to facilitate the attachment of the cell to the fluidic ports in the chuck, but also to provide the bottom surface of the photoacoustic cavity. Indium or vacuum grease was used to attach the cell to the plate. The indium had the advantage of being inorganic, so that there was no danger of contamination with its use. However, the indium sealant had very little "give." As the base plate was tightened down on the chuck the membrane would sometimes distort and bend, even when a thick base plate was used. The vacuum grease was more pliable, insulating the membrane from the strain of the pressure fitting to the chuck. This strain was further minimized by the use of vacuum grease between the chuck and base plate as well, instead of o-ring seals. The grease was kept away from the cavity region of the base plate. While contamination from the organic grease could have been a problem, background absorption was not observed in the μPA chemical detector.

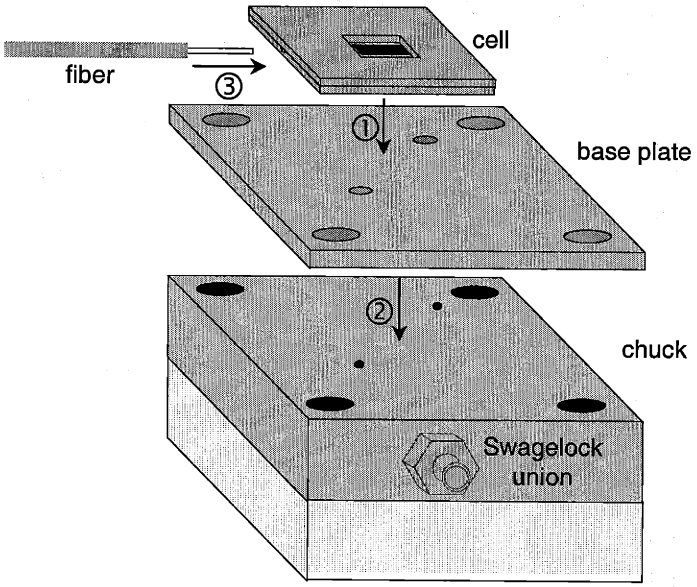

Figure 5-6: Mounting the μPA cell. It's not quite as easy as 1-2-3

After mounting the cell on the base plate, the base plate was mounted onto the chuck. The chuck had two parts: a brass piece that contained fluidic connections, and a Teflon piece that could be screwed down to an optical board. After mounting the plate onto the chuck, I inserted the fiber into the cell, fixing it to the base plate with epoxy, while also applying dots of epoxy to the corners of the cell. It was important to apply the epoxy only after the base plate had been mounted on the chuck, so that the cell could adjust to the strain of the base plate clamp.

As in the case of the brass cell detectors, the transmission of the optical fiber was measured before inserting it into the cell. Unlike the brass cell detectors, however, I was unable

to directly measure the light lost as it passed through the cavity in order to confirm that no further light was lost in the packaging process, and to determine the sidewall loss parameter δ for the specific cell. The measurement was approximated with a sacrificial μPA cell, cleaved to expose the cavity just before the viewport. Comparing the light output of a fiber before and after being inserted into the exposed cavity yielded a value for δ of about 1000 m^{-1}. As there was only one experiment, the standard deviation was estimated from the maximum fractional standard deviation observed for the brass cells (20%, or 200). This δ value seems high; α for propane is ~921 m^{-1}, while the brass cell value was 13 m^{-1}. This measurement method could not distinguish between light lost from sidewall absorption and light lost because of being blocked by the fiber stop.

5.1.4. *Acoustic transduction*

A Philtec [177] fiber optic displacement sensor monitored the motion of the membrane. The sensor head is actually a bundle of fibers, some of which emit light and others monitor the light reflected back to the head. The fraction of light returned, which is proportional to the output voltage, could be correlated to the distance of the fiber head from the surface. Figure 5-7 shows the relationship between the voltage and the separation of the sensor head from the substrate.

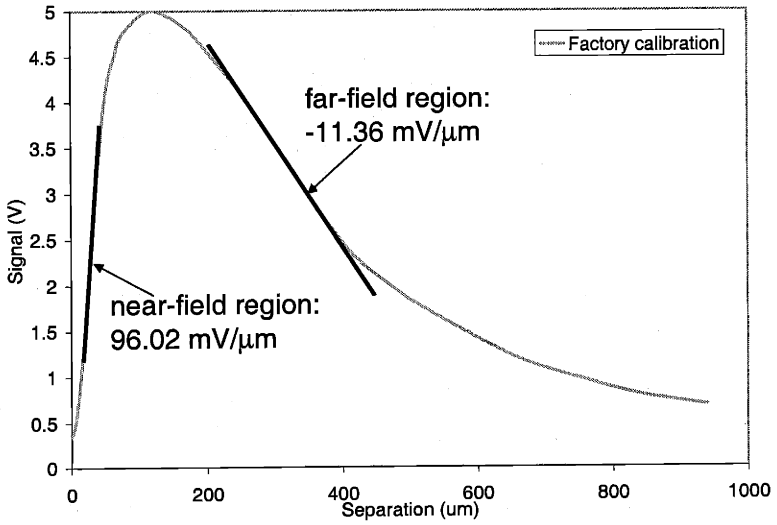

Figure 5-7: Factory calibration for the Philtec displacement sensor

There are two linear regions of operation, one in the near field with a larger sensitivity and range of 15 μm, and one in the far field with a smaller sensitivity but a range of 140 μm. The

μPA devices used the near-field range. The sensor was very sensitive to the angle of the fiber bundle head to the surface, but had an adjustable resistor to account for changing surface reflectivity. The fiber head was mounted on a 3-axis micromanipulator with micrometer actuators for positioning and calibration, the results of which are shown in Figure 5-8.

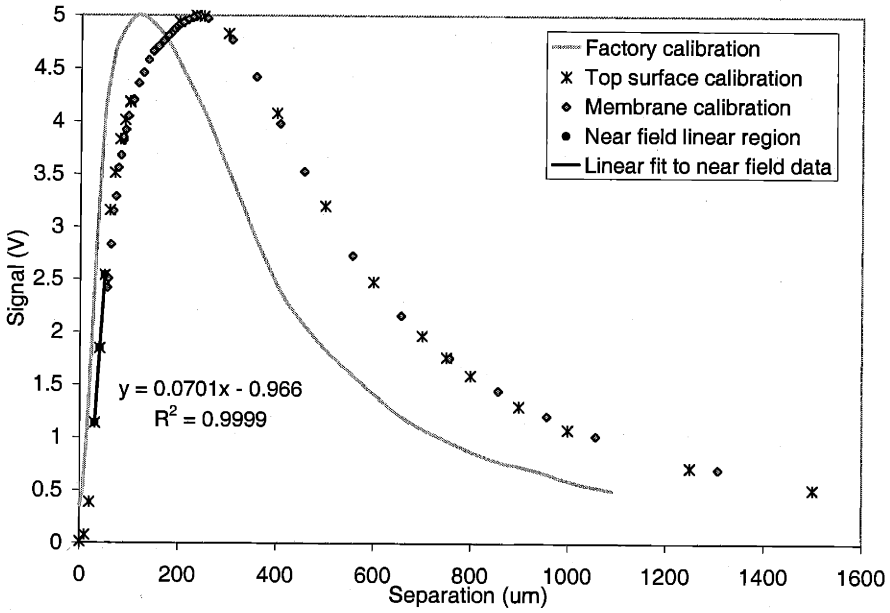

Figure 5-8: Comparing calibrations for the Philtec sensor

The sensor was calibrated in its sensing position against a Newport* Vernier micrometer. This insured that the angular position of the fiber head was the same for both the calibration and the experiment. One calibration was done against the top surface, where the sensor could be pressed completely down to the surface. I also did a calibration against the membrane, but avoided touching down on the surface, lest the sensor head break the membrane. The membrane calibration matched that of the top surface, and a fit to the near-field response showed a slope of 70 mV/μm, which was 27% less than the factory calibration slope. The difference is attributed to a small deviation from perpendicularity. I used 1.63 V as my operating point. The standard deviation of this fit to the slope, calculated from (K-1), was 0.0004 V/um.

It was also important to position the sensor in the center of the membrane. The Philtec sensor diameter was 510 μm, while the membrane had a width of 750 μm. I positioned the

* Newport Corporation, 1791 Deere Avenue, Irvine, CA 92606

sensor head during operation, using the magnitude of the photoacoustic signal to find the center of the membrane.

5.2. *Results*

The membranes of many cells failed during fabrication—the yield was about 50%. When membranes failed they didn't shatter, as is typically observed for tensile membranes. Rather the membranes would just crack, with most of the pieces remaining in place. The "packaging" process was also prone to failure, particularly when using indium for the sealant, which required heating the cell and base plate. I tested two devices, although the first device had a slightly different design (the viewport window was longer, exposing most of the cavity), and was tested before without the capability to measure light levels or to calibrate the Philtec sensor. Most of the data in this section is from the second device. The light power measured out of the fiber prior to its insertion into the μPAS cell was 0.6 mW, with a standard deviation of 0.06 mW.

5.2.1. *Noise Measurement*

Figure 5-9 and Figure 5-10 show the noise measured in the cell. Each plot contains two sets of data, one in which the laser was blocked and another in which the laser was unobstructed, but the cavity only contained nitrogen. In these two plots, each data point represents a single measurement.

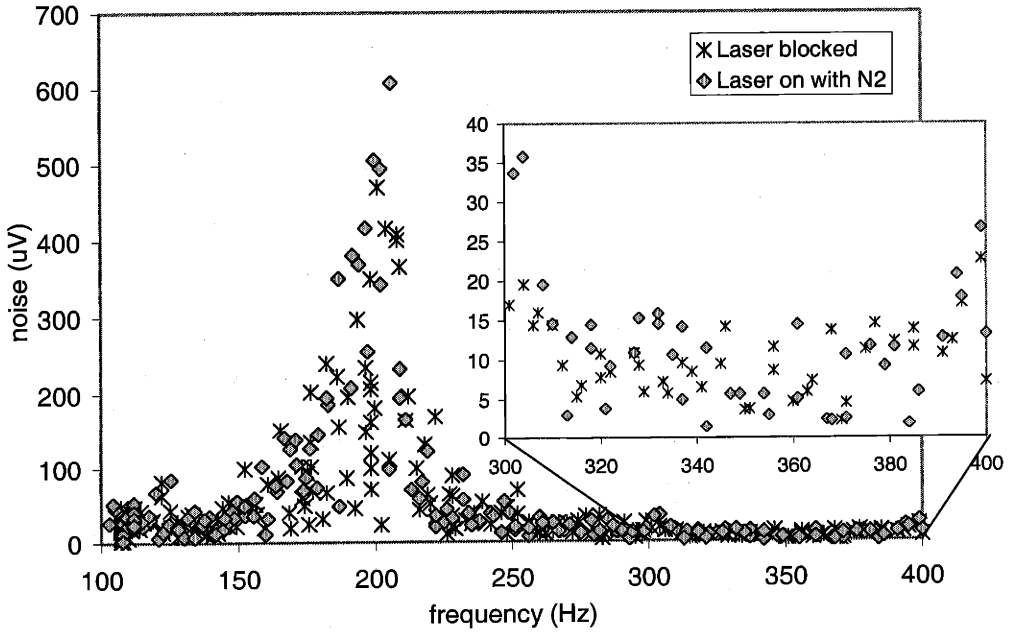

Figure 5-9: Noise measured in the low-frequency range. The inset shows a close-up of 300-400 Hz.

The measured noise levels for both cases are the same, indicating that background absorption is insignificant compared to other noise sources for the μPA detector. There was also a large noise peak around 200 Hz. The data did not exhibit a dependence on the chopper noise as was observed for brass cell detectors. This was perhaps due to the much smaller leak for the μPA cell, because of its long and narrow flow channels. Furthermore, the membrane was oriented perpendicularly to the chopper, and was contained within the fume hood with its walls covered with anechoic acoustic foam. (The brass cell was also contained within the anechoic fume hood, but the gas outlet was pointed out of the hood, and so was susceptible to direct sound waves.) The membrane was, however, oriented towards the vent for the fume hood, which could be responsible for the noise spike at 200 Hz.

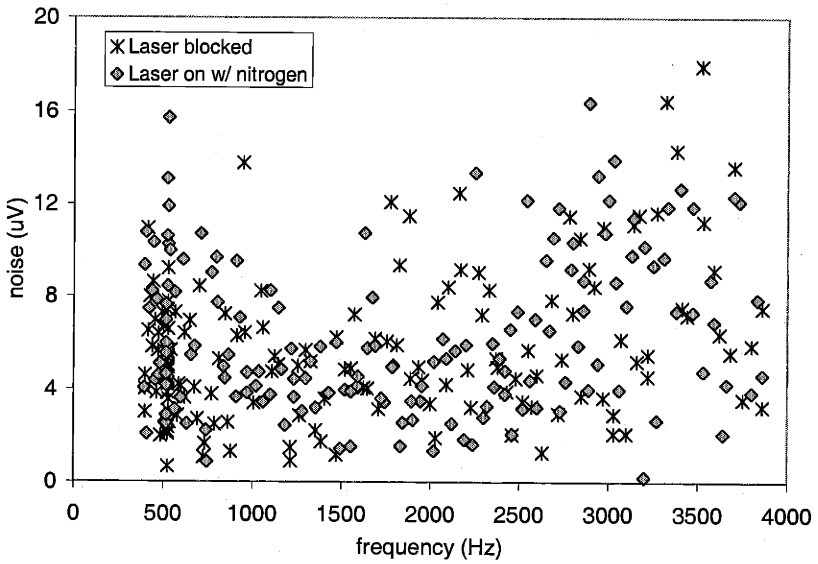

Figure 5-10: High-frequency range noise measurement for the second μPA device

5.2.2. *Frequency Dependence*

Figure 5-11 shows the frequency dependence of the response for pure propane measured in the second μPA cell. Each data point represents a single measurement. The data shows an inverse dependence on frequency, but has some anomaly between 3100 and 3400 Hz. This anomaly is not due to a cavity resonance, as the first longitudinal resonance peak for the μPA cavity should not occur until ~8.3 kHz. It is attributed, instead, to a flow channel resonance, as is discussed below in Section 5.4. It should also be noted that the response of the Philtec sensor is specified to be flat only to 2 kHz, and begins to roll off above that (the 3 dB point is specified to be around 20 kHz).

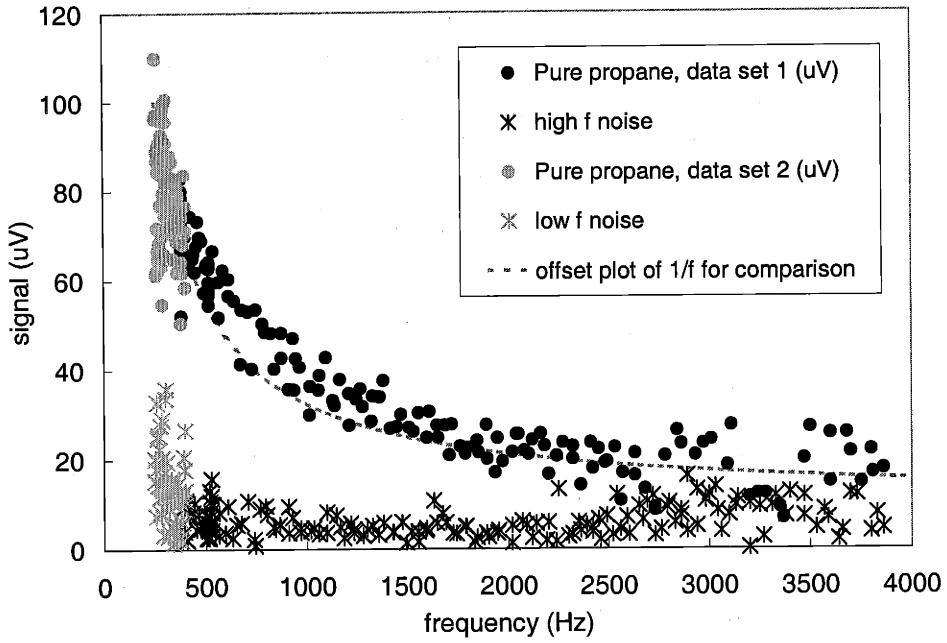

Figure 5-11: Frequency dependence of μPAS cell response. The flow rates were kept constant at 5 mL/min

5.2.3. *Concentration Dependence*

Figure 5-12 shows the propane concentration dependence of the signal at 401 Hz with a total flow rate of 5 mL/min. Each data point represents the average of 50-100 measurements for the same gas mixture settings. While still exhibiting some saturation behavior, the concentration dependence of the μPA detector always increased with concentration level, so that the μPA detector could be used to quantify gas levels even in high concentration mixtures. This was much different than was observed for the brass cell detector. The reason is that not only is the μPA cell photoacoustic cavity physically much shorter than in the brass cells, but also the semi-transparent sidewalls make the effective length of the cavity shorter still.

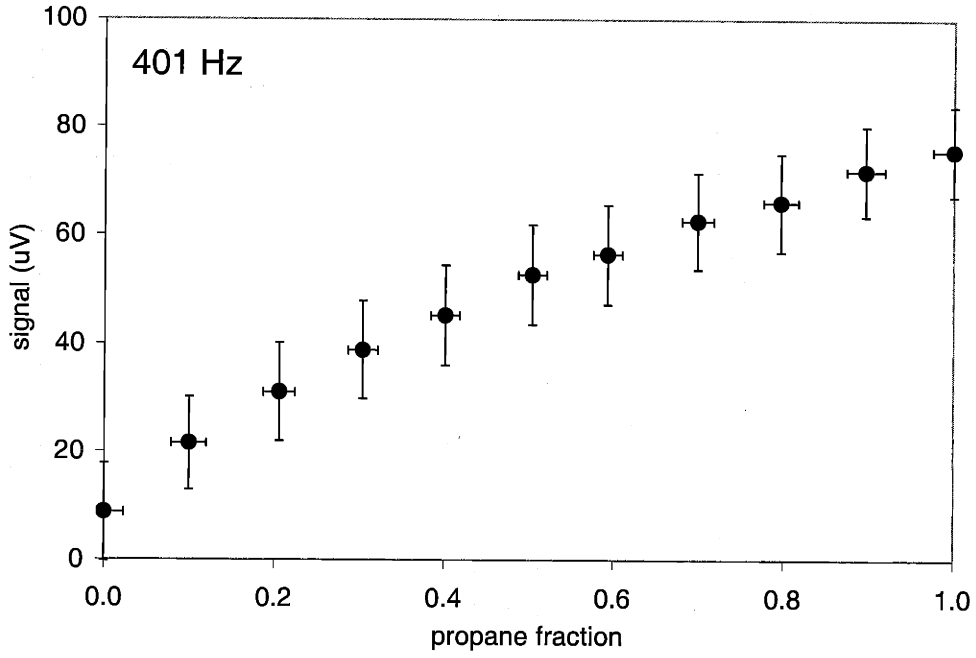

Figure 5-12: Concentration dependence of the μPAS cell response at 401 Hz, with a flow rate of 5 mL/min

5.2.4. *Flow Dependence*

I tested the first device before I was able to measure light power levels and Philtec sensor position. However, it's worth showing some of the data here, because it exhibited a strong flow rate dependence (Figure 5-13). At 50 sccm, the residence time of the μPA cavity was only 3.5 ms. It is no surprise, then, that the signal should be attenuated at this high flow rate at 277 Hz, where the excitation period was 3.6 ms. The lesson of Figure 5-13 is that the residence time must be taken into account as the cell is miniaturized—either the gas flow rate should be reduced, or the excitation frequency increased.

Having learned this lesson with the first μPA cell, I used flow controllers with a lower range for the second μPA cell. There was little flow dependence in the lower flow range, as can be seen from Figure 5-14. The slight upward trend was due to a small leak in the nitrogen MFC, so that the "pure" propane was actually slightly contaminated with nitrogen. The contamination fraction would be greater at lower propane flow rates.

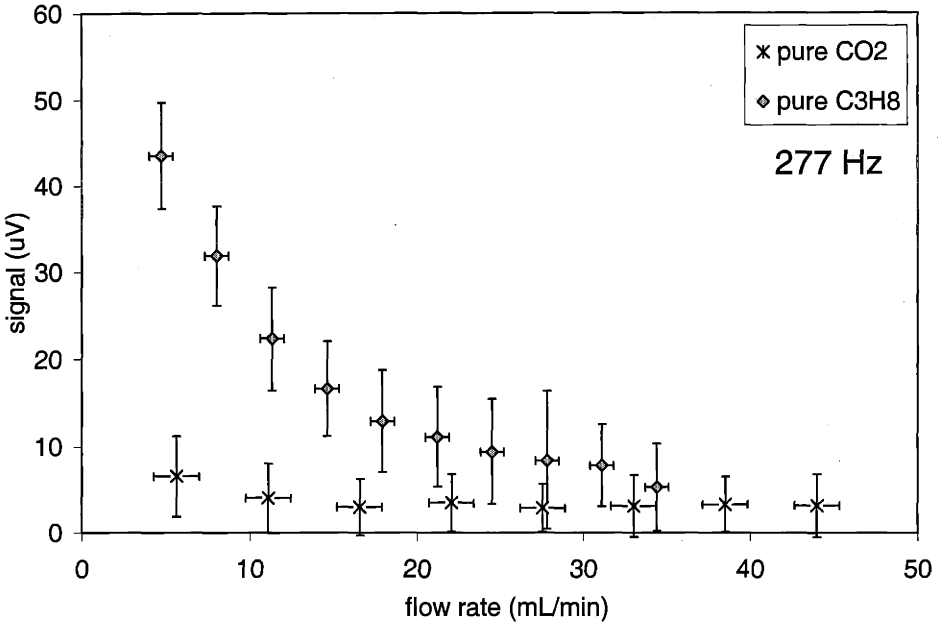

Figure 5-13: Flow dependence of first μPA cell

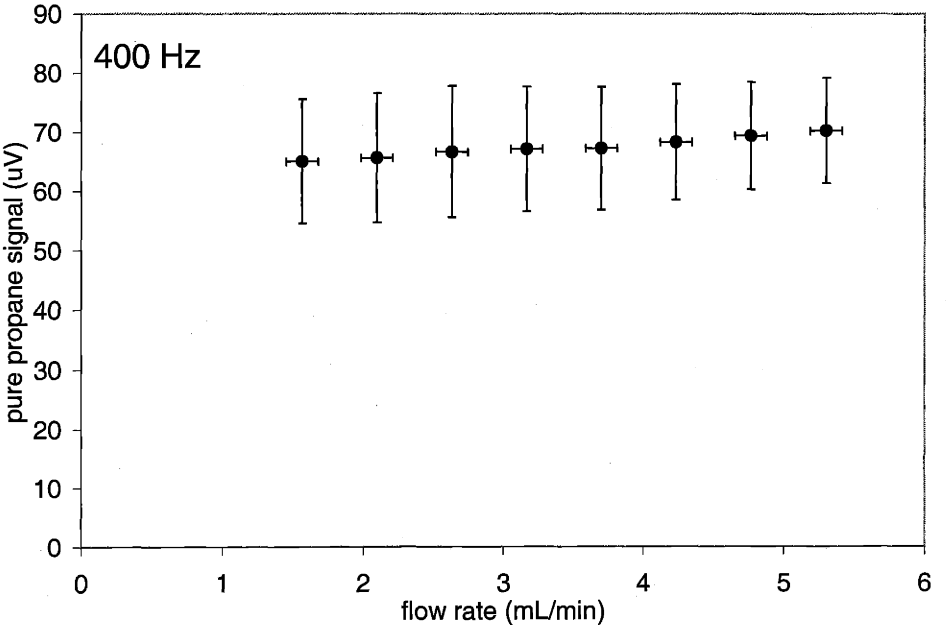

Figure 5-14: Flow dependence for pure propane in second μPA device

5.2.5. *Reproducibility*

Comparing the data in Figure 5-11, Figure 5-12, and Figure 5-14, which were taken over a four-hour stretch on the same day, one could see that the signal measured for 5 sccm propane at 401 Hz ranged from 60-80 μV. The variation is due to noise as well as drift in the deflection

measurement. Comparing Figure 5-11 and Figure 5-13 for 5 sccm propane at 277 Hz, one can see that the second μPA cell was nearly twice as sensitive as the first. The difference could be due to variations in the fiber cleave quality or in the alignment of the deflection sensor to the membrane. Clearly, more work would be required to establish reproducibility for the μPA detector. However, the purpose of the μPA detector work for this thesis was simply to demonstrate how a photoacoustic detector could be microfabricated.

5.3. *Comparison to theory*

5.3.1. *Mechanical properties of the membrane*

In order to compare the data to the transmission line model, the data must be converted to the units of Pa/W. The displacement sensor calibration, shown in Figure 5-8, can be used to convert the voltage reading to a displacement. However, we need to consider the mechanical properties of the membrane in order to estimate the relationship between displacement and pressure.

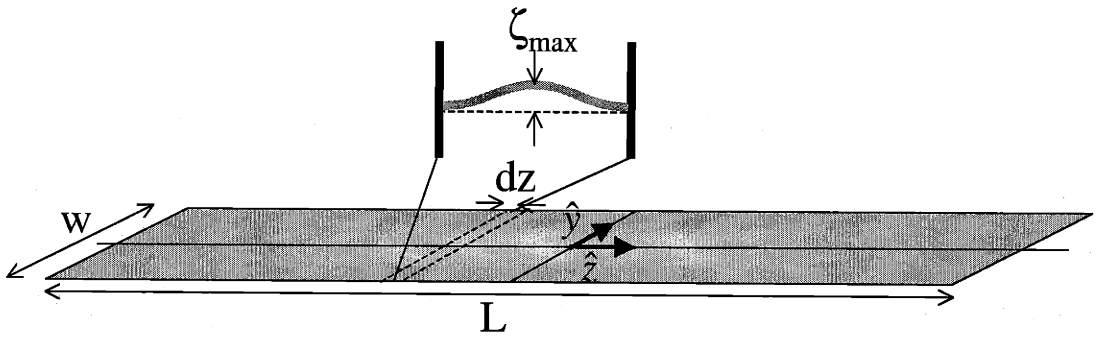

Figure 5-15: Schematic of membrane geometry

If the membrane is monitored in the center, far from either end, the membrane deflection is uniform in the z direction, but varies in the y direction. For small deflections, the general equation for a plate in pure bending in response to a uniform transverse pressure, P, is given by [Timoshenko, 1940 #3]:

$$\nabla^4 \zeta(y,z) = \frac{P}{D_R} \qquad (5\text{-}1)$$

where ζ is the deflection at the position (y,z). D_R is the flexural rigidity of the plate, given by [Timoshenko, 1940 #3]:

$$D_R = \frac{Eh_m^3}{12\left(1-\nu_P^2\right)} \tag{5-2}$$

where h_m is the membrane thickness, E the Young's modulus (166 GPa in this case for Si [173]), and ν_P the Poisson's ratio (~0.28 [173]).

Far from either end of the cavity, (5-1) can be reduced to $\frac{d^4\zeta(y)}{dy^4} = \frac{P}{D_R}$. The boundary conditions for the case of the clamped-clamped beam are that both the deflection and slope of the deflection must be zero at the wall. Furthermore, the solution must be symmetric and have a slope of zero at the center. The resulting solution for the deflection is:

$$\zeta(y) = \frac{P}{24D_R}\left(y^4 - \frac{w^2y^2}{2} + \frac{w^4}{16}\right) \tag{5-3}$$

which can be rewritten in terms of the maximum deflection, which occurs at the center:

$$\zeta(y) = \zeta_{\max}\left(16\left(\frac{y}{w}\right)^4 - 8\left(\frac{y}{w}\right)^2 + 1\right) \tag{5-4}$$

$$\zeta_{\max} = \frac{Pw^4}{384D_R} = \frac{Pw^4\left(1-\nu_P^2\right)}{32Eh_m^3} \tag{5-5}$$

We can use this equation to estimate the relationship between the deflection measured by the displacement sensor and the maximum deflection. The head of the displacement sensor is circular with a radius, R_{ds}, of 255 μm. If we assume that the displacement perceived by the sensor, ζ_{avg}, is the spatial average of the displacement observed within the circle defined by the sensor head, then ζ_{avg} is given by:

$$\zeta_{avg} = \frac{4}{\pi R_{ds}^2}\int_0^{R_{ds}}\int_0^{\sqrt{R_{ds}^2-x^2}}\zeta(y)\,dy\,dx \tag{5-6}$$

which equals $\sim 0.8\zeta_{max}$ for R_{ds} = 255 μm and w = 750 μm. The ratio of the pressure to the measured deflection is therefore given by:

$$\frac{P}{\zeta_{avg}} = 40\frac{Eh_m^3}{w^4\left(1-\nu_P^2\right)} \tag{5-7}$$

For h_m = 2.2 μm and w = 750 μm, this value is 242 Pa/μm. This value should be treated with caution. Assuming dimensional tolerances (2σ) of ±5%, the tolerance of the membrane sensitivity is ±25% (the details of this calculation can be found in J.4.1). Furthermore, this error

does not include uncertainty in the material properties or the possible effects of stress on the performance of the membrane.

The fracture behavior observed for the μPA membrane, combined with the use of the same material for both the membrane and support, suggested that the intrinsic stress in the membrane was small, so that the solution given by (5-7) was appropriate. In order to verify this, I measured the load-deflection characteristic of another membrane from the same wafer lot, which is shown in Figure 5-16. The details of this experiment are given in Appendix K.

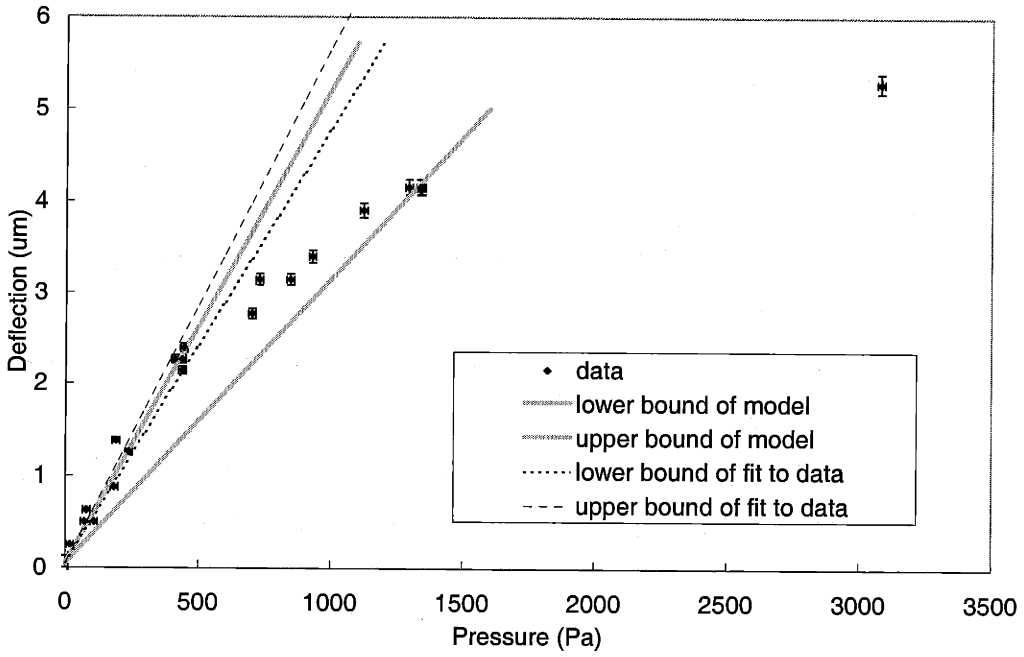

Figure 5-16: Load-deflection measurement

Figure 5-16 shows the measured data compared against the predictions of (5-7). The rollover observed in the figure for higher pressures is the result of the increased contribution of membrane stretching, for which the pressure goes as the cube of the deflection. Figure 5-16 shows a reasonable agreement between the model and our measurement of the load-deflection sample, which further supports the negligence of stress effects in the calculation of the mechanical sensitivity of the membrane.

Finally, our analysis assumed that the operation point is far from any mechanical resonances in the membrane. The resonance can be crudely estimated by considering the membrane as a lumped mass-spring system. (5-5) provides a relationship between maximum

displacement and force for the first bending mode, which should be the lowest order membrane mode. (5-5) implies a spring constant for the mode of:

$$k_{spring} = \frac{P(wL)}{\zeta_{\max}} = \frac{32Eh_m^3(wL)}{w^4(1-\nu_P^2)} \qquad (5\text{-}8)$$

while the mass of the membrane is given by $m_{mem} = \rho_{mem}(wLh_m)$, where ρ_{mem} is the density of the membrane material (2331 kg/m^3 for Si [178]). The resulting resonance is:

$$\omega_{mem} = \sqrt{\frac{k_{spring}}{m_{mem}}} = \sqrt{\frac{32Eh_m^2}{w^4(1-\nu_P^2)\rho_{mem}}} = 1.945 \text{ x } 10^5 \text{ rad/s (31 kHz)} \qquad (5\text{-}9)$$

More precisely, the lowest resonance frequency is given by [179]:

$$\omega_{mem} = 22.4\sqrt{\frac{Eh_m^2}{12w^4(1-\nu_P^2)\rho_{mem}}} = 2.223 \text{ x } 10^5 \text{ rad/s (35 kHz)} \qquad (5\text{-}10)$$

As expected, this is much greater than the excitation frequency, so that the assumption of the static deflection behavior is valid.

Assuming (5-7), and using the calibration for the Philtec sensor described in Figure 5-8 along with the earlier measurement of the light power levels, the data can be translated into Pa/W. Figure 5-17 and Figure 5-18 show the converted data. As was discussed above, this estimate of error neglects uncertainties in the material properties as well as the possibility of stress in the membrane.

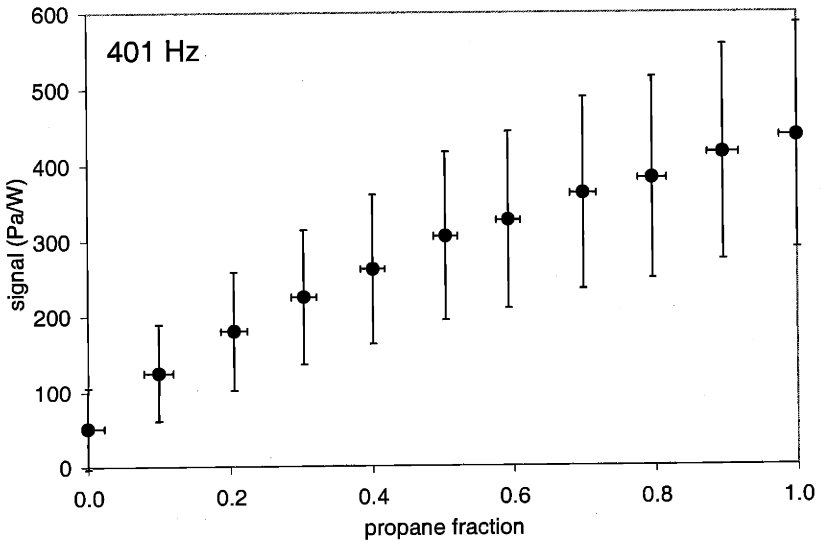

Figure 5-17: Concentration data converted into Pa/W

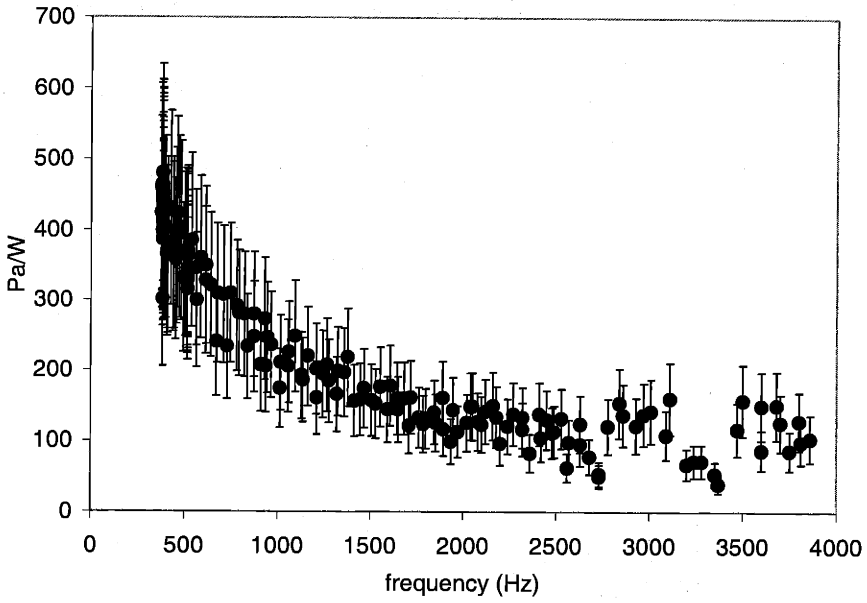

Figure 5-18: Frequency data converted into Pa/W

5.3.2. *Model predictions*

Figure 5-19 shows the data compared against the model. At first, the fit of the unaltered model was very poor; it predicted a response nearly an order of magnitude greater than what was observed in the cell. One cause for the failure of the model was that it assumed that the cavity walls were completely rigid. We can use the spring analogy from (5-8), above, to add the effect of the membrane compliance into the model.

In the mechanical impedance analogy, a spring is a capacitor with a capacitance equal to the inverse of the spring constant. In the conversion of the mechanical circuit analogy to the acoustic circuit analogy, one picks up a factor of the area squared (the mechanical analogy is force and velocity, while the acoustic analogy is pressure and volumetric flow rate). A capacitor in the acoustic circuit analogy represents the effect of a cavity of volume, V, with a value $\mathcal{C}_A = V/\rho_0 c^2$. The compliance of the membrane can therefore be included in the model as an additional volume, with a value V_{eff}, given by:

$$\frac{V_{eff}}{\rho_0 c^2} = \frac{(wL_m)^2}{k_{spring}} \Rightarrow V_{eff} = \frac{\rho_0 c^2 w^4 \left(1-\nu_P^2\right)(wL_m)}{32Eh_m^3} \qquad (5\text{-}11)$$

where L_m is the length of the membrane (which is slightly less than the cavity length L). Using the parameters of the μPA cell, the value of V_{eff} is 6.5 x 10^{-9} m^3, which is more than twice that of the cavity volume alone! The effect of the additional volume can be added to the transmission

line model by adding V_{eff}/L to the cross-sectional area, S, used in the calculation of the incremental capacitance of the transmission line representing the cavity.

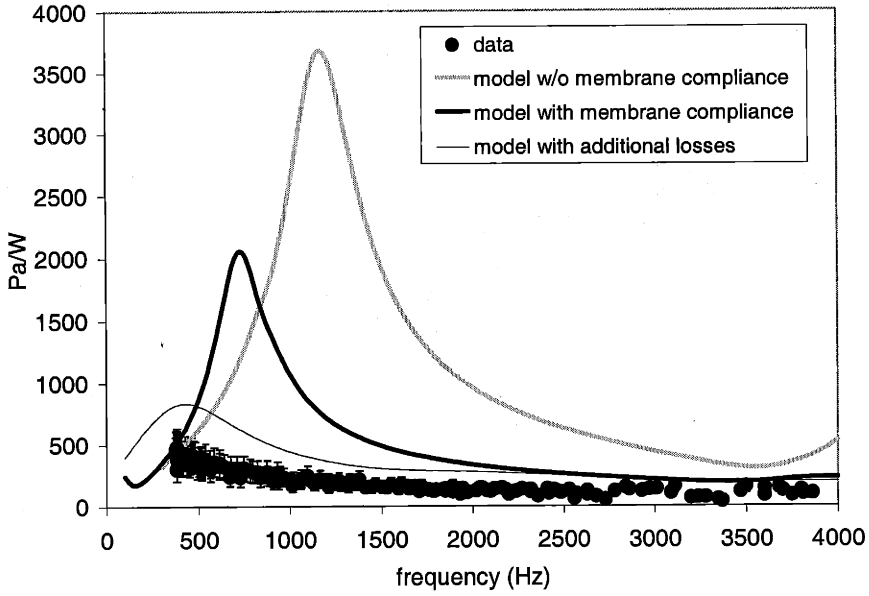

Figure 5-19: Comparison of frequency data with model

Also, as was the case for the brass cell, the transmission line model underestimates many sources of loss in the flow manifold. Figure 5-19 also shows the effect of quadrupling the resistances and capacitances in the model of the leak, which brings the model even closer to the data. Figure 5-20 shows how the modeled concentration behavior, with the membrane compliance included, compares to the data. If a significant fraction of the light from the fiber were blocked by the fiber stop, then the actual incident power in the cell would be less than was measured; this would result in higher values for the data in Pa/W. The fit of both the frequency and concentration model was also dependent on the correct value for δ, the sidewall absorption coefficient, which was determined experimentally. Even with these considerations, however, the model agrees fairly well with the data, particularly when the membrane compliance is included.

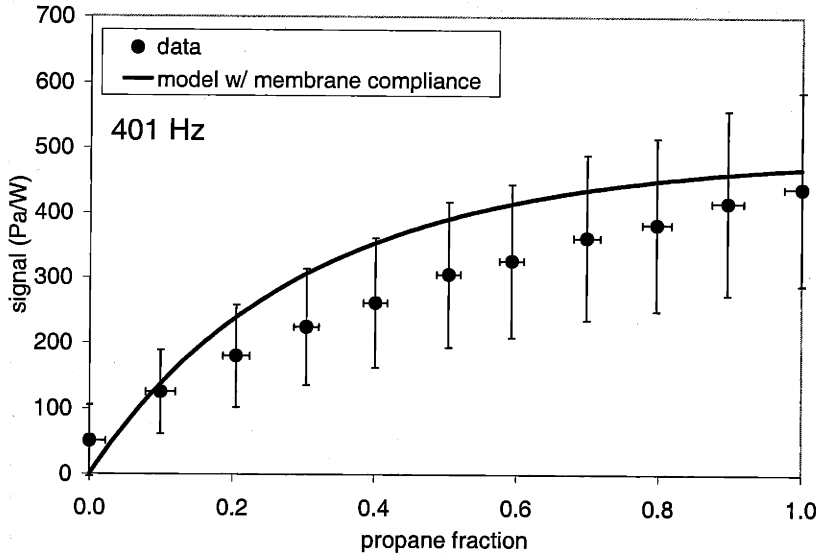

Figure 5-20: Comparison of concentration data with model

5.4. *Improving the μPA detector*

The purpose of the μPA cell experiments was to demonstrate that a photoacoustic detector could be microfabricated. This design, therefore, had met the goals of the thesis. However, several improvements could be made to enhance the performance of this detector.

Like in the brass cell detectors, leak effects were significant for these devices, although the μPA cell behavior was not nearly as dependent on the external flow manifold. This can be seen in Figure 5-21. The nature of the leak is clearly revealed in a plot over a larger frequency range (Figure 5-22). According to the formula $\omega_0 = c\pi/L_{ch}$, the first resonance of the flow channels should occur at 3846 Hz. The multiple nodes of the impedance plot represent these resonance points. This first channel resonance was probably responsible for the dip observed in the data between 3100 and 3400 Hz.

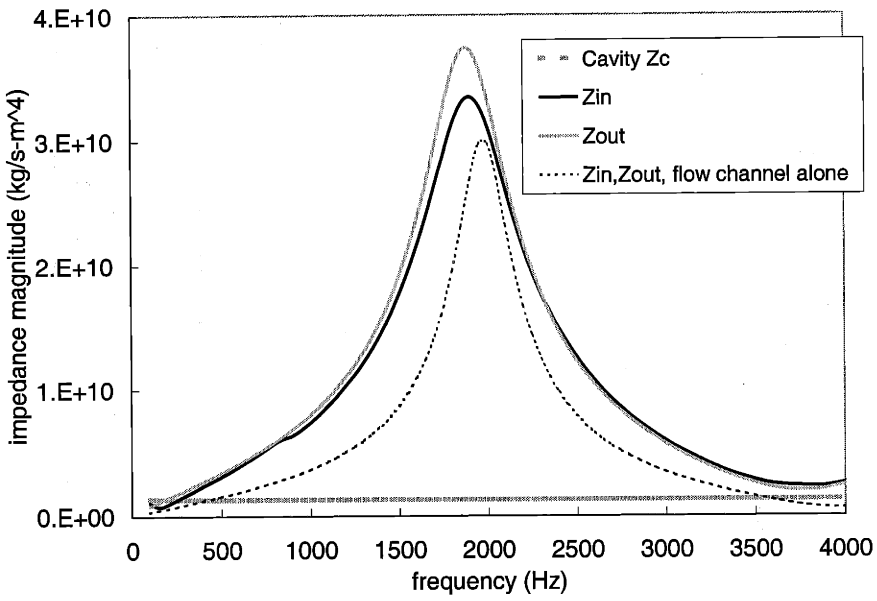

Figure 5-21: Comparison of impedances in the system

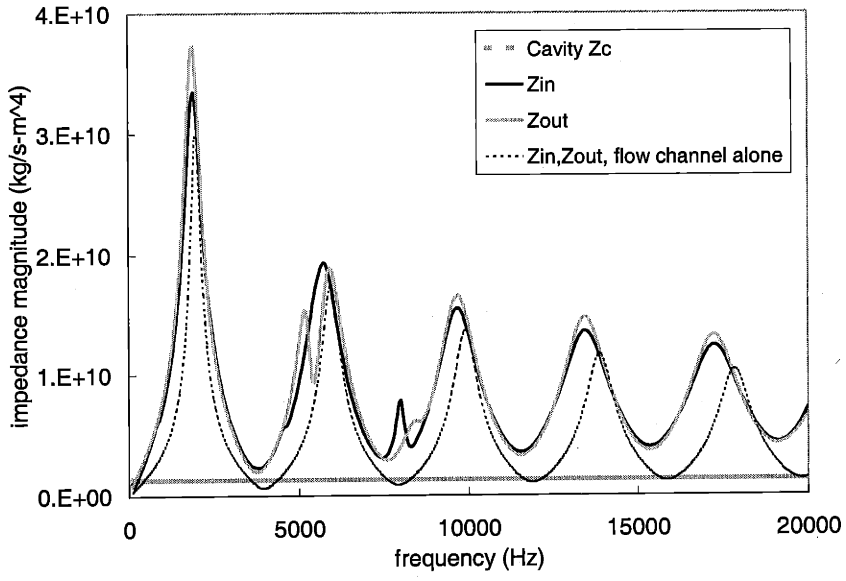

Figure 5-22: Comparison of impedances over a larger frequency range

This device demonstrates how having long channels is not sufficient for diminishing the effect of the leak if the channels are not exceedingly narrow in comparison to the cavity. The cross-sectional area of the flow channels was ~0.15 mm^2, while the cross-sectional area of the cavity was ~0.20 mm^2. Microfabrication techniques could easily be used to achieve much smaller channel dimensions. Figure 5-23 shows the frequency response if the channel cross-section were semicircular with a radius of 10 μm, so that the leak effect were negligible. This

would require modifying the fabrication process to create the channels and optical fiber stop in separate etch steps.

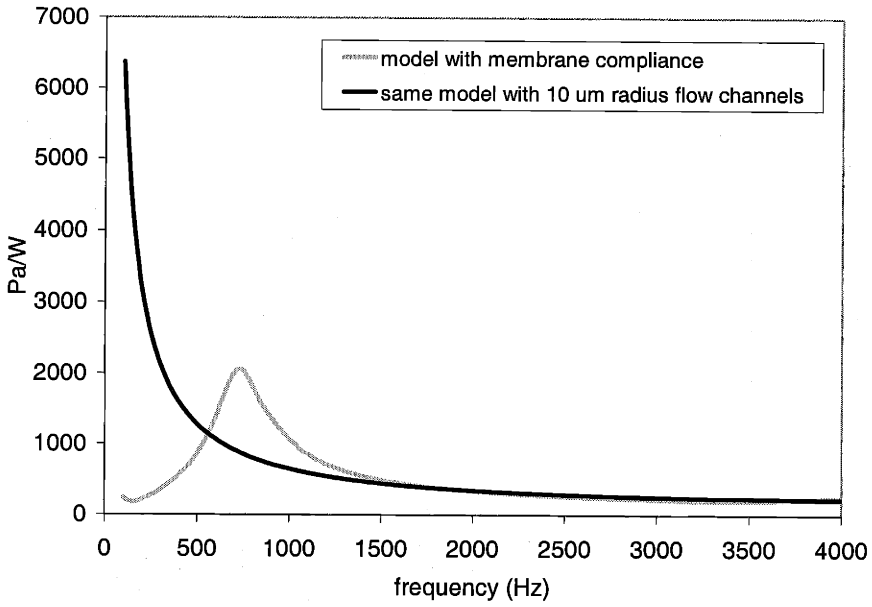

Figure 5-23: Effect of changing channel dimensions

Another improvement, the effect of which can be seen in Figure 5-20, would be to make the membrane a much smaller fraction of the cavity wall. These membranes were 750 μm wide and 10 mm long. They could be shortened to 3 mm with little loss in mechanical sensitivity. Combined with smaller flow channels, this could further increase the signal for pure propane (Figure 5-24). The reduced membrane length should be combined with smaller channel dimensions, because otherwise the gains of the membrane reduction are offset by an increased leak effect as the total "volume" of the cavity is reduced.

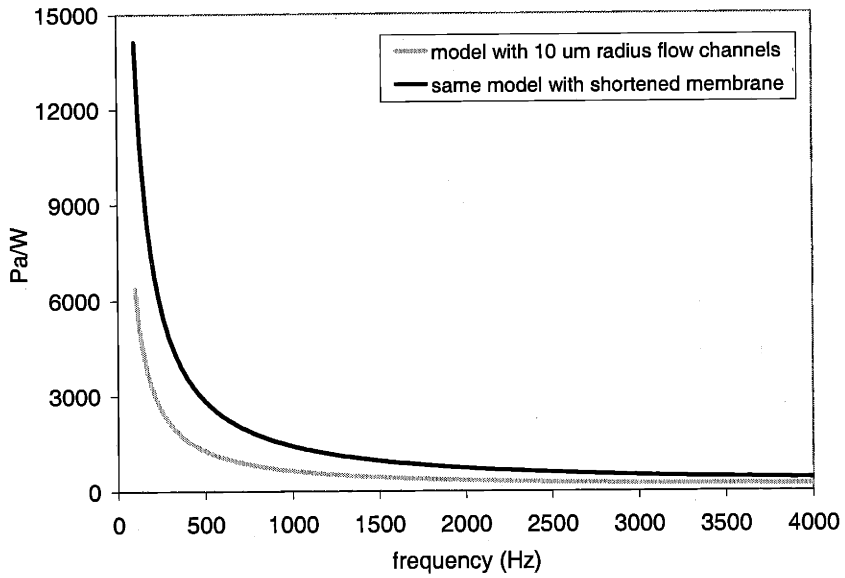

Figure 5-24: Effect of shortening membrane to 3 mm

With these two changes, the pure propane response of the μPA detector could be as high as 4000 Pa/W at 400 Hz. In contrast, the response of the NSL brass detector, in the absence of leak effects, was calculated in Chapter 4 to be 400 Pa/W at 400 Hz. The size reduction from microfabrication could potentially produce a factor of 10 in sensitivity enhancement. Even for the real systems, including leaks and the membrane compliance, the response of the μPA cell at 400 Hz, 400 Pa/W, was more than double that measured for the NSL brass detector (200 Pa/W). The resolution of the μPA detector, however, was much poorer than that of the brass cell detector. The noise level of 10 μV limited the minimum detectable concentration (with a 0.6 mW source) to about 5% propane in nitrogen.

The concentration resolution of the μPA cell could be improved by reducing the flow channel diameter and by decreasing the membrane length. It could be improved further by changing to a more sophisticated microphone or by coating the sidewalls of the cavity with a reflective material. The semi-transparent nature of the cavity walls is a double-edged sword. While it effectively shortens the cell, increasing the concentration range over which the detector can operate, it also dramatically reduces the amount of light power that can be contained in the cavity. I measured a light loss parameter, δ, of 1000 m^{-1} for the cavity, which implied that even in the absence of absorbing gas, the light in the cavity was attenuated by a factor of 10 after 2.3 mm. Therefore, the bulk of the cavity is "wasted space," in which no heat could be generated. In the absence of leaks, the additional space only increases the total surface area over which the

force, generated by the absorption in the front part of the cell, is distributed. (When a leak is present, the additional volume buffers the effect of the leak, as was discussed in Section 4.4.) Therefore, one way to increase the sensitivity and resolution of the detector without increasing saturation effects would be to make the cavity very short. Figure 5-25 shows the concentration dependence of the μPA cell with a variety of modifications. Reducing of the leak also affects the range of the detector; it slightly decreases the maximum resolvable concentration.

Another way to increase the sensitivity and resolution of the μPA detector would be to coat the inside walls of the cavity with a metal such as gold to enhance their reflectivity. This would greatly increase the resolution of the detector, but would reduce the total concentration range. With small flow channels and a reflective coating, the μPA detector could detect 400 ppm of propane, even with the simplified optical microphone.

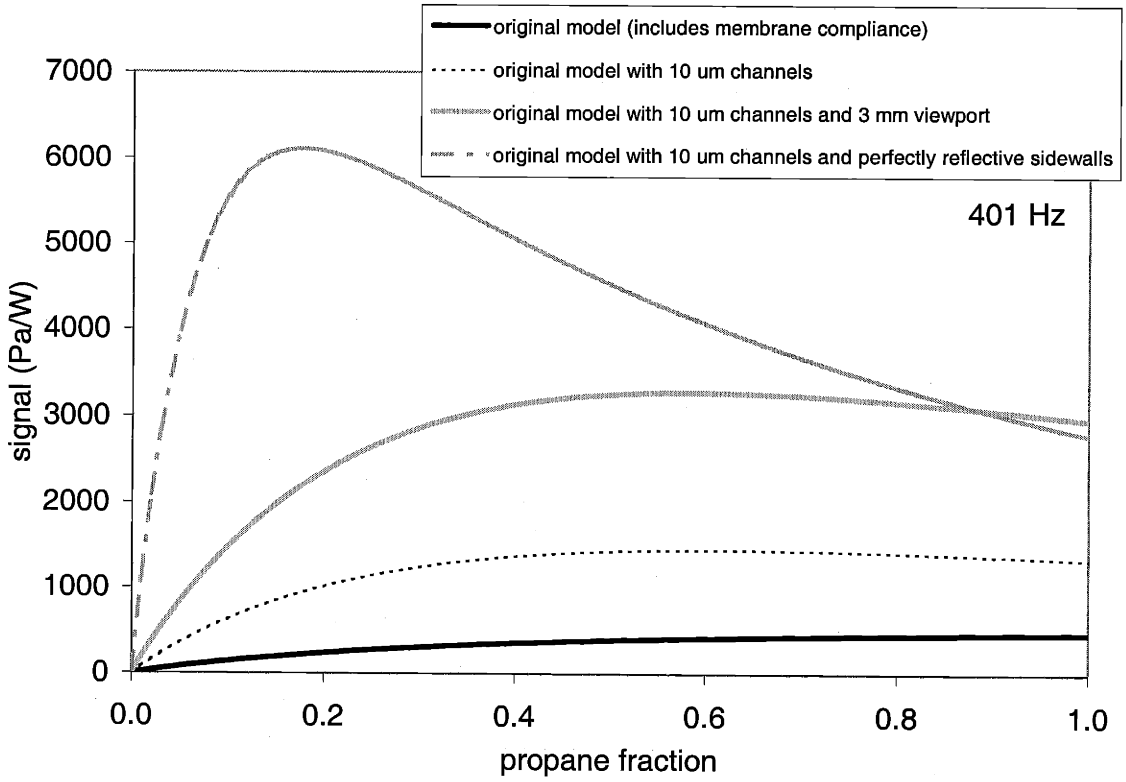

Figure 5-25: Improvements to the concentration resolution

6. Conclusions

6.1. *Contributions of this thesis*

This thesis makes several contributions to the miniaturized chemical analysis research community:

- Quantitative analysis of the dimensional dependence of the gas-phase photoacoustic effect, with a transmission-line-model that applies to both dilute and high-concentration mixtures.
- Demonstration of gas-phase photoacoustic detection on the miniature scale in a variety of configurations.
- Demonstration of a microfabricated photoacoustic detector for gas-phase species.
- Demonstration of miniaturized gas-phase photoacoustic detection in a system.

This work represents the first demonstration of gas-phase photoacoustic detection on the meso-scale. There is much potential for further development. However, there are also some issues particular to photoacoustic spectroscopy that have appeared repeatedly in this thesis.

6.2. *Limitations of photoacoustic spectroscopy*

6.2.1. *Concentration range limitations*

Photoacoustic detection may be inappropriate to systems with large variations in gas composition. There are two reasons for this: high optical absorption levels and changing acoustic properties. This limitation is best illustrated by the highly non-linear concentration dependence exhibited in Figures 4-18 and 4-19. High optical absorption levels are only a problem for strong absorption peaks, such as the 3.39 μm propane peak used in this work. Switching to the weaker absorption bands, or using a differential excitation technique could eliminate absorption saturation effects.

The greater problem with applying photoacoustic spectroscopy to systems with large gas composition changes is that the photoacoustic signal depends not only on the absorptivity of the gas but also on properties such as γ and the speed of sound, c. This problem is far worse in

systems where there are large acoustic leak effects, because the magnitude of such leaks depends on the viscosity and thermal conductivity of the gas.

For chemical systems where the component identities are known in advance, a possible solution to this dilemma would be to use a low-leak, resonant photoacoustic cell with a feedback loop to control the acoustic frequency. There would then be two pieces of information from each reading—the speed of sound and the photoacoustic signal level—from which to determine the gas composition. Problems with changing acoustic properties could also be avoided in solid- or liquid-phase systems, where an unchanging, inert gas carries the acoustic signal.

Other techniques may be better for detection in systems with high gas concentrations. The light absorption saturation "problem" is a testament to how strong the mid-infrared absorption lines for some gases can be—they don't require a particularly sensitive detector. A conventional absorption spectroscopy technique is more appropriate for such a system, even though its ultimate sensitivity is less.

However, photoacoustic detection may be the best technique for detecting small changes in concentration level, such as in the case of dilute mixtures. In Section 4.5 I discussed the detection of 10 ppm levels of propane in nitrogen, in a relatively unsophisticated photoacoustic detector with a weak laser source and all the problems of acoustic leaks and ambient noise. This corresponded to a total absorbed power of 370 nW. The literature suggests that ppb levels of detection are easily within reach with photoacoustic detection. Such sensitivities far exceed those of other gas-phase absorption spectroscopy work in miniaturized cavities [69].

6.2.2. *Confinement of the acoustic signal*

The other issue that was recurrent in this work was that of acoustic leaks. This is particularly problematic for integration of photoacoustic detection with other systems, where it is difficult to acoustically isolate the photoacoustic cavity from other components in the system. The connecting flow channel must be long relative to the acoustic wavelength, and very narrow. This presents three strategies for the integration of photoacoustic detection: using very long flow channels, using high acoustic frequencies, or making the whole system the photoacoustic cavity.

The most straightforward strategy is to have long, narrow flow channels connecting the photoacoustic cavity to the rest of the system. In 4.4, I discussed how one could eliminate leak effects in the μPA cell by maintaining the same long channel length and decreasing the channel radius to 10 μm. The advantage of this strategy is that it allows one to still use low acoustic

frequencies, for which there is a large non-resonant response. However, the disadvantage of this integration method is that the long flow channels could potentially introduce a large delay in the system response, particularly if the flow rate is also limited. Also, they would increase the size of the total system.

The connecting flow channel could be much shorter and broader if a higher acoustic frequency were used. In such an implementation, resonant detection would be preferable to non-resonant. For example, an H-cell type resonator, such as that shown in Figure 2-6, might be readily implemented with microfabrication techniques. A further advantage of resonant cells is that the flow channels could be placed at the nodes of the resonant mode, reducing their influence.

Finally, one could abandon the modular approach and design the photoacoustic cavity to include other parts of the system. For example, one could combine the microreactor and photoacoustic cavity. The advantage of this integration method would be a fast time response, allowing the study of chemical reactions *in situ*. Reactor chambers and photoacoustic cavities are routinely combined for kinetics studies of solid-phase catalysts. However, the disadvantage of this system would be that it the photoacoustic cavity could place additional constraints on the chemical reactor design, such as limits to the flow rate or operation temperature. Also, the chemical reaction could interfere with the photoacoustic signal transduction, or the optical stimulation could interfere with the reaction.

6.3. *Future work*

6.3.1. *Improvements to the gas-phase detector design*

The elimination of leak effects through better channel and cavity design could dramatically improve the performance of these miniaturized gas detectors. Armed with the transmission line model—which applies to resonant systems as well as non-resonant—one could go on to design miniaturized resonant cells. An H-cell resonator, which uses the longitudinal modes, could be a logical first step.

Another improvement would be to replace the optical microphone with an integrated capacitive microphone. Such a step would eventually be necessary for a miniaturized system as the current microphone is quite bulky.

6.3.2. *Miniaturized solid and liquid phase spectroscopy*

The great commercial success of photoacoustic spectroscopy has been not in gas phase systems but in the study of solid phase catalysts. An array of packed-bed microchemical systems with parallel detection would be extremely useful for commercial catalyst discovery. One challenge for a miniaturized solid-phase photoacoustic system, however, would be thermally isolating the catalyst particles from the chamber walls.

The non-invasive nature of photoacoustic detection may lead to another commercial success in biological monitoring, with devices such as Spanner and Niessner's glucose monitor [118]. Miniaturization could spur this development, allowing detectors to match the size scale of many organic systems.

6.3.3. *Extension of detection to spectroscopy*

The commercial success of FT-PAS for catalyst studies holds a few lessons for the development of other PAS applications. If laboratories or industrial facilities are the market for integrated microchemical systems using photoacoustic detection, the FTIR method is the best means of achieving spectroscopy, particularly if the photoacoustic detection unit is compatible with an existing analysis system. Such facilities are likely to already have FTIR systems, and their operators would already be familiar with the operation procedure. For many applications, the best method for achieving spectroscopy might be the integration of laser diode arrays (for spectroscopy in the near IR), or of a miniaturized light source combined with an integrated interferometer or programmable diffraction grating, such as the polychromator. This would allow for a completely portable system.

In summary, this thesis represents only a first step towards the integration of miniaturized photoacoustic spectroscopy with micro total analysis systems. Photoacoustic detection has been found to be unsuitable for systems with large variations in gas composition, but has been shown to have extreme sensitivity to dilute mixtures. The natural progression of future work would be to apply the transmission line model to develop a leak-free photoacoustic device and to focus on reducing noise sources in order to establish the sensitivity limits of miniaturized photoacoustic detection. One could then extend this system from detection to spectroscopy, and integrate it with another system.

Appendix A : *A photoacoustic lexicon*

A.1. *Variables for photoacoustic system geometry*

Symbol	Units (SI)	Description
L	m	photoacoustic cavity length
R	m	photoacoustic cavity radius (or effective radius for a non-cylindrical cavity)
V_C	m^3	photoacoustic cavity volume
S	m^2	cross-sectional area of the photoacoustic cavity
D	m	cross-sectional perimeter of the photoacoustic cavity
$\vec{r}$	--	general position vector = $[r, \phi, z]$ for cylinder
r	m	radial position in the cylindrical photoacoustic cavity
z	m	axial position along the cylindrical photoacoustic cavity
ϕ	rad	azimuthal position in the cylindrical photoacoustic cavity
V_M	m^3	volume representing the compliance of the microphone
w	m	membrane width in μPA cell
y	m	position along the width of the μPA membrane
$\zeta(y,z)$	m	deflection at the position (y,z) of the μPA membrane
h_m	m	membrane thickness

A.2. *Variables for optical excitation and heat generation*

Symbol	Units (SI)	Description
H	W/m^3	heat generation rate
α	m^{-1}	absorbance (transmission through a length l given is by $e^{-\alpha l}$)
I	W/m^2	light intensity (= W/S)
n_1	m^{-3}	density of absorbing molecules in the upper state of a two-level system
N	m^{-3}	total density of absorbing molecules
h	J s	Planck's constant
ν	s^{-1}	optical frequency
$\Delta\nu$	s^{-1}	frequency width of the absorption line
S_l	m^2/s	strength of the absorption line
τ_R	s	radiative lifetime
τ_C	s	collisional lifetime
τ	s	upper state lifetime for low-level radiation ($\tau^{-1} = \tau_R^{-1} + \tau_C^{-1}$)
a	m^2/mol	decadic molar extinction coefficient ($\alpha = ac_0 ln10x$, where c_0 is the overall molar concentration and x is the mole fraction of the absorbing gas)
$N_{0,molar}$	mol/m^3	total molar concentration of the gas (including diluent)
X	--	fraction of absorbing gas
$W(t)$	J/s	input power function (includes modulation)
W_0	J/s	peak-to-peak amplitude of the input power
δ	m^{-1}	sidewall absorption coefficient
$\mathbf{T}_{empty}$	--	optical transmission through an empty cell, measured in order to determine δ
α'	m^{-1}	total absorption constant, $\alpha' = \alpha + \delta$
λ	m	light wavelength

A.3. *Variables for material properties*

Symbol	Units (SI)	Description
ρ_0	kg/m^3	average gas density
c	m/s	speed of sound
γ	--	ratio of the specific heat at constant pressure to that at constant volume
C_P	J/(kg K)	heat capacity at constant pressure
C_V	J/(kg K)	heat capacity at constant volume
M	kg/mol	molecular weight
κ	W/(m K)	thermal conductivity
η	Pa s	viscosity
R_d	J mol^{-1} K^{-1}	gas constant (= 8.3144 J mol^{-1} K^{-1})
ν_P	--	Poisson's ratio
E	Pa	Young's modulus
σ_0	Pa	Instrinsic stress

A.4. *Acoustic variables*

Symbol	Units (SI)	Description
p	N/m^2	acoustic pressure
P_0	N/m^2	average pressure
P	N/m^2	total pressure ($P = p + P_0$)
u	m/s	acoustic velocity
U	m^3/s	volumetric acoustic velocity ($U = Su$)
ω	rad/s	radial acoustic frequency
f	1/s	acoustic frequency ($\omega = 2\pi f$)
A_j	Pa	amplitude of the *jth* normal acoustic mode in the photoacoustic cavity
$p_j(\vec{r})$	--	the envelope for the *jth* normal acoustic mode
k_z	1/m	acoustic wavevector axial value
k_r	1/m	acoustic wavevector radial value
Q_j	--	quality factor of the jth acoustic mode
E_L	J	energy dissipated per cycle
E_T	J	energy stored in the standing wave

A.5. *Circuit analogy variables*

Symbol	Units (SI)	Description
$\mathcal{R}_A$	Ns/m^5 or Ω	resistance in acoustic circuit analogy
$\mathcal{C}_A$	m^5/N or F	capacitance in acoustic circuit analogy
$\mathcal{M}_A$	kg/m^4or H	inductance in acoustic circuit analogy
$\mathcal{R}_i$	Ns/m^6 or Ω/m	incremental resistance in acoustic transmission line analogy
$\mathcal{C}_i$	m^4/N or F/m	incremental capacitance in acoustic transmission line analogy
$\mathcal{M}_i$	kg/m^5 or H/m	incremental inductance in acoustic transmission line analogy
$\mathcal{Z}_i$	Ns/m^6 or Ω/m	impedance/length of a transmission line
$\mathcal{Y}_i$	$m^3s^{-1}N^{-1}$ or $\Omega^{-1}m^{-1}$	admittance/length of a transmission line
β	1/m	propagation constant ($\beta = (Z_iY_i)^{1/2}$)
$\mathcal{Z}_c$	Ns/m^5 or Ω	characteristic impedance of the transmission line ($Z_c = (Z_i/Y_i)^{1/2}$)
Γ	--	reflection constant
$\mathcal{T}_{i,n}$	--	transmission line section
A, B	--	constants in the transmission line equations, to be solved for with boundary conditions

A.6. *Additional variables*

Symbol	Units (SI)	Description
τ_T	s	thermal damping time
d_V	m	viscous boundary layer thickness
d_H	m	thermal boundary layer thickness
T	K	temperature
t	s	time
s	--	non-dimensionalized radius
ξ	--	non-dimensionalized time
θ	--	non-dimensionalized temperature
ψ_n	--	nth basis function for non-dimensionalized temperature
k	J/K	Boltzmann constant

Appendix B : *Consistency of transmission line model*

The transmission line equations for a distributed source are given by:

$$\frac{dp(z)}{dz} = -Z_i U(z) \qquad \text{(B-1)}$$

$$\frac{dU(z)}{dz} = U_0 e^{-\alpha' z} - Y_i p(z) \qquad \text{(B-2)}$$

One can combine these expressions into one:

$$\frac{d^2 p(z)}{dz^2} = -Z_i U_0 e^{-\alpha' z} + Y_i Z_i p(z) \qquad \text{(B-3)}$$

To check if this is consistent with the established theory, consider the case where viscous and thermal losses are ignored. In this case, $Z_i = j\omega\rho_0/S$, $Y_i = j\omega S/\rho_0 c^2$ and $U_0=(\gamma-1)\alpha W/(\rho_0 c^2)$. (B-3) can therefore be rewritten as:

$$\frac{d^2 p(z)}{dz^2} - \left(\frac{j\omega S}{\rho_0 c^2}\right)\left(\frac{j\omega\rho_0}{S}\right)p(z) = -\left(\frac{j\omega\rho_0}{S}\right)\frac{(\gamma-1)\alpha W}{\rho_0 c^2} e^{-\alpha' z} \qquad \text{(B-4)}$$

which simplifies to:

$$\frac{d^2 p(z)}{dz^2} + \frac{\omega^2}{c^2} p(z) = -\frac{j\omega(\gamma-1)\alpha W}{c^2 S} e^{-\alpha' z} \qquad \text{(B-5)}$$

In the case of uniform excitation ($e^{-\alpha' z} \sim 1$), this expression matches (3-6), and so is consistent with established theory.

Appendix C : *MATLAB code for models*

C.1. *"leak_calc" function: calculating Z_{in} and Z_{out}*

```
function[Zin,Zout]= leak_calc(w,inlet,visc,gamma,c,k,dens,Cp)
%Calculates leak impedances
%input is frequency array, inlet radius (in mm), and then gas properties:
%viscosity, gamma, c, k, density, Cp

% viscous and thermal loss terms
dV = (2*visc./(dens*w)).^0.5;          %viscous boundary layer (m)
dH = (2*k./(dens*Cp*w)).^0.5;          %thermal boundary layer (m)

% inlet load impedance

   % Dimensions
   Lin = [9;2.5;7;8;80;14;14;50;50]*1e-3;
   Rin = [inlet;2.16;0.794;0.635;0.254;0.635;0.635;0.254;3.2]*1e-3;
   Sin = pi*Rin.^2;
   Din = 2*pi*Rin;

   % Properties of each line
   Ri = dens*(Din./(2*Sin.^2))*(w.*dV);
   Gi = (Din./(2*dens*c.^2))*(w.*((gamma-1)*dH));
   Li = dens./Sin;                                    %kinetic energy
inductance/length
   Ci = Sin/(dens*c^2);                               %potential energy
   Zi = Ri + j*Li*w;                                  %impedance
   Yi = j*Ci*w + Gi;                                  %admittance
   betaj = (Zi.*Yi).^0.5;                             %propagation constant (1/m)
   Zj = (Zi./Yi).^0.5;                                %char. impedance

   % Calculations for inlet, with Zin = inf at the MFC
   len = length(Lin);
   Refl = -1*exp(2*Lin(len)*betaj(len,:));
   Zlast = -Zj(len,:).*(1-Refl)./(1+Refl);
   for index = 1:(len-1)
      ind = len-index;
      Refl = exp(2*Lin(ind)*betaj(ind,:)).*((Zj(ind,:)+Zlast)./(Zj(ind,:)-
Zlast));
      Zlast = -Zj(ind,:).*(1-Refl)./(1+Refl);
      if ind==5
         Zlast = Zlast/2;
      end
   end
   Zin = Zlast;

% outlet load impedance

   % Dimensions
   Lin = [9;9]*1e-3;
```

```
Rin = [inlet;2.16]*1e-3;
Sin = pi*Rin.^2;
Din = 2*pi*Rin;

% Properties of each line
Ro = dens*(Din./(2*Sin.^2))*(w.*dV);
Go = (Din./(2*dens*c.^2))*(w.*((gamma-1)*dH));
Lo = dens./Sin;
Co = Sin/(dens*c^2);
Zo = Ro + j*Lo*w;
Yo = j*Co*w + Go;
betaj = (Zo.*Yo).^0.5;                          %propagation constant (1/m)
Zj = (Zo./Yo).^0.5;                             %char. impedance

len = length(Lin);
Zlast = 0.159*w.^2*dens/c + j*w*0.270*dens/c;  %radiation impedance

% Calculations
for index = 1:len
   ind = len-index+1;
   Refl = exp(2*Lin(ind)*betaj(ind,:)).*((Zj(ind,:)+Zlast)./(Zj(ind,:)-
Zlast));
   Zlast = -Zj(ind,:).*(1-Refl)./(1+Refl);
end
Zout = Zlast;
```

C.2. *Calculating microphone effect*

Many versions of this program were created. This version includes the full Knowles circuit model. The function Find_Zele, which calculated the impedance of the electric circuit portion of the Knowles model is described below.

```
function[Hout,Ztot] = mic(w,visc,c,dens)
%program for determining effect of microphone on signal
%input is the frequency vector, and the viscosity, speed of sound, and gas
density
%output is the transfer function and impedance vector

%Dimensions
lmicin = 2.1e-3;
rconn = 0.2e-3;
lconn = 0.1e-3;
rmic = 0.9e-3;
lmic = 1.8e-3;
Vmic = lmic.*pi.*rmic.^2;
Vmicin = lmicin.*pi.*rmic.^2;

%Element values
Rconn = (lconn.*dens./(pi*rconn.^3))*(2*w*visc/dens).^0.5;
Rmicin = ((lmicin + lmic)*dens./(pi*rmic.^3))*(2*w*visc/dens).^0.5;
Lmicin = (lmicin + lmic)*dens./(pi*rmic.^2);
Cmicin = (Vmic + Vmicin)/(dens*c.^2);

%microphone impedance innards
```

```
RK583 = 75e8*((visc*dens)/(1.86e-5*1.18))^0.5*ones(size(w));
LK583 = 1e3*dens/1.18;
CK583 = 8.8e-14;
RK582 = 1.3e8*ones(size(w));
LK582 = 2.5e3;
CK582 = 20e-14*(1.18*345^2)/(dens*c^2);
CK581 = 2.5e-14*(1.18*345^2)/(dens*c^2);
RK581 = 2.3e8*((visc*dens)/(1.86e-5*1.18))^0.5*ones(size(w));
LK581 = 2.5e3*dens/1.18;
Zele = Find_Zele(w);

Z1 = RK582 + j*w*LK582 + 1./(j*w*CK583) + Zele;
Z2 = j*w*LK583 + RK583;
Z585 = 1./((1./Z1)+(1./Z2));
Z3 = Z585 + (1./(j*w*CK582));
Z590 = 1./(j*w*CK581+(1./Z3));
Zmic = RK581 + (j*w*LK581) + Z590;

%total impedance
Z20mic = Rmicin + j*Lmicin*w + Zmic;
Z20= 1./(1./Z20mic + j*Cmicin*w);
Ztot = Z20 + Rconn;
V2_V3 = Z20./Ztot;
V1_V2 = Zmic./Z20mic;
Hout = V2_V3.*V1_V2;
```

C.2.1.1. *Find_Zele function*

```
function[Zele] = Find_Zele(w)
%Simplifies electronic portion of circuit
%Returns resistance in SI acoustic ohms

CK588 = -0.61e-12;
CK585 = 5.5e-12;
RK586 = 4e9*ones(size(w));
RK587 = 1e12*ones(size(w));
CK587 = 1.6e-12;
CK586 = 3.2e-12;
G = 0.325e-3*ones(size(w));
RK585 = 22e3*ones(size(w));
RK591 = 1e6*ones(size(w));
N = 1*((1e5)^0.5);  %turns ratio

C1 = CK585 + CK587;
R1 = 1./(1./RK586 + 1./RK587);
Z1 = 1./(1./R1 + j*w*C1);
Z2 = 1./(1./RK585 + 1./RK591);
Z588 = 1./(j*w*CK588);
Z586 = 1./(j*w*CK586);

T1 = (G + 1./Z586)./(G + 1./Z586 + 1./Z2);
Zsub = 1./(1./Z1 + 1./Z586 - T1./Z586);
Ztot = Z588 + Zsub;
Zele = Ztot*N^2;
```

C.3. *Frequency dependence*

```
%Compare frequency plot of narrow inlet, low leak, and wide cell w/ outlet
disconnected
%with better detail of inlet
%also with microphone model added
clear all;

% excitation and gas properties
W0 = 0.6366;                    %assumes peak height of 1 W( sinusoid
transfer)
alpha = 921;                    %alpha (1/m), assumes a = 10 m2/mol
visc = 8e-6;                    %viscosity (Ns/m2)
gamma = 1.124;
c = 250;                        %speed of sound (m/s)
k = 0.018;                      %thermal conductivity (W/mK)
dens = 1.796;                   %density (kg/m3)
Cp = 1.68e3;                    %heat capacity (J/kgK)
M = 44.094;
I0 = (gamma-1)*W0*alpha/(dens*c^2);
Is = (gamma-1)*W0/(dens*c^2);

% define frequency range
f = [100:10:4000];
wo = 2*pi*f;

% viscous and thermal loss terms
dVo = (2*visc./(dens*wo)).^0.5;       %viscous boundary layer (m)
dHo = (2*k./(dens*Cp*wo)).^0.5;       %thermal boundary layer (m)

% dimension arrays for std,wide,ninlet,lowlk,widestd,short,qtrwave
r_array = [0.75;1.5;0.75;1.6;1.6;1.6;1.6]*1e-3;
in_array = [0.4;0.55;0.2;0.17;0.4;0.4;0.4];
l_array = [40;40;40;40;40;20;40]*1e-3;

for index = 2:4
   l = l_array(index);              %cell length (m)
   r = r_array(index);              %cell radius (m)
   Vc = l*pi*r^2;                   %cell volume (m3)
   S = pi*r^2;                      %cell cross-sectional area (m2)
   D = 2*pi*r;                      %cross-section circumference
   inlet = in_array(index);

   for index2 = 1:length(wo)
      dV = dVo(index2);
      dH = dHo(index2);
      w = wo(index2);
      % transmission line parameters
      R = dens*w.*dV*D/(2*S^2);
      G = w.*((gamma-1)*dH)*D/(2*dens*c^2);
      L = dens/S;                          %kinetic energy inductance/length
      C = S/(dens*c^2);                    %potential energy
      Z = R + j*w*L;                       %impedance
      Y = j*w*C + G;                       %admittance
      beta = (Z.*Y).^0.5;                  %propagation constant (1/m)
      Zc = (Z./Y).^0.5;                    %char. impedance
```

```
[Zin,Zout] = leak_calc(w,inlet,visc,gamma,c,k,dens,Cp);
gunk = 17*ones(size(alpha));
alphap = alpha + gunk;
denom = alphap^2 - beta^2;
alp = alphap/denom * I0;
bet = beta/denom * I0;

%distributed calculation with microphone
[Hout, Ztot] = mic(w,visc,c,dens);
Mat(1,1) = 0;
Mat(1,2) = 0;
Mat(1,3) = (-Zc-Zout)*exp(beta*l);
Mat(1,4) = (Zc-Zout)*exp(-beta*l);
Mat(2,1) = exp(beta*l/2);
Mat(2,2) = -exp(-beta*l/2);
Mat(2,3) = -exp(beta*l/2);
Mat(2,4) = exp(-beta*l/2);
Mat(3,1) = exp(beta*l/2);
Mat(3,2) = exp(-beta*l/2);
Mat(3,3) = -(1-Zc/Ztot)*exp(beta*l/2);
Mat(3,4) = -(1+Zc/Ztot)*exp(-beta*l/2);
Mat(4,1) = Zc-Zin;
Mat(4,2) = -Zc-Zin;
Mat(4,3) = 0;
Mat(4,4) = 0;

Sol(1) = (-alphap*Zout+beta*Zc)/denom *I0*exp(-alphap*l);
Sol(2) = 0;
Sol(3) = -Zc/Ztot*bet*exp(-alphap*l/2);
Sol(4) = -Zc*bet - Zin*alp;

Mat1 = Mat;
Mat2 = Mat;
Mat1(:,1) = Sol';
Mat2(:,2) = Sol';

Al = det(Mat1)/det(Mat);
Bl = det(Mat2)/det(Mat);

V_half = -Zc*(Al*exp(beta*l/2)-Bl*exp(-beta*l/2)+bet*exp(-alphap*l/2));
Vdm(index, index2) = V_half*Hout;

% distributed calculation without microphone
Mat(1,1) = 0;
Mat(1,2) = 0;
Mat(1,3) = (-Zc-Zout)*exp(beta*l);
Mat(1,4) = (Zc-Zout)*exp(-beta*l);
Mat(2,1) = exp(beta*l/2);
Mat(2,2) = -exp(-beta*l/2);
Mat(2,3) = -exp(beta*l/2);
Mat(2,4) = exp(-beta*l/2);
Mat(3,1) = exp(beta*l/2);
Mat(3,2) = exp(-beta*l/2);
Mat(3,3) = -exp(beta*l/2);
Mat(3,4) = -exp(-beta*l/2);
Mat(4,1) = Zc-Zin;
Mat(4,2) = -Zc-Zin;
```

```
      Mat(4,3) = 0;
      Mat(4,4) = 0;

      Sol(1) = (-alphap*Zout+beta*Zc)/denom *I0*exp(-alphap*l);
      Sol(2) = 0;
      Sol(3) = 0;
      Sol(4) = -Zc*bet - Zin*alp;

      Mat1 = Mat;
      Mat2 = Mat;
      Mat1(:,1) = Sol';
      Mat2(:,2) = Sol';

      Al = det(Mat1)/det(Mat);
      Bl = det(Mat2)/det(Mat);

      V_half = -Zc*(Al*exp(beta*l/2)-Bl*exp(-beta*l/2)+bet*exp(-alphap*l/2));
      Vdnm(index, index2) = V_half;

      % localized calculation without microphone
      Refl = exp(2*beta*l).*(Zc + Zout)./(Zc - Zout);       %reflection
coeff.
      A = Is ./((1+Refl)-((Zc./Zin).*(1-Refl)));
      Vlnm (index, index2) = -Zc.*(A.*exp(beta*l/2)-A.*Refl.*exp(-beta*l/2));

      % localized calculation without microphone
      [Hout,Ztot] = mic(w,visc,c,dens);
      Refl = exp(beta*l).*(Zc + Zout)./(Zc - Zout);
      Ztrans2 = -Zc.*(1-Refl)./(1+Refl);                    %impedance
looking into line2
      Zload = 1./(1./Ztot + 1./Ztrans2);                    %load impedance
for line1
      Refl = exp(beta*l).*(Zc + Zload)./(Zc - Zload);
      Ztrans = -Zc.*(1-Refl)./(1+Refl);
      V0 = Is*1./(1./Zin + 1./Ztrans);                      %pressure at x=0
      Vlm(index,index2) = (V0.*(exp(beta*l/2)-Refl.*exp(-beta*l/2))./(1-
Refl)).*Hout;

      end
end

FID = fopen('distmicout.txt','w');
Data =
[f;abs(Vdm(3,:));angle(Vdm(3,:))*360/(2*pi);abs(Vdm(4,:));angle(Vdm(4,:))*360
/(2*pi);abs(Vdm(2,:));angle(Vdm(2,:))*360/(2*pi)];
fprintf(FID,'%d\t%12.8f\t%3.1f\t%12.8f\t%3.1f\t%12.8f\t%3.1f\n',Data)
fclose(FID);

FID = fopen('distnomicout.txt','w');
Data =
[f;abs(Vdnm(3,:));angle(Vdnm(3,:))*360/(2*pi);abs(Vdnm(4,:));angle(Vdnm(4,:))
*360/(2*pi);abs(Vdnm(2,:));angle(Vdnm(2,:))*360/(2*pi)];
fprintf(FID,'%d\t%12.8f\t%3.1f\t%12.8f\t%3.1f\t%12.8f\t%3.1f\n',Data)
fclose(FID);

FID = fopen('locmicout.txt','w');
```

```
Data =
[f;abs(Vlm(3,:));angle(Vlm(3,:))*360/(2*pi);abs(Vlm(4,:));angle(Vlm(4,:))*360
/(2*pi);abs(Vlm(2,:));angle(Vlm(2,:))*360/(2*pi)];
fprintf(FID,'%d\t%12.8f\t%3.1f\t%12.8f\t%3.1f\t%12.8f\t%3.1f\n',Data)
fclose(FID);

FID = fopen('locnomicout.txt','w');
Data =
[f;abs(Vlnm(3,:));angle(Vlnm(3,:))*360/(2*pi);abs(Vlnm(4,:));angle(Vlnm(4,:))
*360/(2*pi);abs(Vlnm(2,:));angle(Vlnm(2,:))*360/(2*pi)];
fprintf(FID,'%d\t%12.8f\t%3.1f\t%12.8f\t%3.1f\t%12.8f\t%3.1f\n',Data)
fclose(FID);
```

C.4. *Concentration dependence*

```
clear all;

freq = input('Enter frequency: ');
w = 2*pi*freq;

% gas properties
alpha0 = 921;                   %alpha (1/m), assumes a = 10 m2/mol
visc_C3H8 = 8e-6;               %viscosity (Ns/m2)
visc_N2 = 1.78e-5;
gamma_C3H8 = 1.124;
gamma_N2 = 1.4;
c_C3H8 = 250;                   %speed of sound (m/s)
c_N2 = 353;
k_C3H8 = 0.018;                 %thermal conductivity (W/mK)
k_N2 = 0.026;
dens_C3H8 = 1.796;              %density (kg/m3)
dens_N2 = 1.123;
Cp_C3H8 = 1.68e3;               %heat capacity (J/kgK)
Cp_N2 = 1.04e3;
M_C3H8 = 44.094 * 1e-3;         %molecular weight (kg/mol)
M_N2 = 28.013 * 1e-3;
Rd = 8.3144;                    %gas constant (J/molK)
s12 =
(1/(8*(1+M_N2/M_C3H8)))^0.5*(1+(visc_N2/visc_C3H8)^0.5*(M_C3H8/M_N2)^0.25)^2;
s21 =
(1/(8*(1+M_C3H8/M_N2)))^0.5*(1+(visc_C3H8/visc_N2)^0.5*(M_N2/M_C3H8)^0.25)^2;

% gas property arrays
conc = [0:0.01:1];               % concentration range
alphaM = alpha0*conc;
densM = dens_N2+(dens_C3H8 - dens_N2)*conc;
viscM = ((1-conc).*visc_N2./((1-conc)+conc*s12))+(conc.*visc_C3H8./(conc+(1-
conc)*s21));
kM = ((1-conc).*k_N2./((1-conc)+conc*s12))+(conc.*k_C3H8./(conc+(1-
conc)*s21));
MM = M_N2+(M_C3H8 - M_N2)*conc;

CpM = kM./viscM - ((5/4)*(Rd*ones(size(conc))./MM));
CvM = CpM - (Rd*ones(size(conc))./MM);
gammaM = CpM./CvM;
cM = ((gammaM*101.325e3)./densM).^0.5;
```

```
% current source
W0 = 0.6366;                        %assumes square wave height of 1 W( sinusoid
transfer)
I0M = (gammaM-1).*alphaM.*W0./(densM.*cM.^2);
IsM = (gammaM-1).*W0./(densM.*cM.^2);

% viscous and thermal loss terms
dVo = (2*viscM./(densM*w)).^0.5;        %viscous boundary layer (m)
dHo = (2*kM./(densM.*CpM*w)).^0.5;        %thermal boundary layer (m)

% dimension arrays for std,wide,ninlet,lowlk,widestd,short,qtrwave
r_array = [0.75;1.5;0.75;1.6;1.6;1.6;1.6]*1e-3;
in_array = [0.4;0.55;0.2;0.17;0.4;0.4;0.4];
l_array = [40;40;40;40;40;20;40]*1e-3;
gunk_array = [0;20;15;25;0;0;0];

for index = 2:4
   l = l_array(index);              %cell length (m)
   r = r_array(index);              %cell radius (m)
   Vc = l*pi*r^2;                   %cell volume (m3)
   S = pi*r^2;                      %cell cross-sectional area (m2)
   D = 2*pi*r;                      %cross-section circumference
   inlet = in_array(index);

   for index2 = 1:length(conc)
      dV = dVo(index2);
      dH = dHo(index2);
      I0 = I0M(index2);
      alpha = alphaM(index2);
      dens = densM(index2);
      visc = viscM(index2);
      k = kM(index2);
      Cp = CpM(index2);
      gamma = gammaM(index2);
      c = cM(index2);
      % transmission line parameters
      R = dens*w.*dV*D/(2*S^2);
      G = w.*((gamma-1)*dH)*D/(2*dens*c^2);
      L = dens/S;                          %kinetic energy inductance/length
      C = S/(dens*c^2);                    %potential energy
      Z = R + j*w*L;                       %impedance
      Y = j*w*C + G;                       %admittance
      beta = (Z.*Y).^0.5;                  %propagation constant (1/m)
      Zc = (Z./Y).^0.5;                    %char. impedance
      [Zin,Zout] = leak_calc(w,inlet,visc,gamma,c,k,dens,Cp);
      gunk = gunk_array(index);
      alphap = alpha + gunk;
      denom = alphap^2 - beta^2;
      alp = alphap/denom * I0;
      bet = beta/denom * I0;

      %calculation with microphone
      [Hout, Ztot] = mic(w,visc,c,dens);
      Mat(1,1) = 0;
      Mat(1,2) = 0;
      Mat(1,3) = (-Zc-Zout)*exp(beta*l);
      Mat(1,4) = (Zc-Zout)*exp(-beta*l);
```

```
Mat(2,1) = exp(beta*l/2);
Mat(2,2) = -exp(-beta*l/2);
Mat(2,3) = -exp(beta*l/2);
Mat(2,4) = exp(-beta*l/2);
Mat(3,1) = exp(beta*l/2);
Mat(3,2) = exp(-beta*l/2);
Mat(3,3) = -(1-Zc/Ztot)*exp(beta*l/2);
Mat(3,4) = -(1+Zc/Ztot)*exp(-beta*l/2);
Mat(4,1) = Zc-Zin;
Mat(4,2) = -Zc-Zin;
Mat(4,3) = 0;
Mat(4,4) = 0;

Sol(1) = (-alphap*Zout+beta*Zc)/denom *I0*exp(-alphap*l);
Sol(2) = 0;
Sol(3) = -Zc/Ztot*bet*exp(-alphap*l/2);
Sol(4) = -Zc*bet-Zin*alp;

Mat1 = Mat;
Mat2 = Mat;
Mat1(:,1) = Sol';
Mat2(:,2) = Sol';

Al = det(Mat1)/det(Mat);
Bl = det(Mat2)/det(Mat);

V_half = -Zc*(Al*exp(beta*l/2)-Bl*exp(-beta*l/2)+bet*exp(-alphap*l/2));
Vout(index, index2) = V_half*Hout;

%calculation without microphone
Mat(1,1) = 0;
Mat(1,2) = 0;
Mat(1,3) = (-Zc-Zout)*exp(beta*l);
Mat(1,4) = (Zc-Zout)*exp(-beta*l);
Mat(2,1) = exp(beta*l/2);
Mat(2,2) = -exp(-beta*l/2);
Mat(2,3) = -exp(beta*l/2);
Mat(2,4) = exp(-beta*l/2);
Mat(3,1) = exp(beta*l/2);
Mat(3,2) = exp(-beta*l/2);
Mat(3,3) = -exp(beta*l/2);
Mat(3,4) = -exp(-beta*l/2);
Mat(4,1) = Zc-Zin;
Mat(4,2) = -Zc-Zin;
Mat(4,3) = 0;
Mat(4,4) = 0;

Sol(1) = (-alphap*Zout+beta*Zc)/denom *I0*exp(-alphap*l);
Sol(2) = 0;
Sol(3) = 0;
Sol(4) = -Zc*bet - Zin*alp;

Mat1 = Mat;
Mat2 = Mat;
Mat1(:,1) = Sol';
Mat2(:,2) = Sol';
```

```
        Al = det(Mat1)/det(Mat);
        Bl = det(Mat2)/det(Mat);

        V_half = -Zc*(Al*exp(beta*l/2)-Bl*exp(-beta*l/2)+bet*exp(-alphap*l/2));
        Vold(index, index2) = V_half;

        %calc w/o mic or gunk
        gunk = 0*ones(size(alpha));
        alphap = alpha + gunk;
        denom = alphap^2 - beta^2;
        alp = alphap/denom * I0;
        bet = beta/denom * I0;
        Mat(1,1) = 0;
        Mat(1,2) = 0;
        Mat(1,3) = (-Zc-Zout)*exp(beta*l);
        Mat(1,4) = (Zc-Zout)*exp(-beta*l);
        Mat(2,1) = exp(beta*l/2);
        Mat(2,2) = -exp(-beta*l/2);
        Mat(2,3) = -exp(beta*l/2);
        Mat(2,4) = exp(-beta*l/2);
        Mat(3,1) = exp(beta*l/2);
        Mat(3,2) = exp(-beta*l/2);
        Mat(3,3) = -exp(beta*l/2);
        Mat(3,4) = -exp(-beta*l/2);
        Mat(4,1) = Zc-Zin;
        Mat(4,2) = -Zc-Zin;
        Mat(4,3) = 0;
        Mat(4,4) = 0;

        Sol(1) = (-alphap*Zout+beta*Zc)/denom *I0*exp(-alphap*l);
        Sol(2) = 0;
        Sol(3) = 0;
        Sol(4) = -Zc*bet - Zin*alp;

        Mat1 = Mat;
        Mat2 = Mat;
        Mat1(:,1) = Sol';
        Mat2(:,2) = Sol';

        Al = det(Mat1)/det(Mat);
        Bl = det(Mat2)/det(Mat);

        V_half = -Zc*(Al*exp(beta*l/2)-Bl*exp(-beta*l/2)+bet*exp(-alphap*l/2));
        Vcln(index, index2) = V_half;
    end
end

figure(1);
plot(conc,abs(Vout(2,:)),'k-',conc,abs(Vout(3,:)),'m-
',conc,abs(Vout(4,:)),'c-
',conc,abs(Vold(2,:)),'k:',conc,abs(Vold(3,:)),'m:',conc,abs(Vold(4,:)),'c:')
legend('Wide, with mic','Narrow Inlet, with mic','Low Leak, with mic','Wide,
without mic','Narrow Inlet, without mic','Low Leak, without mic');
xlabel('Concentration');
ylabel('Signal Magnitude (Pa/W)');

figure(2);
```

```
plot(conc,abs(Vcln(2,:)),'k-',conc,abs(Vcln(3,:)),'m-
',conc,abs(Vcln(4,:)),'c-
',conc,abs(Vold(2,:)),'k:',conc,abs(Vold(3,:)),'m:',conc,abs(Vold(4,:)),'c:')
xlabel('Concentration');
ylabel('Signal Magnitude (Pa/W)');

FID = fopen('micout.txt','w');
Data =
[conc;abs(Vout(3,:));angle(Vout(3,:))*360/(2*pi);abs(Vout(4,:));angle(Vout(4,
:))*360/(2*pi);abs(Vout(2,:));angle(Vout(2,:))*360/(2*pi)];
fprintf(FID,'%d\t%12.8f\t%3.1f\t%12.8f\t%3.1f\t%12.8f\t%3.1f\n',Data)
fclose(FID);

FID = fopen('cleanout.txt','w');
Data =
[conc;abs(Vcln(3,:));angle(Vcln(3,:))*360/(2*pi);abs(Vcln(4,:));angle(Vcln(4,
:))*360/(2*pi);abs(Vcln(2,:));angle(Vcln(2,:))*360/(2*pi)];
fprintf(FID,'%d\t%12.8f\t%3.1f\t%12.8f\t%3.1f\t%12.8f\t%3.1f\n',Data)
fclose(FID);

FID = fopen('nomicout.txt','w');
Data =
[conc;abs(Vold(3,:));angle(Vold(3,:))*360/(2*pi);abs(Vold(4,:));angle(Vold(4,
:))*360/(2*pi);abs(Vold(2,:));angle(Vold(2,:))*360/(2*pi)];
fprintf(FID,'%d\t%12.8f\t%3.1f\t%12.8f\t%3.1f\t%12.8f\t%3.1f\n',Data)
fclose(FID);
```

Appendix D : *Temperature calculation*

The equation governing the temperature inside a cylinder with homogeneous heat generation is given by:

$$\kappa \frac{1}{r}\frac{\partial}{\partial r}\left(r\frac{\partial T}{\partial r}\right)+H=\rho_0 C_P\frac{\partial T}{\partial t} \qquad \textbf{(D-1)}$$

In the "worst case" scenario of complete absorption and steady illumination the value of H is given by:

$$H=\frac{W_0}{V_C} \qquad \textbf{(D-2)}$$

One can non-dimensionalize (D-1) with the following substitutions:

$$s=\frac{r}{R} \qquad \textbf{(D-3)}$$

$$\xi=\frac{t}{\left(\frac{\rho_0 C_P R^2}{\kappa}\right)} \qquad \textbf{(D-4)}$$

$$\theta=\frac{T-T_0}{\left(\frac{HR^2}{\kappa}\right)} \qquad \textbf{(D-5)}$$

This results in the following simplified expression:

$$\frac{1}{s}\frac{\partial}{\partial s}\left(s\frac{\partial \theta}{\partial s}\right)+1=\frac{\partial \theta}{\partial \xi}$$
$$\frac{\partial \theta(0,\xi)}{\partial s}=0 \quad \theta(1,\xi)=0 \quad \theta(s,0)=0 \qquad \textbf{(D-6)}$$

The boundary conditions for our model are the requirement of symmetry, that the walls are at room temperature (T_0), and that everything is at room temperature at t = 0. The non-dimensionalization can give us some insight into the temperature at the center of the cell without even solving (D-6). For example, (D-4) shows that the scale for t is the thermal damping time discussed in 3.1.2.1 (without a factor of 2). For 100% propane, τ_T is 50 ms for carbon dioxide

and 94 ms for propane. (D-5) tells us that the value of the peak temperature increase will be of order HR^2/κ, which for the wider brass cells (R = 1.5 mm) with a 1 mW light source and 100% propane is equal to 1.6 K. This implies that the temperature increase is negligible for our system.

One could confirm this by applying the Finite Fourier Transform method [180] to solve (D-6). In this method, the function is written as the sum of basis functions, which are Bessel functions for cylindrical coordinates.

$$\theta(s,\varsigma)=\sum_{n=1}^{\infty}\theta_n(\xi)\psi_n(s) \qquad \textbf{(D-7)}$$

$$\psi_n(s)=\sqrt{2}\frac{J_0(\lambda_n s)}{J_1(\lambda_n)} \qquad \textbf{(D-8)}$$

where λ_n is given by $J_0(\lambda_n)=0$

θ_n is defined such that $\theta_n(\xi)=\int_0^1\phi_n(s)\theta(s,\xi)sds$ **(D-9)**

We can solve for $\theta_n(\xi)$ by transforming (D-6) by multiplying by the basis function and integrating over 0 to 1. This yields:

$$\frac{d\theta_n}{d\xi}+\lambda_n^2\theta_n=\sqrt{2} \qquad \textbf{(D-10)}$$

Solving for (D-10) and plugging the result back into (D-7), the expression for the temperature in the cell is given by:

$$\theta(s,\xi)=2\sum_{n=1}^{\infty}\frac{\left(1-e^{-\lambda_n^2\tau}\right)J_0(\lambda_n s)}{\lambda_n^2 J_1(\lambda_n)} \qquad \textbf{(D-11)}$$

We can evaluate this in the case of large ξ and $s = 0$ (the center of the cylinder):

$$\theta(0,\infty)\approx 2\left(\frac{1}{(2.4^2)(0.52)}+\frac{1}{(5.5^2)(-0.34)}+\frac{1}{(8.65^2)(0.27)}+..\right)\approx 0.55 \qquad \textbf{(D-12)}$$

So the maximum temperature increase in the case of continuous illumination is (0.55)(1.6K) or 0.88 K. This temperature increase is indeed negligible in the calculation of average pressure.

Appendix E : *MFC calibrations*

The mass flow controllers (MFCs) were calibrated using bubble tests. In this method, the gas line is fed into the bottom of a gradated cylinder just above a rubber sac filled with soapy water. By squeezing the sac one generates soap bubbles that then move up the column, pushed by the flow. A data point at each flow setting x_i requires two measurements: the volume ΔV_i and the time Δt_i, and the flow rate, F_i, is taken as the ration $\Delta V_i/\Delta t_i$. It is assumed that the flow rate is linear with MFC setting for the range of 5-100. The data from each set of measurements was fit to a line with the method of least squares [181]. The linear correlation was then later used in determining the gas composition of the photoacoustic measurements. The error in the linear correlation was determined from the standard deviation, σ, of the data from the linear model.

The use of this standard deviation in the calculation of the error in gas composition is described further in Appendix J. The following plots show the results of the bubble tests, along with the linear fit. As can be seen from the R^2 values, the flow behavior of the MFCs was quite linear. The dotted lines on the plots show $\pm 2\sigma$. Table E-1 summarizes the calibration results.

gas	controller	slope of fit	fit intercept	σ
C_3H_8	"50 sccm C_3H_8"	0.3300	1.4133	0.3538
C_3H_8	"5 sccm C_3H_8"	0.0534	-0.0376	0.0568
100 ppm C_3H_8 in N_2	"5 sccm C_3H_8"	0.1692	-0.0252	0.0897
N_2	"5 sccm CO_2"	0.0700	-0.0389	0.0620
N_2	"50 sccm CO_2"	0.7145	-0.3329	0.3359
CO_2	"50 sccm CO_2"	0.5486	0.1183	0.6736

Table E-1: Summary of MFC calibration results (units in mL/min)

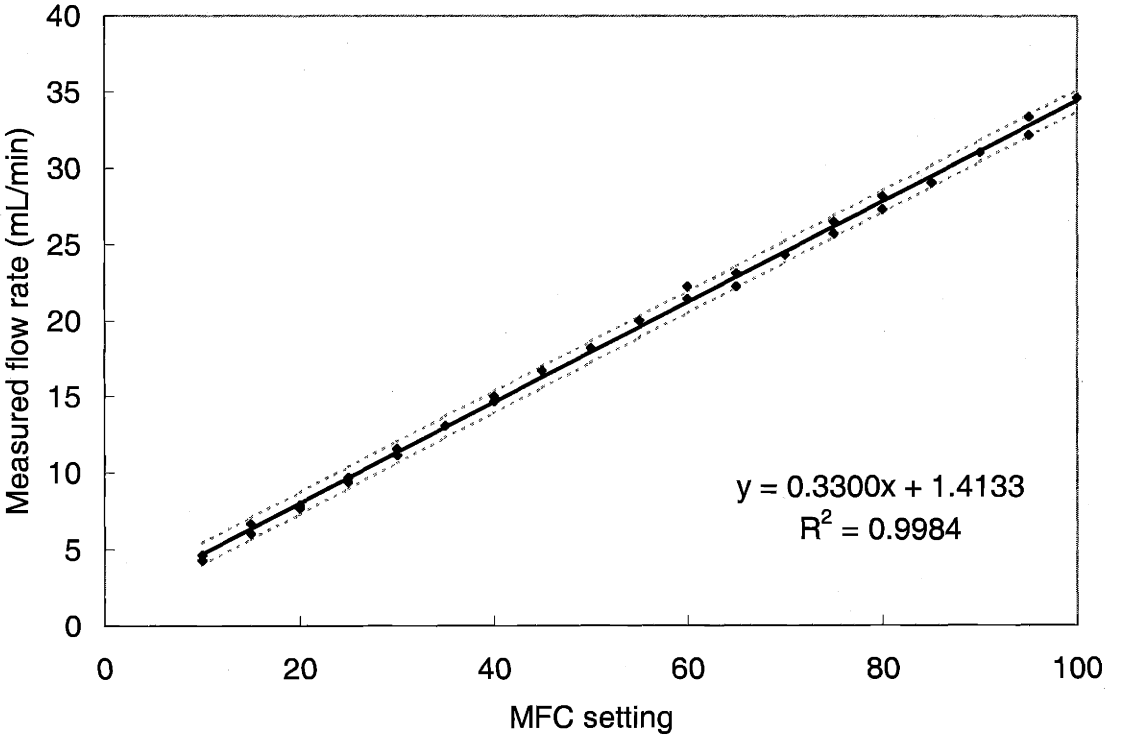

Figure E-1: C_3H_8 on "50 sccm C_3H_8" MFC

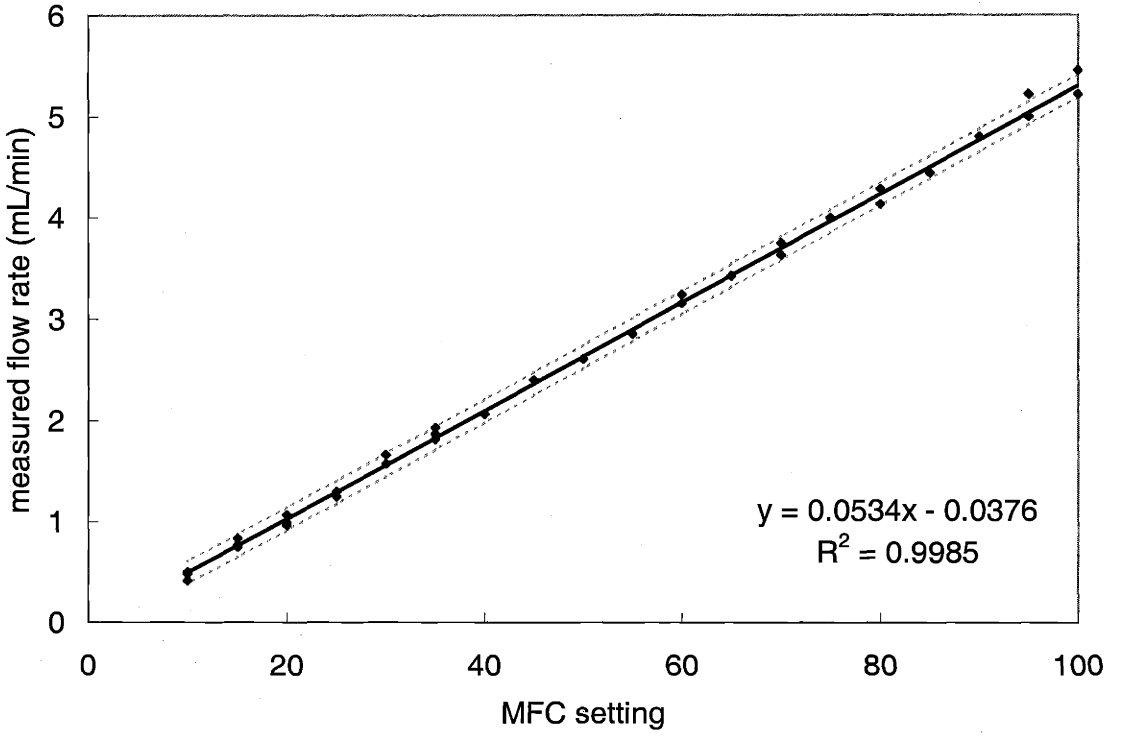

Figure E-2: C_3H_8 on "5 sccm C_3H_8" MFC

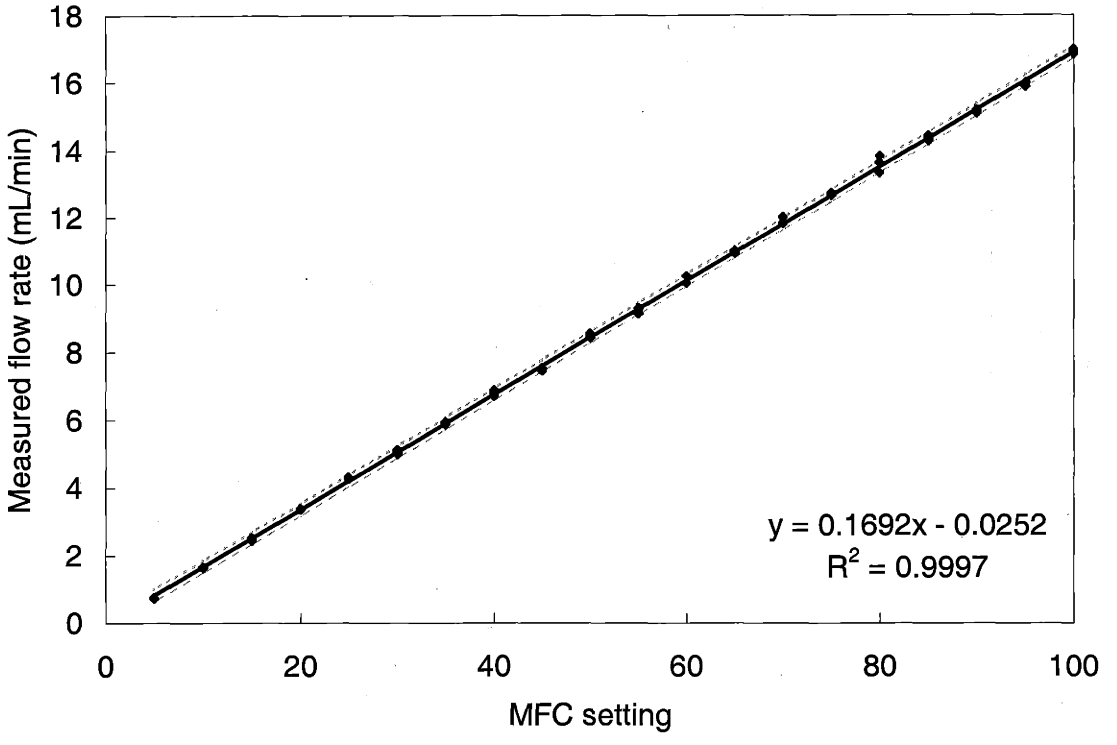

Figure E-3: 100 ppm C_3H_8 in N_2 on "5 sccm C3H8" MFC

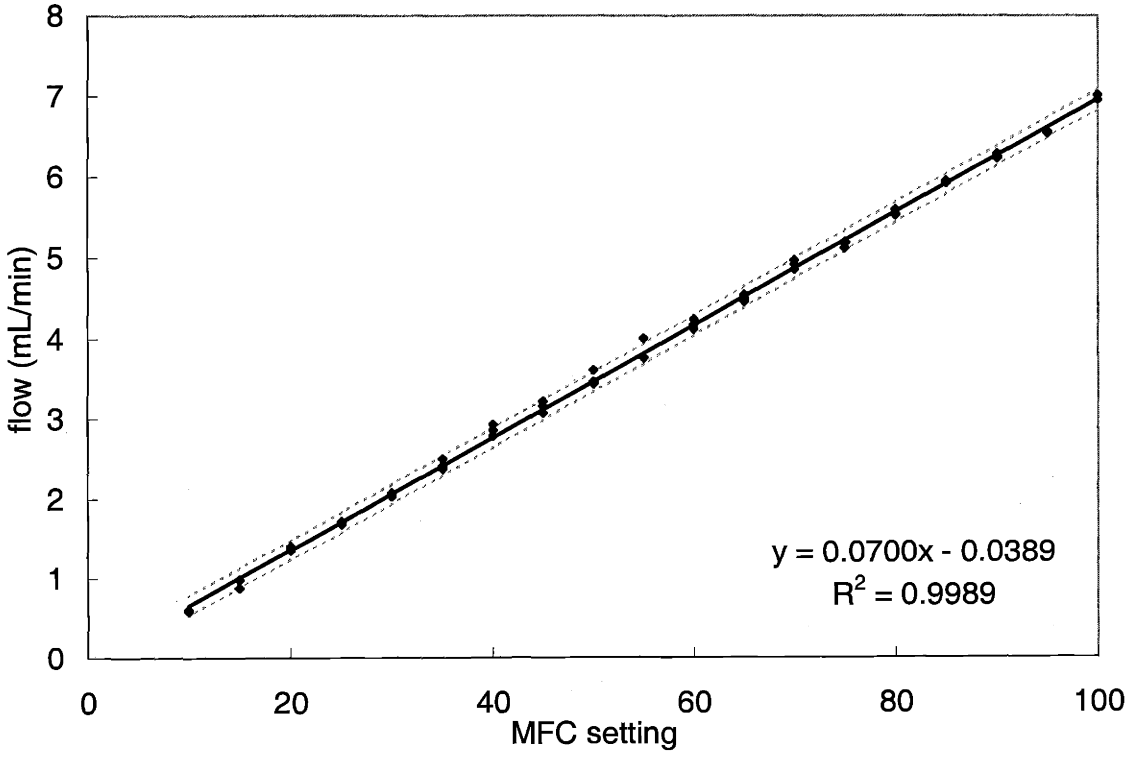

Figure E-4: N_2 on "5 sccm CO_2" controller

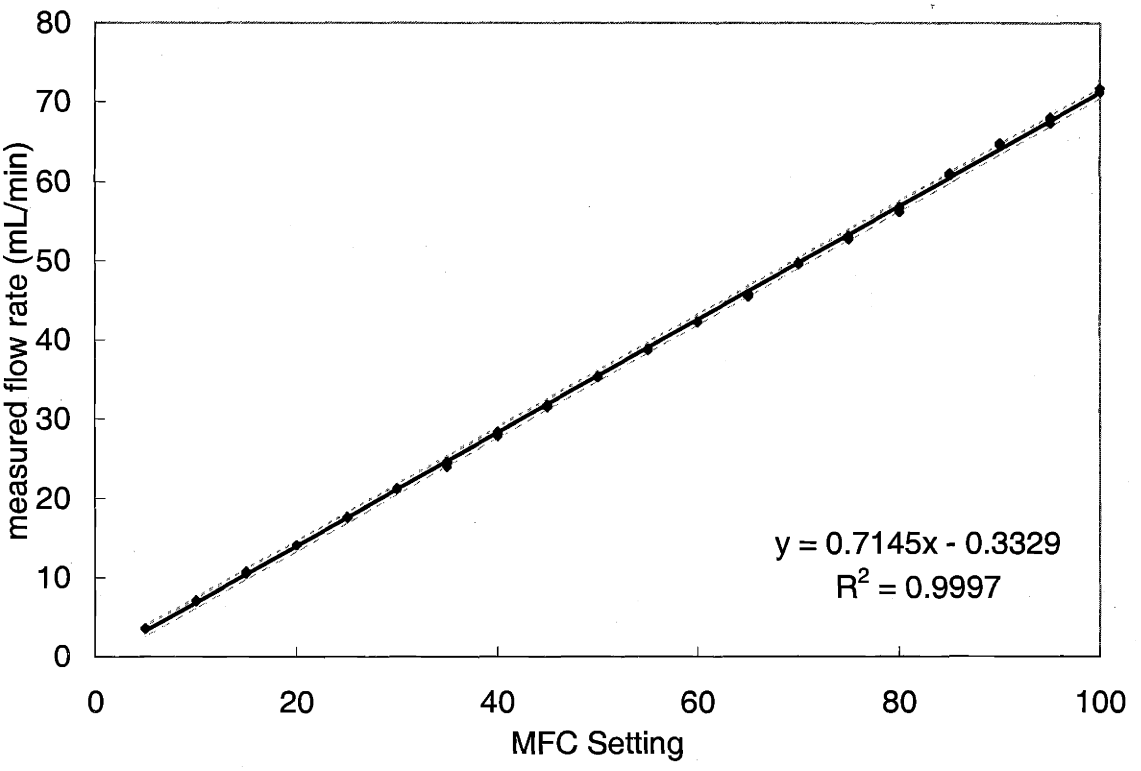

Figure E-5: N_2 on "50 sccm CO_2" controller

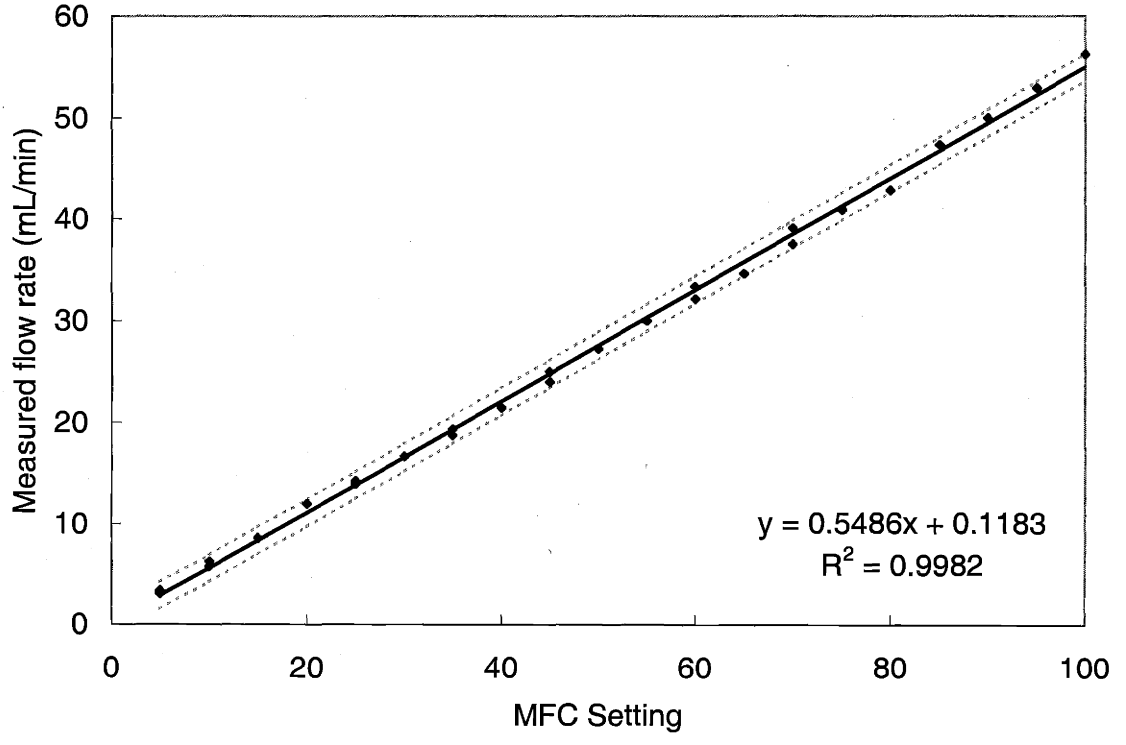

Figure E-6: CO_2 on "50 sccm CO_2" controller

Appendix F : *AutoCAD cell drawings*

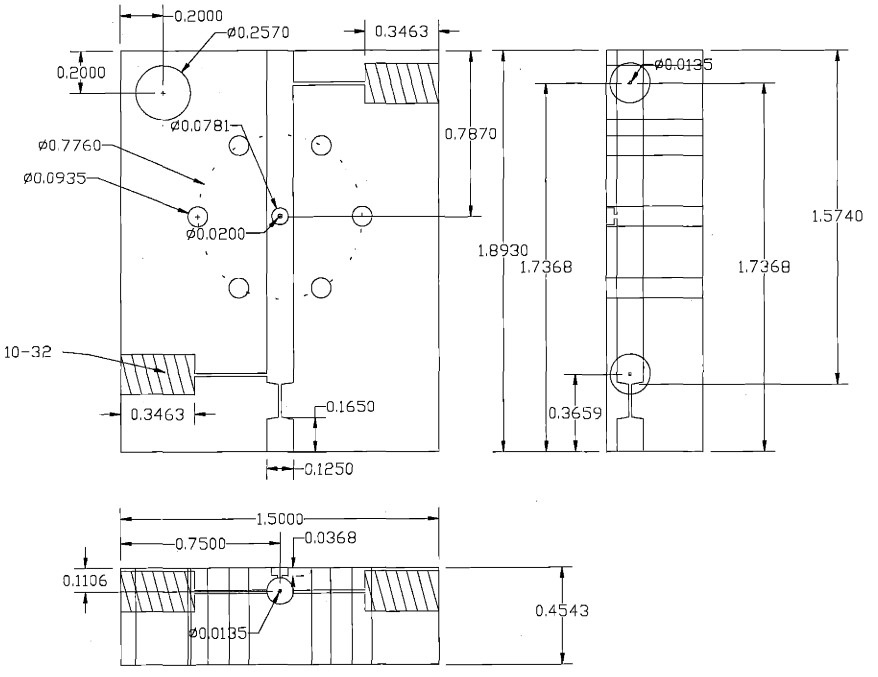

Figure F-1: WSL cell (dimensions in inches)

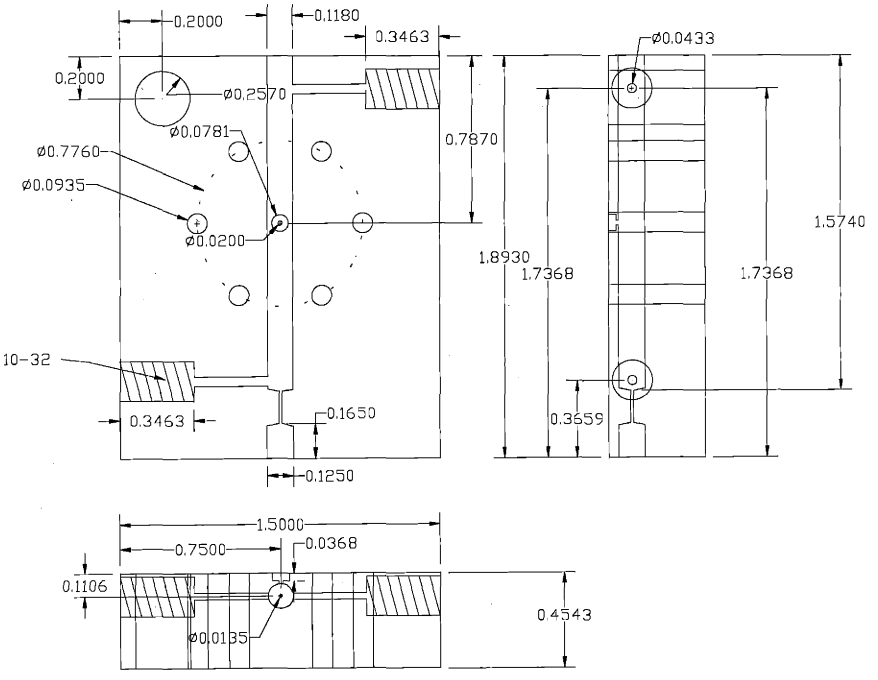

Figure F-2: WBL cell (dimensions in inches)

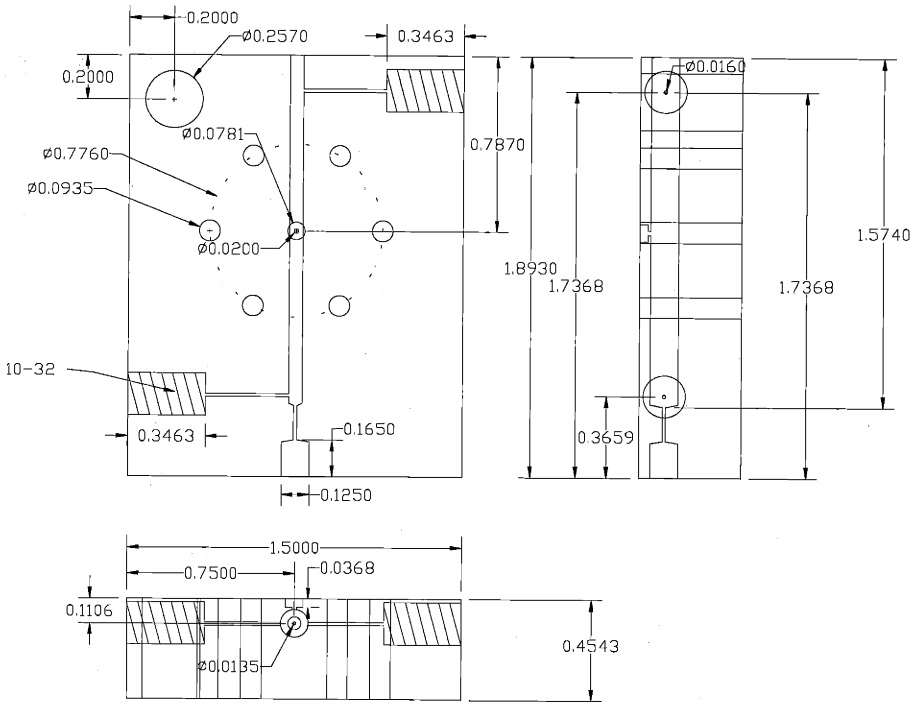

Figure F-3: NSL cell (dimensions in inches)

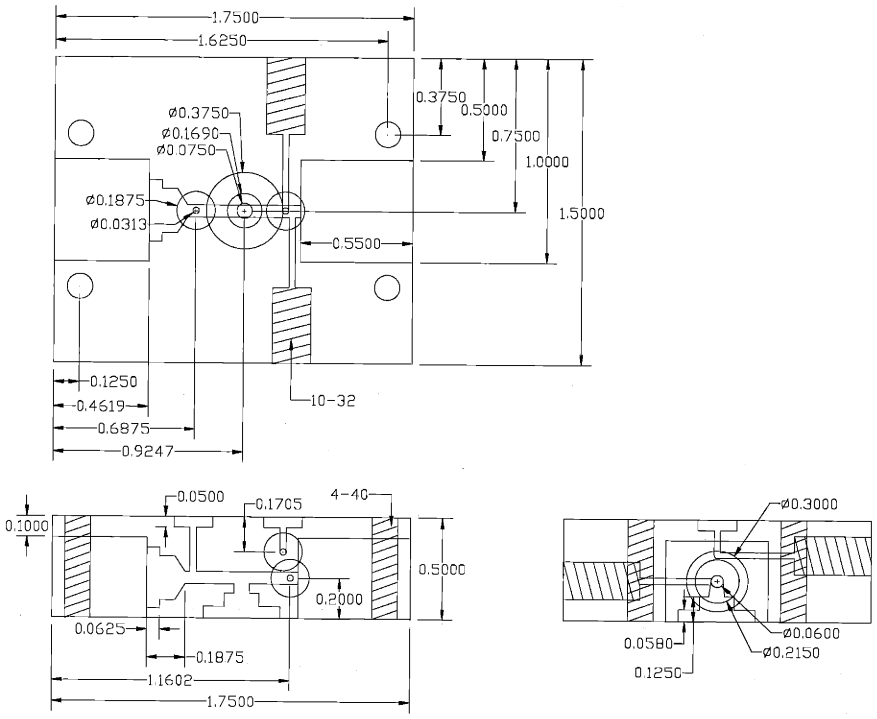

Figure F-4: diode cell

Appendix G : *Microphone calibration*

G.1. *Fixture design*

The calibration tube at the University of Florida requires that the fixture be mounted into a 1-inch cylinder, with a flange 0.5 inches from the end. This design is meant to satisfy both the requirements of the calibration apparatus and also allow a low dead volume connection to the brass cells. My design has three parts. Part 1 is the main mounting block, which holds the microphone. Parts 2 and 3 held the microphone and electrical socket in place.

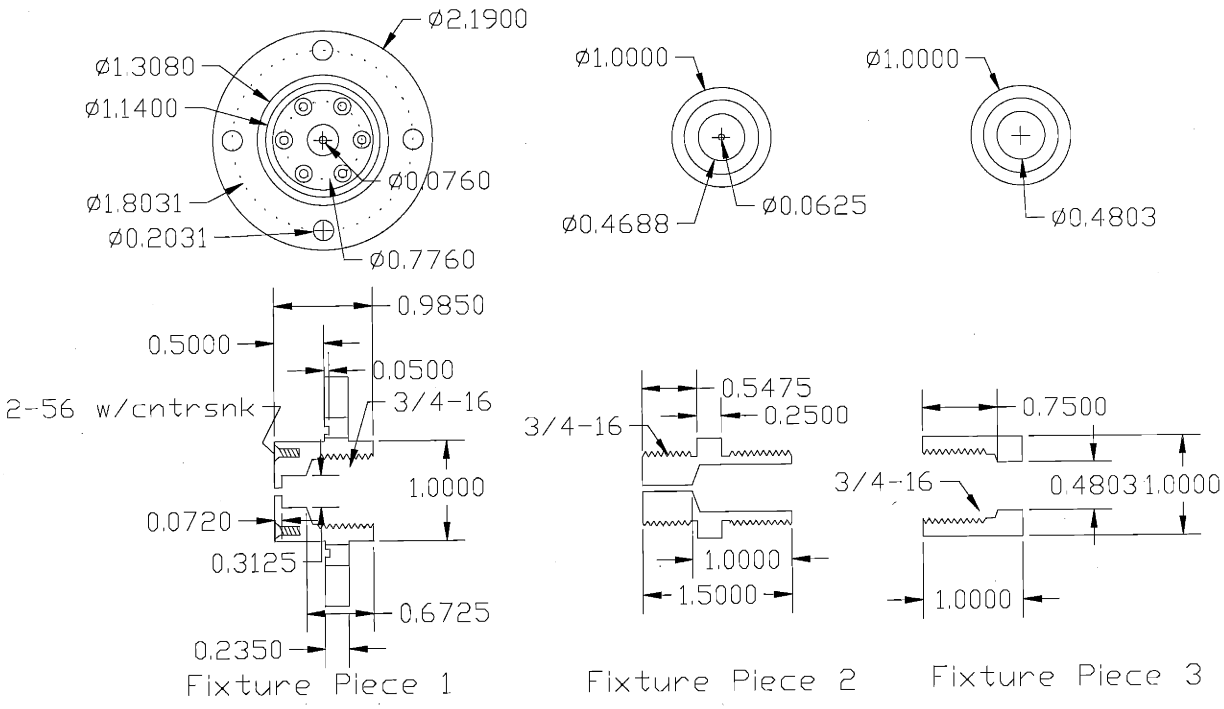

Figure G-1: AutoCAD drawing of microphone fixture

In assembly, I place a small ring of silly putty (recommended by Prof. Sheplak at the University of Florida as an inexpensive and readily available acoustic putty) around the "snout" of the microphone, after soldering wire-wrap wire to the microphone contacts. I then insert the microphone into the part, pushing its snout into the small center hole where it will make contact to the outside world. The length of the center hole was tailored in the shop so that the snout was

flush with the fixture head. I packed silly putty in behind the part, and drew the wires out and through the narrow hole in part 2. Then I screwed part 2 into part 1, which stabilized the microphone and insured hermeticity (because of the putty) between the microphone and the fixture. I then stripped the thin wire leads and soldered them to an S-video cable socket. Part 3 was designed to fit the socket. Screwing part 3 down onto part 2 securely held the socket in place.

G.2. *Calibration results*

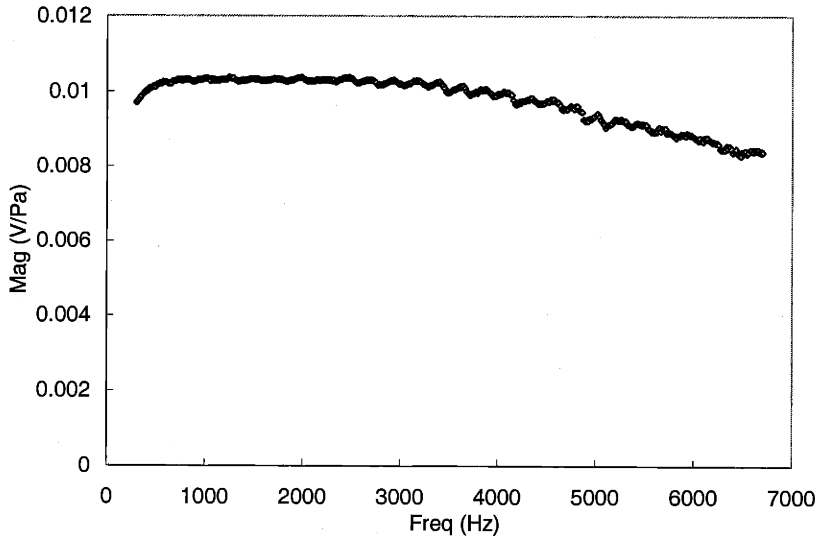

Figure G-2: Packaged microphone frequency response

Figure G-2 shows the measured frequency response for the packaged microphone used for the brass cell experiments. The microphone was used in three types of tests: frequency tests in the range of 400-4000 Hz, frequency tests in the range of 100-400 Hz, and concentration scans at a single frequency. Figure G-3 shows the calibration in the region of 400-4000 Hz, along with the 6th-order polynomial fit that was used for converting the voltage data into a pressure response, which had the equation:

$$S_{mic} = -8.175\times10^{-24} f^6 + 1.281\times10^{-19} f^5 - 8.030\times10^{-16} f^4 + 2.531\times10^{-12} f^3 - 4.211\times10^{-9} f^2 + 3.492\times10^{-6} f + 9.194\times10^{-3} \quad \text{(G-1)}$$

The standard deviation for this fit is 0.04531 mV/Pa.

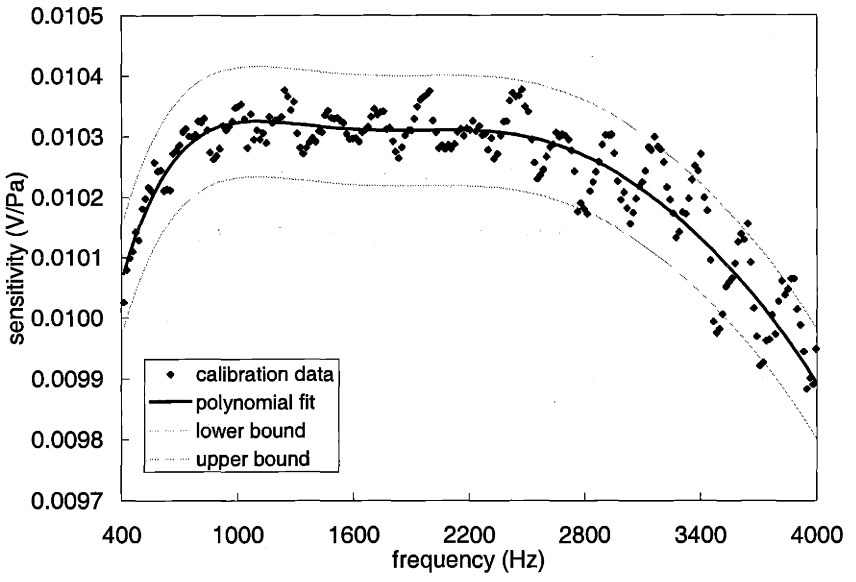

Figure G-3: Calibration for 400-4000 Hz range, with polynomial fit

A few data points were taken at frequencies between 100 and 300 Hz, for which there was no calibration information. For these frequencies, the calibration was taken from an extrapolation of the data between 300 and 1000 Hz, as is shown in Figure G-4.

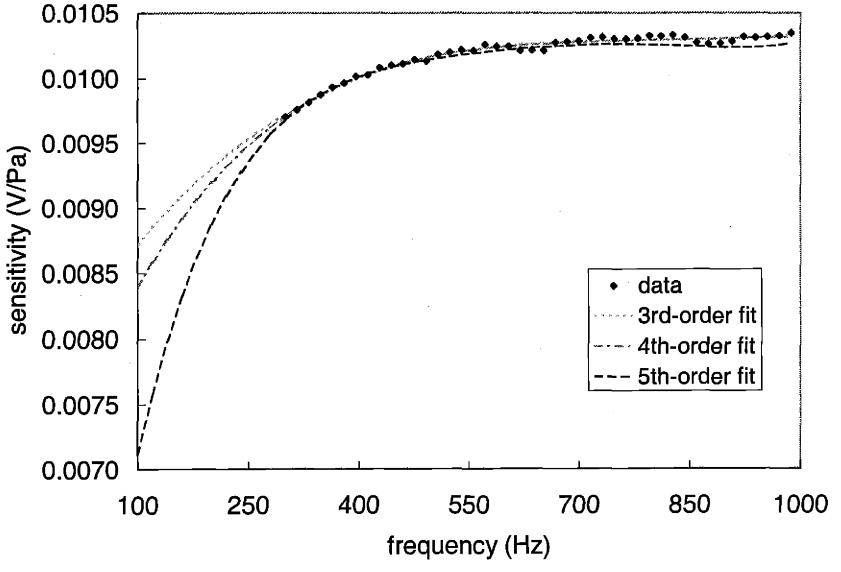

Figure G-4: Extrapolation of fit to low frequency data

The data could be fit equally well (R^2 ~0.98) with a 3rd, 4th, or 5th order polynomial. The sixth-order fit that was used for the data from 400 to 1000 Hz resulted in an unreasonable extrapolation prediction for the low-frequency response (it predicted a local maxima at 200 Hz). I used the average of the 3rd and 5th order models to determine the extrapolation, given by:

$$S_{mic} = \begin{aligned} & 2.326\times10^{-17} f^5 - 7.770\times10^{-14} f^4 + 1.052\times10^{-10} f^3 \\ & - 7.383\times10^{-8} f^2 + 2.758\times10^{-5} f + 5.804\times10^{-3} \end{aligned} \quad \text{(G-2)}$$

The error for the fit between 100 and 300 Hz was approximated by the boundaries of the 3rd and 5th order models, resulting in an estimated value of σ_S of:

$$"\sigma_S"\big|_{100<f<300} = \begin{aligned} & -1.163\times10^{-17} f^5 + 3.885\times10^{-14} f^4 - 5.024\times10^{-11} f^3 \\ & + 3.133\times10^{-8} f^2 - 9.367\times10^{-6} f + 1.099\times10^{-3} \end{aligned} \quad \text{(G-3)}$$

The standard deviation of the fit for the data from 300 to 400 Hz was 0.028 mV/Pa. Figure G-5 shows a plot of these extrapolation and its bounds. This extrapolation naturally results in a large error, and was only used for a small fraction of the data.

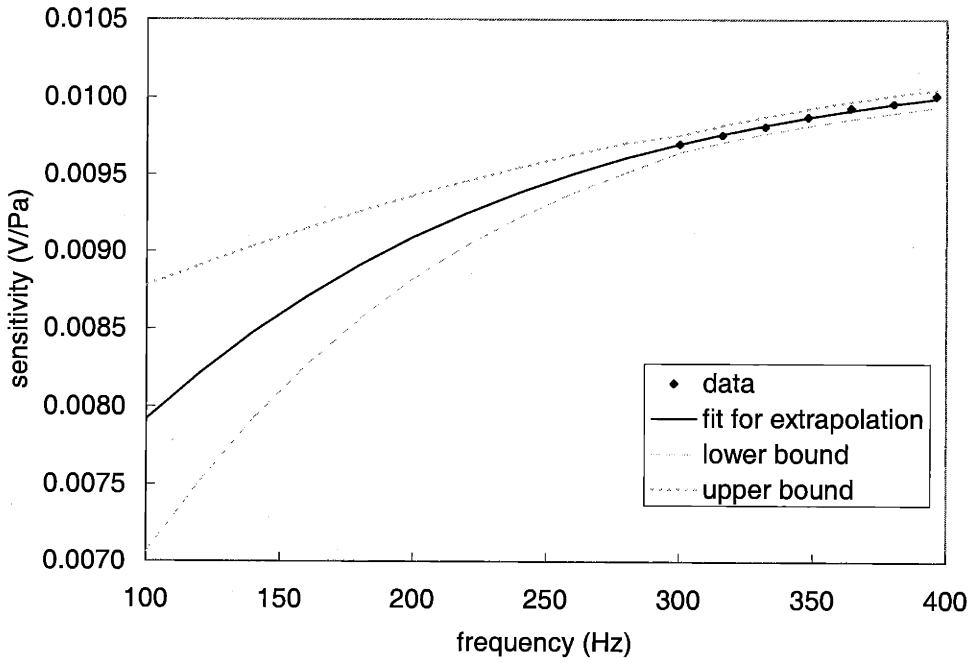

Figure G-5: Fit for extrapolation of low frequency

Appendix H : *Masks for μPA process*

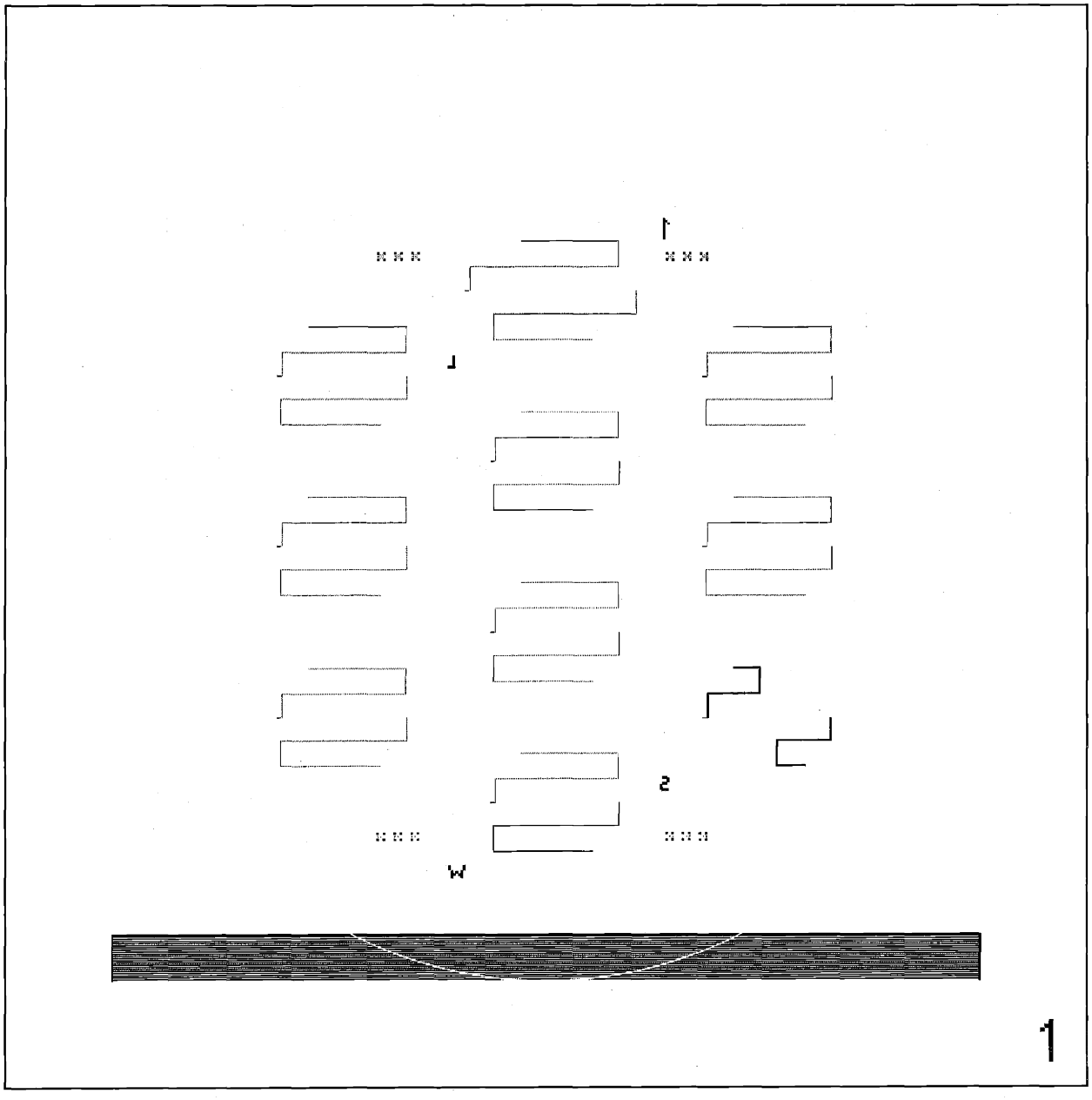

Figure H-1: Flow channel mask (inverted field)

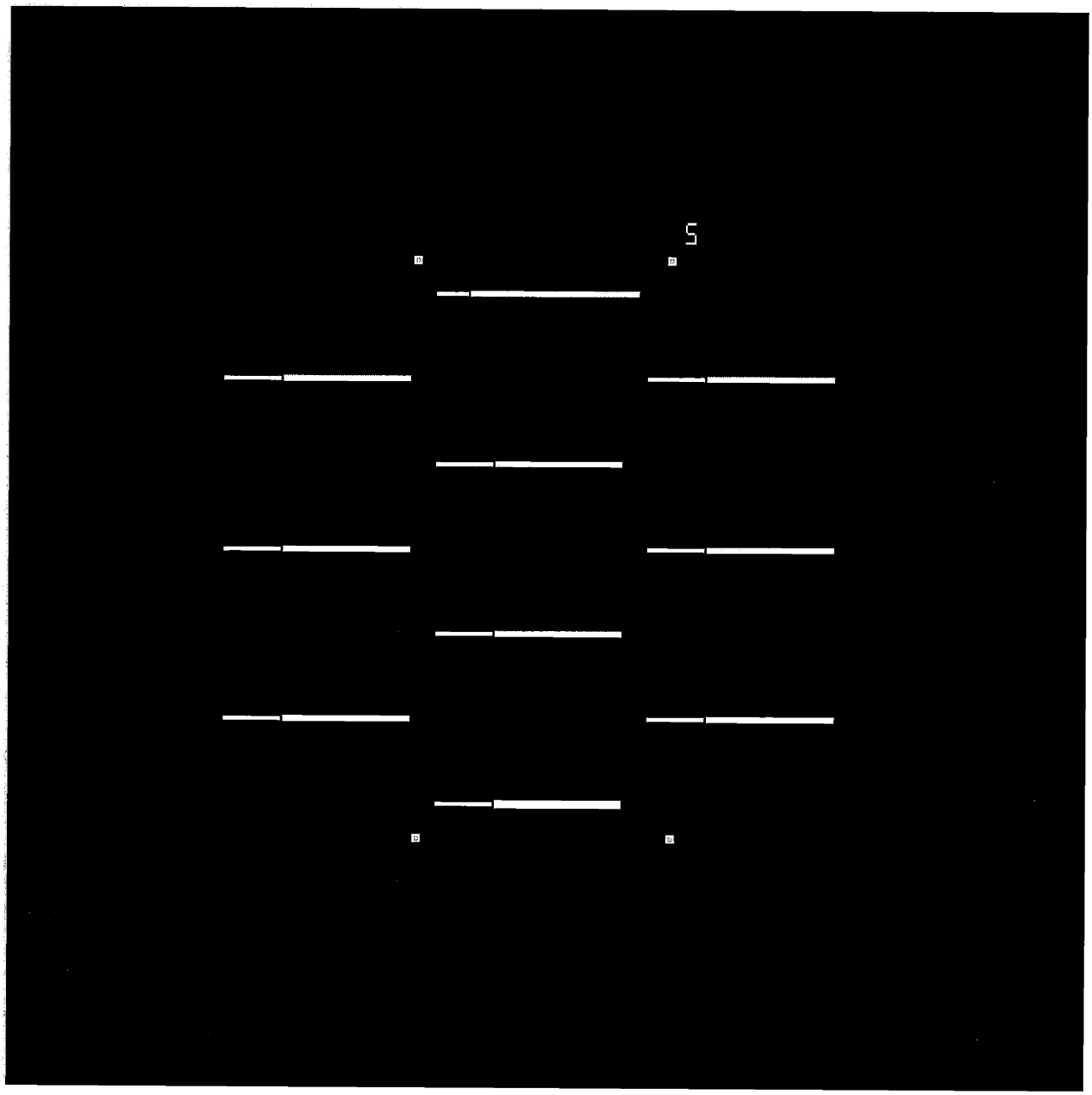

Figure H-2: Cavity mask

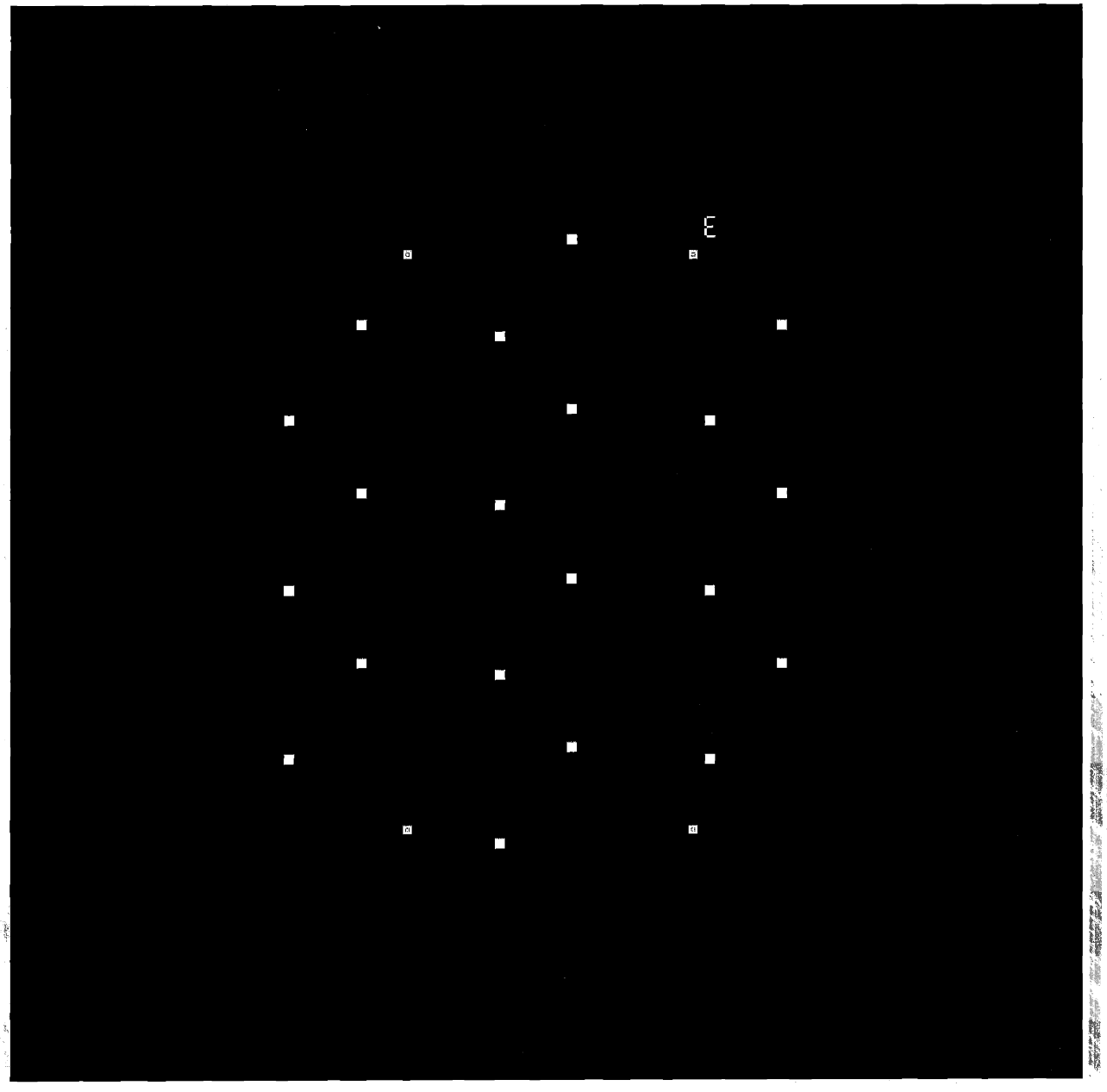

Figure H-3: Flow inlet mask

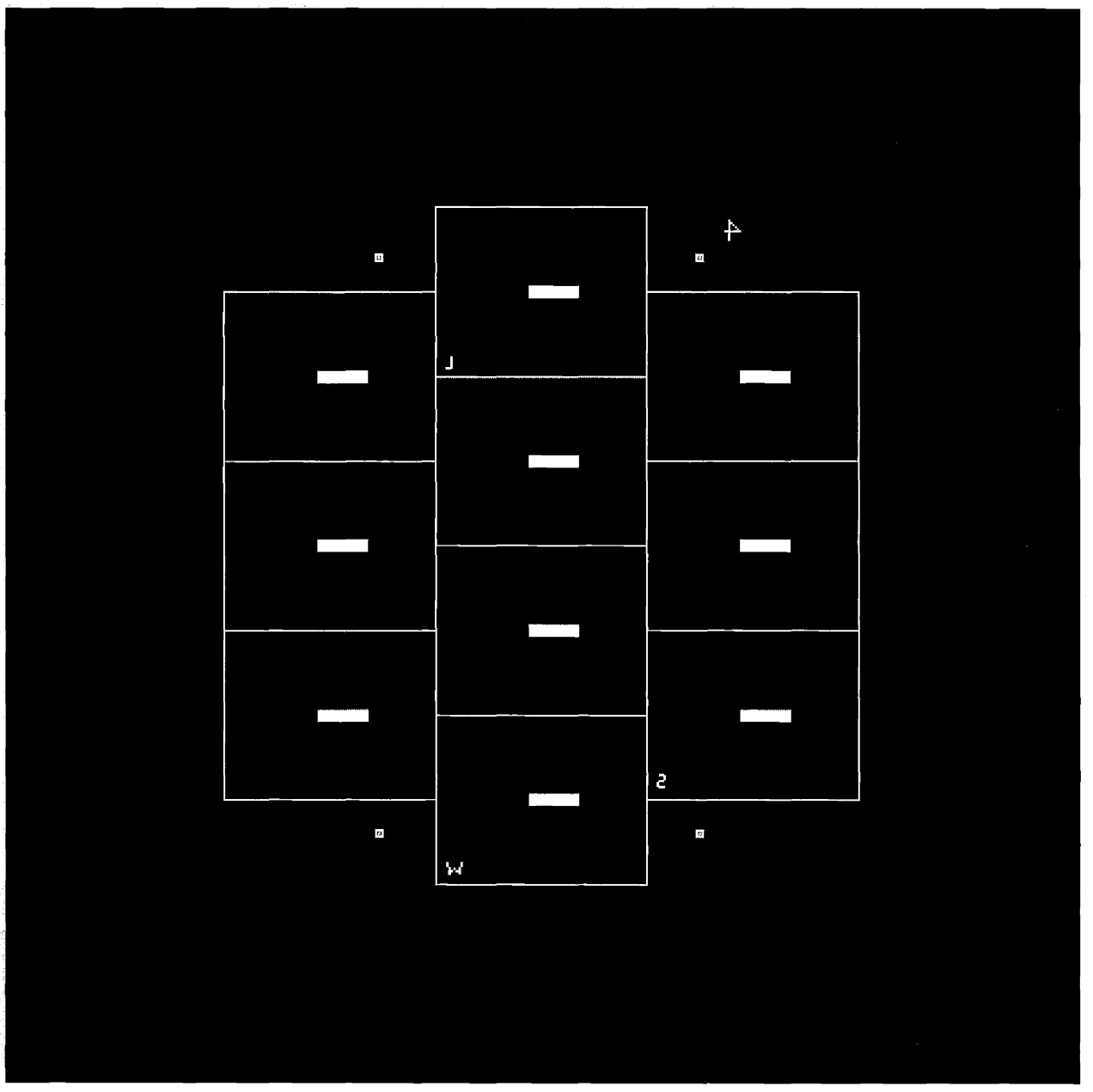

Figure H-4: Viewport mask

Appendix I : *μPA cell process flow*

1) Deposition of STS nested masking layer

1.1	ICL	RCA	RCA of device wafers
1.2	ICL	TubeA3	Growth of 1.5 um oxide

2) Pattern top surface for future STS etch of fluid channels

2.1	TRL	HMDS	HMDS of device wafers
2.2	TRL	coater	coat back of wafer with photoresist for protection
2.3	TRL	prebakeovn	5 min. bake to set backside photoresist
2.4	TRL	coater	coat front of wafer with photoresist
2.5	TRL	prebakeovn	25 min. bake
2.6	TRL	ks2/ks1	expose to flow channel mask
2.7	TRL	photowet-1	develop
2.8	TRL	postbake	30 min
2.9	TRL	acidhood	etch exposed oxide, remove photoresist

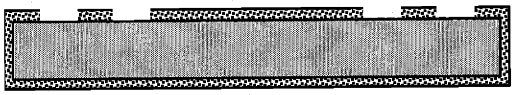

after patterning of STS mask

3) Deposit nitride to act as KOH mask

3.1	ICL	RCA	clean of wafers
3.2	ICL	tubeA3	SRO
3.3	ICL	tubeA5	deposit 1500 A Si3N4

4) Pattern top surface of device wafer for KOH

4.1	TRL	HMDS	HMDS of device wafers
4.2	TRL	coater	coat back of wafer with photoresist for protection
4.3	TRL	prebakeovn	5 min. bake to set backside photoresist
4.4	TRL	coater	coat front of wafer with photoresist
4.5	TRL	prebakeovn	25 min. bake
4.6	TRL	ks2/ks1	expose to cavity mask
4.7	TRL	photowet-1	develop
4.8	TRL	postbake	30 min
4.9	ICL	AME5000	etch exposed nitride
4.10	TRL	acidhood	remove photoresist

5) Pattern bottom surface of device wafer for KOH

5.1	TRL	HMDS	HMDS of device wafers
5.2	TRL	coater	coat back of wafer with photoresist for protection
5.3	TRL	prebakeovn	5 min. bake to set backside photoresist

5.4	TRL	coater	coat front of wafer with photoresist
5.5	TRL	prebakeovn	25 min. bake
5.6	TRL	ks2/ks1	expose to flow inletmask
5.7	TRL	photowet-1	develop
5.8	TRL	postbake	30 min
5.9	ICL	AME5000	etch exposed nitride
5.10	TRL	acidhood	remove photoresist, BOE dip to remove oxide

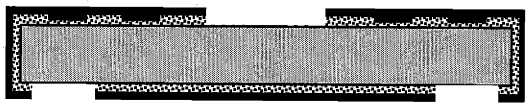

after patterning of KOH mask

6) KOH etch and post-KOH clean

6.1	RGL	KOH	KOH etch
6.2	TRL	acidhood	rinse, pirahna, and a BOE dip
6.3	TRL	rca	rca to complete post-KOH clean

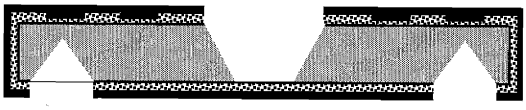

after KOH

7) Oxidation of wafer to protect channel walls

7.1	ICL	rca	rca clean
7.2	ICL	tubeA3	grow 1 um oxide

8) Removal of nitride to expose STS mask

8.1	ICL	oxide	quick BOE dip to strip oxynitride
8.2	ICL	nitride	removal of nitride in hot phosphoric
8.3	ICL	oxide	another quick BOE dip to strip SRO

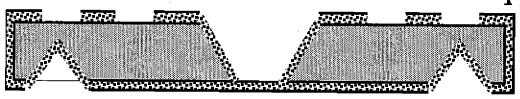

before STS

9) Mount onto handle wafer with photoresist and etch channels

9.1	TRL	coater	coat handle wafer with thick resist
9.2	TRL	prebakeovn	adhere to device wafer and prebake for 60 minutes
9.3	TRL	sts	etch ~150 um into wafer

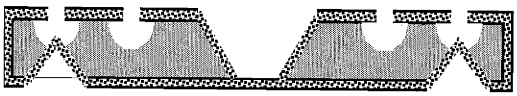

after isotropic etch

10) Bond

10.1	TRL	acidhood	strip oxide
10.2	TRL	rca	clean of both device and SOI wafers
10.3	TRL	evbonder	contact device and SOI wafers in boat
10.4	ICL	tubeA3	anneal bonded pair

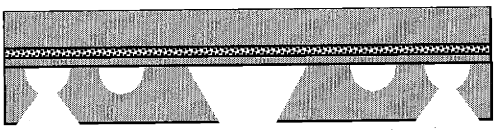

after bond

11) Pattern photoresist mask on top of wafer for KOH

11.1	TRL	HMDS	HMDS of wafers
11.2	TRL	coater	coat front of wafer with photoresist
11.3	TRL	prebakeovn	25 min. bake
11.4	TRL	ks2/ks1	expose to viewport mask
11.5	TRL	photowet-1	develop
11.6	TRL	postbake	30 min
11.7	TRL	coater	mount onto 6" handle wafer with photoresist

12) DRIE etch

12.1	TRL	sts2	etch to expose membrane
12.2	TRL	acidhood	piranha to remove resist and handle, BOE dip and HF vapor etch to remove all oxide

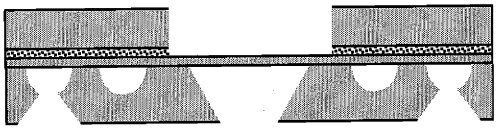

after DRIE membrane release

13) Blanket e-beam of metal to enhance reflectivity of membrane (optional)

13.1	TRL	e-beam	thin layer (~50 nm) of Al

14) Exit clean room

14.1	ICL	diesaw	separate die and open optical port

Appendix J : *Error determination*

Most of the data plotted in this thesis is derived from several measured quantities. For example, the brass cell signal in Pa/W is derived from a signal measured in volts, divided by the measured microphone sensitivity and the measured power level. Each of these measurements has some error that contributes to the total error of the data. In general, if we consider a quantity Q that is calculated from the observables a, b, c..., i.e. $Q = f(a,b,c,...)$, than the standard deviation of Q, σ_Q, can be calculated from the standard deviation for each observable by the application of [181]:

$$\sigma_Q^2 = \left(\frac{\partial Q}{\partial a}\right)^2 \sigma_a^2 + \left(\frac{\partial Q}{\partial b}\right)^2 \sigma_b^2 + \ldots \qquad \text{(J-1)}$$

This equation assumes that the error for each observable is small and evenly distributed about the mean. This equation is applied repeatedly throughout this thesis in the determination of error bars for data. This section summarizes the details of how it was applied.

J.1. *Error in the determination of δ*

Table 4-2 summarized the results of the power measurements made for determining W and δ for the brass cells. The equation for δ is given by:

$$\delta = -\frac{1}{L_{cav}} \ln\left(\frac{W_{cell}}{W_{fiber}}\right) \qquad \text{(J-2)}$$

Ignoring the error in the cavity length, which is much smaller than the error in the power measurements, the application of (J-1) results in the standard deviation of δ being given by:

$$\sigma_\delta = \frac{1}{L_{cav}^{\ 2}} \left(\frac{\sigma_{W_{cell}}^2}{W_{cell}^2} + \frac{\sigma_{W_{fiber}}^2}{W_{fiber}^2}\right) \qquad \text{(J-3)}$$

J.2. *Error in concentration determination*

The concentration level of propane, X_{C3H8}, was determined from the propane and nitrogen flow rates (F_{C3H8} and F_{N2}, respectively) with the following formula:

$$X_{C_3H_8} = \frac{F_{C_3H_8}}{F_{C_3H_8} + F_{N_2}} \qquad \text{(J-4)}$$

Following (J-1), the error in X_{C3H8} is therefore given by:

$$\sigma_X^2 = \left(\frac{1}{F_{C_3H_8} + F_{N_2}} - \frac{F_{C_3H_8}}{\left(F_{C_3H_8} + F_{N_2}\right)^2} \right)^2 \sigma_{F_{C3H8}}^2 + \left(-\frac{F_{C_3H_8}}{\left(F_{C_3H_8} + F_{N_2}\right)^2} \right)^2 \sigma_{F_{N2}}^2 \qquad \text{(J-5)}$$

The variance of F_{C3H8} and F_{N2} can be determined from the bubble calibration data, described above in Appendix E. The error bars for concentration are $\pm 1\sigma_X$.

J.3. *Error in brass cell signal determination*

The brass cell detector signal amplitude A_{brass}, with units Pa/W, is also derived from multiple experimental measurements:

$$A_{brass} = \frac{\upsilon_{brass}}{S_{mic} W_{fib}} \qquad \text{(J-6)}$$

where υ_{brass} is the signal measured in volts, S_{mic} is the microphone sensitivity in V/Pa and W_{fib} is the power measured out of the pre-packaged optical fiber in W. Following (J-1), the error in A_{brass} is therefore given by:

$$\sigma_A^2 = \left(\frac{1}{S_{mic} W_{fib}} \right)^2 \sigma_\upsilon^2 + \left(-\frac{\upsilon_{brass}}{S_{mic} W_{fib}^2} \right)^2 \sigma_W^2 + \left(-\frac{\upsilon_{brass}}{S_{mic}^2 W_{fib}} \right)^2 \sigma_S^2 \qquad \text{(J-7)}$$

In the frequency plots, where each data point represents a single voltage measurement, the voltage term in the variance is dropped. In the concentration plots, where each data point represents the mean of several voltage measurements, the variance of the voltage is taken directly from the experimental data. Similarly, the variance of the power measurement is taken directly from the statistical analysis of the power level measurement data summarized in Table 4-2. The variance in the microphone was calculated as was described above in Appendix G.

J.4. *Error in μPA cell signal determination*

The μPA cell signal requires even more observables than the brass cell. The signal amplitude $A_{\mu PA}$, with units Pa/W is derived from the measured signal in volts, $v_{\mu PA}$, the Philtec sensitivity in V/μm, S_{Ph}, the mechanical sensitivity of the membrane in μm/Pa, S_{mem}, and the measured power level, W_{fib}, by:

$$A_{\mu PA} = \frac{v_{\mu PA}}{S_{mem} S_{Ph} W_{fib}} \qquad \text{(J-8)}$$

The error in $A_{\mu PA}$ is therefore given by:

$$\sigma_A^2 = \left(\frac{1}{S_{mem} S_{Ph} W_{fib}}\right)^2 \sigma_v^2 + \left(-\frac{v_{\mu PA}}{S_{mem} S_{Ph} W_{fib}^2}\right)^2 \sigma_W^2 + \left(-\frac{v_{\mu PA}}{S_{mem}^2 S_{Ph} W_{fib}}\right)^2 \sigma_{S_{mem}}^2 + \left(-\frac{v_{\mu PA}}{S_{mem} S_{Ph}^2 W_{fib}}\right)^2 \sigma_{S_{Ph}}^2 \qquad \text{(J-9)}$$

The variance in voltage and power were calculated in the same manner as in the brass cell tests. The variance in the Philtec sensitivity was determined from the calibration, as is described above in 5.1.4. The variance in the mechanical sensitivity of the membrane, however, is another propagation of errors problem.

J.4.1. *Load-deflection characteristic*

There is a large error in the load-deflection characteristic, due to dimensional sensitivity of the membrane spring constant. For a membrane without stress, the relationship between pressure and deflection in the small deflection limit is given by:

$$S_{mem} = \frac{P}{\zeta_{avg}} = 40 \frac{E h_m^3}{w^4 \left(1 - \nu_P^2\right)} \qquad \text{(J-10)}$$

Assuming that the dominant error contributions come from uncertainty in the geometry and not in the material properties, the variance in S_{mem} is given by:

$$\sigma_{S_{mem}}^2 = \left(120 \frac{E h_m^2}{w^4 \left(1 - \nu_P^2\right)}\right)^2 \sigma_{h_m}^2 + \left(-160 \frac{E h_m^3}{w^5 \left(1 - \nu_P^2\right)}\right)^2 \sigma_w^2 \qquad \text{(J-11)}$$

In this case, we are more interested in the fractional standard deviations, for which (J-11) can be rewritten:

$$\left(\frac{\sigma_{S_{mem}}}{S_{mem}}\right)^2 = 9\left(\frac{\sigma_{h_m}}{h_m}\right)^2 + 16\left(\frac{\sigma_w}{w}\right)^2 \qquad \textbf{(J-12)}$$

If one assumes that the membrane thickness and width have a tolerance (2σ) of 5%, (J-12) than the fractional standard deviation for the membrane sensitivity is 12.5%.

Appendix K : *Load-deflection tests*

Membrane load-deflection behavior is commonly measured for the determination of thin film material properties [178]. In the typical load-deflection set up, pressure is applied to one side of a membrane, the deflection of which is measured by a microscope with a shallow depth of field and a calibrated z-axis [182]. In these tests, the Philtec deflection sensor was used to determine load-deflection behavior directly on the μPA chuck.

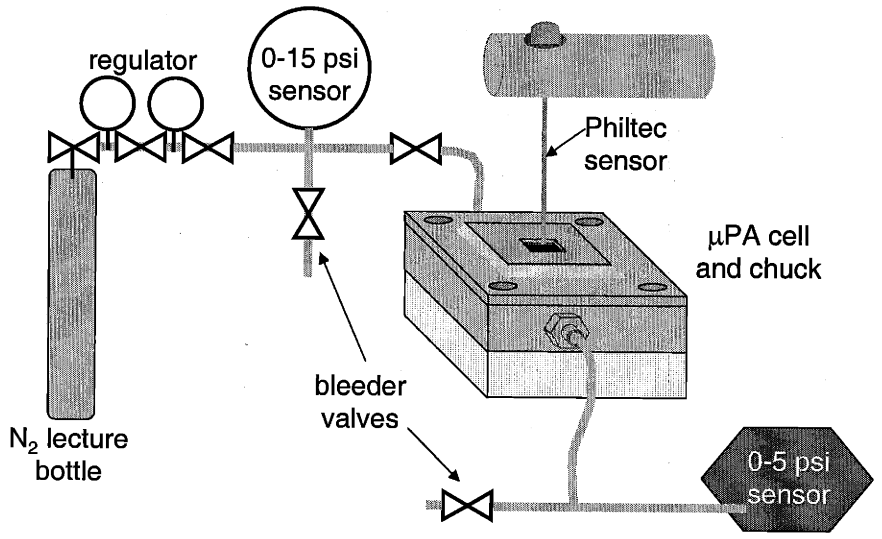

Figure K-1: Sketch of load deflection measurement apparatus

A lecture bottle of nitrogen provided the pressure source. Several pressure stages in the gas manifold allowed for better control. The critical pressure measurement was made with a Honeywell MicroSwitch 142PC05G pressure sensor, with a range of 0-5 psi (0-35000 Pa).

I found that the vacuum grease seal used for my photoacoustic measurements was not able to withstand the higher pressures of the load-deflection tests, so I added a ring of epoxy at the cell-base plate seal, and more vacuum grease at the base plate-chuck seal. The changes to the apparatus and sealing required the use of a new cell. The calibration for the Philtec sensor on the load-deflection sample cell is shown in Figure K-2. Far-field operation was preferred over near field operation because of the greater safety of this range. (The dominant failure mode for the packaged membranes was puncture by the Philtec sensor head.)

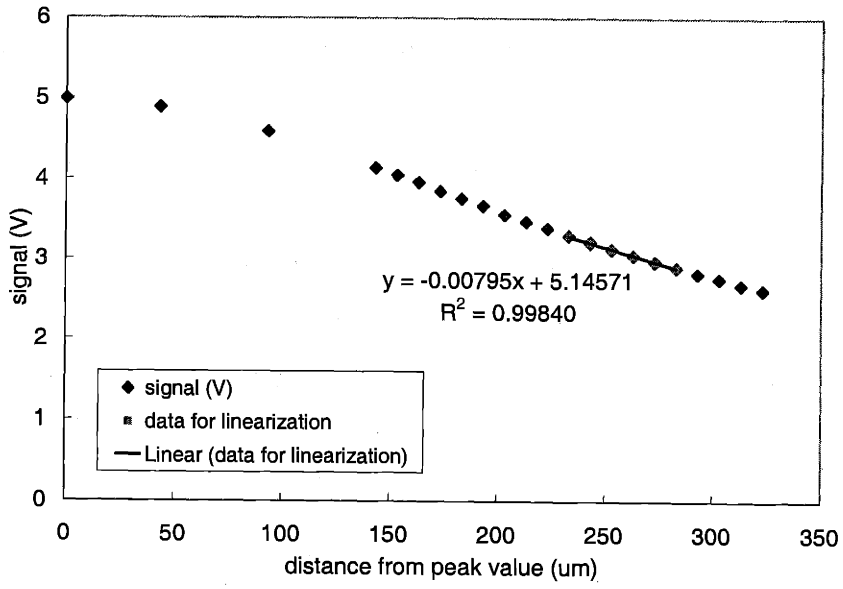

Figure K-2: Calibration of Philtec sensor for load-deflection tests

The data in Figure K-2 was fit to a line with the method of least squares in the area over which measurements were made. The standard deviation in the slope was 0.00010, calculated from [181]:

$$\sigma_m^2 = \frac{N\sigma^2}{\Delta} \qquad \textbf{(K-1)}$$

where N is the total number of data points, and σ^2 and Δ are given by:

$$\sigma^2 = \frac{1}{N}\sum (mx_i + b - y_i)^2 \qquad \textbf{(K-2)}$$

$$\Delta = N\sum x_i^2 - \left(\sum x_i\right)^2 \qquad \textbf{(K-3)}$$

This calibration was used to obtain the values shown in Figure 5-16, which is shown again below. The deflection error for each measurement was calculated from the error in slope for the Philtec calibration, while the error in pressure was calculated from the standard deviation of 5 measurements taken at 1 atmosphere. Also plotted on the model is the upper and lower bound (using $\pm 2\sigma$) for the fit to the low pressure data, as well as the upper and lower bound of the model, as was discussed above in J.4.1.

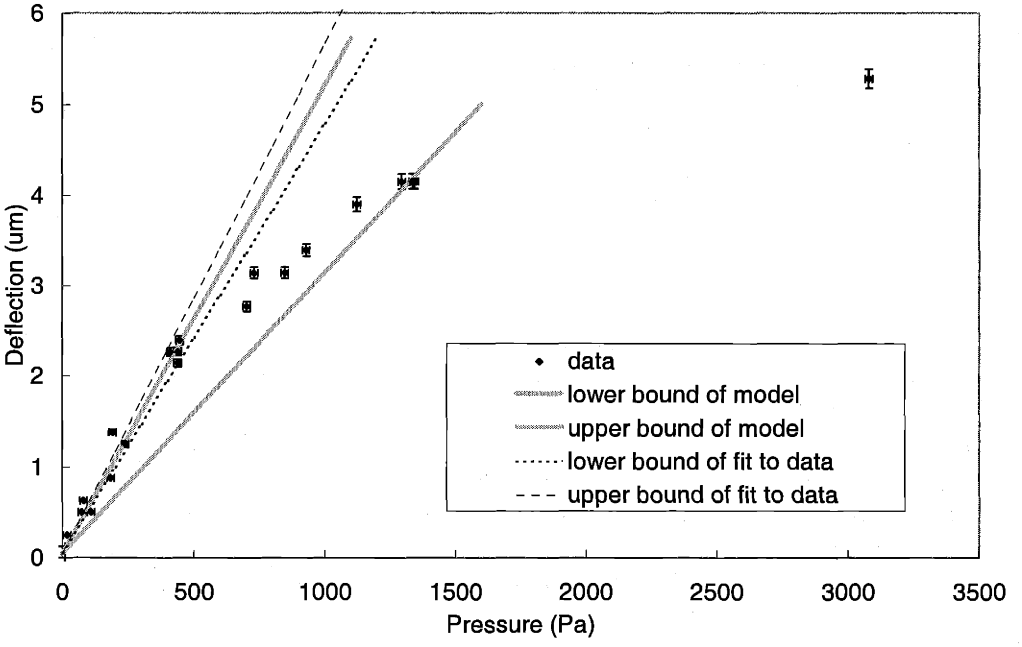

Figure K-3: Load-deflection measurement compared to model

Bibliography

[1] R. Srinivasan, I.-M. Hsing, P. E. Berger, K. F. Jensen, S. L. Firebaugh, M. A. Schmidt, M. P. Harold, J. J. Lerou, and J. F. Ryley, "Micromachined reactors for catalytic partial oxidation reactions," *AIChE J.*, vol. 43, pp. 3059-3069, 1997.

[2] W. H. Weinberg, B. Jandeleit, K. Self, and H. Turner, "Combinatorial methods in homogeneous and heterogeneous catalysis," *Curr. Opin. Solid State Mat. Sci.*, vol. 3, pp. 104-110, 1998.

[3] Y.-H. Pao, "Optoacoustic Spectroscopy and Detection,". New York, San Francisco, London: Academic Press, 1977, pp. 244.

[4] P. R. Scheeper, A. G. H. v. d. Donk, W. Olthuis, and P. Bergveld, "A review of silicon microphones," *Sens. & Act. A*, vol. 44, pp. 1-11, 1994.

[5] L. B. Kreuzer, "Ultralow gas concentration infrared absorption spectroscopy," *J. Appl. Phys.*, vol. 42, pp. 2934-2943, 1971.

[6] F. J. M. Harren, R. Berkelmans, K. Kuiper, S. t. L. Hekkert, P. Scheepers, R. Dekhuijzen, P. Hollander, and D. H. Parker, "On-line laser photoacoustic detection of ethene in exhaled air as biomarker of ultraviolet radiation damage of the human skin," *Appl. Phys. Lett.*, vol. 74, pp. 1761-1763, 1999.

[7] M. W. Sigrist, "Laser photoacoustics for gas analysis and materials testing," *Opt. Eng.*, vol. 34, pp. 1916-1922, 1995.

[8] A. C. Tam, "Applications of photoacoustic sensing techniques," *Rev. Mod. Phys.*, vol. 58, pp. 381-431, 1986.

[9] S. L. Firebaugh, K. F. Jensen, and M. A. Schmidt, "Miniaturization and integration of photoacoustic detection with a microfabricated chemical reactor system," presented at Micro Total Analysis Systems 2000 Symposium, Enschede, The Netherlands, 2000.

[10] A. G. Bell, *American Journal of Science*, vol. 20, pp. 305, 1880.

[11] C. F. Dewey, "Design of optoacoustic systems," in *Optoacoustic Spectroscopy and Detection*, Y.-H. Pao, Ed. London: Academic Press Inc., 1977, pp. 47-77.

[12] A. Rosencwaig, *Photoacoustics and Photoacoustic Spectroscopy*, Reprint ed. Malabar, Florida: Robert E. Krieger Publishing Company, 1990.

[13] J. J. Lerou, M. P. Harold, J. Ryley, J. Ashmead, T. C. O'Brien, M. Johnson, J. Perrotto, C. T. Blaisdell, T. A. Rensi, and J. Nyquist, "Microfabricated minichemical systems: technical feasibility," presented at Workshop on Microsystem Technology, Mainz, Germany, 1995.

[14] J. P. Baselt, A. Förster, J. Herrmann, and D. Tiebes, "Microreactor technology: focusing the German activities in this novel and promising field of chemical process engineering," presented at Process Miniaturization: 2nd International Conference on Microreaction Technology, New Orleans, Louisiana, 1998.

[15] D. L. Brenchley and R. S. Wegeng, "Status of microchemical systems development in the United States of America," presented at Process Miniaturization: 2nd International Conference on Microreaction Technology, New Orleans, Louisiana, 1998.

[16] O. Wörz, K. P. Jäckel, T. Richter, and A. Wolf, "Microreactors, a new efficient tool for optimum reactor design," presented at Process Miniaturization: 2nd International Conference on Microreaction Technology, New Orleans, Louisiana, 1998.

[17] G. Wießmeier and D. Hönicke, "Microfabricated components for heterogeneously catalysed reactions," *J. Micromech. & Microeng.*, vol. 6, pp. 285-289, 1996.

[18] G. Weißmeier and D. Hönicke, "Strategy for the development of micro channel reactors for heterogeneously catalyzed reactions," presented at Process Miniaturization: 2nd International Conference on Microreaction Technology, New Orleans, Louisiana, 1998.

[19] D. Honicke and G. Wiessmeier, "Heterogeneously catalyzed reactions in a microreactor," presented at Workshop on Microsystem Technology, Mainz, Germany, 1995.

[20] A. L. Y. Tonkovich, J. L. Zilka, M. R. Powell, and C. J. Call, "The catalytic partial oxidation of methane in a microchannel chemical reactor," presented at Process Miniaturization: 2nd International Conference on Microreaction Technology, New Orleans, Louisiana, 1998.

[21] J.-C. Roulet, K. Fluri, E. Verpoorte, R. Völkel, H.-P. Herzig, N. F. d. Rooij, and R. Dändliker, "Micro-optical systems for fluorescence detection in μTAS applications," presented at Micro Total Analysis Systems '98, Banff, Canada, 1998.

[22] A. E. Bruno, E. Baer, R. Völkel, and C. S. Effenhauser, "Microoptical fluorescence detection for chip-based multiplexed analysis systems," presented at Micro Total Analysis Systems '98, Banff, Canada, 1998.

[23] G. C. Frye-Mason, R. J. Kottenstette, E. J. Heller, C. M. Matzke, S. A. Casalnuovo, P. R. Lewis, R. P. Manginell, W. K. Schubert, V. M. Hietala, and R. J. Shul, "Integrated chemical analysis systems for gas phase CW agent detection," presented at Micro Total Analysis Systems '98, Banff, Canada, 1998.

[24] M. A. Burns, B. N. Johnson, S. N. Brahmasandra, K. Handique, J. R. Webster, M. Krishnan, T. S. Sammarco, P. M. Man, D. Jones, D. Heldsinger, C. H. Mastrangelo, and D. T. Burke, "An integrated nanoliter DNA analysis device," *Science*, vol. 282, pp. 484-487, 1998.

[25] A. Yotsumoto, R. Nakamura, S. Shoji, and T. Wada, "Fabrication of an integrated mixing/reaction micro flow cell for μTAS," presented at Micro Total Analysis Systems '98, Banff, Canada, 1998.

[26] I.-M. Hsing, R. Srinivasan, M. P. Harold, K. F. Jensen, and M. A. Schmidt, "Finite element simulation strategies for microfluidic devices with chemical reactions," presented at 1997 International Conference on Solid-State sensors and Actuators (Transducers 97), Chicago, IL, 1997.

[27] K. F. Jensen, S. L. Firebaugh, A. J. Franz, D. Quiram, R. Srinivasan, and M. A. Schmidt, "Integrated gas phase microreactors," presented at Micro Total Analysis Systems '98, Banff, Canada, 1998.

[28] R. Srinivasan, I.-M. Hsing, J. Ryley, M. P. Harold, K. F. Jensen, and M. A. Schmidt, "Micromachined chemical reactors for surface catalyzed reactions," presented at Solid State Sensors and Actuators Workshop, Hilton Head, SC, 1996.

[29] R. Srinivasan, S. L. Firebaugh, I.-M. Hsing, J. Ryley, M. P. Harold, K. F. Jensen, and M. A. Schmidt, "Chemical performance and high temperature characterization of micromachined chemical reactors," presented at 1997 International Conference on Solid-State sensors and Actuators (Transducers 97), Chicago, IL, 1997.

[30] K.-P. Jäckel, "Microtechnology: application opportunities in the chemical industry," presented at Workshop on Microsystem Technology, Mainz, Germany, 1995.

[31] E. Reddington, A. Sapienza, B. Gurau, R. Viswanathan, S. Sarangapani, E. S. Smotkin, and T. E. Mallouk, "Combinatorial electrochemistry: a highly parallel, optical screening method for discovery of better electrocatalysts," *Science*, vol. 280, pp. 1735-1737, 1998.

[32] F. C. Moates, M. Somani, J. Annamalai, J. T. Richardson, D. Luss, and R. C. Willson, "Infrared thermographic screening of combinatorial libraries of heterogeneous catalysts," *Ind. Eng. Chem. Res.*, vol. 35, pp. 4801-4803, 1996.

[33] S. M. Senkan, "High-throughput screening of solid-state catalyst libraries," *Nature*, vol. 394, pp. 350-353, 1998.

[34] O. Leistiko and P. F. Jensen, "Integrated bio/chemical microsystems employing optical detection: the clip on," *J. Micromech. & Microeng.*, vol. 8, pp. 148-150, 1998.

[35] A. Ehlert and S. Büttgenbach, "Automatic sensor system for water analysis," presented at Micro Total Analysis Systems '98, Banff, Canada, 1998.

[36] T. Kitamori, M. Fujinami, T. Odake, M. Tokeshi, and T. Sawada, "Photothermal ultrasensitive detection and microchemistry in the integrated chemistry lab," presented at Micro Total Analysis Systems '98, Banff, Canada, 1998.

[37] R. Srinivasan, "Microfabricated Reactors for Partial Oxidation Reactions," PhD. Thesis,. Cambridge, Massachusetts: Massachusetts Institute of Technology, 1998, pp. 155.

[38] T. M. Floyd, M. W. Losey, S. L. Firebaugh, K. F. Jensen, and M. A. Schmidt, "Novel liquid phase microreactors for safe production of hazardous specialty chemicals," presented at 3rd International Conference on Microreaction Technology, Frankfurt, Germany, 1999.

[39] W. A. Bryden, R. C. Benson, S. A. Ecelberger, T. E. Phillips, T. Cornish, and R. J. Cotter, "Tiny-TOF-MALDI mass specrometry for particulate drug and explosives detection," *Proc. SPIE*, vol. 2511, pp. 153-164, 1995.

[40] S. Hiroki, T. Abe, Y. Murakami, Y. Takano, M. Higuchi, and M. Miyake, "Development of a QMS with a ceramic single-piece quadrupole," *Vacuum*, vol. 44, pp. 71-74, 1993.

[41] R. R. A. Syms, T. J. Tate, M. M. Ahmad, and S. Taylor, "Fabrication of a microengineered quadrupole electrostatic lens," *Electron. Lett.*, vol. 32, pp. 2094-2095, 1996.

[42] R. R. A. Syms, T. J. Tate, M. M. Ahmad, and S. Taylor, "Design of a microengineered electrostatic quadrupole lens," *IEEE Trans. Electron Dev.*, vol. 45, pp. 2304-2311, 1998.

[43] S. Taylor, J. J. Tunstall, R. R. A. Syms, T. Tate, and M. M. Ahmad, "Initial results for a quadrupole mass spectrometer with a silicon micromachined mass filter," *Electron. Lett.*, vol. 34, pp. 546-547, 1998.

[44] R. J. Ferran and S. Boumsellek, "High-pressure effects in miniature arrays of quadrupole analyzers for residual gas analysis from 10-9 to 10-2 Torr," *J. Vacuum Sci. Tech. A*, vol. 14, pp. 1258-1265, 1996.

[45] M. Kimura, J. Manaka, S. Satoh, S. Takano, N. Igarashi, and K. Nagai, "Application of the air-bridge microheater to gas detection," *Sens. & Act. B*, vol. 24-25, pp. 857-860, 1995.

[46] G. Pollak-Diener and E. Obermeier, "Heat-conduction microsensor based on silicon technology for the analysis of two- and three-component gas mixtures," *Sens. & Act. B*, vol. 13-14, pp. 345-347, 1993.

[47] J. Hale, G. Stehle, and I. Bals, "Gas analysis using a thermal conductivity method," *Sens. & Act. B*, vol. 7, pp. 665-671, 1992.

[48] T. S. J. Lammerink, F. Dijkstra, Z. Houkes, and J. v. Kuijk, "Intelligent gas-mixture flow sensor," *Sens. & Act. A*, vol. 46-47, pp. 380-384, 1995.

[49] V. I. Anisimkin, M. Penza, V. A. Osipenko, and L. Vasanelli, "Gas thermal conductivity sensor based on SAW," *IEEE Trans. Ultrason. Ferroelec. Freq. Control*, vol. 42, pp. 978-980, 1995.

[50] S. C. Terry, J. H. Jerman, and J. B. Angell, "A gas chromatographic air analyzer fabricated on a silicon wafer," *IEEE Trans. Electron Dev.*, vol. ED-26, pp. 1880-1886, 1979.

[51] S. Sorge and T. Pechstein, "Fully integrated thermal conductivity sensor for gas chromatography without dead volume," *Sens. & Act. A*, vol. 63, pp. 191-195, 1997.

[52] B. Ghodsian, M. Parameswaran, and M. Syrzycki, "Gas detector with low-cost micromachined field ionization tips," *IEEE Electron Dev. Lett.*, vol. 19, pp. 241-243, 1998.

[53] M. J. Madou and S. R. Morrison, "High-field operation of submicrometer devices at atmospheric pressure," presented at Transducers '91, 1991.

[54] R. R. Reston and J. Edward S. Kolesar, "Silicon-micromachined gas chromatography systems used to separate and detect ammonia and nitrogen dioxide--part I: design, fabrication, and integration of the gas chromatography system," *Journal of Microelectromechanical Systems*, vol. 3, pp. 134-154, 1994.

[55] H. Wohltjen, "Mechanism of operation and design considerations for surface acoustic wave device vapour sensors," *Sens. & Act.*, vol. 5, pp. 307-325, 1984.

[56] I. Lundström, M. Armgarth, A. Spetz, and F. Winquist, "Gas sensors based on catalytic metal-gate field-effect devices," *Sens. & Act.*, vol. 10, pp. 399-421, 1986.

[57] S. D. Senturia, "The role of the MOS structure in integrated sensors," *Sens. & Act.*, vol. 4, pp. 507-526, 1983.

[58] N. Fabricius, G. Gauglitz, and J. Ingenhoff, "A gas sensor based on an integrated optical Mach-Zehnder interferometer," *Sens. & Act. B*, vol. 7, pp. 672-676, 1992.

[59] B. Maisenhölder, H. P. Zappe, R. E. Kunz, P. Riel, M. Moser, and J. Edlinger, "A GaAs/AlGaAs-based refractometer platform for integrated optical sensing applications," *Sens. & Act. B*, vol. 38-39, pp. 324-329, 1997.

[60] A. Brecht and G. Gauglitz, "Recent developments in optical transducers for chemical or biochemical applications," *Sens. & Act. B*, vol. 38-39, pp. 1-7, 1997.

[61] Y. Beregovski, O. Hennig, M. Fallahi, F. Guzman, R. Clemens, S. Mendes, and N. Peyghambarian, "Design and characteristics of a DBR-laser-based environmental sensor," *Sens. & Act. B*, vol. 53, pp. 116-124, 1998.

[62] G. Stewart and B. Culshaw, "Optical waveguide modelling and design for evanescent field chemical sensors," *Opt. Quant. Electron.*, vol. 26, pp. S249-S259, 1994.

[63] H. Tai, K. Yamamoto, M. Uchida, S. Osawa, and K. Uehara, "Long-distance simultaneous detection of methane and acetylene by using diode lasers coupled with optical fibers," *IEEE Photon. Tech. Lett.*, vol. 4, pp. 1041-1135, 1992.

[64] G. Stewart, W. Jin, and B. Culshaw, "Prospects for fibre-optic evanescent-field gas sensors using absorption in the near-infrared," *Sens. & Act. B*, vol. 38-39, pp. 42-47, 1997.

[65] T. Buffeteau, B. Desbat, and D. Eyquem, "Attenuated total reflection Fourier transform infrared microspectroscopy: theory and application to polymer samples," *Vibrat. Spectrosc.*, vol. 11, pp. 29-36, 1996.

[66] S. D. Collins, R. L. Smith, C. González, K. P. Stewart, J. G. Hagopian, and J. M. Sirota, "Fourier-transform optical microsystems," *Optics Letters*, vol. 24, pp. 844-846, 1999.

[67] C. Marxer, O. Manzardo, H.-P. Herzig, R. Dändliker, and N. F. De Rooij, "An electrostatic actuator with large dynamic range and linear displacement-voltage behaviour for a miniature spectrometer," presented at Transducers '99, 1999.

[68] J. H. Correia, M. Bartek, and R. F. Wolffenbuttel, "High-selectivity single-chip spectrometer in silicon for operation at visible part of the spectrum," *IEEE Trans. Electron. Dev.*, vol. 47, pp. 553-559, 2000.

[69] T. Corman, E. Kälvesten, M. Huiku, K. Weckström, P. T. Meriläinen, and G. Stemme, "An optical IR-source and CO_2-chamber systems for CO_2 measurements," *J. Microelectromech. Syst.*, vol. 9, pp. 509-516, 2000.

[70] G. B. Hocker, D. Youngner, M. Butler, M. Sinclair, T. Plowman, E. Deutsch, A. Volpicelli, S. Senturia, and A. J. Ricco, "The polychromator: a programmable MEMS diffraction grating for synthetic spectra," presented at Solid-State Sensor and Actuator Workshop, Hilton Head Island, South Carolina, 2000.

[71] M. B. Sinclair, M. A. Butler, A. J. Ricco, and S. D. Senturia, "Synthetic spectra: a tool for correlation spectroscopy," *Appl. Opt.*, vol. 36, pp. 3342-3348, 1997.

[72] M. B. Sinclair, M. A. Butler, S. H. Kravitz, W. J. Zubrzycki, and A. J. Ricco, "Synthetic infrared spectra," *Opt. Lett.*, vol. 22, pp. 1036-1038, 1997.

[73] A. G. Bell, "Upon the production of sound by radiant energy," *Philos. Mag.*, vol. 11, pp. 510-528, 1881.

[74] J. Tyndall, "Action of an intermittent beam of radiant heat upon gaseous matter," *Proc. R. Soc. Lon.*, vol. 31, pp. 307-317, 1881.

[75] W. C. Röntgen, "On tones produced by the intermittent irradiation of a gas," *Philos. Mag.*, vol. 11, pp. 308-310, 1881.

[76] M. E. Delany, "The optic-acoustic effect in gases," *Sci. Progr.*, vol. 47, pp. 459-467, 1959.

[77] L. B. Kreuzer and C. K. N. Patel, "Nitric oxide air pollution: detection by optoacoustic spectroscopy," *Science*, vol. 173, pp. 45-47, 1971.

[78] L. B. Kreuzer, N. D. Kenyon, and C. K. N. Patel, "Air pollution: sensitive detection of ten pollutant gases by carbon monoxide and carbon dioxide lasers," *Science*, vol. 177, pp. 347-349, 1972.

[79] L. B. Kreuzer, "Laser optoacoustic spectroscopy for GC detection," *Anal. Chem.*, vol. 50, pp. 597A-606A, 1978.

[80] C. F. Dewey, R. D. Kamm, and C. E. Hackett, "Acoustic amplifier for detection of atmospheric pollutants," *Appl. Phys. Lett.*, vol. 23, pp. 633-635, 1973.

[81] S. Bernegger and M. W. Sigrist, "CO-laser photoacoustic spectroscopy of gases and vapours for trace gas analysis," *Infr. Phys.*, vol. 30, pp. 375-429, 1990.

[82] A. Miklós and P. Hess, "Modulated and pulsed photoacoustics in trace gas analysis," *Anal. Chem.*, vol. 72, pp. 30A-37A, 2000.

[83] R. D. Kamm, "Detection of weakly absorbing gases using a resonant optoacoustic method," *J. Appl. Phys.*, vol. 47, pp. 3550-3558, 1976.

[84] L.-G. Rosengren, "Optimal optoacoustic detector design," *Appl. Opt.*, vol. 14, pp. 1960-1976, 1975.

[85] J. Davidsson, J. H. Gutow, and R. N. Zare, "Experimental improvements in recording gas-phase photoacoustic spectra," *J. Phys. Chem.*, vol. 94, pp. 4069-4073, 1990.

[86] P. C. Claspy, C. Ha, and Y.-H. Pao, "Optoacoustic detection of NO_2 using a pulsed dye laser," *Appl. Opt.*, vol. 16, pp. 2972-2973, 1977.

[87] C. K. N. Patel and A. C. Tam, "Pulsed optoacoustic spectroscopy of condensed matter," *Rev. Mod. Phys.*, vol. 53, pp. 517-550, 1981.

[88] M. A. Leugers and G. H. Atkinson, "Quantitative detection of NO_2 using a pulsed dye laser," *Anal. Chem.*, vol. 56, pp. 925-929, 1984.

[89] C. Brand, A. Winkler, P. Hess, A. Miklós, Z. Bozóki, and J. Sneider, "Pulsed-laser excitation of acoustic modes in open high-Q photoacoustic resonators for trace gas monitoring: results for C_2H_4," *Appl. Opt.*, vol. 34, pp. 3257-3266, 1995.

[90] S. Schäfer, A. Miklós, and P. Hess, "Quantitative signal analysis in pulsed resonant photoacoustics," *Appl. Opt.*, vol. 36, pp. 3202-3211, 1997.

[91] I. G. Calasso, V. Funtov, and M. W. Sigrist, "Analysis of isotropic CO2 mixtures by laser photoacoustic spectroscopy," *Appl. Opt.*, vol. 36, pp. 3212-3216, 1997.

[92] S. Schäfer, A. Miklós, A. Pusel, and P. Hess, "Absolute measurement of gas concentrations and saturation behavior in pulsed photoacoustics," *Chem. Phys. Lett.*, vol. 285, pp. 235-239, 1998.

[93] F. J. M. Harren, F. G. C. Bijnen, J. Reuss, C. J. Voesenek, and C. W. P. M. Blom, "Sensitive intracavity photoacoustic measurements with a CO_2 waveguide laser," *Appl. Phys. B*, vol. 50, pp. 137-144, 1990.

[94] X. Yang, C. J. Petrillo, and C. Noda, "Photoacoustic detection of N_2O and CO_2 overtone transitions in the near-infrared," *Chem. Phys. Lett.*, vol. 214, pp. 536-540, 1993.

[95] T. Fink, S. Büscher, R. Gäbler, Q. Yu, A. Dax, and W. Urban, "An improved CO_2 laser intracavity photoacoustic spectrometer for trace gas analysis," *Rev. Sci. Instrum.*, vol. 67, pp. 4000-4004, 1996.

[96] P. D. Goldan and K. Goto, "An acoustically resonant system for detection of low-level infrared absorption in atmospheric pollutants," *J. Appl. Phys.*, vol. 45, pp. 4350-4355, 1974.

[97] K. M. Adams, "Real-time in situ measurements of atmospheric optical absorption in the visible via photoacoustic spectroscopy. 1: Evaluation of photoacoustic cells," *Appl. Opt.*, vol. 27, pp. 4052-4056, 1988.

[98] R. A. Rooth, J. L. Verhage, and L. W. Wouters, "Photoacoustic measurement of ammonia in the atmosphere: influence of water vapor and carbon dioxide," *Appl. Opt.*, vol. 29, pp. 3643-3653, 1990.

[99] F. G. C. Bijnen, J. Reuss, and F. J. M. Harren, "Geometrical optimization of a longitudinal resonant photoacoustic cell for sensitive and fast trace gas detection," *Rev. Sci. Instrum.*, vol. 67, pp. 2914-2923, 1996.

[100] S. Schäfer, M. Mashni, J. Sneider, A. Miklós, P. Hess, H. Pitz, K.-U. Pleban, and V. Ebert, "Sensitive detection of methane with a 1.65 μm diode laser by photoacoustic and absorption spectroscopy," *Appl. Phys. B*, vol. 66, pp. 511-516, 1998.

[101] J. G. Parker, "Optical absorption in glass: investigation using an acoustic technique," *Appl. Opt.*, vol. 12, pp. 2974-2977, 1973.

[102] B. A. Paldus, T. G. Spence, R. N. Zare, J. Oomens, F. J. M. Harren, D. H. Parker, C. Gmachl, F. Cappasso, D. L. Sivco, J. N. Baillargenn, A. L. Hutchinson, and A. Y. Cho, "Photoacoustic spectroscopy using quantum-cascade lasers," *Opt. Lett.*, vol. 24, pp. 178-180, 1999.

[103] P. L. Meyer and M. W. Sigrist, "Atmospheric pollution monitoring using CO2-laser photoacoustic spectroscopy and other techniques," *Rev. Sci. Instrum.*, vol. 61, pp. 1779-1807, 1990.

[104] R. Gerlach and N. M. Amer, "Brewster window and windowless resonant spectrophones for intracavity operation," *Appl. Phys.*, vol. 23, pp. 319-326, 1980.

[105] M. Fehér, Y. Jiang, J. P. Maier, and A. Miklós, "Optoacoustic trace-gas monitoring with near-infrared diode laser," *Appl. Opt.*, vol. 33, pp. 1655-1658, 1994.

[106] M. H. d. Paula, C. A. Vinha, and R. G. Badini, "High-sensitivity optical microphone for photoacoustics," *Rev. Sci. Instrum.*, vol. 63, pp. 3487-3491, 1992.

[107] J. Breguet, J. P. Pellaux, and N. Gisin, "Photoacoustic detection of trace gases with an optical microphone," *Sens. & Act., A*, vol. 48, pp. 29-35, 1995.

[108] P. C. Beard, F. Pérennès, E. Draguioti, and T. N. Mills, "Optical fiber photoacoustic-photothermal probe," *Opt. Lett.*, vol. 23, pp. 1235-1237, 1998.

[109] M. J. Adams, B. C. Beadle, and G. F. Kirkbright, "Optoacoustic spectroscopy in the near-infrared region," *Anal. Chem.*, vol. 50, pp. 1371-1374, 1978.

[110] L. T. Petkovska, M. S. Trtica, M. M. Stoiljkovic, G. S. Ristic, and S. S. Miljanic, "CO_2-laser photoacoustic absorption spectra of carbon dioxide as a function of temperature," *J. Quant. Spectrosc. Radiat. Transfer*, vol. 54, pp. 509-520, 1995.

[111] K. Walzer, M. Tacke, and G. Busse, "Optoacoustic spectra of some molecular gases at CO_2 laser wavelengths between 9 and 11 μm," *J. Chem. Phys.*, vol. 73, pp. 3095-3097, 1980.

[112] G. Busse and B. Bullemer, "Use of the opto-acoustic effect for rapid scan fourier spectroscopy," *Infr. Phys.*, vol. 18, pp. 631-634, 1978.

[113] M. M. Farrow, R. K. Burnham, and E. M. Eyring, "Fourier-transform photoacoustic spectroscopy," *Appl. Phys. Lett.*, vol. 33, pp. 735-737, 1978.

[114] L. B. Lloyd, R. K. Burnham, W. L. Chandler, E. M. Eyring, and M. M. Farrow, "Fourier transform photoacoustic visible spectroscopy of solids and liquids," *Anal. Chem.*, vol. 52, pp. 1595-1601, 1980.

[115] D. Débarre, A. C. Boccara, and D. Fournier, "High-luminosity visible and near-IR Fourier-transform photoacoustic spectrometer," *Appl. Opt.*, vol. 20, pp. 4281-4286, 1981.

[116] J. B. Kinney and R. H. Staley, "Photoacoustic cell for Fourier transform infrared spectrometry of surface species," *Anal. Chem.*, vol. 55, pp. 343-348, 1983.

[117] B. S. H. Royce and J. B. Benziger, "Fourier transform photoacoustic spectroscopy of solids," *IEEE Trans. Ultrason. Ferroelectr. Freq. Control*, vol. UFFC-33, pp. 561-572, 1986.

[118] G. Spanner and R. Niessner, "Noninvasive determination of blood constituents using an array of modulated laser diodes and a photoacoustic sensor head," *Fresnius J. Anal. Chem.*, vol. 355, pp. 327-328, 1996.

[119] X. Luo, F. Y. Shi, and J. X. Lin, "CO-Laser photoacoustic detection of phosgene ($COCl_2$)," *Int. J. Infrared Millim. Waves*, vol. 12, pp. 141-147, 1991.

[120] F. Kühnemann, K. Schneider, A. Hecker, A. A. E. Martis, W. Urban, S. Schiller, and J. Mlynek, "Photoacoustic trace-gas detection using a cw single-frequency parametric oscillator," *Appl. Phys. B*, vol. 66, pp. 741-745, 1998.

[121] U. Simon, Z. Benko, M. W. Sigrist, R. F. Curl, and F. K. Tittel, "Design considerations of an infrared spectrometer based on difference-frequency generation in $AgGaSe_2$," *Appl. Opt.*, vol. 32, pp. 6650-6655, 1993.

[122] W. C. Eckhoff, R. S. Putnam, S. Wang, R. F. Curl, and F. K. Tittel, "A continuously tunable long-wavelength cw IR source for high-resolution spectroscopy and trace-gas detection," *Appl. Phys. B*, vol. 63, pp. 437-441, 1996.

[123] J. Faist, F. Capasso, D. L. Sivco, A. L. Hutchinson, M. Beck, S. N. G. Chu, and A. Y. Cho, "Short wavelength ($\lambda \sim 3.4$ μm) quantum cascade laser based on strained compensated InGaAs/AlInAs," *Appl. Phys. Lett.*, vol. 72, pp. 680-682, 1998.

[124] C. Gmachl, F. Capasso, A. Tredicucci, D. L. Sivco, A. L. Hutchinson, and A. Y. Cho, "Long wavelength ($\lambda \sim 13$ μm) quantum cascade lasers," *Electron. Lett.*, vol. 34, pp. 1103-1104, 1998.

[125] N. B. Colthup, L. H. Daly, and S. E. Wiberley, *Introduction to Infrared and Raman Spectroscopy*, Third ed. San Diego, CA: Academic Press, 1990.

[126] D. W. Vidrine, "Photoacoustic Fourier transform infrared spectroscopy of solid samples," *Appl. Spectrosc.*, vol. 34, pp. 314-319, 1980.

[127] L.-G. Rosengren, E. Max, and S. T. Eng, "A study of laser-acoustic pollution monitors," *J. Phys. E*, vol. 7, pp. 125-133, 1974.

[128] M. A. Gondal, "Laser photoacoustic spectrometer for remote monitoring of atmospheric pollutants," *Appl. Opt.*, vol. 36, pp. 3195-3201, 1997.

[129] P. Helander, "An open photoacoustic cell," *J. Photoacoustics*, vol. 1, pp. 103-120, 1982.

[130] P. Helander, "Flow-through photoacoustic cell," *Rev. Sci. Instrum.*, vol. 53, pp. 1626-1627, 1982.

[131] N. Corp., "http://www.nicolet.com/labsys/Accessories/specacc.html,".

[132] F. G. C. Bijnen, F. J. M. Harren, J. H. P. Hackstein, and J. Reuss, "Intracavity CO laser photoacoustic trace gas detection: cyclic CH_4, H_2 and CO_2 emission by cockroaches and scarab beetles," *Appl. Opt.*, vol. 35, pp. 5357-5368, 1996.

[133] J. Oomens, H. Zuckermann, S. Persijn, D. H. Parker, and F. J. M. Harren, "CO-laser-based photoacoustic trace-detection: applications in postharvest physiology," *Appl. Phys. B*, vol. 67, pp. 459-466, 1998.

[134] G. Lei and B. D. Bartolo, "Measurement of rotational and vibrational relaxation in gases by photoacoustic resonance: application to SF_6," *J. Appl. Phys.*, vol. 79, pp. 2890-2895, 1996.

[135] M. Fiedler and P. Hess, "High precision study of chemical relaxation in the system N_2O_4=$2NO_2$ by photoacoustic resonance spectroscopy," *J. Chem. Phys.*, vol. 93, pp. 8693-8702, 1990.

[136] V. Zeninari, B. A. Tikhomirov, Y. N. Ponomarev, and D. Courtois, "Preliminary results on photoacoustic study of the relaxation of vibrationally excited ozone," *J. Quant. Spectrosc. Radiat. Transfer*, vol. 59, pp. 369-375, 1998.

[137] E. Hey and K. Gollnick, "Optoacoustic relaxation of periodically irradiated solutions," *J. Photoacoustics*, vol. 1, pp. 1-20, 1982.

[138] H. Takekoshi and S. Hayashi, "Photodissociation of iodobenzene and photoacousic detection of the products using a dual-purpose Q-switched YAG laser," *Jpn. J. Appl. Phys., part 1*, vol. 35, pp. 2921-2924, 1996.

[139] D. A. Hutchins and A. C. Tam, "Pulsed photoacoustic materials characterization," *IEEE Trans. Ultrasonics, Ferroelectrics, and Frequency Control*, vol. UFFC-33, pp. 429-449, 1986.

[140] J. J. Barrett and M. J. Berry, "Photoacoustic Raman spectroscopy (PARS) using cw laser sources," *Appl. Phys. Lett.*, vol. 34, pp. 144-146, 1979.

[141] Y. Oki, N. Kawada, T. Ogawa, Y. Abe, and M. Maeda, "Sensitive H_2 detection using a new technique of photoacoustic Raman spectroscopy," *Jap. J. Appl. Phys.*, vol. 36, pp. L1172-L1174, 1997.

[142] T. W. Kenny, J. K. Reynolds, J. A. Podosek, E. C. Vote, L. M. Miller, H. K. Rockstad, and W. J. Kaiser, "Micromachined infrared sensors using tunneling displacement transducers," *Rev. Sci. Instrum.*, vol. 67, pp. 112-128, 1996.

[143] K. Yamashita, A. Murata, and M. Okuyama, "Miniaturized infrared sensor using silicon diaphragm based on golay cell," *Sens. & Act. A*, vol. A66, pp. 29-32, 1998.

[144] J.-B. Chévrier, K. Baert, and T. Slater, "An infrared pneumatic detector made by micromachining technology," *J. Micromech. Microeng.*, vol. 5, pp. 193-195, 1995.

[145] M. J. E. Golay, "Theoretical consideration in heat and infra-red detection, with particular reference to the pneumatic detector," *Rev. Sci. Instrum.*, vol. 18, pp. 347-356, 1947.

[146] K. Uchiyama, A. Hibara, H. Kimura, T. Sawada, and T. Kitamori, "Thermal lens microscope," *Jap. J. Appl. Phys., Part 1*, vol. 39, pp. 5316-5322, 2000.

[147] U. Bonne, B. E. Cole, and R. E. Higashi, "Micromachined Integrated Opto-Flow Gas/Liquid Sensor,". US: Honeywell Inc., Minneapolis, Minn., 1999.

[148] L. B. Kreuzer, "The physics of signal generation and detection," in *Optoacoustic Spectroscopy and Detection*, Y.-H. Pao, Ed. London: Academic Press Inc., 1977, pp. 1-25.

[149] J. I. Steinfeld, J. S. Francisco, and W. L. Hase, *Chemical Kinetics and Dynamics*. Upper Saddle River, New Jersey: Prentice Hall, 1989.

[150] L.-G. Rosengren, "A new theoretical model of the opto-acoustic gas concentration detector," *Infr. Phys.*, vol. 13, pp. 109-121, 1973.

[151] L. L. Beranek, *Acoustics*. Cambridge, MA: Acoustical Society of America, 1996.

[152] A. P. Institute, *Selected infrared spectral data*. College Station, TX: Texas A&M University, Thermodynamics Research Center, 1975.

[153] T. Tsuboi, K. Inomata, Y. Tsunoda, A. Isobe, and K.-i. Nagaya, "Light Absorption by Hydrocarbon Molecules at 3.392 μm of He-Ne laser," *Japanese Journal of Applied Physics*, vol. 24, pp. 8-13, 1985.

[154] A. B. Antipov, B. A. Antipov, and V. A. Sapozhnikova, "Absorption coefficients of some hydrocarbons in region of emission of a laser with $\lambda = 3.39$ μ," *Izvestiya Vysshikh Uchebnykh Zavedenii Fizika*, vol. 2, pp. 157-158, 1974.

[155] C. D. Hodgman, R. C. Weast, and S. M. Selby, "Handbook of Chemistry and Physics",, Thirty-Eighth ed. Cleveland, Ohio: Chemical Rubber Publishing Company, 1956.

[156] F. P. Incropera and D. P. DeWitt, *Fundamentals of heat and mass transfer*, Fourth ed. New York: John Wiley & Sons, 1996.

[157] D. R. Lide, "Handbook of Chemistry and Physics",, Eightieth ed. Cleveland, Ohio: Chemical Rubber Publishing Company, 1999.

[158] J. R. Howell and R. O. Buckius, *Fundamentals of engineering thermodynamics*, Second ed. New York: McGraw-Hill, Inc., 1992.

[159] R. B. Bird, W. E. Stewart, and E. N. Lightfoot, *Transport Phenomena*. New York: John Wiley & Sons, 1960.

[160] I. F. Golubev, *Viscosity of gases and gas mixtures*. Jerusalem: Israel Program for Scientific Translations, 1970.

[161] Y. Abe, J. Kestin, H. E. Khalifa, and W. A. Wakeham, "The viscosity and diffusion coefficients of the mixtures of light hydrocarbons with other polyatomic gases," *Ber. Bunsenges. Phys. Chem.*, vol. 83, pp. 271-276, 1979.

[162] P. M. Morse and K. U. Ingard, *Theoretical Acoustics*, First Princeton University Press edition, with errata page, 1986. ed. Princeton, New Jersey: Princeton University Press, 1968.

[163] Jodon, Inc., 62 Enterprise Drive, Ann Arbor, Michigan 48103.

[164] Stanford Research Systems, Inc.,1290D-T Reamwood Avenue, Sunnyvale, CA 94089.

[165] Thorlabs, Inc., 435 Route 206 North, Newton, NJ, 07860.

[166] Galileo Corp., Galileo Park, P.O. Box 550, Sturbridge, MA 01566.

[167] Molectron Detector, Inc., 7470 SW Bridgeport Road, Portland, OR 97224-7286.

[168] Thermo Spectra-Tech, 2 Research Drive, Shelton, CT 06484-0869.

[169] Knowles Electronics, Inc., 1151 Maplewood Drive, Itasca, Illinois 60143.

[170] National Instruments Corp., 11500 N. Mopac Expressway, Austin, TX 78759-3504.

[171] Laser Monitoring, Ltd., 18 Durham Way, Heathpark Industrial Estate, Honiton, Devon EX14-8SQ, UK

[172] Apex Microtechnology Corp., 5980 N. Shannon Road, Tucson, AZ 85741-5230

[173] S. D. Senturia, *Microsystem Design*. Dordrecht, The Netherlands: Kluwer Academic Publishers, 2001.

[174] G. T. A. Kovacs, *Micromachined Transducers Sourcebook*: McGraw-Hill, 1998.

[175] N. Maluf, *An Introduction to Microelectromechanical Systems Engineering*: Artech House, 1999.

[176] Pageworks, Inc., 501 Cambridge St., Cambridge, MA 02141.

[177] Philtec Inc., 1021 St. Margaret's Drive, Annapolis, MD 21401.

[179] C. M. Harris and C. E. Crede, *Shock and vibration handbook*, 2nd ed. New York: McGraw-Hill, 1976.

[180] W. H. Deen, *Analysis of Transport Phenomena*: Oxford University Press, 1996.

[181] H. D. Young, *Statistical Treatment of Experimental Data*. New York: McGraw-Hill, 1962.

[182] J. Y. Pan, "A study of suspended-membrane and acoustic techniques for the determination of the mechanical properties of thin polymer films," PhD Thesis, Cambridge, MA: M.I.T., 1991.